國立臺灣大學電機資訊學院電子工程學研究所

博士論文

Graduate Institute of Electronics Engineering
College of Electrical Engineering and Computer Science
National Taiwan University
Doctoral Dissertation

鍺錫磊晶薄膜之光學、穿隧與載子傳輸特性

Optical, Tunneling, and Carrier Transport Properties in GeSn Epitaxial Films

劉家佑

Chia-You Liu

指導教授：李峻霣 教授

Advisor: Professor Jiun-Yun Li

中華民國 112 年 2 月

February, 2023

doi:10.6342/NTU202300648

國立臺灣大學博士學位論文
口試委員會審定書

PhD DISSERTATION ACCEPTANCE CERTIFICATE
NATIONAL TAIWAN UNIVERSITY

鍺錫磊晶薄膜之光學、穿隧與載子傳輸特性

Optical, Tunneling, and Carrier Transport Properties in GeSn Epitaxial Films

本論文係劉家佑(F05943058)在國立臺灣大學電子工程研究所完成之博士學位論文，於民國 112 年 2 月 23 日承下列考試委員審查通過及口試及格，特此證明。

The undersigned, appointed by the Graduate Institute of Electronics Engineering on 2 / 3 / 2023 have examined a PhD dissertation entitled above presented by Chia-You Liu (F05943058) candidate and hereby certify that it is worthy of acceptance.

口試委員 Oral examination committee:

李敏鴻

（指導教授 Advisor）

林浩雄　吳肇欣　羅廣禮

張子璿　林建中　張書維

系主任/所長 Director: 江介宏

誌謝

轉眼間，已經在台大度過了十幾個春夏秋冬，每年的杜鵑花都開得那麼燦爛，陪伴著一屆屆的學長學弟們驕傲的飛遠。感謝一路上所有幫助我、陪伴我成長的所有人，如今我也已準備好啟程，面對人生的下一個階段。

首先感謝指導老師李峻霣教授一直以來的用心指導，從大四專題生開始持續到博士畢業將近八年的時間，在學術研究的道路上不斷鞭笞我更加的精進。也感謝能讓我在研究所生涯中接觸並操作各種常見與罕見的實驗機台，培養我各式各樣的實驗與做人處事的能力，使我在能力與心智上都成為一個合格的博士，面對以後的難關時不會覺得懷才不遇，並且能發揮所學解決問題。

再來要真心感謝在 QEL 實驗室的各位夥伴，隨時有人可以尋求幫助、一起討論研究上遇到的問題，這種感覺實在很棒，就算只是吃飯聊天講八卦也都很開心。感謝博士班的各位一起奮鬥支撐起 QEL 大大小小的日常運作與實驗。謝謝影響我研究主題最深得莊嚴學長，帶領我了解鍺錫與磊晶的有趣美妙之處，各種修理機台的技術也讓我偷學了很多。謝謝韋志學長各種大小瑣事的幫忙，在 QEL 裡的所有事沒有你不知道的。謝謝祥順每次都二話不說的陪我吃午餐、晚餐和大餐。謝謝俞叡和旻叡讓 QEL 成為真正的量子、絕對的低溫實驗室，讓我在後期的低溫量測都相當的順利。謝謝冠宇、誼炘、保全、梓弘、敬琮學長們，雖然只有最初幾年共同研究的日子，但卻讓我知道什麼是既厲害又認真的人，作為當初懵懂無知的我學習的優秀榜樣。謝謝我同名同姓的兄弟，達成了劉家佑既是碩士又是博士的疊加態。謝謝立耘、乃文、嘉澤、燿均、子茗、志穎、凱瑩、宗穎，或多或少我都藉由幫忙磊晶的名義，學到了你們各式各樣的研究主題和知識，讓我能有同時做好幾份研究的錯覺。也謝謝目前還在努力的學弟們，志力、蘇遙、睿濬、宸嶢、士傑...，陪我度過最後難產論文的階段，祝你們盡早順利的畢業。

我想特別感謝，從求學到研究陪伴我最久的柏元，從最初高中三年同窗，一起奮鬥指考到了台大，然後又每每選修你推薦我物理與半導體相關的課，還被你一路推坑進到了 QEL，又在這個實驗室裡一起奮鬥的好幾年。謝謝柏元一直以來的支援，學科上遇到不懂就可以直接找你問，實驗上遇到困難就找你幫忙，都會得到滿意的答案和結果，點出來的銀膠又好又漂亮。有太多有趣的和難忘的回憶，有太多

doi:10.6342/NTU202300648

學術和研究上的共同話題。我知道去美國讀 PhD 是你一直以來的規劃，但我就先在台大幫你解鎖部分的成就了。

另外，要謝謝英倫願意花許多時間和我研究論文最後的理論計算和物理觀念，讓我有機會在緊迫的時間內完成令人滿意的模擬結果。謝謝芝晨不斷的監控我寫論文的進度，雖然還是沒有放到期待的假期，但沒有超過死線的情況下畢業已經很慶幸了。也謝謝高中到現在的好朋友們，遠哲、騏瑄、政中、怡真、明澤、昀晉，聚餐聊天、騎車、打球、出遊、打牌，讓我苦悶的研究生日子過得沒那麼無聊。

最後一段要獻給我的家人，感謝父母從小到大一路以來的支持，感謝包容我的任性，都是我自己決定好走什麼領域和讀博士學位後才跟你們講，即使如此仍繼續無條件的默默支持我，讓我拖到現在才出社會工作賺錢。今後，我會努力做好身為兒子的本份的。

再次感謝大家，謝謝!

劉家佑 謹誌於

2023 年 3 月 1 日

doi:10.6342/NTU202300648

中文摘要

鍺錫(GeSn)材料因具有直接能隙和兼容於傳統矽製程的特性，而在許多研究應用上受到廣大的矚目。由於在其直接能谷(Γ)的電子擁有小的等效質量，因此可利用直接能隙的鍺錫材料來製作高性能的光電子元件，而得到高電子遷移率和高穿隧機率等優點。本篇論文利用化學氣相沉積法磊晶高品質的鍺錫薄膜，並使用許多材料分析技術來觀測其材料性質，包含穿透式電子顯微鏡、原子力顯微術、二次離子質譜法、X 光繞射與倒置空間圖譜技術。在鍺錫材料中，藉由增加其錫比例或施加拉伸應力來達到鍺錫直接能隙的條件。

直接能隙的鍺錫在許多材料特性上有顯著的進步與表現，例如量子穿隧、載子傳輸與光學性質。本篇論文利用化學氣相沉積法磊晶高品質的鍺錫薄膜，製作相關的鍺錫元件來探討上述的材料特性，並研究鍺錫中間接-直接能隙的轉換在材料性上的表現。為了增加鍺錫薄膜中的錫比例，我們探討磊晶成長過程中的各種條件，如氣體先驅物流量、磊晶溫度和鬆弛緩衝層。在鍺錫完全應變於鍺虛擬基板的結構中，可磊晶錫比例高達 18%的鍺錫薄膜，其薄膜受到相當大的壓縮應變達-2.4%。藉由成長與利用鍺錫鬆弛緩衝層，可使鍺錫薄膜的錫比例增加至最高 24%。

接下來，利用光致發光頻譜量測鍺錫磊晶薄膜中直接能隙與相關的光學性質。根據室溫下光致發光頻譜的結果，鍺錫直接能隙的大小會隨著錫比例增加而持續減少。在錫比例 24%的鍺錫薄膜中，其最窄的能隙達到只有 0.295 eV，此對應的發光波長為 4.2 微米。另外，量測低溫變溫(最低溫約 15 K)光致發光頻譜的結果顯示，鍺錫間接-直接能隙轉換發生在錫比例 8%附近。

為了研究鍺錫量子穿隧的特性，我們製作鍺錫穿隧二極體並具有良好的負微分電阻特性，藉由量測其峰值穿隧電流來探討鍺錫的能帶間穿隧效應特性。我們首次在室溫下在鍺錫穿隧二極體中展現負微分電阻特性。並且在應變鬆弛 $Ge_{0.925}Sn_{0.075}$ 元件中，分別在室溫與 4 K 低溫下，得到極高的峰谷電流比例達到 15 倍與 219 倍。比較各種應變條件的 $Ge_{0.925}Sn_{0.075}$ 的元件，藉由壓縮應變的鬆弛或更加施以拉伸應變，隨著直接能隙的穿隧效應逐漸的主導，其穿隧電流會隨之有顯著的增加。在拉伸應變鍺錫穿隧二極體中，分別在室溫與 4 K 低溫下達到 325 和 545 kA/cm^2 的峰值穿隧電流密度，此數值為所有四族穿隧二極體中最高的紀錄。藉由

doi:10.6342/NTU202300648

分析峰值穿隧電流隨溫度的變化，以及聲子輔助穿隧頻譜的量測，分析得到隨著施加拉伸拉伸應力，愈來越多電子於處在直接能谷(Γ)中並擁有較小的等校質量，導致較高的能帶間的穿隧機率。

論文最後的部分，以霍爾量測來探討鍺錫薄中電子傳輸性質。其中在 N 型 $Ge_{0.82}Sn_{0.18}$ 薄膜中，於 75 K 低溫下量到最高 9,500 cm^2/Vs 的電子遷移率。藉由比較所有樣品在 4K 低溫下的電子遷移率，可以清楚地發現在錫比例 8%以上的樣品中，電子遷移率會隨著錫比例增加而明顯的增高，並在錫比例 18%的鍺錫薄膜中達到最高值。電子遷移率隨著錫比例的變化也可以利用鍺錫的間接-直接能隙轉換所解釋，因為在電子在直接能谷(Γ)比在間接能谷(L) 擁有較小的等效質量，所以隨著直接能谷的電子數量變多，鍺錫整體的電子遷移率也隨之增高。此外，此章節也包含完整的理論計算來模擬鍺錫電子遷移率隨許多因素的變化趨勢，並可以清楚地解釋電子遷移率因為間接-直接能隙轉換而增加的過程。

關鍵字：鍺錫磊晶、化學氣相沉積、直接能隙、光致發光、能帶間穿隧效應、電子遷移率, 穿隧(江崎)二極體

doi:10.6342/NTU202300648

Abstract

GeSn has drawn great attention due to its direct-bandgap characteristic and the compatibility with Si VLSI technology. While high-performance optoelectronic devices were fabricated using direct-bandgap GeSn, high carrier mobility and tunneling probability have been demonstrated owing to its small electron effective mass in the direct Γ valley. In this work, high-quality epitaxial GeSn films were grown by chemical vapor deposition (CVD), and characterized by various material metrology tools, such as transmission electron microscopy (TEM), atomic force microscopy (AFM), secondary ion mass spectrometry (SIMS), X-ray diffraction (XRD), and reciprocal space mapping (RSM). Increasing its Sn fraction or applying tensile stresses is used to achieve a direct bandgap in GeSn. In order to achieve a high Sn fraction in GeSn, the effects of the flow rates of precursors, growth temperature, and relaxed buffer are investigated. For compressive-strained GeSn films on a Ge virtual substrate (VS), the Sn fraction up to 18 % was demonstrated with a large compressive strain of -2.4 %. Using a GeSn relaxed buffer, the highest Sn fraction of ~ 24 % is achieved in compressive-strained GeSn films.

Photoluminescence (PL) measurements were performed to characterize the bandgap energy in GeSn epitaxial films. At room temperature, the direct-bandgap energy of GeSn monotonically decreases with the Sn fraction. The smallest bandgap energy of 0.295 eV is demonstrated in the $Ge_{0.76}Sn_{0.24}$ film, corresponding to the wavelength of ~ 4.2 μm. The cryogenic (~ 15 K) PL spectra suggest that the indirect-to-direct bandgap transition in GeSn occurs at a Sn fraction around 8 %.

Esaki tunnel diodes with negative differential resistance (NDR) were used to characterize the band-to-band tunneling (BTBT) properties in GeSn. The GeSn Esaki diodes with clear NDR at room temperature are presented for the first. In the strain-

doi:10.6342/NTU202300648

relaxed $Ge_{0.925}Sn_{0.075}$ Esaki diodes, extremely high peak-to-valley ratios (PVCRs) of 15 and 219 are achieved at RT and 4 K, respectively. The tunneling current is increased by strain relaxation and further enhanced as the GeSn epitaxial film is under tensile stresses since the direct BTBT dominates. High peak current densities of 325 and 545 kA/cm^2 are demonstrated in the tensile-strained $Ge_{0.925}Sn_{0.075}$ diodes at RT and 4 K, respectively, which is the highest reported among group-IV Esaki diodes. Both temperature-dependence of the peak current density and phonon-assisted tunneling spectra suggest that by applying tensile stresses on GeSn, more electrons populate in the Γ valley, leading to a higher BTBT rate owing to its small electron effective mass.

Last, electron transport in GeSn is investigated by Hall measurements. The highest Hall mobility is 9,500 cm^2/Vs at 75 K in a n-type $Ge_{0.82}Sn_{0.18}$ film. At 4 K, the electron mobility increases with the Sn fraction as the Sn fraction is above 8 %. The mobility enhancement results from more electrons in the direct Γ valley, where electrons have a smaller effective mass than that in the L valley. The theoretical calculation on the GeSn electron mobility is also presented and suggests that the mobility enhancement is attributed to the indirect-to-direct bandgap transition.

Keywords: GeSn epitaxy, chemical vapor deposition, direct bandgap, photoluminescence, band-to-band tunneling, electron mobility, Esaki diodes.

doi:10.6342/NTU202300648

Contents

doi:10.6342/NTU202300648

doi:10.6342/NTU202300648

doi:10.6342/NTU202300648

doi:10.6342/NTU202300648

doi:10.6342/NTU202300648

List of Figures

doi:10.6342/NTU202300648

doi:10.6342/NTU202300648

doi:10.6342/NTU202300648

doi:10.6342/NTU202300648

doi:10.6342/NTU202300648

doi:10.6342/NTU202300648

doi:10.6342/NTU202300648

doi:10.6342/NTU202300648

doi:10.6342/NTU202300648

doi:10.6342/NTU202300648

List of Tables

doi:10.6342/NTU202300648

Chapter 1 Introduction

1.1 Motivation

GeSn alloys, belonging to the family of Group-IV semiconductors, draw much attention since it has direct-bandgap characteristics, enabling high-performance electrical and optical devices. Since GeSn is compatible to the Si VLSI technology, compared to high-cost III-V (or II–VI) materials, it is very promising for future device applications. Figure 1-1 illustrates the bandgap energy versus the lattice parameter for Group-IV and III-V materials [1]. In SiGe and GeSn alloys, there exist a transition of indirect-to-direct bandgap from the indirect (X, L) valley to the direct (Γ) valley in the conduction band. GeSn becomes a direct-bandgap material at a Sn faction of ~ 10 % [2] and is predicted as a zero-bandgap material at a Sn faction of ~ 35 % [3]. The direct-bandgap feature makes GeSn an promising material with high luminescence and absorption efficiency. Besides, the bandgap energy of GeSn covers the light bands of short-wave infrared (SWIR: 1.5 ~ 3 μm), mid-wave infrared (MWIR: 3 ~ 8 μm), and long-wave infrared (LWIR: 8 ~14 μm).

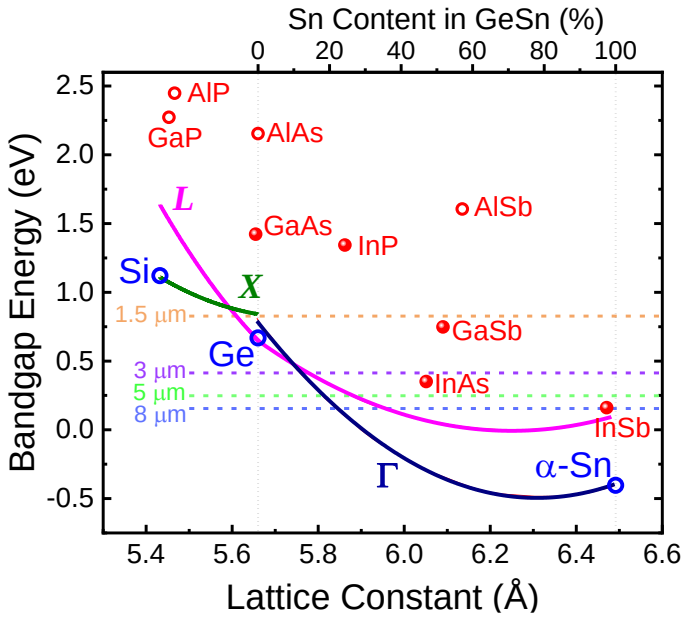

Figure 1-1 Bandgap energy versus lattice constant of group IV and III-V semiconductors [1].

doi:10.6342/NTU202300648

Many infrared applications would benefit from GeSn-based optoelectronic devices by their compatibility with the Si technology [1][4].

In addition to optoelectronic applications, the high carrier mobility in GeSn is also promising to for logic applications. Figure 1-2 shows carrier mobilities of group IV and III-V semiconductors versus their bandgap energy [5]. Among the bulk materials, Ge has the highest hole mobility (1,900 cm^2/Vs) and a very high electron mobility (3,900 cm^2/Vs). For GeSn alloys, the hole mobility can be even enhanced by compressive strain due to the small hole effective mass [6], which has been demonstrated in GeSn p-MOSFETs [7].. Besides, the electron mobility in GeSn is expected to be further boosted to 10^5 cm^2/V-s [8] due to the direct-bandgap characteristics with a very small effective mass of electrons in the Γ valley [9]. The electron mobility of direct-bandgap GeSn is comparable to high-electron-mobility III-V semiconductors, such as GaAs and InAs.

The direct-bandgap characteristic is not only promising for high-performance electronic device applications, but also can enable high-efficiency quantum devices, such as tunneling logic [10] or spintronic devices [11]. The tunneling probability can be effectively enhanced owing to its direct bandgap and smaller effective mass [2], enabling

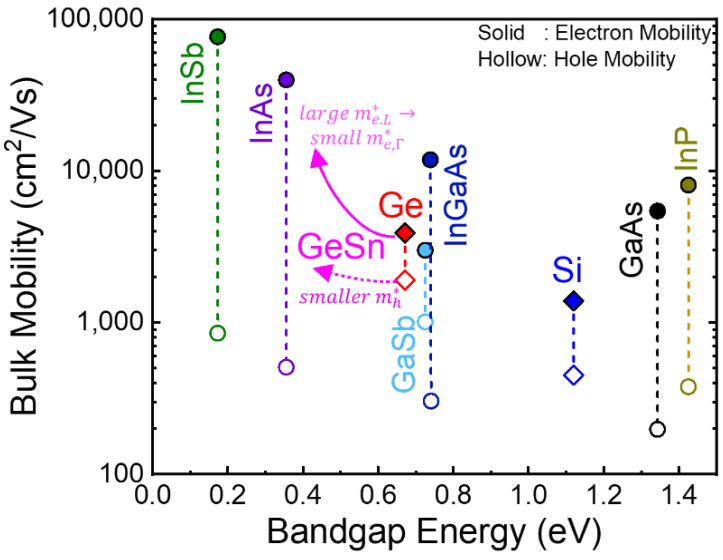

Figure 1-2 Bandgap energy versus lattice constant of group IV (Si, Ge, Sn) and III-V semiconductors [5].

doi:10.6342/NTU202300648

ultra-low power logic applications [12]. In addition to the tunneling application, GeSn has strong spin-orbit coupling (SOC) effects, a key to the next-generation spintronic logic [13] and quantum computing [14]. By varying the Sn fraction and strains in GeSn, the SOC strength can be modulated effectively [15]. A spin ballistic transport was reported in Ge for the first [16], enabling the spin logic for low-power application. Strong SOC in Ge enhances the spin flipping rates, which facilitates high-fidelity spin qubits [17]. GeSn is also cost-effective owing to its compatibility with the Si VLSI technology and could be used to realize high-performance electronic, optoelectronic, spintronic, and quantum devices in a single chip in the future.

1.2 Direct Bandgap in GeSn

1.2.1 Band Structure of GeSn

Figure 1-3 shows the calculated band structure of unstrained GeSn with different Sn fractions. For Ge, the energy difference between the direct (Γ) and indirect (L) valleys is $E_\Gamma - E_L \sim 140$ meV. By adding more Sn atoms into a Ge crystal, the energies of both the

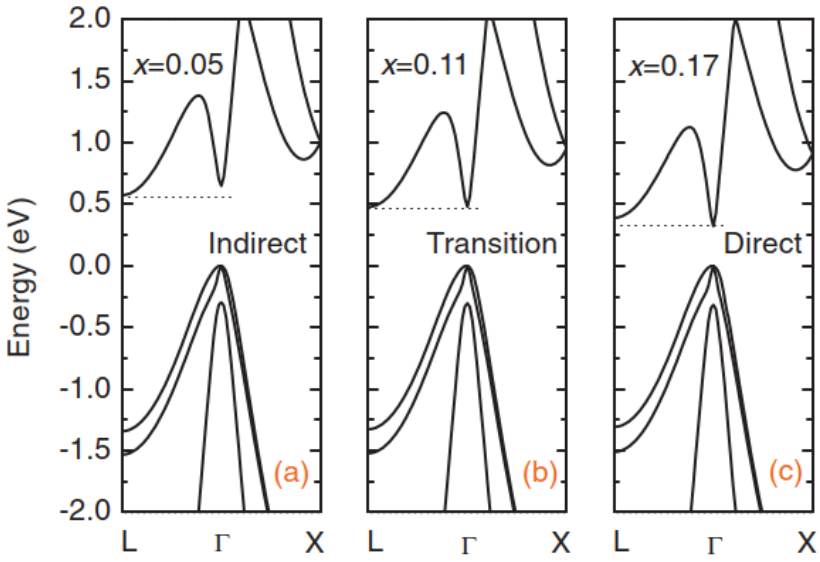

Figure 1-3 Bandgap structure of $Ge_{1-x}Sn_x$ with (a) x = 5 %, (b) x = 11 %, and (c) x = 17 % [2]. GeSn becomes a direct-bandgap material at a higher Sn fraction.

doi:10.6342/NTU202300648

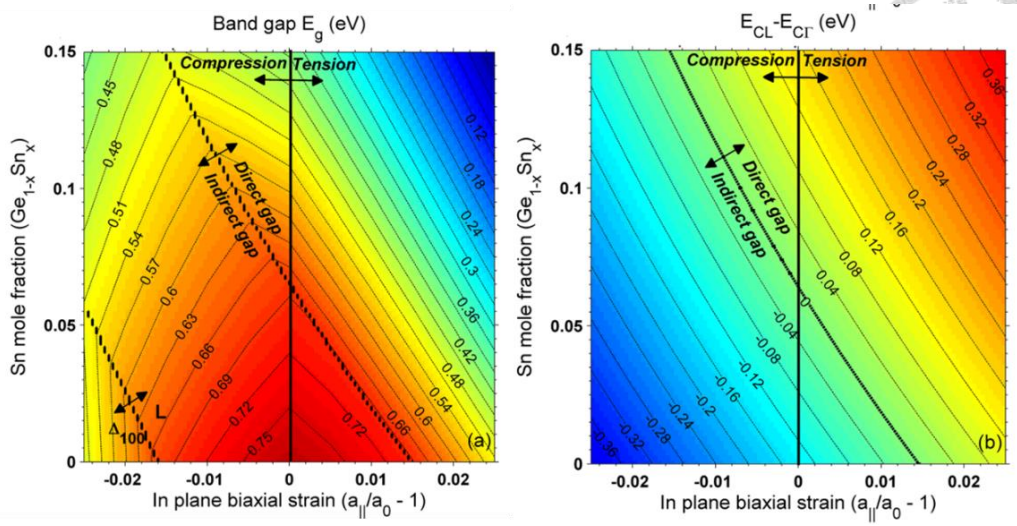

Figure 1-4 Contour of (a) bandgap energy and (b) energy difference between direct Γ and indirect L valley in $Ge_{1-x}Sn_x$ with different in-plane biaxial strain [18].

L-valley and Γ-valley decrease, while the energy of the Γ-valley decreases with a faster rate than the L-valley. At a low Sn fraction of ~ 5 % in Figure 1-3(a), GeSn remains an indirect-bandgap material like Ge, but with a smaller energy difference. The indirect-to-direct bandgap transition occurs at Sn fractions of 6 % ~11 %, while the crossover slightly varies in different simulation result [18][19]. For GeSn with a high Sn fraction (~ 17 % in Figure 1-3(c)), it becomes direct-bandgap, and the "direct" energy difference (E_L - E_Γ) increases by further increasing the Sn fraction. However, an elastic strain in GeSn-based heterostructures would deform its band structure. In the simulation results (Figure 1-4 [18]), the biaxial strain deforms both bandgap energy and change the energy difference. The compressive strain enhances the 'indirect' energy difference (E_Γ - E_L). Thus, the indirect-to-direct crossover is also dependent on the strain condition in GeSn films.

1.2.2 Electron Effective Mass in GeSn

The direct bandgap of GeSn is intuitively considered one of the most promising properties for optoelectronic devices for high efficiency of light absorption and luminescence. Moreover, in GeSn, the electron effective mass in the Γ-valley is smaller

doi:10.6342/NTU202300648

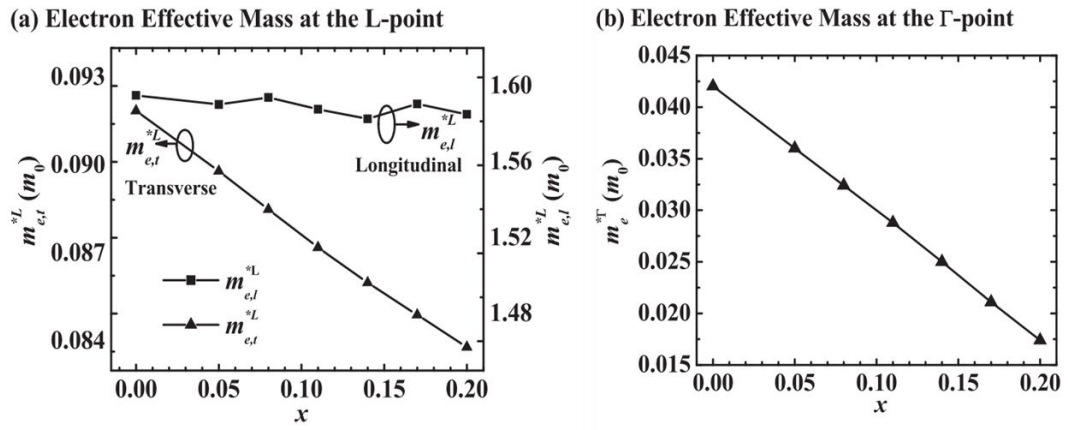

Figure 1-5 (a) Longitudinal and transverse electron effective mass at L-point, (b) Electron effective mass at Γ-point of $Ge_{1-x}Sn_x$ for x ranging from 0 to 0.2 [2].

than that in the L-valley. Figure 1-5 shows the calculated effective masses at the L-point and Γ-point in the $Ge_{1-x}Sn_x$ band structure [2]. The effective mass of L-electrons is at least three-time larger than that of Γ-electrons. In addition, the effective mass of Γ-electrons decreases significantly at a higher Sn fraction. The overall electron mobility of GeSn is determined by the electron population ratio in Γ-valley and L-valley, which complicates the analysis of electron transport properties in GeSn. This topic will be addressed in this work.

1.3 Challenges in Material Growth of GeSn

1.3.1 Low Solid Solubility of Sn (~ 1.1 %) in Ge

Despite many excellent properties in direct-bandgap GeSn, there are still some issues or challenges. One of the major issues is the low solid solubility of Sn fraction of 1.1 % in Ge (Figure 1-6 [20]). This thermodynamic constraint introduces great difficulty to obtain high-quality crystalline layers with a Sn fraction for direct-bandgap GeSn. Accordingly, material preparation by non-equilibrium methods is required to achieve metastable diamond-structure GeSn alloys. Low-temperature epitaxial processes using molecular beam epitaxy (MBE) or chemical vapor deposition (CVD) allows the

doi:10.6342/NTU202300648

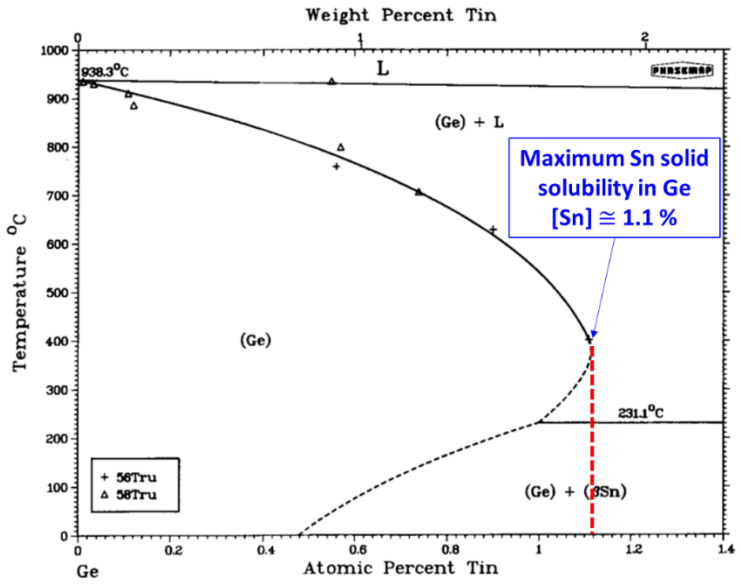

Figure 1-6 Enlarged view of 0 ~ 1.4 % Sn fraction of Ge-Sn phase diagram [20].

preparation of metastable GeSn films with crystalline quality. Even a high-quality GeSn alloy can be synthesized, the thermal budget in the fabrication process is severely limited due to the phase separation. The thermal budget becomes less with a higher Sn fraction in GeSn. Upon the phase separation occurs, the diamond-structure $Ge_{1-x}Sn_x$ film irreversibly becomes a mixture of $Ge_{0.99}Sn_{0.01}$ and β-Sn [21]. To avoid the material breakdown, the low-temperature process is also requested for device fabrication [22].

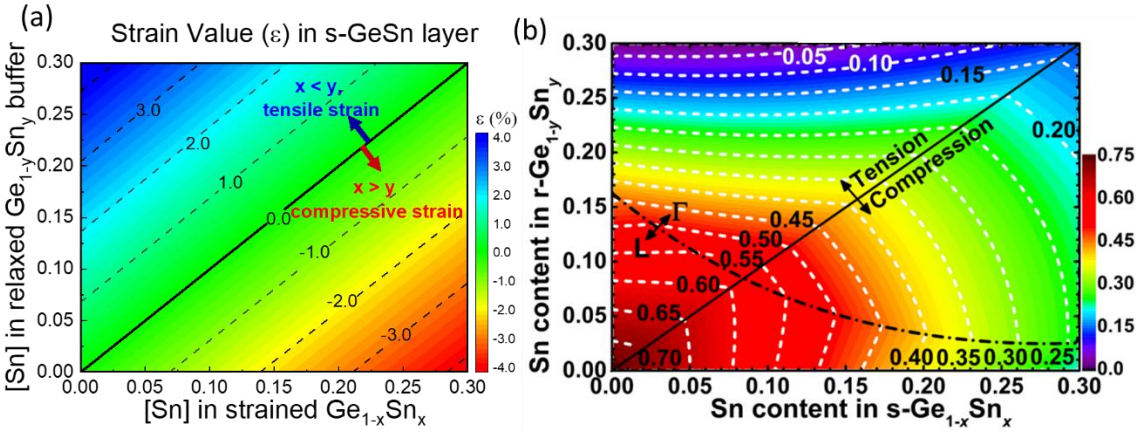

Figure 1-7 (a) Strain value of strained $Ge_{1-x}Sn_x$ coherently grown on relaxed $Ge_{1-y}Sn_y$ buffer and (b) the corresponding bandgap energy in the strained $Ge_{1-x}Sn_x$ [19].

doi:10.6342/NTU202300648

1.3.2 High-Quality GeSn Epitaxial Films and Strain Engineering

To aim at the monolithic integration of GeSn on a Si platform, epitaxial growth of GeSn films on Si wafers is commonly adopted. The issue of a very large lattice mismatch between Si and $Ge_{1-x}Sn_x$ is inevitable, leading to poor quality of GeSn epitaxial films. The lattice mismatch between Ge and Si lattices is 4.2% (Figure 1-1), and the mismatch is up to 16 % between Ge and Sn. Early prior works used Ge wafer as the starting substrate for GeSn epitaxy [23], while most of the recent works deposited a Ge buffer layer on Si as a virtual substrate (VS) for GeSn epitaxy [24]. Due to the larger lattice constant than Ge, epitaxial GeSn layers are compressive-strained. On the other hand, to grow a tensile trained GeSn layer, a substrate or a GeSn buffer with a larger lattice constant is required. Figure 1-7(a) shows the contour mapping of strained $Ge_{1-x}Sn_x$ coherently grown on a relaxed $Ge_{1-y}Sn_y$ buffer, and Figure 1-7(b) shows the corresponding bandgap energy in the strained $Ge_{1-x}Sn_x$ layer [19]. Although applying more tensile stresses on the GeSn films leads to direct-bandgap characteristics (upper region in the diagram), it is difficult to grow high-quality GeSn relaxed buffer a higher Sn fraction to provide the required tensile stresses. While preliminary results were reported to induce the local strain relaxation and tensile strain in GeSn films [25][26] ,further work is still required for high-quality and stain-tunable GeSn epitaxy for practical applications

1.4 Dissertation Organization

In this dissertation, we demonstrate GeSn epitaxy on the Si platform by CVD with a wide range of the Sn fraction by strain engineering (Chapter 2). Optical properties of GeSn are characterized by photoluminescence (PL) spectra at low temperatures and the indirect-to-direct bandgap crossover is investigated (Chapter 3). The tunneling properties of GeSn are characterized by the band-to-band tunneling (BTBT) current in GeSn Esaki

doi:10.6342/NTU202300648

tunnel diodes. The tunneling current is largely increased due to the direct-tunneling process and the temperature dependence of the peak tunneling current was investigated to understand the tunneling and bandgap characteristics (Chapter 4 and 5). Last, the transport properties of GeSn are characterized by Hall measurements on n-type GeSn films. The resulting large enhancement on the electron Hall mobility suggests the direct-bandgap GeSn is promising for electronic devices (Chapter 6). Then this thesis concludes with discussion, unsolved issues, and future direction in Chapter 7.

doi:10.6342/NTU202300648

Chapter 2 GeSn Epitaxy by Chemical Vapor Deposition

Epitaxy of single crystalline GeSn with high material quality is challenging due to the low equilibrium solid solubility (~1 %) of α-Sn in Ge [20]. The epitaxy technologies under a non-equilibrium condition are required to increase the Sn fraction higher than the 1 % for useful device applications, such as lasers [25][26], transistors [7][27], and spintronic devices [11]. The non-equilibrium GeSn epitaxy is usually achieved by low-temperature growth, such as molecular beam epitaxy (MBE) [23], magnetron sputtering [28], and chemical vapor deposition (CVD) [29]. The first attempt to grow GeSn alloys was based on MBE technology in 1990s [30]. However, the low throughput is its main drawback for mass production. Magnetron sputtering has been reported recently to increase the throughput issue, while this technique is still immature and the material quality needs much further improvement [28]. On the other hand, CVD technique for GeSn epitaxy is promising due to the high throughput and uniformity for a large wafer size up to 300-mm [31]. High-quality and low-cost GeSn epitaxial films were grown on Si wafers using a Ge buffer as a virtual substrate by both ultra-high vacuum (UHV) CVD [32] and reduced-pressure (RP) CVD [24]. In this work, a commercial RPCVD system is used to grow GeSn epitaxial layers on Si substrates.

2.1 Introduction

A commercial CVD system (ASM Epsilon 2000, Figure 2-1) is used to grow GeSn epitaxial films on Si wafers in this work. It is a 200-mm single-wafer system. The processing pressure of this system is designed to be 10 ~ 100 torr. The reaction chamber is made of a cold-wall quartz, where an 8-inch wafer is placed on a graphite susceptor. A

doi:10.6342/NTU202300648

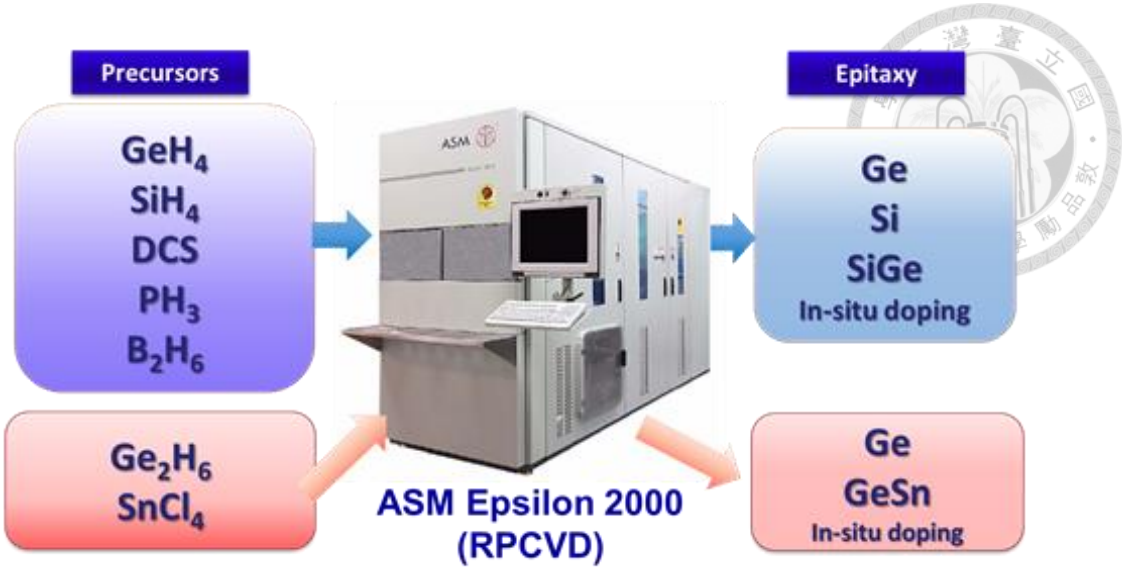

Figure 2-1 An ASM Epsilon 2000 RPCVD system. The original and extended precursor gas systems are used for Si/Ge/SiGe or Ge/GeSn epitaxy.

wafer is heated by an array of tungsten halogen lamps, and real-time temperature monitoring in different zones is performed by thermocouples. The power of the lamps is adjusted by a PID controller to achieve high uniformity of epitaxial films. Since the wafer and the susceptor are heated directly by lamps with a heating rate over 2 ºC/sec, the system is also called a rapid-thermal chemical vapor deposition (RTCVD) system.

The precursors for the growth of Si, Ge, and SiGe epitaxial films are silane (SiH_4), DCS (dichlorosilane, SiH_2Cl_2), and germane (GeH_4). For the growth of GeSn, an extended gas system of digermane (Ge_2H_6) and tin tetrachloride ($SnCl_4$) was established.

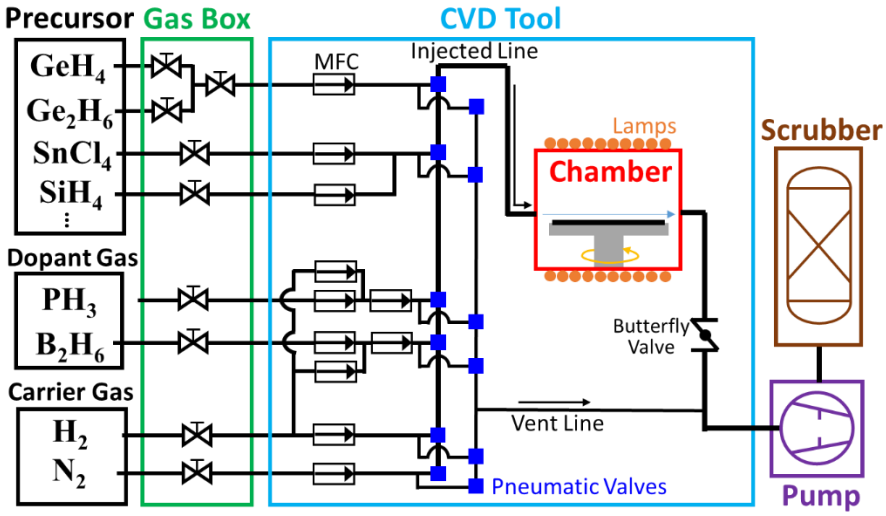

Figure 2-2 RPCVD system gas delivery diagram.

doi:10.6342/NTU202300648

High-purity H_2 (99.9999%) or N_2 (99.9999 %) is used as the carrier gas.

Figure 2-2 shows gas delivery and the RPCVD system. The flow rates of the precursors are controlled by individual mass flow controllers (MFCs) before the precursors are mixed with the carrier gas and then delivered to the reactor. PH_3 and B_2H_6 are served as the n-type and p-type dopant gases, respectively. For a wider range of doping concentrations, the dopant gases are diluted with H_2. The chamber is pumped continuously with a two-stage rotary vane pump, and the processing pressure is controlled by a butterfly valve between the chamber outlet and the pump. At last, the exhaust gas is delivered to a local scrubber for burn-out.

According to the Ge-Sn phase diagram (Figure 1-6), it is impossible to achieve a Sn fraction over 1.1 % by the thermal-equilibrium growth method. Therefore, to grow GeSn alloys with a high Sn fraction, a non-equilibrium process is required, such as low-temperature growth (e.g. below 350 ^oC). The low temperature could suppress the Sn precipitation due to the lower thermal energy for the activation of phase separation. To facilitate the growth process, more active precursors is preferred. Since high-order silicon hydrides provides a higher growth rate for Si epitaxy [33], high-order germanium hydrides, such as digermane (Ge_2H_6) and trigermane (Ge_3H_8), are good candidates for the GeSn epitaxy. Since Ge_2H_6 is gaseous and Ge_3H_8 is liquid at room temperature, Ge_2H_6 is selected as the precursor for the GeSn growth to avoid using a bubbler.

Since the bonding energy of Ge-Ge (188 kJ/mol) in Ge_2H_6 is smaller than that of Ge-H (288 kJ/mol) in GeH_4, Ge_2H_6 molecules tend to decompose into GeH_3 radicals in the gas phase at a lower temperature. The growth mechanism is schematically depicted in Figure 2-3 with the following reaction:

$$Ge_2H_{6(g)} + \underline{H} \rightarrow \underline{Ge}H_{3(g)} + GeH_{4(g)} \qquad \text{Eq. 2-1}$$

The underlines represent an atom is bonded on the growth surface (Figure 2-3).

doi:10.6342/NTU202300648

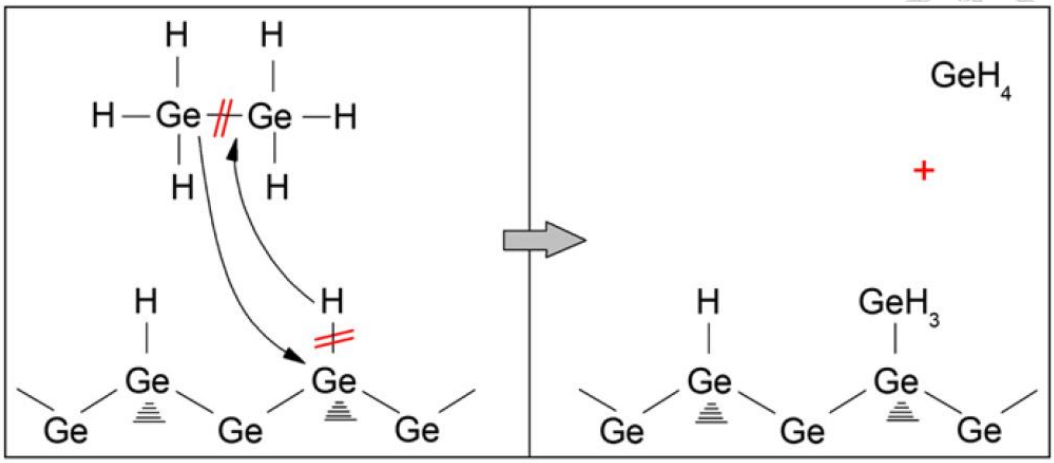

Figure 2-3 Schematic diagram of the GeH_3 adsorption from $Ge_2H_{6(s)}$ onto a H-passivated surface [29].

The Ge-Ge bond of the Ge_2H_6 molecule and the Ge-H bond are broken, and GeH_3 radicals are adsorbed on the surface with the formation of GeH_4 molecules as by-products, which is less reactive than Ge_2H_6, especially at a very low temperature. It is noteworthy that the reaction doesn't require open sites for the GeH_3 adsorption, so it is less limited by the H-covered surface for low-temperature growth. Figure 2-4(a) shows an Arrhenius plot of the Ge growth rate using Ge_2H_6 at the temperature range of 275 ~ 800 °C [29]. The transition of Ge_2H_6 between the mass-flow regime and the surface-reaction regime is at 350 ~ 400 °C, ~ 100 °C lower than that of GeH_4 [34][35]. Figure 2-4(b) compares the growth rates of Ge using GeH_4 and Ge_2H_6 at temperatures of ~ 400 °C [34]. Using H_2 as the carrier gas and under the same partial pressure, the Ge growth rate by Ge_2H_6 is 3.5 times higher than that by GeH_4. Both the lower transition temperature and the higher growth rate are attributed to the lower bonding energy of Ge-Ge in Ge_2H_6. Besides, the Ge_2H_6 growth rate using N_2 as the carrier gas is slightly higher that using H_2 because more open surface sites without hydrogen passivation enhance the adsorption of the precursor molecules. As a result, Ge_2H_6 is more suitable for low-temperature epitaxy. In practice, since the boiling point of Ge_2H_6 (29 °C) is slightly higher than room temperature, we utilize the diluted 10% Ge_2H_6 in H_2 stored in a gas cylinder to prevent condensation.

doi:10.6342/NTU202300648

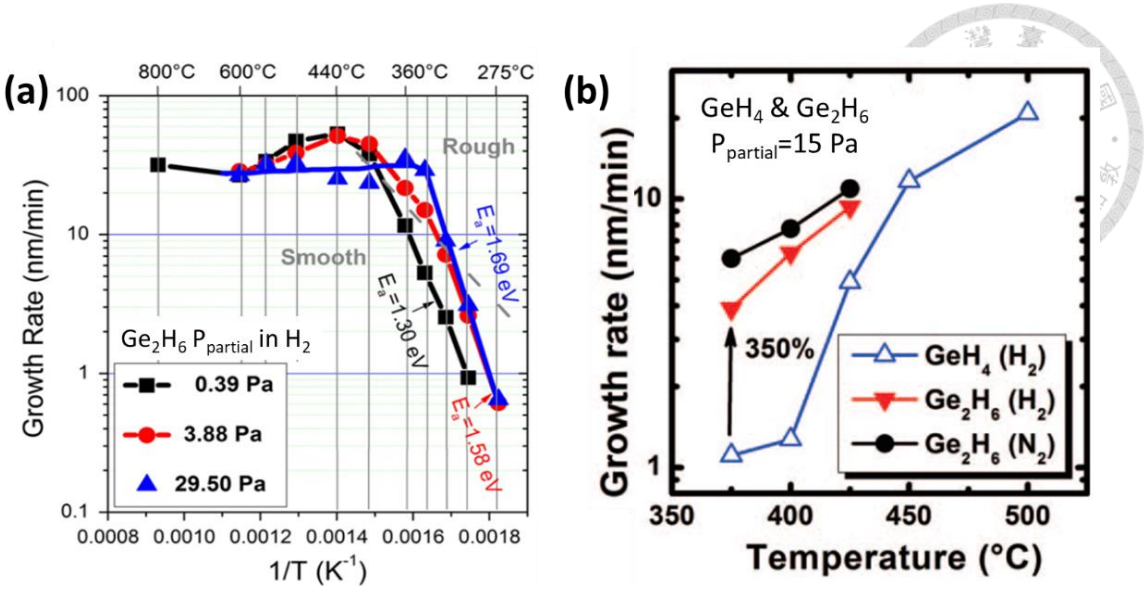

Figure 2-4 (a) Arrhenius plot of Ge growth rate by Ge_2H_6 [29]. (b) Ge growth rate as a function of the temperature by GeH_4 and Ge_2H_6 [34]

For GeSn CVD epitaxy, only tin-deuterium (SnD_4) [36] and tin-tetrachloride ($SnCl_4$) [29] were reported. Since SnD_4 is also a hydride, whose characteristics are similar to SiH_4 and GeH_4, it might be more ideal for the CVD growth. However, its poor stability leads to safety concerns for storage. Even though highly diluted SnD_4 (~ 1 % in H_2) could slow down the SnD_4 decomposition, it can only remain stable for six days and be completely decomposed within two days at room temperature, where the deposited tin metal catalyzed the further SnD_4 decomposition in the cylinder [37]. Although some solutions can be adopted to extend the storage time, such as special passivation on a storage cylinder [37] or being stored at liquid nitrogen temperature (-196 °C) [36], it is not cost effective.

On the other hand, although $SnCl_4$ is liquid at room temperature, it is widely used for its stability, low cost, and well development for metal-organic chemical vapor deposition (MOCVD) and atomic layer deposition (ALD). It is convenient and cost-effective to extend the gas system for the GeSn epitaxy. Figure 2-5(a) shows a $SnCl_4$ bubbler system in a CVD system. H_2 is injected to the bubbler of liquid $SnCl_4$ and mixed with $SnCl_4$ vapors. Then the mixed gases are delivered to the CVD reactor. The volume

doi:10.6342/NTU202300648

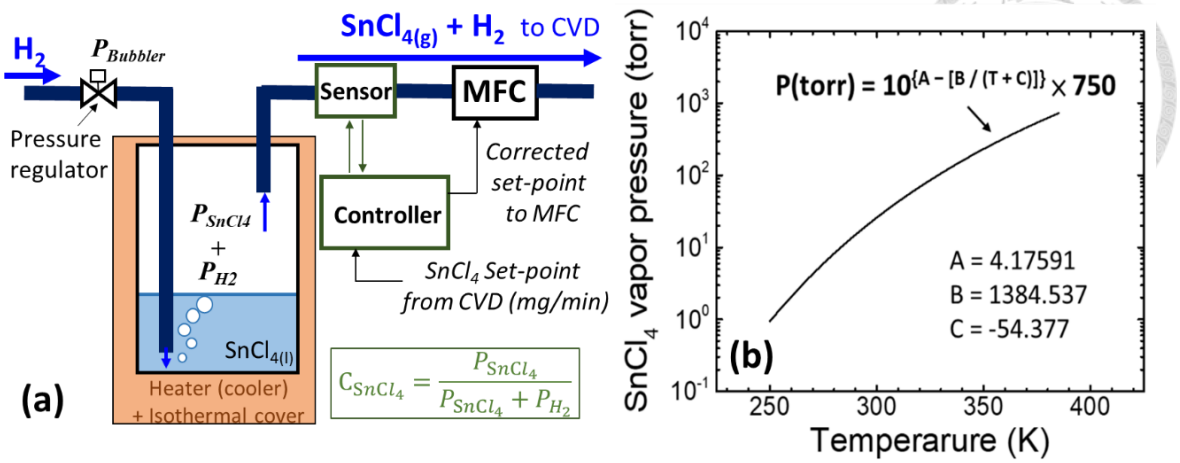

Figure 2-5 (a) A schematic diagram of a $SnCl_4$ bubbler system with a real-time concentration sensor (b) $SnCl_4$ vapor pressure versus temperature [38].

concentration of $SnCl_4$ (C_{SnCl_4}) in the mixed gases can be adjusted by the total bubbler pressure ($P_{Bubbler}$) and the vapor pressure of $SnCl_4$:

$$C_{SnCl_4} = \frac{P_{SnCl_4}}{P_{SnCl_4} + P_{H_2}} = \frac{P_{SnCl_4}}{P_{Bubbler}} \qquad \text{Eq. 2-2}$$

The total bubbler pressure is fixed at 3,000 torr by a pressure regulator in the inlet of H_2, while the vapor pressure of $SnCl_4$ is controlled by the liquid temperature of $SnCl_4$ (5 °C). According to Figure 2-5(b) [38], the vapor pressure of $SnCl_4$ is 7 torr. Since a deviation of dynamic pressure and bubbler temperature would result in the fluctuation of the $SnCl_4$ concentration in the mixed gas, a real-time concentration sensor (Vecco Piezocon®) is installed in series before MFC. The real-time $SnCl_4$ concentration is sensed by measuring the acoustic speed of mixing gas, and the sensor controller will feedback the corrected gas flow rate ($F_g\{SnCl_4/H_2\}$ in the unit of sccm) to the MFC. The mass transfer rate of $SnCl_4$ ($F_m\{SnCl_4\}$ in the unit of mg/min) is calculated by

$$F_m\{SnCl_4\}(\text{mg/min}) = C_{SnCl_4} \times F_g\{SnCl_4/H_2\}(\text{sccm}) \times \frac{260.5\ \text{(g/mol)}}{22.4\ \text{(L/mol)}} \qquad \text{Eq. 2-3}$$

The gas flow rate is then adjusted accordingly based on the measured $SnCl_4$ concentration to calibrate the mass transfer rate of $SnCl_4$ more accurately.

doi:10.6342/NTU202300648

2.2 GeSn Epitaxial Layers on Si Substrates

Due to the large lattice mismatch between Si and GeSn, direct GeSn growth on a Si surface is not preferred for high-quality GeSn films [34][39]. Figure 2-6(a) shows the TEM figure of $Ge_{0.92}Sn_{0.08}$ films directly grown on a Si substrate, and quite a few defects and dislocations are generated in the GeSn layer. The estimated threading dislocation density (TDD) from the TEM figure is ~ 10^{11} cm^{-3}. The additional thermal treatment to eliminate dislocations is not suitable due to the low thermal budget limited by the GeSn phase separation. The high dislocation density in the GeSn layer may accelerate the evolution of Sn precipitation. Reference [40] showed that a high density of Sn atoms are accumulated along the prorogation line of the threading dislocation from the atom probe tomography (APT) image. Therefore, we used relaxed Ge buffers as the virtual substrates (VS) for GeSn epitaxy. Figure 2-6(b) presents a well-developed Ge VS with a lower threading dislocation density of ~ 10^{8} cm^{-3}, enabling the high-quality GeSn epitaxial growth. Since the GeSn layer is fully strained on the Ge VS, no additional dislocation is induced in the strained GeSn layer (no visible defect found in the TEM figure). As the thickness of the GeSn layer becomes larger, the GeSn film will be relaxed again, and dislocations will be generated.

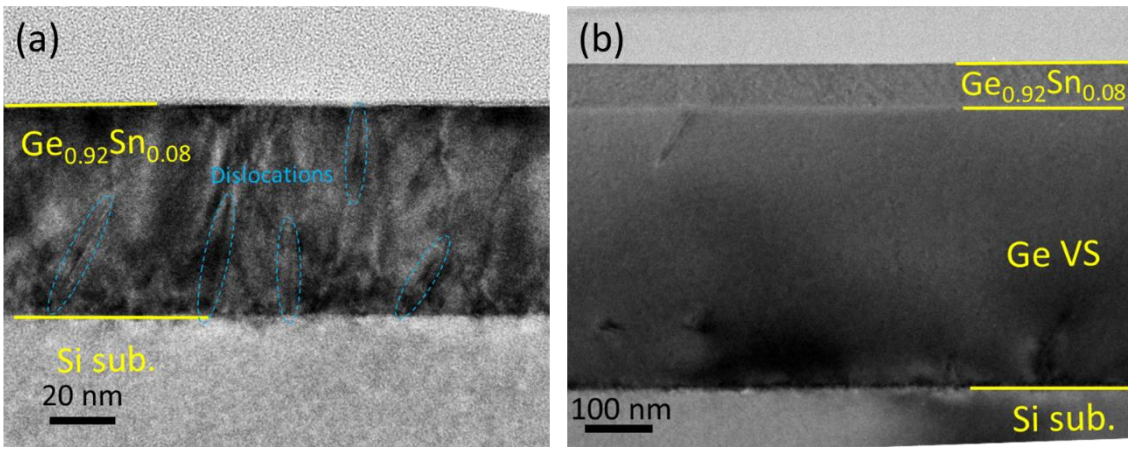

Figure 2-6 TEM images of GeSn epitaxial layers: (a) a GeSn film directly grown on a Si substrate and (b) a GeSn film pseudomorphically grown on a Ge VS.

doi:10.6342/NTU202300648

2.2.1 CVD Processes of GeSn Epitaxy

Prime-graded 200-mm Si (001) wafers were used for the GeSn epitaxy. Doping types and the resistivity of wafers depend on the device applications. Before the epitaxial growth, Si wafers were dipped in diluted 1:50 HF for 120 seconds and spin-dried in a warm N_2 ambience. The wafers were placed into the loadlock of the CVD tool and then transferred into the reactor chamber. Figure 2-7 shows a general process flow of the GeSn growth. The quartz chamber was first heated to 1170 ºC, and the chamber coatings due to the previous runs were etched by gaseous HCl. The temperature of the susceptor was set to 600 ºC during the wafer loading step. Then the wafer was baked in-situ at 1100 ºC in a H_2 ambience to remove native oxides, and the Si surface was covered by hydrogen and ready for the epitaxial steps. A Ge buffer layers (100 ~ 500 nm) was deposited on the Si substrate at temperatures below 400 ºC, preventing the three-dimensional island nucleation in the Stranski–Krastanow (S-K) growth mode [41]. In order to achieve strain-relaxation and eliminate threading dislocation of the Ge layer, the wafer was in-situ annealed by H_2 at 800 ◦C for 10 minutes [42][43]. This strain-relaxed Ge layer is served as a virtual substrate (VS) for the subsequent GeSn deposition. GeSn layers were grown at a low temperature of ~ 320 ºC, and a lower temperature is required for a higher Sn

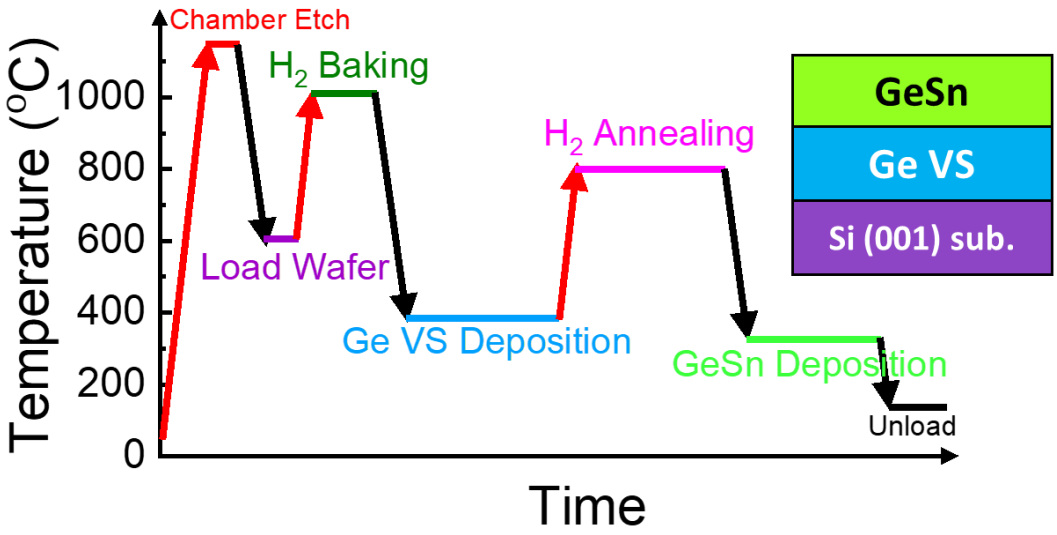

Figure 2-7 A process flow of the GeSn growth.

doi:10.6342/NTU202300648

fraction in GeSn. After the growth steps were finished, the wafer was cooled down below 200 ºC and unloaded to the loadlock chamber.

2.2.2 Ge Virtual Substrate

The Ge VS is a cornerstone for Ge-based heteroepitaxy on Si substrates, such as Ge/GeSi and Ge/GeSn heterostructures. In the early approaches for high-quality Ge growth, the SiGe graded relaxed buffers from 0 % to 100 % were used, requiring a fairly thick SiGe buffer layer (~ 10 μm) and a chemical-mechanical polishing (CMP) process [44]. In contrast, the Ge VS by high-temperature annealing can achieve high relaxation rates, a smoother surface (few nanometers in roughness), and a TDD of ~ 10^8 cm^{-2} with a thinner buffer thickness of a few-hundred-nm [42]. The surface roughness and TDD can be improved further by increasing the Ge thickness to 1 ~ 2 μm or performing more deposition-annealing cycles [45]. Figure 2-8 explains the growth mechanism of Ge VS by thermal annealing at high temperatures [46]. Due to the large lattice mismatch of 4.2 % between Si and Ge, the fully strained Ge layer can remain only about 3 monolayers (~ 0.8 nm), beyond which the 3D island-type growth would occur at a sufficiently high growth temperature [41]. This growth mode is called Stranski–Krastanow (S-K) mode. To obtain a thicker Ge layer, the initial Ge growth on the Si surface requires the low-

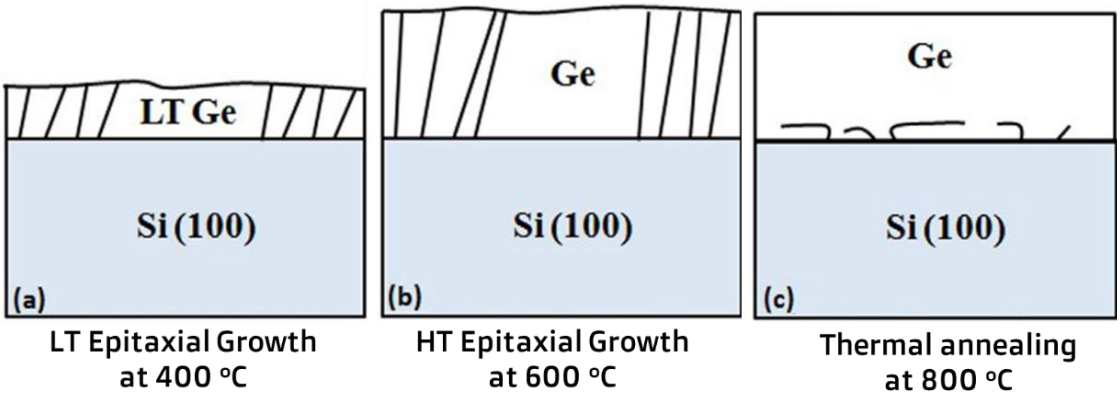

Figure 2-8 Schematic diagram of the growth mechanism of Ge VS by (a) 400 ºC, (b) 600 ºC, and (c) 800 ºC thermal annealing [46].

doi:10.6342/NTU202300648

temperature deposition to guarantee a layer-by-layer growth mode, or called Frank–van der Merwe (FM) mode. A large number of threading dislocations would occur in the Ge layer. With a relatively thick Ge layer deposited at low temperatures, another Ge layer is deposited at a higher temperature with a reasonable growth rate. At last, another high-temperature thermal annealing is performed to glide and annihilate the threading dislocations. Misfit dislocations are confined at the bottom of the Ge VS, and the density of threading dislocations is effectively reduced [42] (Figure 2-6(b)). Note that while the Ge VS is expected to be fully relaxed after the annealing steps, in practice, it is slightly tensile-strained on the Si substrate, which is due to the difference of the thermal expansion coefficients between Si and Ge [43][46].

Here, we introduce some useful parameters for the strain engineering of GeSn epitaxy in this work. First, the strain ε describes the elastic condition of an epitaxial layer, which can be divided into a lateral strain $\varepsilon_{\parallel}$ along the in-plane directions and a vertical strain $\varepsilon_{\perp}$ along the out-of-plane direction:

$$\varepsilon_{\parallel} = \frac{a_{\parallel} - a_0}{a_0} \quad and \quad \varepsilon_{\perp} = \frac{a_{\perp} - a_0}{a_0} \qquad \text{Eq. 2-4}$$

where $a_{\parallel}$ and $a_{\perp}$ represent the lattice constant of the layer parallel and vertical to the surface plane, respectively, and a_0 denotes the unstrained (fully relaxed) lattice constant of the layer. Since the epitaxial films are grown on a 8” wafer, the strain (ε) of the film along the in-plane x- and y-directions are the same and defined as the biaxial strain($\varepsilon_{\parallel}$).

$$\text{Biaxial strain } \varepsilon = \varepsilon_{\parallel} = \varepsilon_{\mathrm{x}} = \varepsilon_{\mathrm{y}} \qquad \text{Eq. 2-5}$$

The biaxial strain ε < 0 means the layer is compressive-strained, while ε > 0 means the layer is tensile-strained. The relationship between $\varepsilon_{\parallel}$ and $\varepsilon_{\perp}$ can be described with the Poisson’s ratio ν of the material:

doi:10.6342/NTU202300648

$$\frac{\varepsilon_{\perp}}{\varepsilon_{\parallel}} = -\frac{2\nu}{1-\nu} \quad \text{Eq. 2-6}$$

The relaxation rate *R* describes the relaxation degree of an epitaxial layer:

$$R = -\frac{a_{\parallel} - a_S}{a_0 - a_S} \times 100 \ \ (\%) \quad \text{Eq. 2-7}$$

where a_S represents the in-plane lattice constant, of the substrate layer. *R* = 0 means the layer is fully strained on the substrate (buffer layer), and *R* = 100% means the layer is fully relaxed.

The strain condition of the Ge VS can be calculated from the Ge peak in XRD curves (Figure 2-10(a)). The strain of the Ge VS is +0.18 % with the relaxation *R* of 104 % relative to a Si substrate. Thus, the Ge VS is tensile-strained on a Si substrate, which is consistent with prior works [43][46]. This tensile strain on a Ge VS leads to a slightly larger lateral lattice constant than that of bulk Ge. When considering the strain condition of GeSn films on the Ge VS, the modified lattice constant due to this tensile strain are used in this work.

2.2.3 Compressive-Strained GeSn on Ge Virtual Substrate

Compressive-strained $Ge_{1-x}Sn_x$ films were pseudomorphically grown on the Ge VS, with the Sn fraction x up to 18 %. The thickness of GeSn was carefully controlled below the critical thickness to avoid additional dislocations in the GeSn layer. For example, the cross-section TEM of compressive-strain $Ge_{0.92}Sn_{0.08}$ on Ge is shown in Figure 2-6(b), and the high-resolution TEM figure at the GeSn/Ge heterointerface is shown in Figure 2-9(a). The clear atomic image at the defect-free interface shows the high crystallinity and coherent growth of the strained GeSn layer. Figure 2-9(b) shows the surface morphology of compressive-strained $Ge_{0.92}Sn_{0.08}$ by atomic force microscope (AFM). The root-mean-square (RMS) surface roughness of 3.16 nm is relatively low and the

doi:10.6342/NTU202300648

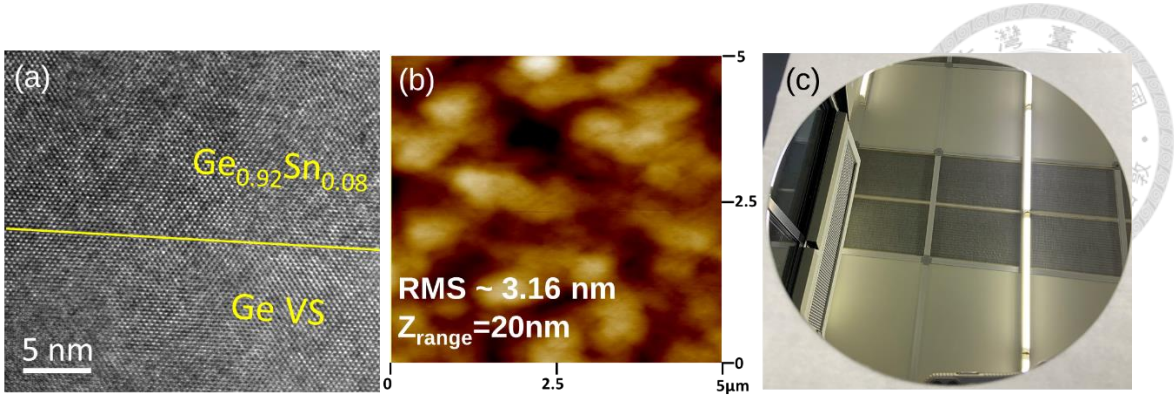

Figure 2-9 (a) A HRTEM image of a GeSn/Ge heterointerface. (b) Surface morphology of compressive-strained GeSn by AFM. (c) Mirror-like surface of GeSn epitaxy.

GeSn surface is mirror-like (Figure 2-9(c)). Due to the conformal GeSn growth on Ge VS without strain relaxation, the GeSn is as flat as the Ge VS [29].

X-ray diffraction (XRD) is a very useful technique to study crystal structures, such as lattice constants and strain conditions. In this work, the Sn fraction and strain condition of the GeSn films were determined by single-axis omega-2theta scanning (rocking curve) or further two-axis XRD mapping (reciprocal space mapping, RSM). The high-resolution XRD tool (PANalytical X'Pert Pro) was used with an ω-2θ angular resolution up to 0.0001°. The incident X-ray is Cu-Kα line with a wavelength of 0.154 nm.

Figure 2-10(a) shows XRD (004) rocking curves of compressive-strained GeSn on

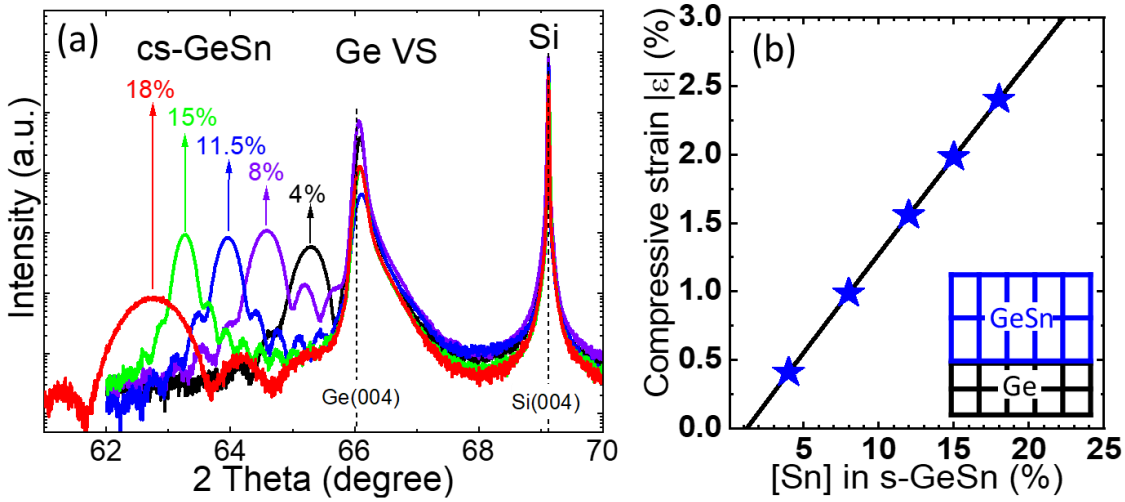

Figure 2-10 (a) XRD rocking curves of compressive-strained GeSn films on Ge VS. (b) The compressive strain of GeSn films vs. the extracted Sn fractions.

doi:10.6342/NTU202300648

the Ge VS with Sn fractions from 4 % to 18 %. The normal vector of the measured sample is calibrated by the (004) peak position of the Si substrate ($2\theta=69.126^{o}$). The peak positions of all Ge VSs are close and at slightly higher angles than that of bulk Ge. According to the Bragg's law, a higher diffracting angle means a smaller vertical lattice constant. The Ge VS is slightly tensile-strained along in-plane directions, and the out-of-plane lattice constant is shrunk. The peaks of GeSn layers are at smaller angles than that of the Ge VS. As the Sn fraction increases, the angle of GeSn peaks becomes, indicating the a larger lattice constant in the GeSn films. Pendellösung fringes are observed along with the GeSn peaks for all curves, showing high crystal quality and coherent stacking of the fully strained GeSn films. Since the angular spacing of the fringes is inversely proportional to the layer thickness, the thickness of GeSn can be directly extracted in this case. FWHM (full width at half maximum) of an XRD peak can be used to characterize the film quality. In order to prevent strain relaxation, the thickness of the GeSn strained layers are below the critical thickness (10 ~ 50 nm), reducing the signals and leading to a broad FWHM due to Scherrer broadening (Figure 2-10(a)). On the other hand, the presence of the Pendellösung fringes associated with the GeSn peak suggests the high crystallinity of these epilayers. The strains and the corresponding Sn fraction in GeSn were extracted from the peak position by the Vegard's law, where the lattice constant and the Poisson's ratio of the GeSn films are assumed the linear combination of those for Ge and α-Sn. Figure 2-10(b) shows the strains and extracted Sn fractions. The highest compressive strain is up to -2.4 % in the $Ge_{0.82}Sn_{0.18}$ film. The extracted straight line between the Sn fractions and strain doesn't pass through the origin with an intercept at [Sn]= 1.2% due to the slight tensile strain of Ge VS.

To further confirm the strain in the GeSn films, RSM analysis was performed. Figure 2-11(a) shows the normal (224) mapping in a reciprocal space, with the x-axis of the

doi:10.6342/NTU202300648

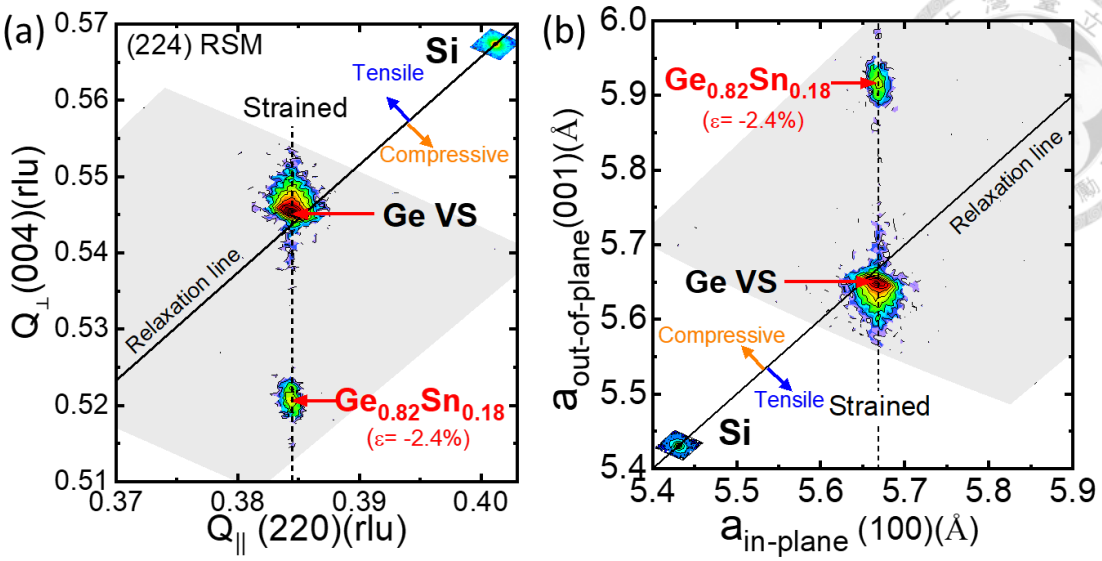

Figure 2-11 RSM contour mapping of strained $Ge_{0.82}Sn_{0.18}$ on Ge VS in terms of (a) reciprocal-space wavevector and (b) real-space lattice constant.

reciprocal along the (220) direction and the y-axis of the reciprocal along the (004) direction. The raw data by RSM were converted into the real-space lattice constant (Figure 2-11(b)). The relaxation line represents the fully relaxed condition of the diamond structure; that is, the in-plane and the out-of-plane lattice constants are equal (Figure 2-11(b)). The peak of Ge VS is close to the relaxation line, but slightly above and below the relaxation line in Figure 2-11(a) and (b), respectively, showing a small tensile strain of 0.18 %. The peak of $Ge_{0.82}Sn_{0.18}$ is far below the relaxation line in the reciprocal space (or above the relaxation line in real space), meaning the GeSn layer is under a large stress. Furthermore, the peaks of Ge VS and $Ge_{0.82}Sn_{0.18}$ are on the same vertical line, which suggests the $Ge_{0.82}Sn_{0.18}$ film and the Ge VS have the same lateral lattice constant and the former is fully strained to the latter.

There exists a critical thickness, which limits the thickness of epitaxial GeSn on a Ge VS. The critical thickness of GeSn on a Ge buffer has been calculated based on Matthews and Blakeslee (M-B) model and People and Bean (P-B) model in previous works [47][48] (black and red lines in Figure 2-12). The M-B model is a mechanical equilibrium model, which describes that the force from the elastic strain energy in the

doi:10.6342/NTU202300648

film is large enough to glide threading dislocations and to create misfit dislocations at the interface [49]. The P-B model is based on the non-equilibrium theory that a thicker film is required to nucleate a dislocation half-loop to form a (threading) dislocation-free film [50]. The region below the line of the M-B model is known as the stable region, while the region between the two lines is known as the metastable region. Due to the near non-equilibrium condition of GeSn growth, the critical thickness would be closer to the calculation of the P-B model. In the lower Sn fraction < 5% region, the GeSn layers became relaxed at a smaller thickness than the number predicted by the P-B model [47]. In the higher Sn fraction > 12% region, some of epitaxial GeSn films have larger critical thicknesses (blue scatters) than those predicted by the P-B model. In [48], a further kinetic-limited model at low temperatures considered both the temperature and growth rate, and suggested a higher critical thickness for GeSn layers by low-temperature CVD and MBE growth. However, the strain relaxation is not the only limiting factor for the critical thickness of strained GeSn, especially for a high Sn fraction >15%. For example, for strained $Ge_{0.82}Sn_{0.18}$ on Ge VS, the Sn precipitation occurs and is observed with lots of white spots scattering on the wafer surface, while shiny-surface part of wafer still presents a clear $Ge_{0.82}Sn_{0.18}$ peak with fringes in XRD (red curve in Figure 2-10(a)).

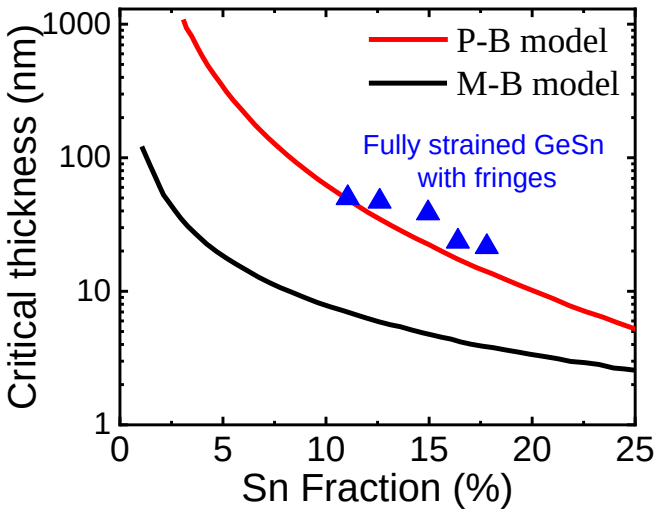

Figure 2-12 Critical thickness calculation for strained $Ge_{1-x}Sn_x$ on a Ge buffer based on M-B and P-B models [47].

doi:10.6342/NTU202300648

2.2.4 Strain-Relaxed GeSn and GeSn Relaxed Buffers

In order to adjust the strain in the GeSn layer and study the strain-dependent characteristics, such as band structure and relevant optical and electrical properties, the strain-relaxed GeSn is served as a relaxed buffer for the tensile-strained GeSn layers. A high-quality GeSn relaxed buffer can confine misfit dislocations in a region away from the active region and effectively suppress the penetration of threading dislocations. At the same time, sufficient relaxation is also important to match the required lateral lattice constant for the active layers. A simple approach for a GeSn relaxed buffer is to use a constant Sn fraction with a sufficient thickness to achieve the required relaxation. The constant buffer has a high defect density near the interface between the buffer and the underlying substrate. Initially, lots of threading dislocations are created and then gradually canceled each other as more layers are deposited during the growth. The drawback of the constant buffer is the required thickness to reduce the threading dislocation density under a suitable level for device applications. In addition, the high defect density during the initial stage of the GeSn growth may accelerate the diffusion and the aggregation of Sn atoms [40], leading to the Sn precipitation. Thus, the constant GeSn buffer is not ideal for the relaxed buffer.

Another approach to grow a high-quality GeSn relaxed buffer is to use a graded relaxed buffer with a gradual change of the Sn fraction in GeSn. Usually, a linear grading of the alloy composition is preferred to make a uniform gradient of lattice constant for reducing the number of defects and dislocations and leading to better crystal quality [51]. In contrast to the high dislocation density of constant buffers near the initial interface, the linear graded buffer is expected to have a uniform volume density of misfit dislocations throughout the layer and creates a lower density of threading dislocations toward the surface due to more space for dislocations to glide [51]. An empirical model indicates that

doi:10.6342/NTU202300648

the threading dislocation density is proportional to the composition gradient [52]; that is, a smaller gradient of the alloy composition leads to fewer threading dislocations. Besides, the growth temperature is also an important factor for the gliding process of dislocations, where the higher temperature is better to drive the motion of dislocation [53].

In this work, a high-quality $Ge_{0.88}Sn_{0.12}$ linearly-graded relaxed buffer was developed. After the growth of Ge VS, the GeSn graded relaxed buffer was deposited with the first layer of $Ge_{0.94}Sn_{0.06}$ grown at 320 °C. Subsequently, the flow of $SnCl_4$ was continuously increased with a fixed flow rate of Ge_2H_6 to obtain a linear gradient of the Sn fraction. The graded buffer ended up with the Sn fraction of 12 %. At last, a $Ge_{0.88}Sn_{0.12}$ layer with a constant Sn fraction (~ 100 nm) was grown to separate the defective region and active layer to provide enough space for threading dislocations to glide and annihilate. Note that the target Sn fraction is 12 % and the actual Sn fraction of the graded relaxed buffer is characterized by RSM (shown in Figure 2-14 later), which is slightly larger than the original design.

Figure 2-13(a) shows the cross-section TEM image of a $Ge_{0.88}Sn_{0.12}$ graded relaxed buffer. Two defective regions with high dislocation densities are observed. The first one

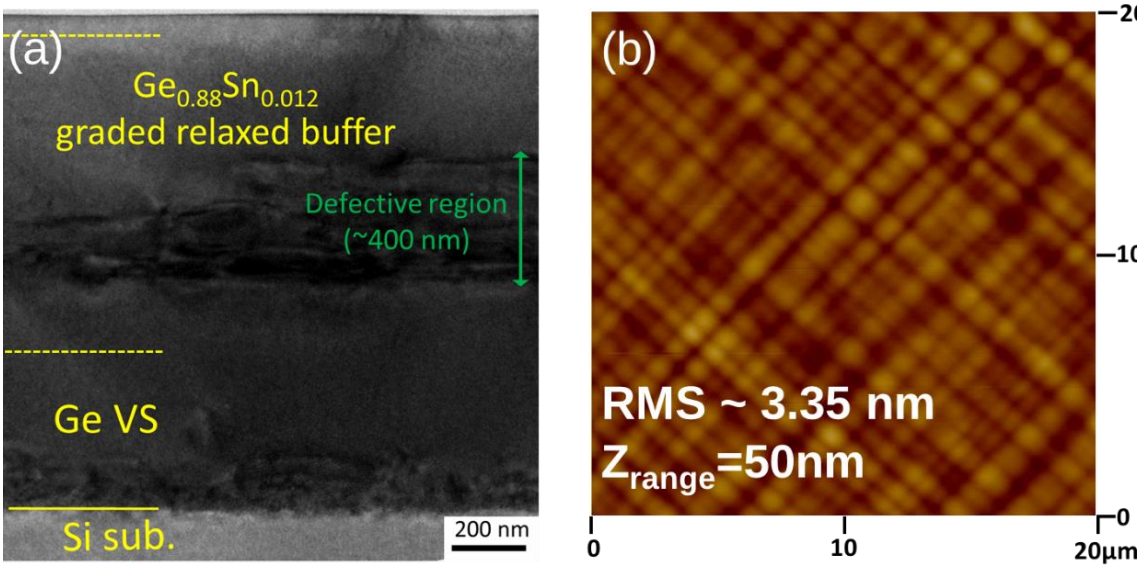

Figure 2-13 (a) A cross-sectional TEM image of a GeSn graded relaxed buffer on a Ge VS/Si substrate. (b) Surface morphology of the GeSn graded relaxed buffer by AFM.

doi:10.6342/NTU202300648

is the bottom region of Ge VS on the Si substrate, which compromises the lattice mismatch between Ge and Si. The second one is in the lower middle of the GeSn graded relaxed buffer, which releases the strain between $Ge_{0.88}Sn_{0.12}$ and Ge. The boundary of the GeSn buffer and the Ge VS is unclear in the TEM image due to the small difference in the alloy composition between GeSn and Ge. The estimated interface is marked based on the thickness of Ge VS measured by a separate experiment. For the GeSn graded buffer, the initial GeSn layer with a lower Sn fraction was grown without any visible defect. As the thickness is over the critical thickness, a large number of dislocations appear to release the compressive strain. With the gradient of the Sn fraction ~ 18 %/nm, the defects are spread in a defective layer of ~ 400 nm (green arrow). Once the strain is released by misfit dislocations, the threading dislocation is hardly observed in the top region of the GeSn relaxed buffer. Thus, the GeSn graded relaxed buffer can provide a high-quality platform for active layers. Figure 2-13(b) shows the surface morphology of the GeSn graded relaxed buffer by AFM. The crosshatch patterns result from the misfit dislocation network in the GeSn relaxed buffer, which indicates the strain relaxation [54]. The RMS surface roughness is 3.35 nm, similar to the roughness of Ge VS, showing high-quality growth of the GeSn graded relaxed buffer.

In addition to film quality, the degree of strain relaxation is also important to a relaxed buffer. Figure 2-14 shows an XRD rocking curve and RSM contour mapping of a $Ge_{0.88}Sn_{0.12}$ graded relaxed buffer. Due to the contributions of the GeSn graded relaxed buffer with different Sn fractions, the signal of the graded buffer is broadened, except for a small peak contributed by the top constant $Ge_{0.88}Sn_{0.12}$ layer. The rocking curve can't provide enough information for the strain condition because the peak position is influenced by both Sn fraction and strain relaxation rates. Thus, RSM technique is used to analyze the strain condition of the relaxed GeSn. The Sn fraction of the top GeSn

doi:10.6342/NTU202300648

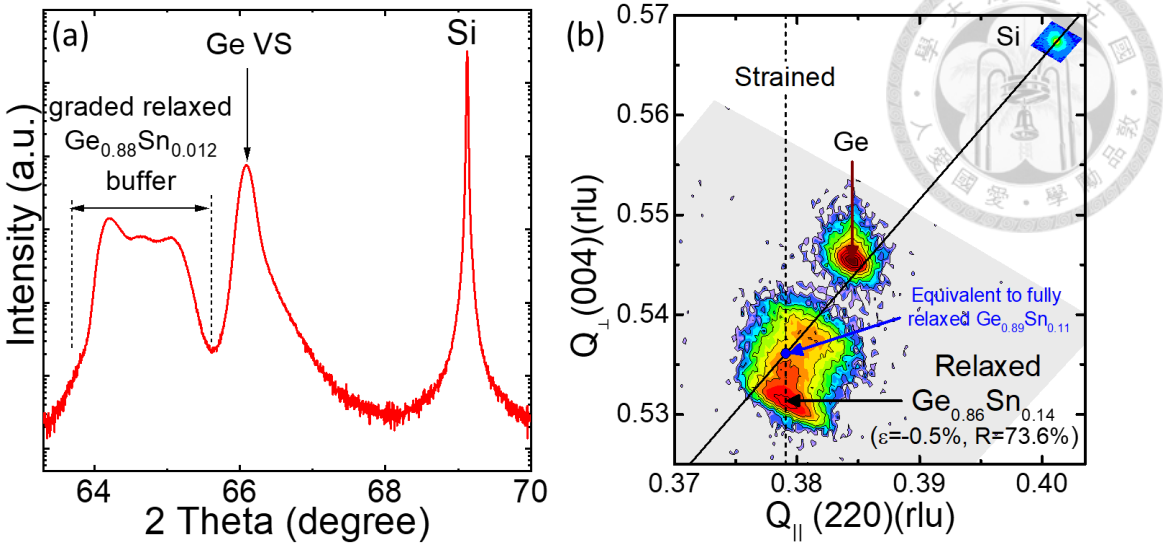

Figure 2-14 (a) An XRD rocking curve and (b) RSM contour mapping of a $Ge_{0.88}Sn_{0.12}$ graded relaxed buffer on a Ge VS/Si substrate.

relaxed buffer is 14 %, which is slightly higher than the designed Sn fraction of 12 %, under the same growth condition for the growth of the compressive-strained GeSn on Ge VS. The deviation is due to the strain relaxation effect, which will be detailed discussed in Section 2.3.3. The peak position of the constant GeSn buffer layer is below the relaxation line, meaning the compressive strain remains in the relaxed buffer. The residual strain ε is -0.5 %, and the relaxation rate R is 73.6 %.

Since residual strains are often remained in a relaxed buffer, the relaxation rate is hardly to reach 100 %. It is required to provide the required Sn fraction and a high relaxation rate of a relaxed buffer at the same time for comparing different relaxed buffers. A better way to evaluate a relaxed buffer is to extract its lateral lattice constant $a_{\parallel}$. In Figure 2-14 (b), the (100) lattice constant is 5.748 Å from the x-value of peak in RSM contour (strained line), equivalent to the original lattice constant of an unstrained $Ge_{0.89}Sn_{0.11}$ (cross point of strained line and relaxation line). Therefore, this $Ge_{0.88}Sn_{0.12}$ graded relaxed buffer is labeled as an "equivalent fully relaxed $Ge_{0.89}Sn_{0.11}$ buffer".

To increase the Sn fraction in the GeSn relaxed buffer, the growth temperature must be reduced (from 320 °C to 305 °C) to further push the growth condition away from

doi:10.6342/NTU202300648

equilibrium. Figure 2-16 show an RSM mapping with a higher Sn fraction of ~ 17 % in the GeSn buffer with a residual strain of -1.58 %. Since the strain is not fully released, the lateral lattice constant is slightly smaller than that for the fully relaxed condition. Moreover, serious Sn precipitation was observed for the GeSn growth with a higher Sn fraction.

2.2.5 Compressive-Strained and Tensile-Strained GeSn on GeSn Relaxed Buffers

A high-quality GeSn relaxed buffer enables strain engineering for GeSn/Ge heterostructures. Two structures are used in this work (Figure 2-15). The GeSn relaxed buffer is used to reduce the large lattice mismatch between Ge VS and $Ge_{1-x}Sn_x$. Particularly, for the Sn fraction x > 20 %, the lattice misfit is too large for GeSn layers to be pseudomorphically grown on the Ge VS. The red rocking curve in Figure 2-15(c), suggests the 22-nm $Ge_{0.76}Sn_{0.24}$ layer is pseudomorphically grown on the $Ge_{0.83}Sn_{0.17}$ graded relaxed buffer. The fringes around the peak of $Ge_{0.76}Sn_{0.24}$ indicate the high quality of both the strained layer and the relaxed buffer. To generate tensile strains in Ge(Sn)

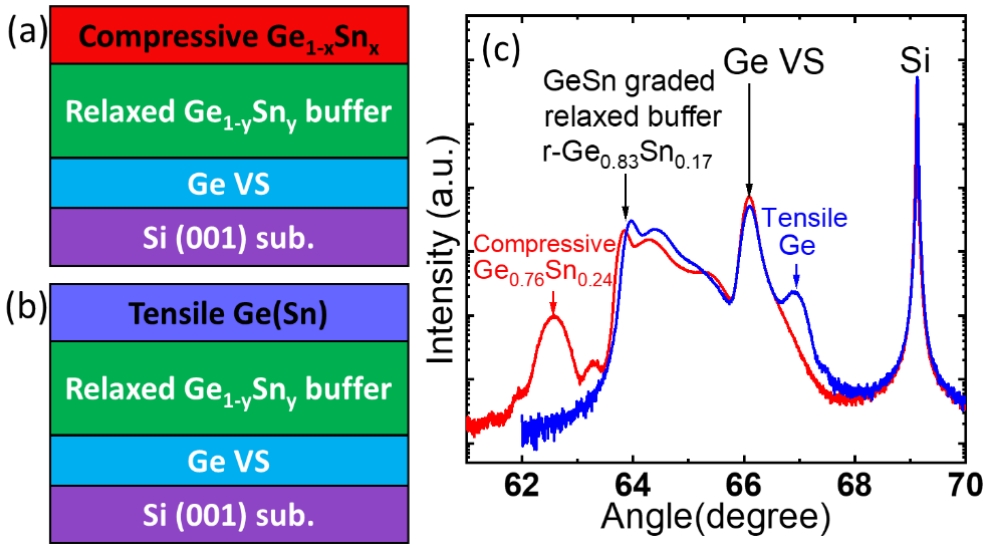

Figure 2-15 Epitaxial structures of (a) compressive-strained GeSn and (b) tensile-strained Ge(Sn) on relaxed GeSn buffers with (c) the associated XRD curves.

doi:10.6342/NTU202300648

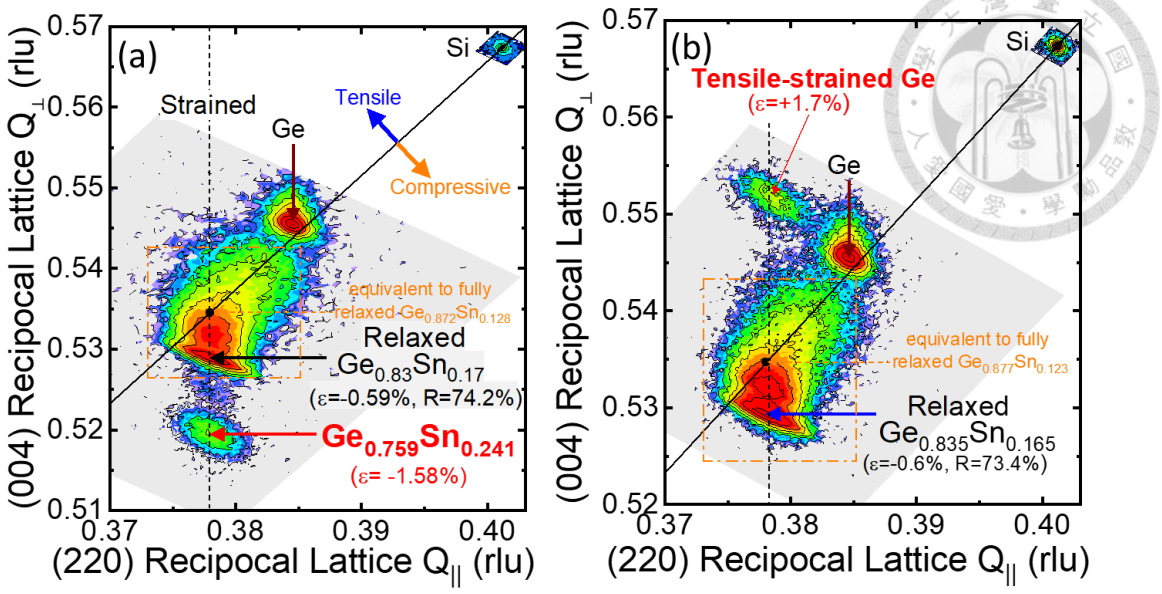

Figure 2-16 RSM contours of (a) compressive-strained $Ge_{0.76}Sn_{0.24}$ and (b) tensile-strained Ge on GeSn graded relaxed buffers.

films, the GeSn relaxed buffer is required since the GeSn buffer has a larger lattice constant than the tensile-strained Ge or GeSn. For the blue rocking curve in Figure 2-15(c), a 30-nm Ge layer is pseudomorphically grown on a GeSn/Ge buffer stack similar to that in Figure 2-14 (b). The peak of tensile-strained Ge is at a larger angle than that of the Ge VS, which shows tensile strains in the top (active) Ge layer.

Figure 2-16(a) shows the strain and Sn fraction of the structure in Figure 2-15(a). The Sn fraction of the active strained GeSn is 24.1 % with a compressive strain of -1.58%. The strain is smaller than that of strained $Ge_{0.82}Sn_{0.18}$ on Ge VS in Figure 2-11. Figure 2-16(b) shows the tensile strain of +1.7 % in the Ge layer on the GeSn relaxed buffer. In both structures, the compressive-strained $Ge_{0.76}Sn_{0.24}$ (Figure 2-16(a)) and tensile-strained Ge (Figure 2-16(b)) are fully strained on their GeSn relaxed buffers.

The Sn fraction over 20 % is also be confirmed by secondary ion mass spectrometry (SIMS) and energy-dispersive X-ray spectroscopy (EDS). Figure 2-17(a) shows the SIMS result of 10-nm $Ge_{0.78}Sn_{0.22}$ on a $Ge_{0.92}Sn_{0.08}$ relaxed buffer (determined by XRD). The Sn fraction is 20 ~ 27 %. Figure 2-17(b) shows the EDS scan on 20-nm $Ge_{0.76}Sn_{0.24}$ on a

doi:10.6342/NTU202300648

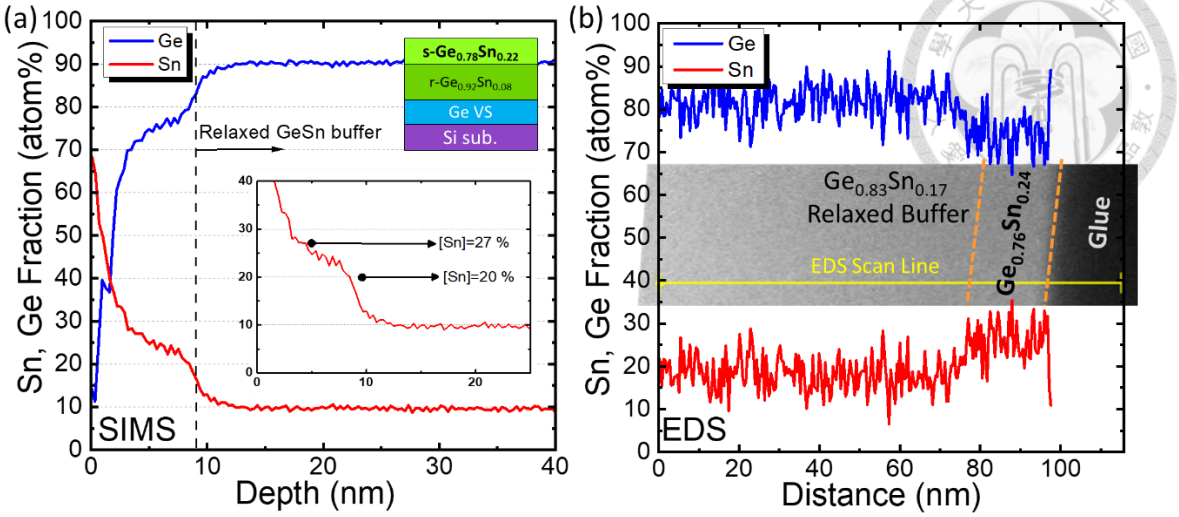

Figure 2-17 (a) SIMS profile and (b) EDS line scan profile of high-Sn GeSn samples.

$Ge_{0.83}Sn_{0.17}$ relaxed buffer. The Sn fraction is ~ 25 % with a error of ±5 %. All Sn fractions and strain values were determined by XRD (or RSM) and marked in the following text.

2.3 Growth Mechanism and Approaches of GeSn Epitaxy with A High Sn Fraction

In order to achieve a high Sn fraction and direct-bandgap in GeSn, the growth mechanisms of GeSn CVD are systemically studied by varying the precursor ratio, growth temperature, and the underneath buffer in this thesis. Due to the non-equilibrium growth of GeSn at low temperatures, growth characteristics and strategies are quite different from the Si/SiGe/Ge epitaxy. For example, apart from the chemical reaction of the precursors, the stress on the surface layer plays an important role in the Sn fraction of the GeSn layer. Thus, the strain condition of the epitaxial films during the growth could influence the Sn fraction of the GeSn films. Different effects on the Sn fraction, such as gas ratio, growth temperature, and relaxed buffer, the epitaxial GeSn films are investigated. At last, the growth strategies for a further higher Sn fraction will be discussed.

doi:10.6342/NTU202300648

2.3.1 Effects of Gas Ratio

Gas flows rates (or mass flow) of the precursors are the first important parameter for the Sn fraction in GeSn. The growth pressure was set at 100 torr, and the carrier gas was 10-slm H_2 for all growth. For the structures with the associated XRD curves in Figure 2-18(a), the growth temperature is 320 °C with a fixed Ge_2H_6 flow rate of 200 sccm (10 % diluted in H_2) and different flow rates of $SnCl_4$. With a higher $SnCl_4$ flow rate, the Sn fraction is increased from 4 % to 11.5 %. Figure 2-18(b) shows the solid Sn/Ge atomic ratio in GeSn alloys with the gas Sn/Ge atomic ratio in precursors. For 200-sccm Ge_2H_6 (blue curve), the solid ratio increases with the gas ratio. However, the solid ratio is saturated at 0.12 as the gas ratio is beyond 0.02, leading to a saturated Sn fraction of ~ 12 %. For a lower Ge_2H_6 flow rate of 100 sccm, the Sn fraction drops abruptly to ~ 1 % with a gas ratio of ~ 3.8 since the serious Sn precipitation occurs by over-supplied $SnCl_4$. For a higher Ge_2H_6 flow rate of 300 sccm, the Sn fraction is higher at the same gas Sn/Ge atomic ratio.

By plotting the Sn fraction vs. the $SnCl_4$ flow rate in Figure 2-19(a), for the $SnCl_4$ flow rate below 5 mg/min, the Sn fractions are independent of the Ge_2H_6 flow rate (black

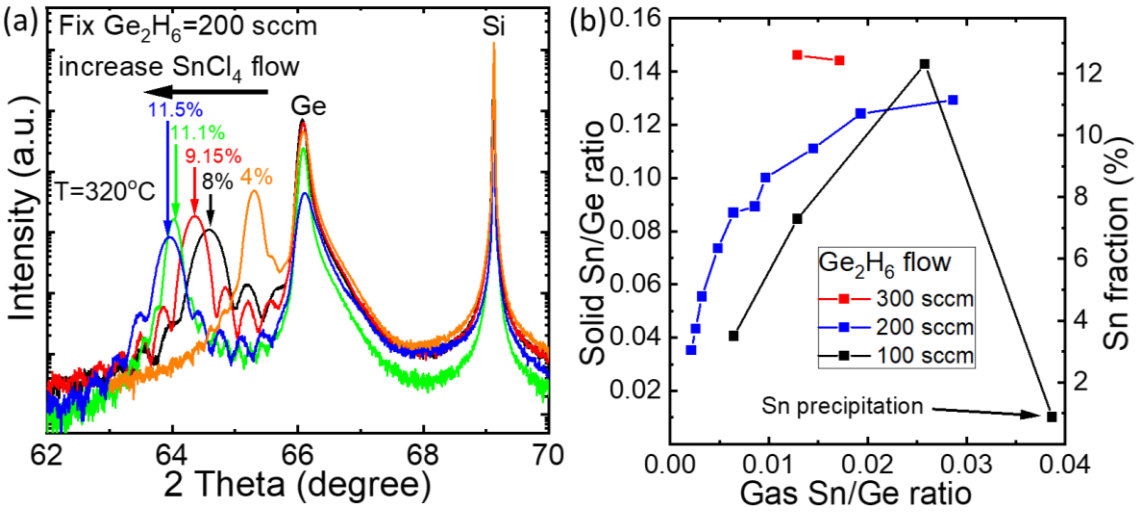

Figure 2-18 (a) XRD rocking curves of GeSn films grown with different $SnCl_4$ flow rates. (b) Solid Sn/Ge ratio and Sn fraction in the GeSn films vs. the gas Sn/Ge ratio.

doi:10.6342/NTU202300648

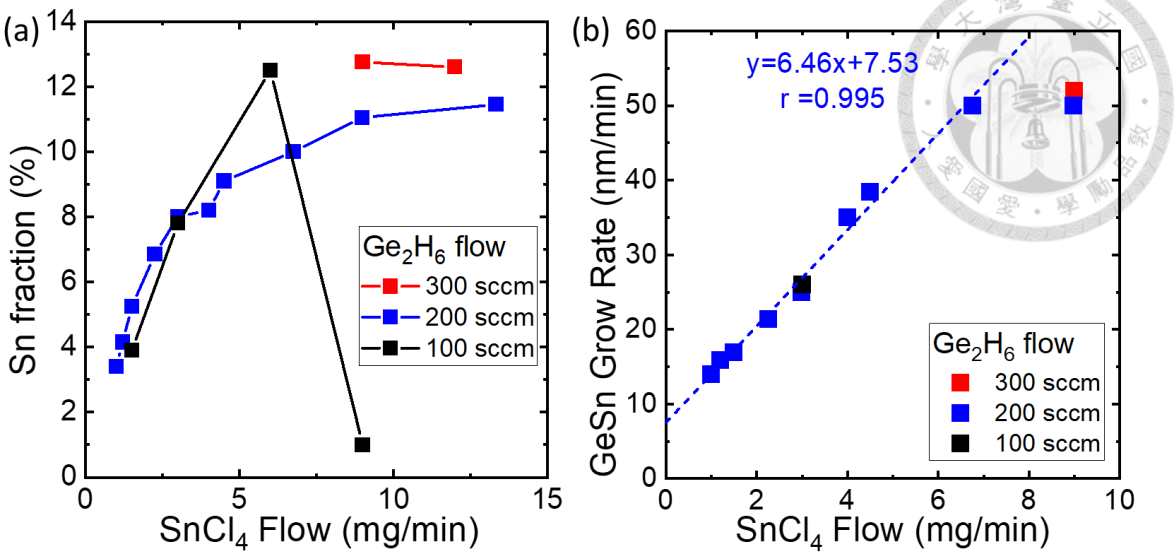

Figure 2-19 (a) Sn fraction and (b) growth rate versus $SnCl_4$ flow rate for GeSn epitaxy at 320 ºC with Ge_2H_6 flow rates of 100, 200, and 300 sccm.

and blue curves). With a higher $SnCl_4$ flow rate and a Ge_2H_6 flow rate of 200 or 300 sccm, the Sn fraction is saturated at 11 ~ 13 %. However, for a lower Ge_2H_6 rate of 100 sccm, the coherent growth of pseudomorphic GeSn layers fails at a very small $SnCl_4$ flow rate due to the large gas Sn/Ge atomic ratio and Sn precipitation . To have a stable growth condition and a higher Sn fraction in epitaxial GeSn layers, the flow rate of Ge_2H_6 must be as high as possible to prevent Sn precipitation, so the Sn fraction in GeSn can be effectively controlled by the $SnCl_4$ flow rate. Furthermore, the growth rate has a linear dependence on the $SnCl_4$ flow (Figure 2-19(b)). This linear relationship was also reported at 325 ºC and 300 ºC in [55], which was attributed to the higher density of the Sn atoms on the epitaxy surface [55]. The surface Sn atoms with weaker Sn-H bonds are easier to desorb from the surface, freeing surface sites for the incorporation of Sn and Ge (Figure 2-3). Besides, the Sn atom may catalyze the decomposition of hydride or other –H bonds [37][56]. Both lead to higher growth rates of GeSn epitaxial layers.

doi:10.6342/NTU202300648

2.3.2 Effects of Growth Temperature

Due to the saturation of the Sn fraction in GeSn at 320 ºC, to achieve a higher Sn fraction requires a lower temperature. By fixing the precursor flow rates of 300-sccm Ge_2H_6 and 12-mg/min $SnCl_4$, the GeSn films were grown at lower temperatures. For the XRD curves in Figure 2-20(a), the GeSn peaks represent the signals of the GeSn layer with high Sn fractions grown at different temperatures. At lower temperatures, the Sn fraction is higher, and GeSn peaks are shifted to a lower angle. Similar to the results in Ref [55], the Sn fraction shows a linear relationship with the growth temperature (blue line in Figure 2-20(b)). The Sn fraction is increased by 1.5 % per 10 ºC decrease in temperature (blue points and fitting line). While the Sn fraction is up to 17.8 % at 285 ºC, the Sn precipitation occurs as the temperature is further reduced to 275 ºC. With a lower flow rate of $SnCl_4$ (Figure 2-20(b)), the Sn fractions are smaller than those with a higher flow rate and a larger slope of 2.16 %/-10 ºC. This suggests the Sn incorporation rate is also affected by the pyrolysis rate of $SnCl_4$ and its surface reactions and further analysis is required.

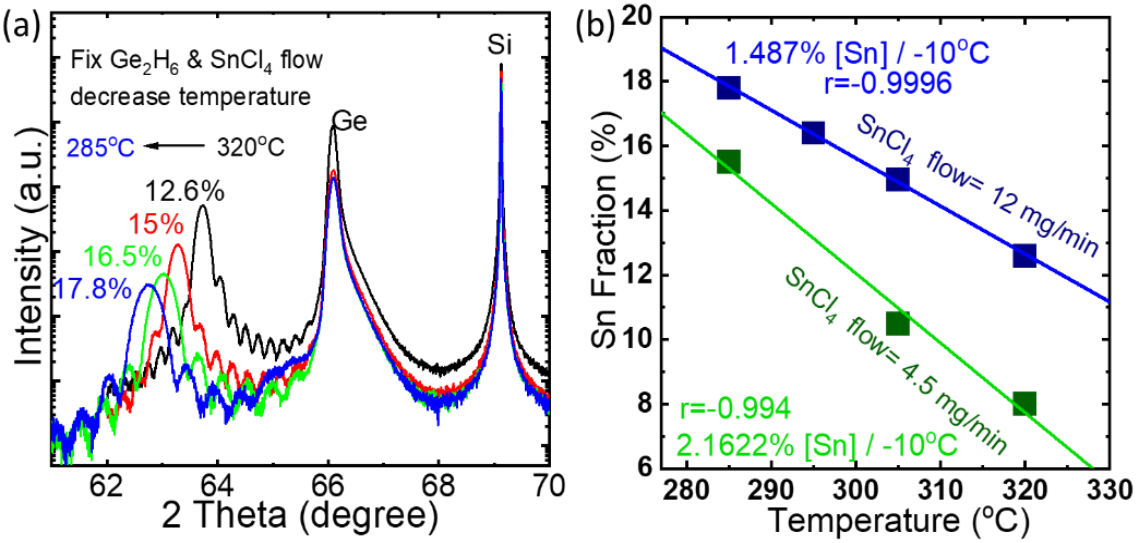

Figure 2-20 (a) XRD rocking curves of GeSn films grown at different temperatures. (b) Sn fraction versus growth temperature with the same gas flow.

doi:10.6342/NTU202300648

2.3.3 Effects of Buffer Layers

For strained GeSn on Ge VS, both increasing the $SnCl_4$ flow rate and reducing the growth temperature cannot further increase the Sn incorporation. One of the reasons is that the compressive strain is larger as the Sn fraction in GeSn increases. The large compressive strain is suggested to limit the Sn incorporation during the growth [57][58], which was explained through the concept of Gibb's free energy with an additional strain energy in the strained GeSn films. As the strained GeSn on Ge VS in last paragraph, the magnitude of the compressive strain is over 2.4 % for $Ge_{0.82}Sn_{0.18}$. From the inspiration of the GeSn relaxed buffer, as the discussion in section 2.2.4, we observed that the smaller compressive strain in the GeSn relaxed buffer seems to enhance the Sn fraction. That is, a reduced strain (or less strain energy) helps the Sn incorporation. The same phenomenon was reported by different groups [57][58] that the Sn fraction in the relaxed GeSn layer with fixed growth parameters increases during the growth since the GeSn layer is gradually relaxed (less compressive strain remained in the GeSn layer), leading to a higher Sn fraction in the subsequent growth. By applying this strategy, a GeSn layer was grown at 280 °C on several GeSn relaxed buffers (with different Sn fractions) with the

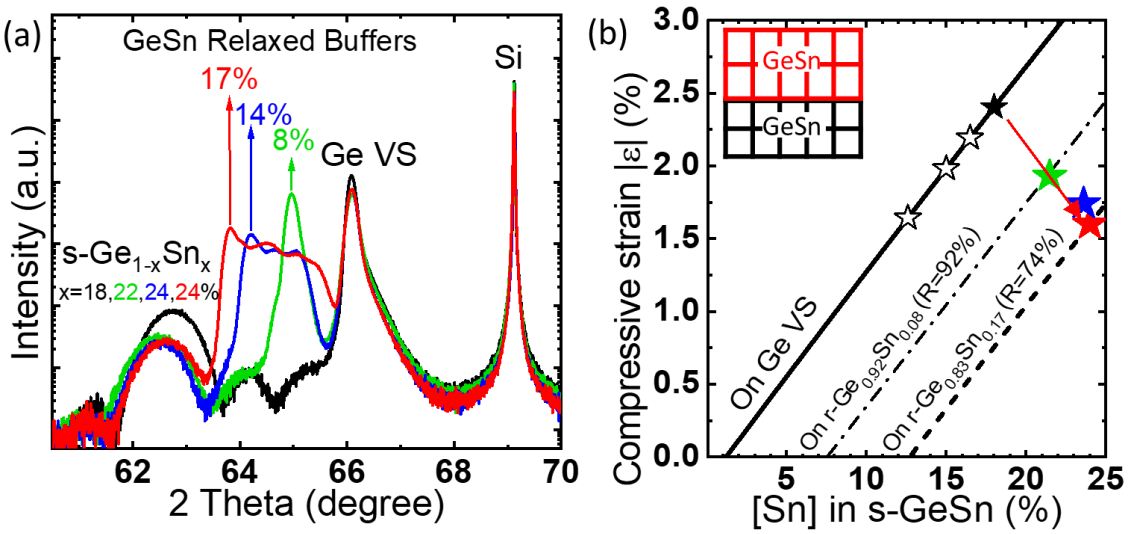

Figure 2-21 (a) XRD rocking curves of GeSn films strained on different relaxed buffers. (b) Compressive strain vs. Sn fraction extracted from RSM data.

doi:10.6342/NTU202300648

associated XRD curves shown in Figure 2-21(a). The strained GeSn films were pseudomorphically grown on GeSn buffers with fringes, showing their high quality. However, the Sn fraction cannot be directly compared from the results of rocking curves. The higher Sn fraction and lower strain have the opposite effects on the peak position. That is, the higher Sn fraction would shift the GeSn peak toward a lower angle, while releasing compressive strain in the GeSn layer would shift the GeSn peak toward a higher angle. Therefore, the Sn fraction and the compressive strain were extracted by RSM data individually and plotted in Figure 2-21(b) (solid stars). The three lines show the relationship between strain and Sn fraction for GeSn films grown on different GeSn buffers. By increasing the Sn fraction, the compressive strain increases while using a Ge(Sn) buffer with a higher Sn fraction, the Sn fraction in the GeSn active layer can be increased effectively with a fixed compressive strain.

To better evaluate a GeSn relaxed buffer, the Sn fraction and strain are plotted against the in-plane lattice constant of the GeSn buffer in Figure 2-22, respectively. The Sn fraction is increased from 18 % of GeSn on the Ge VS ($a_{||}$=5.667 Å) to 24 % of GeSn on a relaxed $GeSn_{0.83}Sn_{0.17}$ buffer, which is equivalent to a fully-relaxed $Ge_{0.87}Sn_{0.13}$ layer

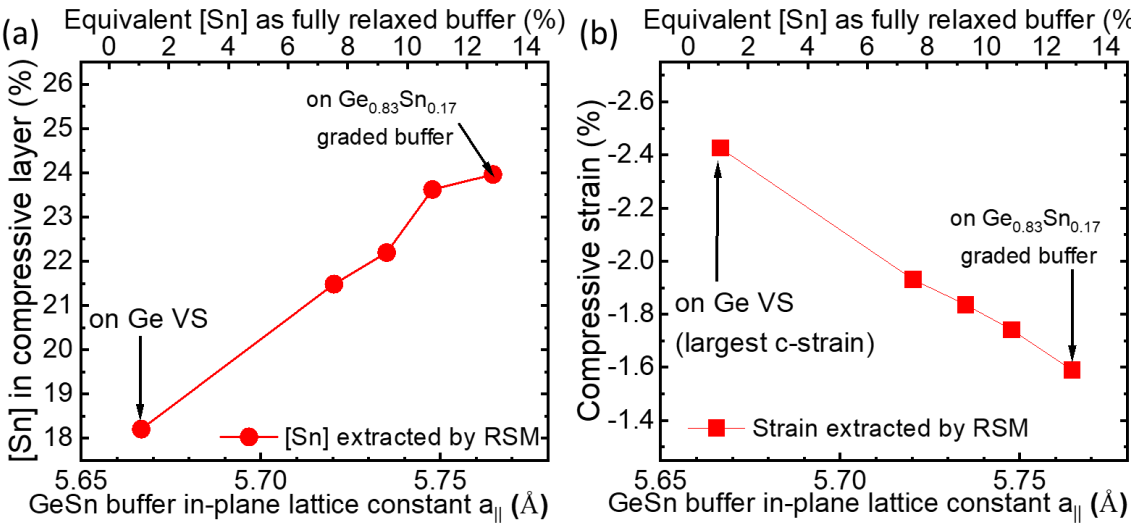

Figure 2-22 (a) Sn fraction and (b) compressive strain in the strained GeSn films on the different relaxed buffers in the aspect of the in-plane lattice constant.

doi:10.6342/NTU202300648

with a lattice constant ($a_{||}$=5.765 Å) based on the argument in section 2.2.4. Meanwhile, the compressive strain is reduced from -2.4 % (on Ge VS) to -1.6 % (on GeSn relaxed buffer).

2.3.4 Discussion

In this work, a record-high Sn fraction is achieved up to 18 % and 24 % for fully strained GeSn on a Ge VS and on a GeSn relaxed buffer, respectively, among GeSn films by CVD. There is still some margin to further increase the Sn fraction. There are two limitations: one is the Sn precipitation at the low temperature < 275 ºC. Another is the further extension of the in-plane lattice constant of the GeSn relaxed buffer. For the first limitation, the current gas ratio may reach the limit of saturated Sn fraction and oversupply of $SnCl_4$ for 275 ºC, as the concept shown in Figure 2-19(a). Thus, the Sn precipitation occurs upon the deposition of high-Sn layer at 275 ºC (with the same gas flow in Figure 2-20), and there is no diffraction peak for high Sn fraction in its XRD. A higher Ge_2H_6 or a lower $SnCl_4$ flow rate can be used to suppress the Sn precipitation. Using high-order Ge hydrides, such as Ge_3H_8, as the precursor is expected to enhance the growth rate and suppress the Sn precipitation at low temperatures, which can further increase the Sn fraction. For the second limitation, a GeSn buffer is required for a high Sn fraction and a high relaxation rate at the same time. In-situ thermal annealing may help to enhance the strain relaxation as long as Sn precipitation doesn't occur. An alternative method is to use a substrate with a large lattice constant. For example, a $Ge_{0.73}Sn_{0.27}$ film was successfully grown by MBE on an InP substrate [57], whose lattice constant is equivalent to unstrained $Ge_{0.75}Sn_{0.25}$ (Figure 1-1).

doi:10.6342/NTU202300648

Chapter 3 Photoluminescence (PL) of Epitaxial GeSn Films

3.1 Introduction to Photoluminescence

Photoluminescence (PL) is powerful for the characterization of the bandgap energy of a semiconductor and the quality of the epitaxial layers. The operation principles are illustrated in Figure 3-1(a). As excitation light is illuminated onto a semiconductor, electron-hole pairs are generated by absorbing photons with energies higher than the bandgap energy. Electrons in the valence band are excited to the conduction band, and then are scattered with lattices and impurities quickly and relax to the bottom of the conduction band. This occurs on a time scale of $10^{-12} \sim 10^{-15}$ seconds [60]. In a radiative recombination process, electrons and holes recombine directly by spontaneously emitting a photon with the energy corresponding to the bandgap energy. Therefore, measuring the emitted photons can determine the bandgap energy of the semiconductor. However, the electron and hole pair can also recombine through non-radiative processes, such as Auger recombination or Shockley-Read-Hall (SRH) recombination. The SRH recombination is enhanced by deep states such as dislocations in epitaxial layers [60]. The light emission

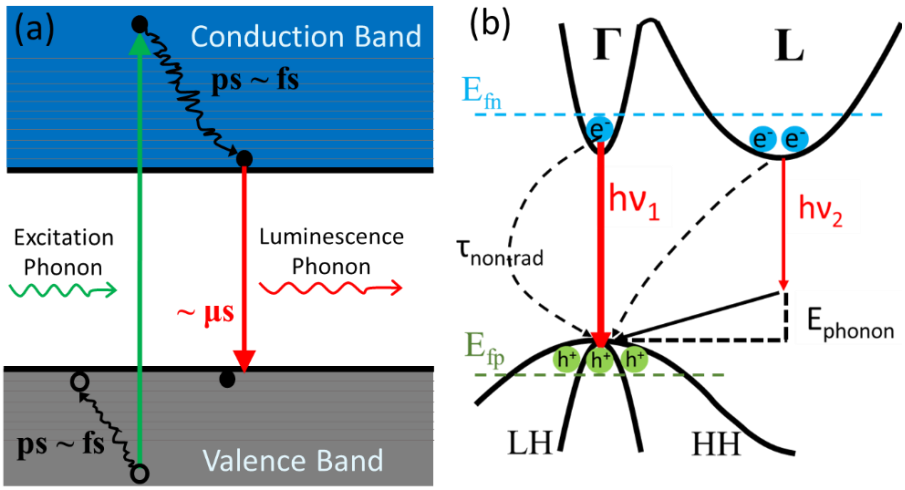

Figure 3-1 (a) Schematic of photoluminescence process in a semiconductor. (b) Radiative and non-radiative recombination process in GeSn.

doi:10.6342/NTU202300648

contributed by electron-hole recombination through the bandgap will be suppressed. Compared to the scattering rates of carriers within the conduction or valence band, the electron-hole recombination rate is much slower, so the carriers accumulate at the band edges and contribute the luminescence with a peak energy close to the bandgap energy [60].

The band structures of GeSn are shown in Figure 3-1(b). Excited electrons populate in both Γ and L valleys. Fewer electrons populate in the Γ valley due to its smaller density-of-state (DOS) effective mass [2]. However, photoemission via this direct transition ($h\nu_1$) is much more efficient than the indirect transition via the L valley ($h\nu_2$) [61]. The photon emission from the indirect bandgap requires additional phonon emission or absorption to conserve the momentum, leading to much reduced emission rates. The light emission via the direct bandgap is comparable to that of the indirect bandgap even in an indirect-

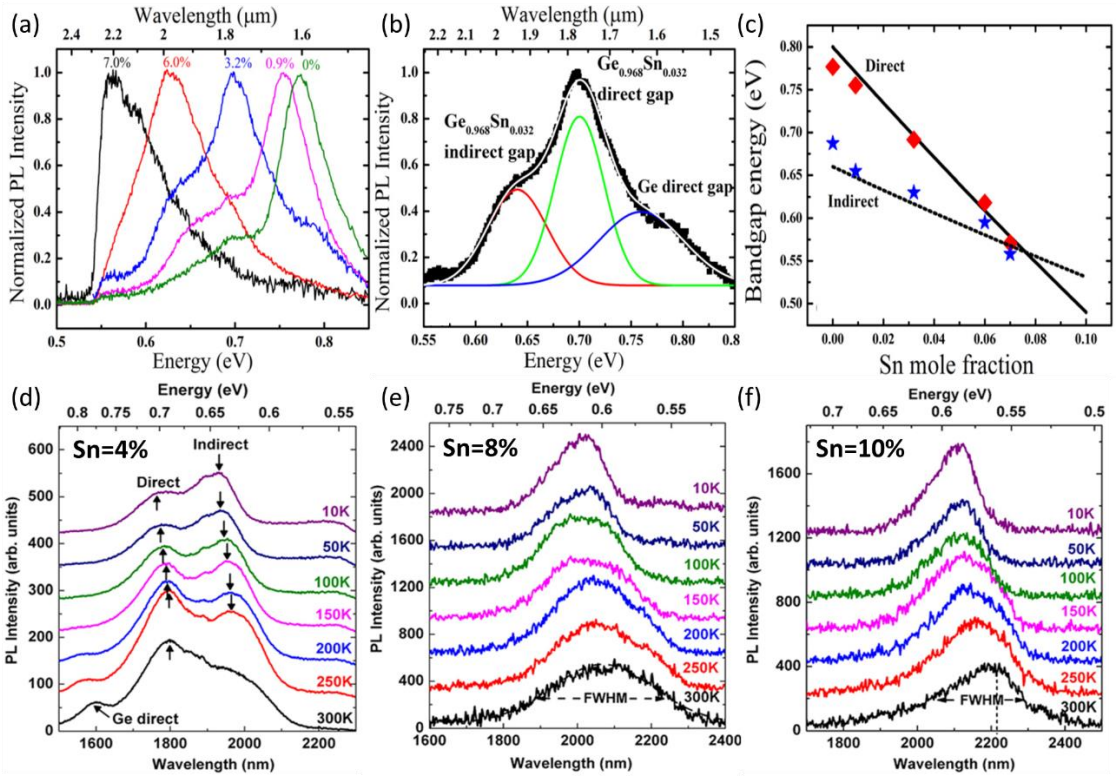

Figure 3-2 (a) Room-temperature GeSn PL spectra with (b) curves and (c) extracted direct and indirect bandgap energies [62]. Low-temperature GeSn PL spectra of (d) $Ge_{0.96}Sn_{0.04}$, (e) $Ge_{0.92}Sn_{0.08}$, and (f) $Ge_{0.9}Sn_{0.1}$ [64].

doi:10.6342/NTU202300648

bandgap GeSn [62][63]. Figure 3-2 shows the GeSn PL results in the literatures [62][64]. Figure 3-2(a) shows the PL spectra of GeSn samples ([Sn]=0 ~ 7 %) at room temperature. For the fitting curves in Figure 3-2(b), the main PL peak is attributed to the direct-bandgap emission (green curve), while the indirect-bandgap emission is also observable with a lower intensity at lower photon energy (red curve). Although the direct-bandgap emission dominates the GeSn PL spectra at room temperature, the spectra suggests that GeSn is still an indirect-bandgap material with Sn fraction below 7 %, where the fitting curves for the indirect and direct bandgap energies show the crossover point of a Sn fraction of 7 % in Figure 3-2(c). In Figure 3-2(d), the low-temperature PL spectra show the separated direct-bandgap and indirect emission in $Ge_{0.96}Sn_{0.04}$. Since the energy difference between direct and indirect bandgap is smaller in $Ge_{0.92}Sn_{0.08}$, the emission peaks from two valleys are merged and less distinguishable (Figure 3-2(e)). In Figure 3-2(f), only one emission peak is observed in $Ge_{0.9}Sn_{0.1}$ PL spectra since the energy difference is too small to be distinguished by PL, suggesting the indirect-to-direct transition around Sn fraction of 10 %. In addition to the bandgap energy, PL measurement could also determine the indirect-to-direct transition in GeSn alloys. In this work, the GeSn epitaxial films with different Sn fractions and under different strain conditions are investigated.

3.2 Measurement of Infrared PL Spectra

In the $Ge_{1-x}Sn_x$ alloy system, the bandgap energy ranges from 0.66 eV of pure Ge to zero bandgap at x ~ 0.35 according to the simulation results [3]. The corresponding wavelength is extended from short-wave infrared (SWIR, 1 ~ 3 μm) to middle-wave infrared (MWIR, 3 ~ 5 μm) and further. Thus, in this work, the PL measurement system was designed to characterize luminescence with λ = 5.5 μm for GeSn with high Sn fractions.

doi:10.6342/NTU202300648

The PL system is shown in Figure 3-3(a). A 532-nm continuous-wave (CW) laser is used as the optical-pumping source. The power of the laser is 500 mW with a beam diameter of 2 mm. The laser beam is modulated by a chopper with a frequency of 37 Hz and a lock-in amplifier is synchronized at the same frequency. The incident laser beam was focused onto the sample by a focal lens. The emitted photons within a certain solid angle are collected by a high-numerical aperture (NA) lens (Lens 1) placed at the distance of its focal length. The second lens focuses the light into the entrance of the monochromator, which splits the light with different wavelengths by gratings. The detectors convert the light signal to a current signal and send it to a lock-in amplifier via a current-to-voltage converter. Two long-wavelength photodetectors were used to detect the IR luminescence of GeSn. One is a TE-cooled InGaAs photodiode with a cutoff wavelength of 2.6 μm. Another one is a liquid-nitrogen-cooled InSb photodiode with a cutoff wavelength of 5.5 μm. Besides the photodetectors, several specialized components were also used. For example, the collecting lenses (Lens #1 and #2) were used for high IR transmissions. A conventional aspherical lens made of crown glass (N-BK7) has a

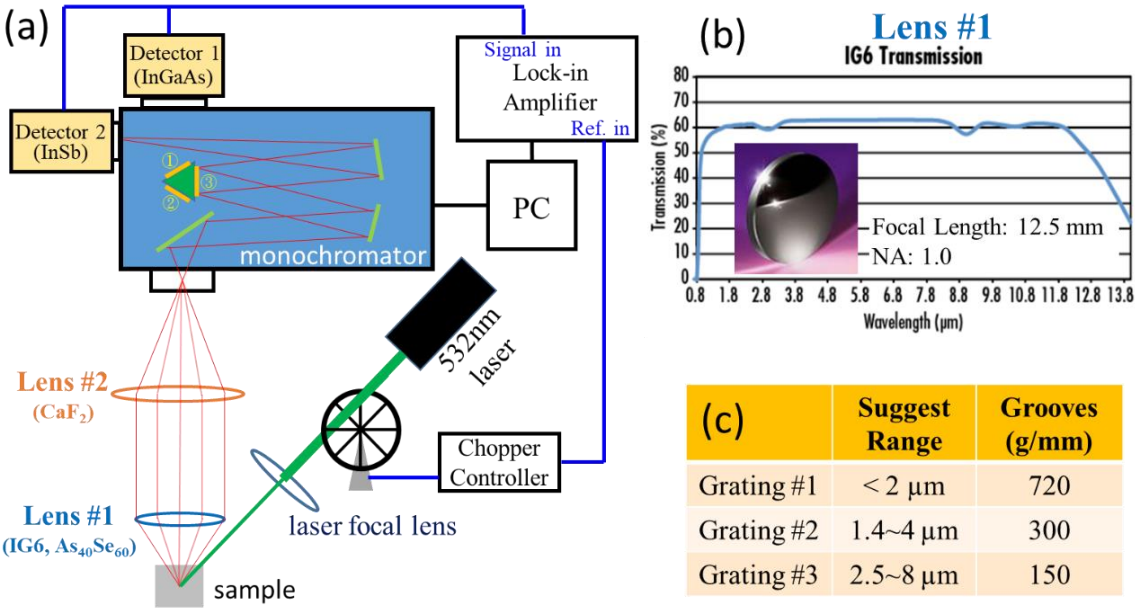

(c)	Suggest Range	Grooves (g/mm)
Grating #1	< 2 μm	720
Grating #2	1.4~4 μm	300
Grating #3	2.5~8 μm	150

Figure 3-3 (a) Schematic of the PL measurement system. (b) Transmission spectrum of IG6($As_{40}Se_{60}$) for Lens #1 [65]. (c) The gratings in the monochromator.

doi:10.6342/NTU202300648

transmission cutoff at the wavelength of 2.7 μm, which is suitable for the NIR and SWIR range, but not enough for the MWIR range. Therefore, an IR aspherical lens made of IG6 ($As_{40}Se_{60}$) has a high NA=1.0 and a flat transmission spectrum up to ~ 10 μm (Figure 3-3(b) [65]). An additional advantage of this lens is that the visible light is blocked due to the short-wavelength cutoff at 900 nm; thus, a long-pass filter is no longer required to filter the scattered light from the incident laser. Second, the gratings also have different working ranges, as shown in Figure 3-3(c). The grating with a shorter working wavelength has a higher spectral resolution due to the larger groove density. For the spectrum with the maximum wavelength shorter (or longer) than 2.6 μm, an InGaAs (or InSb) detector is used with Grating #2 (or Grating #3).

Figure 3-4(a) shows the pictures of a part of PL measurement setup with its sample stage and a 10 K fridge. For room-temperature PL measurement, samples were fixed on a stage, which can switch the different samples by simply moving the stage position (Figure 3-4(b)). The optical path was first set up using a bulk Ge (wafer) sample as a

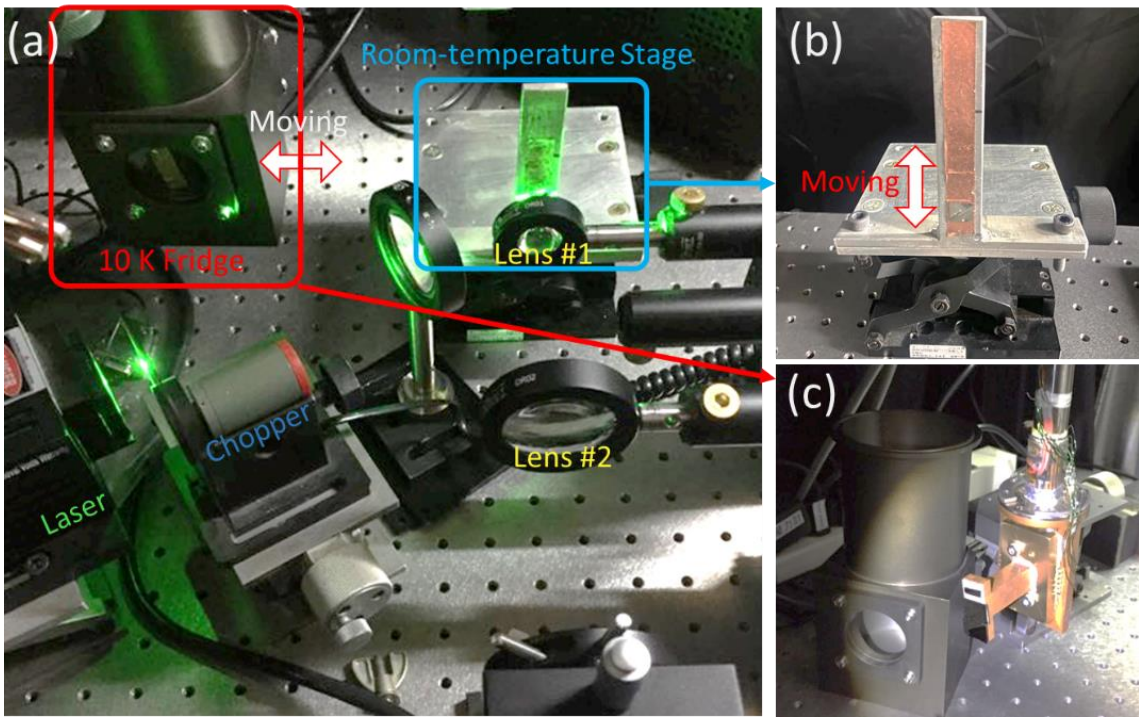

Figure 3-4 (a) Picture of PL measurement setup with (b) its sample stage and (c) 10 K fridge.

doi:10.6342/NTU202300648

reference. Then, the optical path was optimized to maximize the signal intensity by tuning the positions of the laser focal lens and Lens #1. For low-temperature PL measurements, the sample is placed in the 10 K cryostat (Figure 3-4(c), base temperature ~16 K) and the measurement steps are the same as room-temperature steps.

3.3 Room-Temperature PL Spectra of Epitaxial GeSn Films

3.3.1 PL of Compressive-Strained GeSn on a Ge VS

The room-temperature (RT) PL of compressive-strained GeSn on a Ge VS is shown in Figure 3-5. The epitaxial structure is shown in Figure 3-5(a), where all epitaxial layers were undoped (background doping is lightly p-type). As a baseline, the RT-PL spectrum of the epitaxial Ge buffer (VS) was also measured (black curve in Figure 3-5(b)). The emission peak of the Ge VS is at 0.79 eV, corresponding to the direct bandgap in Ge. The indirect-bandgap emission is at ~ 0.68 eV. Similar spectra were also reported by other groups [62][66]. The light emission by the electron-hole recombination from the direct valley for indirect-bandgap Ge is dominant at room temperature. Similar to the Ge VS case, for the PL spectra of GeSn at room temperature, the energy of the emission peak is

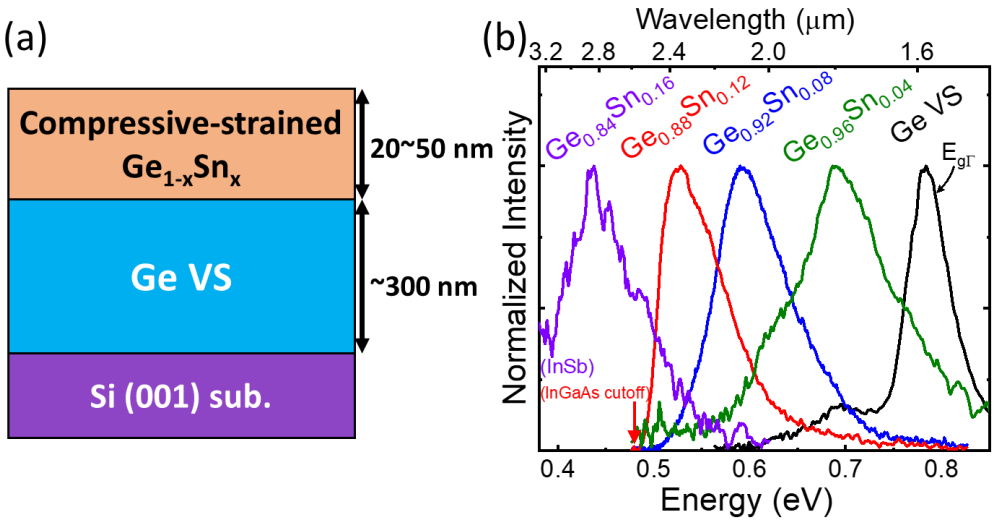

Figure 3-5 (a) Epitaxial structure for the PL measurement of compressive-strained GeSn on Ge VS. (b) Room-temperature PL spectra of compressive-strained GeSn on Ge VS.

doi:10.6342/NTU202300648

also considered the direct bandgap energy of GeSn because the smaller energy difference between direct and indirect valleys in GeSn would make direct emission much more efficient than pure Ge. The RT-PL spectra of GeSn with Sn fractions of 4, 8, 12, and 16% are shown in Figure 3-5(b), where the spectrum of strained $Ge_{0.84}Sn_{0.16}$ was measured by the InSb detector while the others were characterized by the InGaAs detector. The direct bandgap energy of GeSn decreases with the Sn fraction. In strained $Ge_{0.96}Sn_{0.04}$, the indirect-bandgap emission is observable at the left shoulder of the peak (~ 2 μm), and cannot be distinguished in the spectra with Sn fractions high than 8 % due to a very small reduced energy difference or the crossover of indirect-to-direct bandgap. For strained GeSn with a higher Sn fraction (e.g. $Ge_{0.82}Sn_{0.18}$) on a Ge VS, no emission peak was observed. This might be due to the extremely thin GeSn layer (~ 10 nm), leading to strong surface recombination over the radiative recombination.

3.3.2 PL Spectra of Compressive-Strained GeSn on GeSn Relaxed Buffers

The room-temperature PL spectra of compressive-strained GeSn on GeSn relaxed

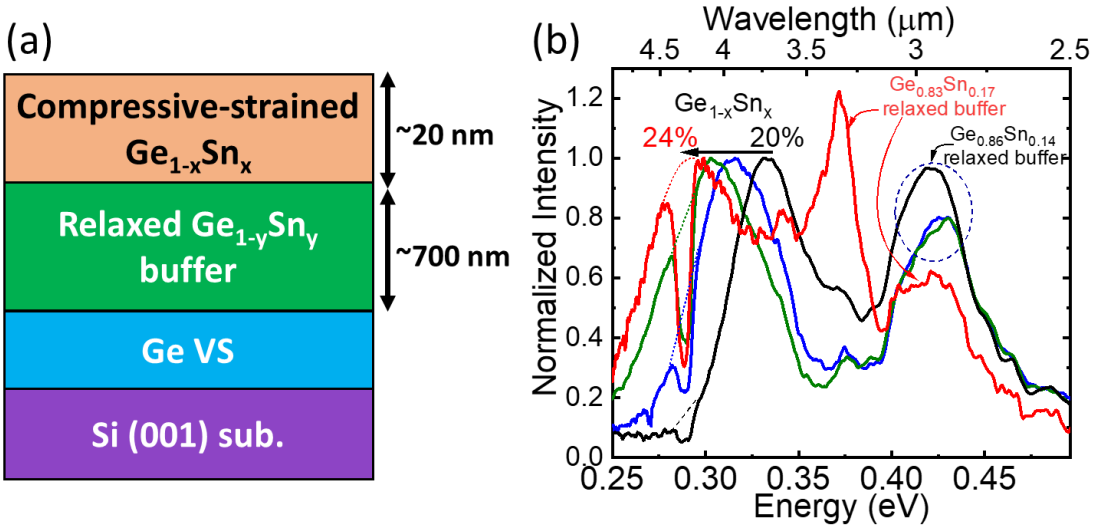

Figure 3-6 (a) Epitaxial structure and (b) Room-temperature PL spectra of compressive-strained GeSn (> 20%) on a GeSn relaxed buffer.

doi:10.6342/NTU202300648

buffer are shown in Figure 3-6. The high-Sn fraction layers are thin (~ 20 nm), while the underneath GeSn relaxed buffers are thick, leading to a high radiative efficiency (Figure 3-6(a)). The luminescence from the GeSn buffer is clearly observed and stronger than the GeSn layer with a higher Sn fraction (Figure 3-6(b)). The $Ge_{0.86}Sn_{0.14}$ relaxed buffers show clear emission peaks at ~ 2.9 μm for three structures with active strained-GeSn layers with different Sn fractions (black, blue, and green curves), while the $Ge_{0.83}Sn_{0.17}$ relaxed buffer shows a discontinuous luminescence profile with a dip at ~ 3.1 μm due to the IR absorption of H_2O, which will be further discussed in Section 3.6. Following the results in the last section, the peaks of the GeSn layer with a high-Sn fraction (> 20%) are contributed by the emission of the direct bandgap. The bandgap energy of GeSn (20 ~ 24 %) decreases with the Sn fraction. The smallest bandgap of 0.295 eV (wavelength ~ 4.2 μm) is demonstrated with the corresponding Sn fraction of 24 %. This is the longest wavelength from PL measurements reported for all group-IV materials. A strong and narrow dip at 4.3 μm is observed for all spectra of GeSn with high-Sn fractions, which results from the IR absorption of CO_2, which will be also discussed in Section 3.6.

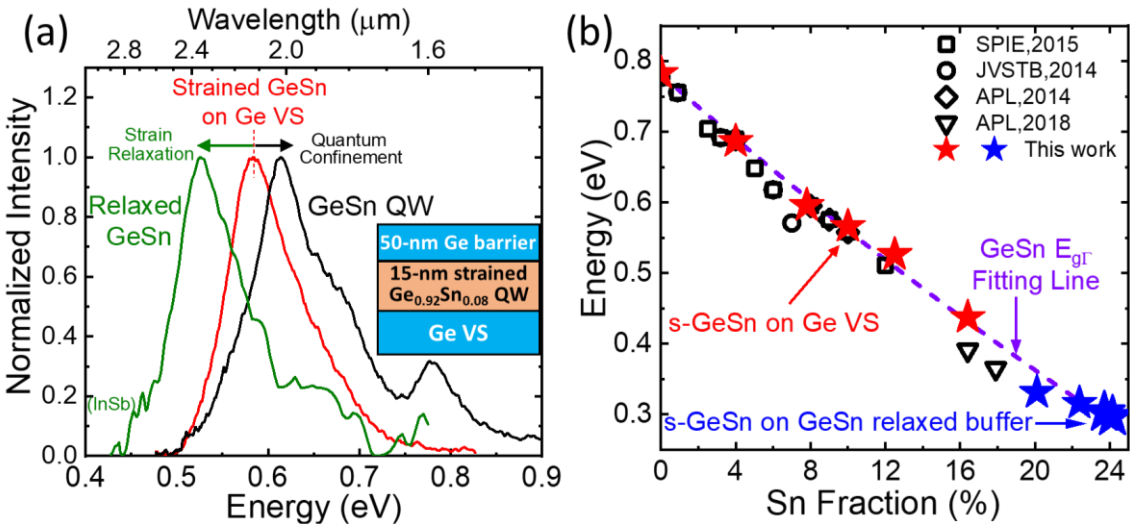

Figure 3-7 (a) $Ge_{0.92}Sn_{0.08}$ RT-PL spectra of strain-relaxed, compressive-strained, and QW structures. (b) Peak energy of RT-PL spectra of strained GeSn versus Sn fraction.

doi:10.6342/NTU202300648

3.3.3 PL Spectra of Strain-Relaxed GeSn Layers and GeSn Quantum Wells

By applying stresses on GeSn epitaxial layers or sandwiching the GeSn layer to form a quantum well, the peak position of PL spectra can be shifted. For example, in Figure 3-7(a), the direct bandgap energy of strained $Ge_{0.92}Sn_{0.08}$ on a Ge VS is 0.58 eV (red curve). The strain relaxation reduces the bandgap of the compressive-strained GeSn (green curve). In contrast, the emission peak is shifted to higher energy in the $Ge_{0.92}Sn_{0.08}$ quantum well (QW), whose structure is shown in the inset. The quantum levels in the conduction and valence bands enlarge the effective bandgap while the emission from the Ge barriers is also observed at ~ 1.6 μm. The RT emission peaks are plotted against the Sn fraction in Figure 3-7(b). The data points of compressive-strained $Ge_{1-x}Sn$ layers on a Ge VS (red stars) and on the GeSn relaxed buffer (blue stars) are labeled. The fitting line is consistent with the results in the literature [62][64][66][67]. However, the prior high-Sn PL data (triangle scatters) is slightly deviated from our fitting line, mainly due to the different strain conditions of the GeSn films by different relaxed GeSn relaxed buffers.

3.4 Low-Temperature PL Spectra of GeSn

By varying the temperature, a lot of information from PL measurements will be given, such as, band structures, radiative efficiency, and even defect luminescence [68][69]. The direct-bandgap emission dominates the room-temperature luminescence even in indirect-bandgap GeSn since the thermal energy results in the finite electrons in the direct valley, leading to efficient emission. At low temperatures, the number of electrons in the direct valley at a higher energy is reduced, so the direct emission is effective suppressed and the indirect-bandgap luminescence is able to observe. The transition between the direct and indirect luminescence can be observed in low-

doi:10.6342/NTU202300648

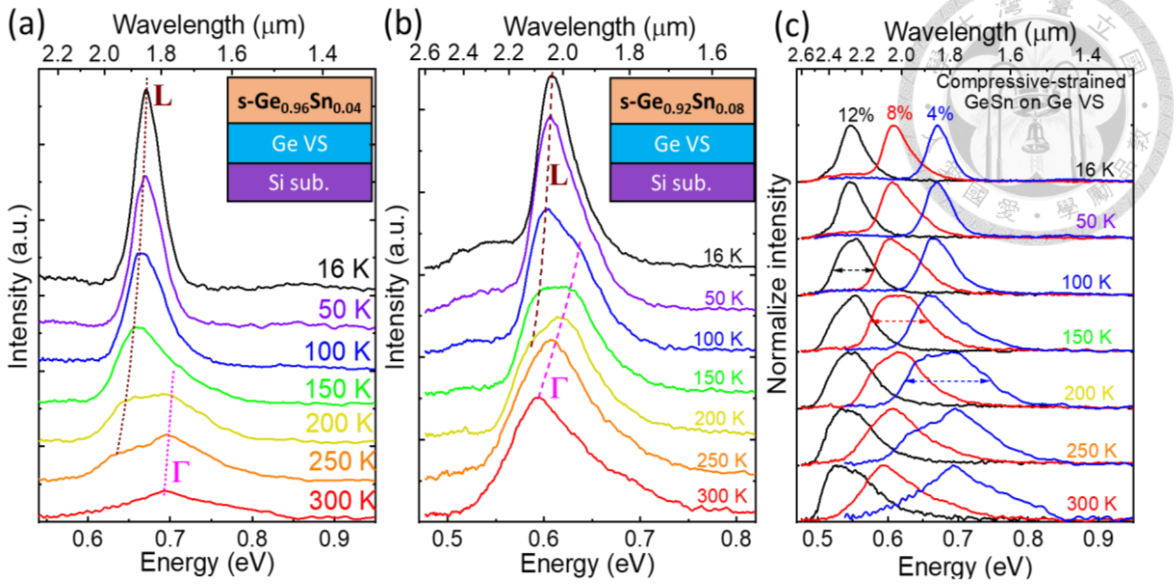

Figure 3-8 PL spectra of compressive-strained (a) $Ge_{0.96}Sn_{0.04}$ and (b) $Ge_{0.92}Sn_{0.08}$ on Ge VS at low temperatures. (c) Normalized LT-PL spectra of compressive GeSn with Sn fractions of 4 %, 8 %, and 12 %.

temperature PL in the indirect GeSn [62] and the indirect GaInP layers [63]. In this work, the low-temperature GeSn PL was measured from 16 K ~ 300 K. The same evolution of the direct and indirect luminescence was also observed in our compressive-strained GeSn on Ge VS. More low-temperature PL results on GeSn of different strain condition and high-Sn GeSn ([Sn]=24%) are presented to further investigate the luminescence in GeSn.

3.4.1 PL Spectra of Compressive-Strained GeSn on Ge VS at Low Temperatures

The PL spectra of compressive-strained $Ge_{0.96}Sn_{0.04}$ and $Ge_{0.92}Sn_{0.08}$ at low temperatures (LT) are shown in Figure 3-8(a) and (b), respectively. At 300 K, the PL spectra were dominated by direct-bandgap (Γ) emission. For both strained $Ge_{0.96}Sn_{0.04}$ and $Ge_{0.92}Sn_{0.08}$ PL spectra, as the temperature decreases, another emission peaks appear at the lower energy and becomes dominant at 16 K. Those lower-energy peaks are attributed to the indirect-bandgap (L) emission. Although the two separated peaks from L

doi:10.6342/NTU202300648

and Γ emission are not clearly distinguished, the broad plateaus at 200 K in Figure 3-8(a) and at 100 K in Figure 3-8(b) clearly indicate the contributions from both types of emission. Both peaks are blue-shifted with a decreasing temperature due to the bandgap broadening. The normalized LT-PL spectra are shown in Figure 3-8(c) with compressive-strained GeSn with three Sn fractions of 4 %, 8 %, and 12 %. For the PL spectra of strained $Ge_{0.88}Sn_{0.12}$, no plateau is observed, which suggests the energy difference between the Γ and L valleys is too smaller to be distinguished in the PL measurements. Furthermore, the plateau width is smaller with the higher Sn fraction, which supports the argument that the energy difference of two valleys decreases with the Sn fraction.

The transition of emission from the L valley to Γ valley is clearly observed in the LT-PL of the strained $Ge_{0.92}Sn_{0.08}$ QW structure (Figure 3-9(a)), where the effective bandgap of direct Γ-valley at RT is enlarged by the quantum confinement effect (Figure

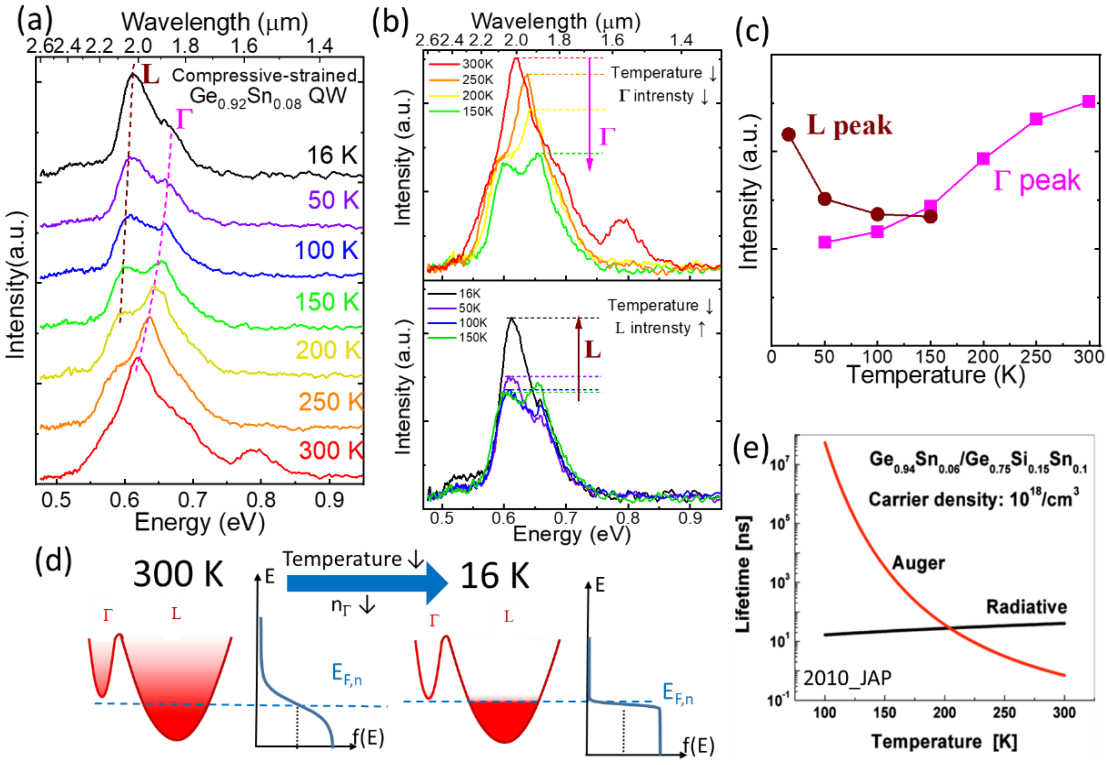

Figure 3-9 (a,b) Stacked LT-PL spectra of a strained $Ge_{0.92}Sn_{0.08}$ QW and (c) extracted peak intensity versus temperature. (d) Schematic of electron distribution at 300 K and 16 K. (e) Lifetime of Auger and radiative versus temperature [71].

doi:10.6342/NTU202300648

3-7(a)). The two peaks are clearly distinguished at 150 K (green curve). As the temperature is reduced, the emission intensity from direct Γ-valley becomes weaker while the indirect-emission becomes stronger. The peak intensity of Γ- and L-emission is extracted and plotted versus temperature in Figure 3-9(c). For the decreasing intensity of Γ- emission with lowering temperatures, the reason is that the electrons number in the Γ valley is reduced at lower temperatures in indirect-bandgap GeSn (Figure 3-9(d)).

On the other hand, for the emission peak of the L valley, the intensity monotonically increases from 150 K to 16 K. The increasing intensity can be explained by a higher radiative efficiency at low temperatures. The radiation efficiency η, also named as internal quantum efficiency (IQE) in optoelectronic devices, is the probability of a photon emitted in the radiative recombination, which is given by:

$$\eta \equiv \frac{1/\tau_{rad}}{1/\tau_{total}} = \frac{1/\tau_{rad}}{1/\tau_{rad} + 1/\tau_{Auger} + 1/\tau_{SRH}} \qquad \text{Eq. 3-1}$$

where $1/\tau_{rad}$ is the radiative recombination rate, and the non-radiative recombination rate is the sum of the Auger recombination rate ($1/\tau_{Auger}$) and SRH recombination rate ($1/\tau_{SRH}$). At room temperature, the carrier lifetime (τ_{total}) is dominated by Auger or SRH recombination in Ge, depending on the excess carrier concentration [70]. Thus, the radiation efficiency is rather low at room temperature. Compared to the radiative recombination, the SRH and Auger recombination rate are highly temperature-dependent and suppressed at low temperatures, as shown in Figure 3-9(e) [71]. In our indirect-bandgap strained $Ge_{0.92}Sn_{0.08}$ sample, since the number of the L electrons is almost constant at these temperatures, the intensity enhancement is attributed to the higher radiative efficiency due to the suppressed non-radiative recombination at low temperatures. Based on the radiative efficiency in Eq. 3-1, the intensity of the band-to-band emission should increase at low temperatures in a pure direct or a pure indirect semiconductor (constant carrier density in the same valley), such as GaAs and Si [72][73].

doi:10.6342/NTU202300648

As a result, the decreasing Γ emission and increasing L emission at a reduced temperature suggests the GeSn layer is indirect-bandgap.

The comparison of PL spectra between the bulk $Ge_{0.92}Sn_{0.08}$ and $Ge_{0.92}Sn_{0.08}$ QW is shown in Figure 3-10(a). The peaks from the Γ emission are clearly shifted by QW structure, while the shifting of L emission peak is less pronounced. The blue-shifted peak is owing to the stronger quantum confinement for the Γ valley, and the energy of the quantum level is larger ($E_{\Gamma,n=1} > E_{L,n=1}$). The energies of Γ and L emissions are extracted and plotted in Figure 3-10(b). For compressive-strained bulk $Ge_{0.92}Sn_{0.08}$ (solid curves), the energy difference is ~ 25 meV at 100 ~ 200 K, which is close to the reported value of 32 meV in $Ge_{0.94}Sn_{0.06}$ [62]. For the $Ge_{0.92}Sn_{0.08}$ QW (dash curves), the energy difference is larger (~ 45 meV), which is attributed to the stronger quantum confinement of the Γ valley ($\overline{\Delta E_\Gamma}$=27.7 meV) than that of the L valley ($\overline{\Delta E_L}$=5.7 meV) due to the smaller effective mass and the larger conduction band offset for the Γ valley (Figure 3-10(c)). The band offsets were calculated by the fitting parameters in the reference [19]. Based on the larger band offset (81 meV) and smaller effective mass (0.03 m_0) of the Γ valley, the first quantum level ($E_{\Gamma,n=1}$) is 23 meV, much larger than that of the L valley ($E_{\Gamma,n=1}$=3 meV).

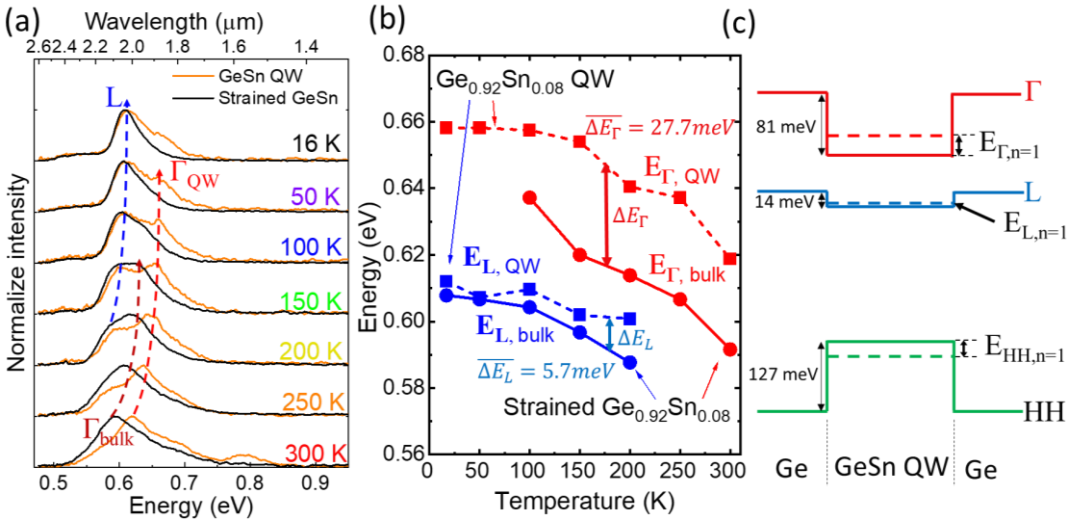

Figure 3-10 (a) Normalized PL spectra of the compressive-strained bulk $Ge_{0.92}Sn_{0.08}$ and QW structures at low temperatures with (b) the extracted peak emission energy versus temperature. (c) Simulated band diagram of 15-nm $Ge_{0.92}Sn_{0.08}$ QW.

doi:10.6342/NTU202300648

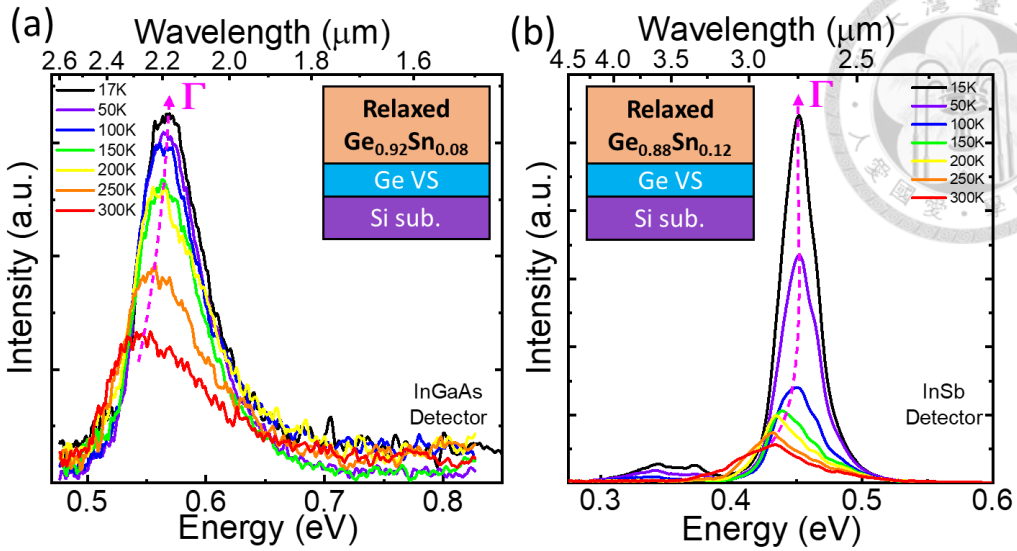

Figure 3-11 LT-PL spectra of strain-relaxed (a) $Ge_{0.92}Sn_{0.08}$ and (b) $Ge_{0.88}Sn_{0.12}$.

3.4.2 LT-PL of Strain-Relaxed GeSn

The LT-PL spectra of strain-relaxed $Ge_{0.92}Sn_{0.08}$ and $Ge_{0.88}Sn_{0.12}$ are shown in Figure 3-11(a) and (b), respectively. The cross-over transition from the Γ-emission to L-emission is no longer observed. There is only one peak whose intensity increases monotonically from 300 K to 15 K, which suggests the Γ-emission dominates. The only peak suggests that Γ-valley and L-valley are too close to be distinguished, so the strained-relaxed $Ge_{0.92}Sn_{0.08}$ is considered at the crossover of indirect-to-direct bandgap transition. For $Ge_{0.88}Sn_{0.12}$, a similar trend is observed, so it is considered a direct bandgap material due to its higher Sn fraction, which is consistent with simulation results in prior works [2][19].

3.4.3 LT-PL of Tensile-Strained Ge and GeSn

The tensile-strained Ge and tensile-strained $Ge_{0.92}Sn_{0.08}$ on relaxed $Ge_{0.88}Sn_{0.12}$ buffers are also characterized by PL measurements at low temperatures. The LT-PL spectra of the 30-nm tensile-strained Ge layer on a relaxed $Ge_{0.88}Sn_{0.12}$ buffer are shown in Figure 3-12(a). At 300 K, a single peak is observed, but not able to be identified as the emission from the tensile-strained Ge layer or the buffer layer. In fact, in Figure 3-12(b),

doi:10.6342/NTU202300648

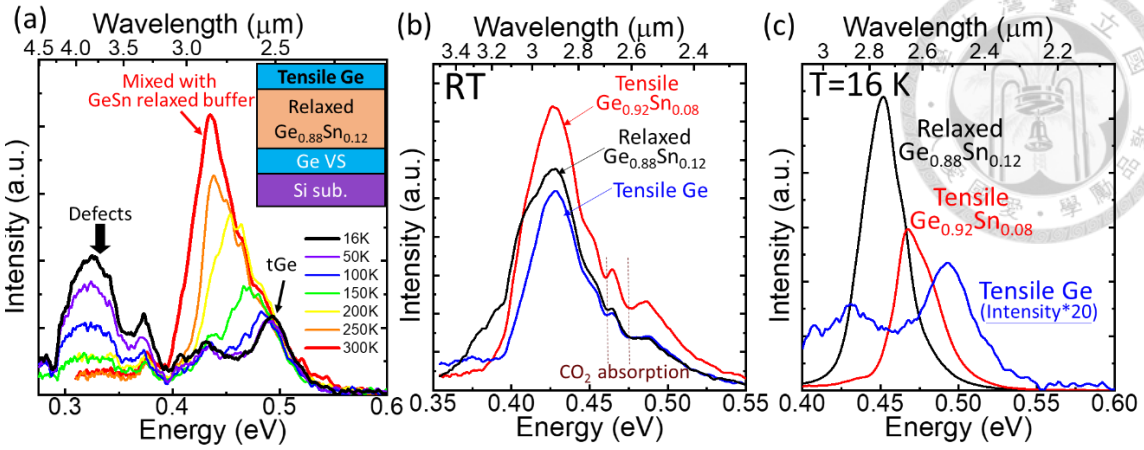

Figure 3-12 (a) LT-PL spectra of tensile-strained Ge on a relaxed $Ge_{0.88}Sn_{0.12}$ buffer. PL spectra of relaxed $Ge_{0.88}Sn_{0.12}$, tensile $Ge_{0.92}Sn_{0.08}$, and tensile Ge layers (b) at room temperature and (c) at 16 K.

the room-temperature PL spectra of relaxed $Ge_{0.88}Sn_{0.12}$, tensile $Ge_{0.92}Sn_{0.08}$, and tensile Ge grown on the same relaxed buffer, exhibit the same peak position at 2.9 μm (0.435 eV), which is attributed to the underlying $Ge_{0.88}Sn_{0.12}$ relaxed buffer. As the temperature decreases, the emission peak is blue-shifted and the intensity becomes weaker. On the other hand, another emission peak at a smaller energy (0.325 eV) appears below 150 K and becomes stronger with decreasing temperatures (Figure 3-12(a)). This smaller-energy peak might be attributed to the defects such as threading dislocation in the epi-layers [69]. The same peak is also shown in the LT-PL spectra of relaxed $Ge_{0.88}Sn_{0.12}$ at 16 K, as shown in Figure 3-11(b), where its intensity is much weaker than the radiative emission of relaxed GeSn.

PL spectra of three different epitaxial layers at 16 K are shown in Figure 3-12(c). The peak intensities of relaxed $Ge_{0.88}Sn_{0.12}$ and tensile $Ge_{0.92}Sn_{0.08}$ are enhanced from 300 K to 16 K by 10 times and 5 times, respectively, while only the intensity of the tensile Ge sample is reduced by 33 % with a blue-shifted emission peak. This further suggests the tensile-strained Ge epitaxial layer (+1.7%) is still an indirect bandgap material while two GeSn films show direct-bandgap characteristics following the argument in the previous

doi:10.6342/NTU202300648

section. Prior work suggested that the tensile Ge layer becomes direct-bandgap under a biaxial tensile strain of ~ 2% [74]. All three structures have the same $Ge_{0.88}Sn_{0.12}$ relaxed buffer layer, but their emission peaks are at different positions at 16 K, which can be used to identify as the emission from the active layers. All emission peaks show blue-shift characteristics and the tensile Ge show the largest bandgap energy. However, the temperature dependence of the PL spectra (Figure 3-12(a)) is quite complex due to the mixing of emission from the active layer and the relaxed GeSn buffer. Thus, it is not an easy task to distinguish those emissions and further work is required.

Figure 3-13 explains why the PL spectrum of the tensile-strained Ge(Sn) epitaxial film is less pronounced than that of the compressive-strained GeSn film. The 532-nm green light has a very short absorption length of ~ 17 nm in Ge [75] and could be further shorter in GeSn alloys due to their smaller bandgap energies. Although the excitation light is absorbed mainly in the top GeSn layer, the excited carriers will diffuse to the relaxed buffer [76] (Figure 3-13(a)). The length scale of carrier diffusion is several micrometers in Ge, much larger than the light absorption length. For compressive-strained GeSn structure (Figure 3-13(b)), the Sn fraction of strained $Ge_{1-x}Sn_x$ is higher than that of

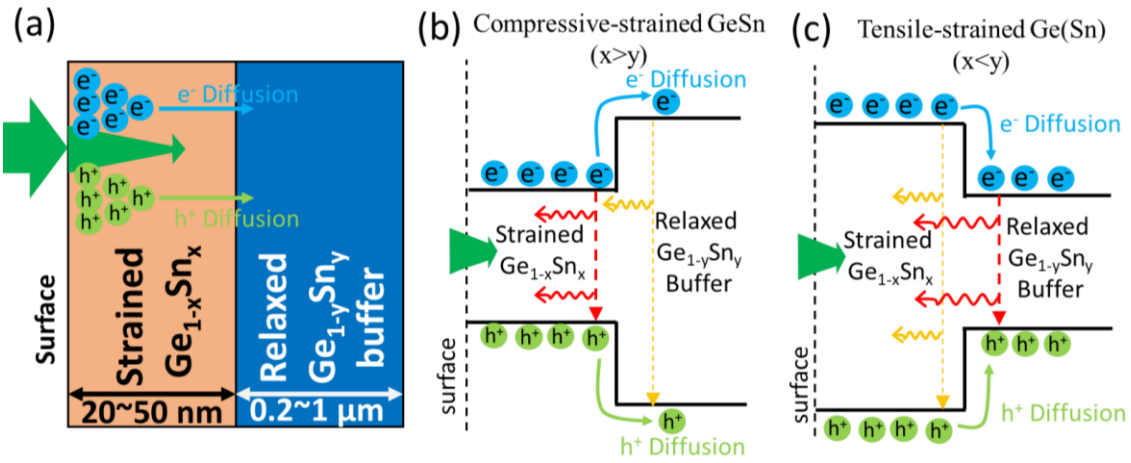

Figure 3-13 (a) Schematic of optical pumping and diffusion of excited carriers in a strained $Ge_{1-x}Sn_x/Ge_{1-y}Sn_y$ heterostructure with the associated band diagrams for (b) compressive-strained $Ge_{1-x}Sn_x$ and (c) tensile-strained Ge (x = 0) active layers.

doi:10.6342/NTU202300648

relaxed $Ge_{1-y}Sn_y$ buffer (x > y), there exist barrier heights for electrons and holes in the compressive-strained GeSn layer [19], reducing diffused carriers into the relaxed buffer. This becomes more effective at lower temperatures. What's more, the emitted photons from the relaxed buffer with a larger energy bandgap will be re-absorbed by the top strained GeSn layer. Therefore, the emission from the relaxed buffer is less observed in the PL spectrum. However, for the tensile-strained Ge(Sn) structure (Figure 3-13(c)), the carrier diffusion wouldn't be suppressed due to the smaller or opposite band offset. The emitted photons from the relaxed buffer can go through the top layer without re-absorption. As a result, the PL spectrum of tensile-strained Ge(Sn) suffers more signal mixing from relaxed GeSn buffer (Figure 3-12).

3.4.4 LT-PL of GeSn ([Sn] ~ 24 %) on GeSn Relaxed Buffers

Last, the RT-PL and LT-PL spectra of the compressive-strained $Ge_{0.76}Sn_{0.24}$ epitaxial layers on a $Ge_{0.83}Sn_{0.17}$ relaxed buffer are shown in Figure 3-14. In Figure 3-14(a), the RT-PL spectrum shows the individual emission peaks for the strained layer and relaxed buffer (pink and black dashed squares, respectively). Note there exist two IR absorption dips at 4.3 and 3.1 μm by CO_2 and H_2O, respectively. The contributions of the $Ge_{0.83}Sn_{0.17}$

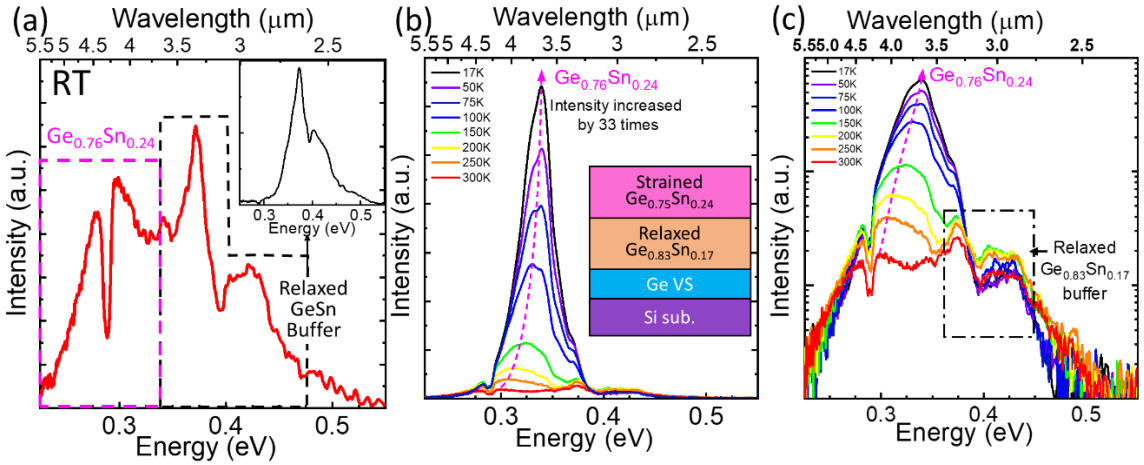

Figure 3-14 PL spectra at (a) room temperature and (b) lower temperatures of a compressive-strained $Ge_{0.76}Sn_{0.24}$ film on a $Ge_{0.83}Sn_{0.17}$ relaxed buffer.

doi:10.6342/NTU202300648

relaxed buffer is confirmed by another epitaxial structure with only the $Ge_{0.83}Sn_{0.17}$ relaxed buffer, as shown in the inset. Due to the thin top layer of 20 nm, the PL intensity of the strained $Ge_{0.76}Sn_{0.24}$ layer is slightly smaller than that of the relaxed buffer. PL spectra at lower temperatures are shown in Figure 3-14(b). As the temperature is reduced, the emission intensity from $Ge_{0.76}Sn_{0.24}$ increases rapidly, while the emission from the relaxed buffer is suppressed by the limited carrier diffusion due to the presence of barrier heights between those two layers. At 16 K, the peak intensity of $Ge_{0.76}Sn_{0.24}$ is enhanced by a factor of 33 with the peak position blue-shifted to 0.33 eV (3.66 μm). At room temperature, due to serious IR absorption, it is difficult to precisely identify the emission peak, while low-temperature PL data offer unambiguous emission peaks.

3.5 IR Absorption Effects on GeSn PL Spectra

3.5.1 IR Absorption in the Lab Environment

Since our PL measurement system is placed in the atmospheric environment, the IR absorption by the molecules in the air is inevitable and results in signal dips at certain positions. For example, two close absorption dips at 2.6 μm and 2.7 μm are observed in Figure 3-12(b) due to the CO_2 absorption. Two more absorption drops at 3.1 μm and 4.3

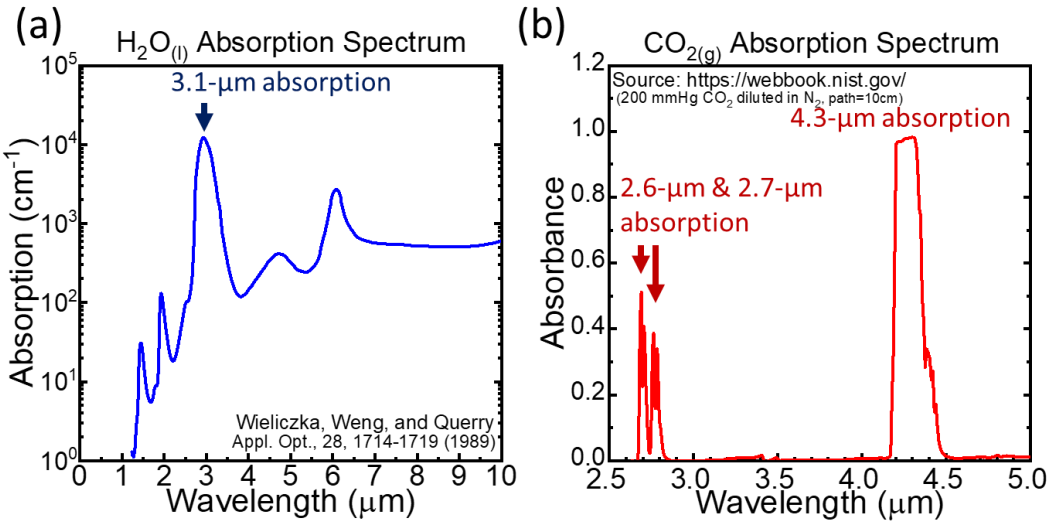

Figure 3-15 Absorption spectra of (a) liquid water [77] and (b) gaseous CO_2 [78].

doi:10.6342/NTU202300648

μm are observed in Figure 3-14 (a), while correspond to H_2O and CO_2 absorption, respectively. The absorption at 3.1 μm results from the water vapors in the air, which can be identified in the absorption spectrum of the water in Figure 3-15(a) [77]. The other three dips (at 2.6 μm, 2.7 μm, and 4.3 μm) are due to CO_2 absorption, whose absorption spectrum is shown in Figure 3-15(b) [78]. The absorption at 4.3 μm is very strong and leads to a deep dip in the PL spectra of GeSn with a very high Sn fraction (~ 24 %).

3.5.2 Calibration of PL Spectra

In order to characterize the absorption in our PL system, the black body radiation spectrum by our system is shown in Figure 3-16. The radiation source is the head of a soldering gun at temperatures of 200 ºC ~ 350 ºC (Figure 3-16(a)). There exists a cutoff at 5.5 μm corresponding to the cutoff wavelength of the InSb photodetector. The normalized spectra are shown in Figure 3-16(b) and three absorption dips are clearly observed. For absorption #2 and #3, the bandwidths of the dips are wider than absorption #1.

The calibrated absorption spectrum is extracted in the 350-ºC spectrum (red curve)

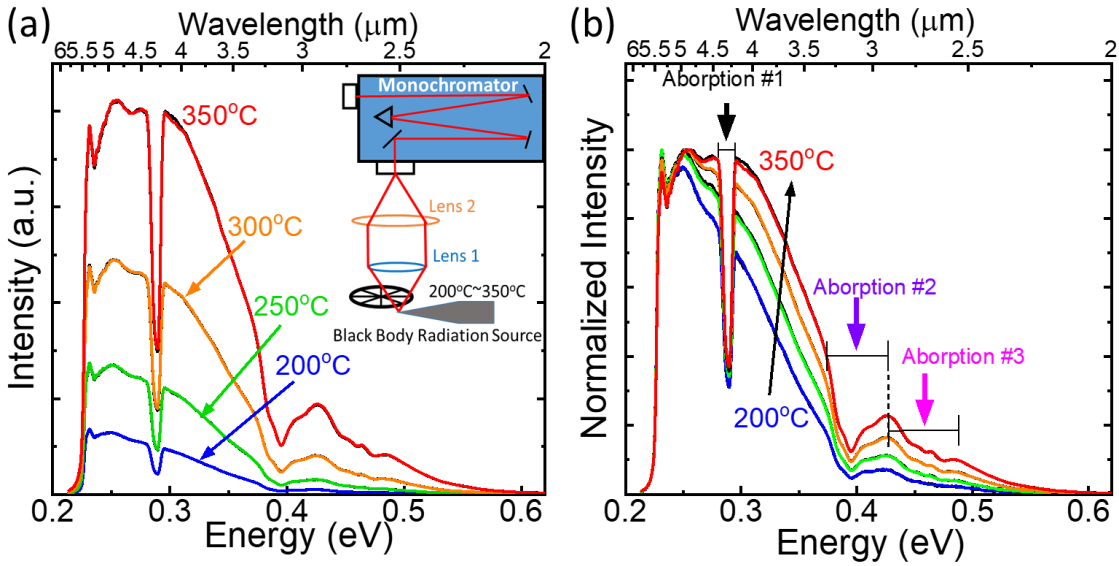

Figure 3-16 (a) Measured spectra and (b) normalized spectra of black body radiation in the PL system with the source temperature 200 ºC ~ 350 ºC.

doi:10.6342/NTU202300648

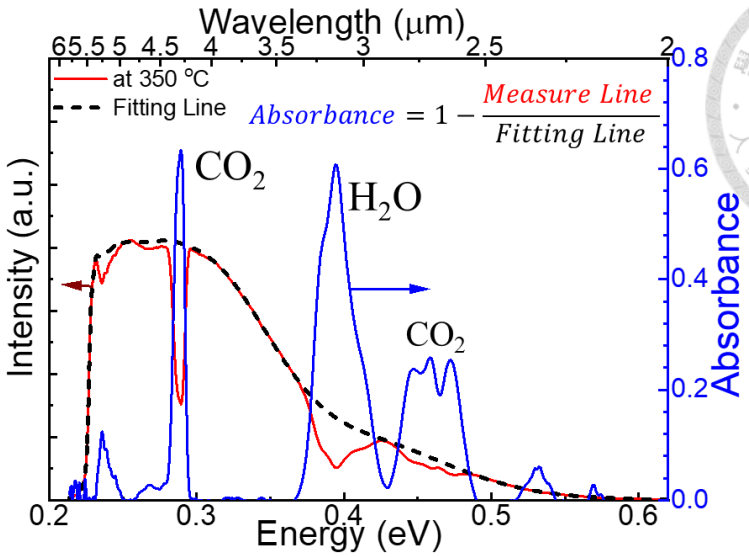

Figure 3-17 Extracted PL spectrum at 350 °C.

by giving the smooth envelop fitting line (dash curve) in Figure 3-17. Since the profile is also distorted by the response spectra of all components (lens, grating, and detector), it is hard to fit the curve by the black body radiation formula. The absorption spectrum is plotted by the absorbance versus wavelength, which represents how much intensity would be absorbed along the optical path. Therefore, the GeSn PL spectra can be approximately calibrated by the absorbance spectrum.

The calibrated PL spectra of strained $Ge_{0.76}Sn_{0.24}$ by excluding the IR absorption are

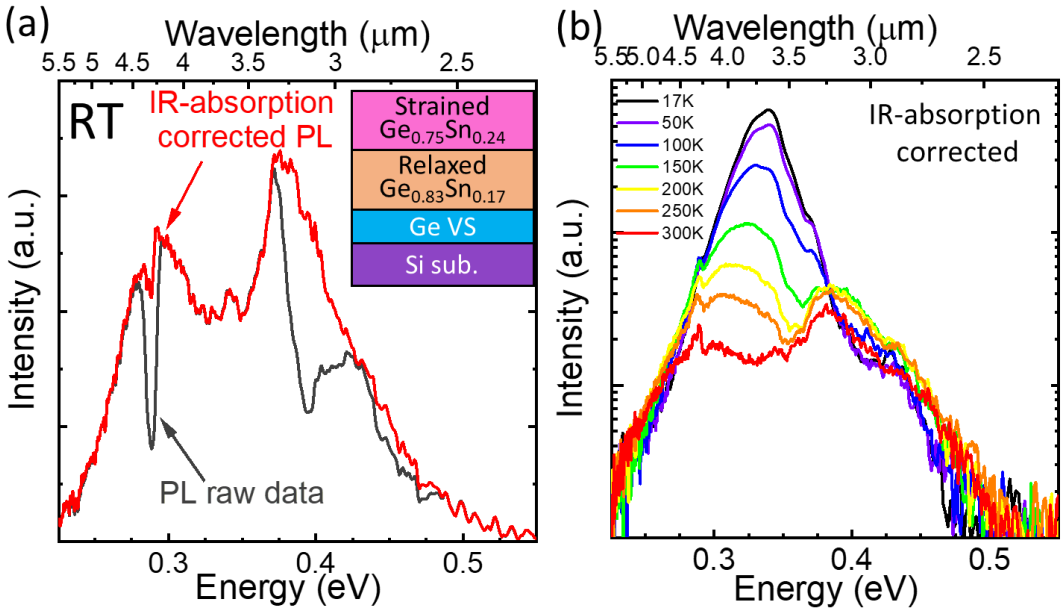

Figure 3-18 (a) RT-PL and (b) LT-PL spectra of strained $Ge_{0.76}Sn_{0.24}$ on GeSn relaxed buffers by the calibrated IR absorption.

doi:10.6342/NTU202300648

shown in Figure 3-18. The two emission peaks (envelopes) at room temperature are much clearer after the IR calibration (Figure 3-18 (a)). Besides, in the calibrated LT-PL spectra (Figure 3-18 (b)), the evolution of the emission peak from the relaxed buffer is much clearer, and the buffer emission is weaker below 100 K. There is still some uncertainties for the calibration steps at the 4.3-μm absorption since the concentrations of CO_2 and H_2O in the air are not constant, leading to deviations for different measurements. Therefore, a more precise method is still required to construct a better PL profile.

doi:10.6342/NTU202300648

Chapter 4 Room-Temperature Characteristics of GeSn Esaki Tunnel Diodes

4.1 Motivation

Moore's law has been driven the scaling of Si complementary metal–oxide–semiconductor (CMOS) transistors for several decades. However, the threshold voltage of logic transistors cannot be scaled down further due to the limited subthreshold swing (SS) of 60 mV/decade at room temperature. Novel devices with different operational principles for a sharper SS than the limit of 60 mV/decade by Boltzmann distribution have been extensively investigated, such as impact ionization MOS (I-MOS) transistors [79], negative-capacitance field-effect transistors (NC-FETs) [80], or tunnel field-effect transistors (TFETs) [81]. Although a sub-60 subthreshold swing has been demonstrated in those devices, some drawbacks need to be overcome for practical applications. For example, the required high gate biases for I-MOS transistors or the hysteresis for NC-FETs are critical issues for reliable integrated circuits. While for TFETs, whose device structures are similar to conventional CMOS transistors, the major issue is the low drive current. A steep SS is achieved by band-to-band tunneling (BTBT) processes between the source and channel regions. Meanwhile, the drive current is limited by the probabilistic tunneling process, which has hampered the TFET applications. Even though TFETs are not competitive with CMOS transistors for logical applications, they are quite suitable for low-power applications, such as the internet-of-things (IoT) [82]. Rather than a high on-state current, a very low static power realized by steep SS is required for these low-power applications. However, in order to obtain a reasonable drive current, increasing the tunneling rate and tunneling current is still the major concern for TFETs. For group-IV materials such as silicon (Si) or germanium (Ge), the BTBT current is low due to their

doi:10.6342/NTU202300648

large bandgap, effective masses of carriers, and the requirement of phonon participation for the indirect-bandgap characteristics [83][84]. Based on the discussion in previous chapters, GeSn is a good candidate for solving those problems due to its direct-bandgap characteristics and the compatibility with Si-based VLSI technology.

To justify the BTBT process and calibrate the tunneling rates, Esaki diodes with negative differential resistance (NDR) are used to characterize the peak current density. Thus far, there is no NDR demonstrated in any GeSn-based Esaki diodes at room temperature. Only Schulte-Braucks *et al.* observed the NDR at a low temperature below 150 K in a GeSn p-i-n structure [85]. The tunneling current was fairly low (< 0.3 A/cm^2), and there is no systematic study on tunneling current in GeSn. In this chapter, high-performance GeSn Esaki diodes with clear NDR and extremely high peak current densities at room temperature are demonstrated. GeSn Esaki tunnel diodes are systematically studied with various material parameters, such as doping levels, Sn fraction, and strain conditions. In the next chapter, temperature-dependent I-V characteristics and phonon spectra at cryogenic temperature are performed to further investigate the direct-bandgap tunneling in GeSn Esaki diodes.

4.2 Introduction to Esaki Diodes (TDs)

4.2.1 Band-to-Band Tunneling (BTBT) and Negative Differential Resistance (NDR)

A tunnel diode with NDR was demonstrated by L. Esaki in 1958 for the first time and has been called the Esaki diode [86]. An anomalous I-V characteristic in the forward bias, that is, a negative-differential-resistance region, was observed in a germanium Esaki diode, which earned him the Nobel Prize in Physics in 1973.

doi:10.6342/NTU202300648

An Esaki tunnel diode consists of a simple p-n junction in which both p-type and n-type regions are both degenerately doped. Since there are some other types of tunnel diodes, such as resonant tunnel diodes (RTD) [87] and resonant interband tunnel diodes (RITD) [88], we use "Esaki" tunnel diode to represent the simple p-n junction structure without any addition quantum wells with aligned quantum levels. Figure 4-1 shows the band diagram of an Esaki tunnel diode under a small forward bias. Due to the degenerate doping, the quasi-Fermi levels in both p^+ and n^+ region, $E_{F,p}$ and $E_{F,n}$, penetrate into the valence band and conduction band, respectively. The amount of doping degeneracy noted as V_p' and V_n' is dependent on doping concentration, material, and even temperature. The minimum doping concentrations of degenerate-doped semiconductors is approximately the effective density of states at room temperature, e.g., 5.0×10^{18} cm^{-3} (valence band) and 1.0×10^{19} cm^{-3} (conduction band) at 300 K for Ge. The electric field, F_{field} in the depletion region is fairly large (usually > 1 MV/cm), resulting in a short tunneling distance of ~ 10 nm. As long as a small voltage bias is applied, the electrons can tunnel through the depletion region from the n^+ region conduction band to the p^+ region valence band, and vice versa.

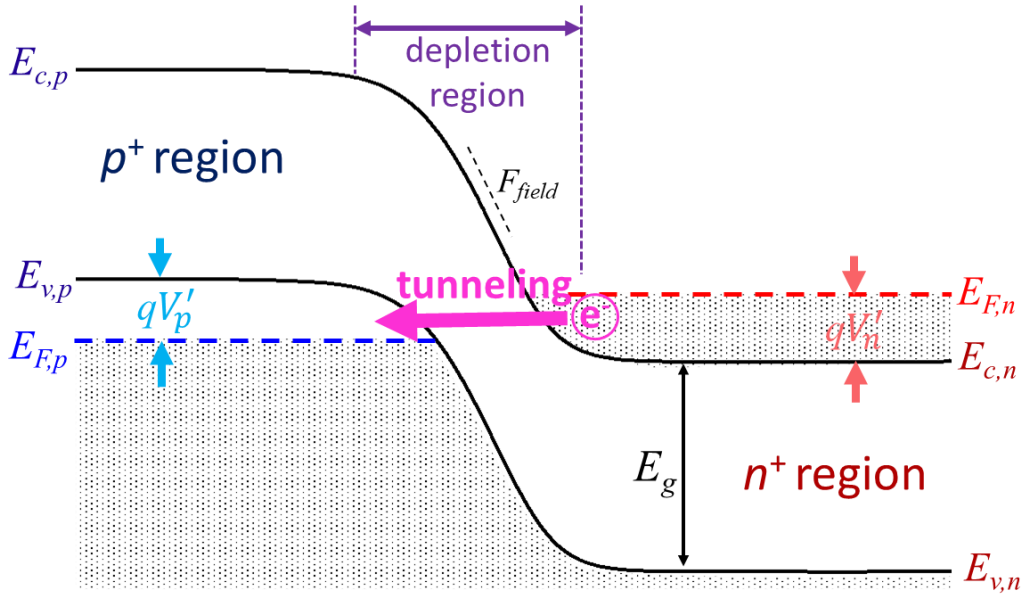

Figure 4-1 A band diagram of an Esaki tunnel diode under a small forward bias.

doi:10.6342/NTU202300648

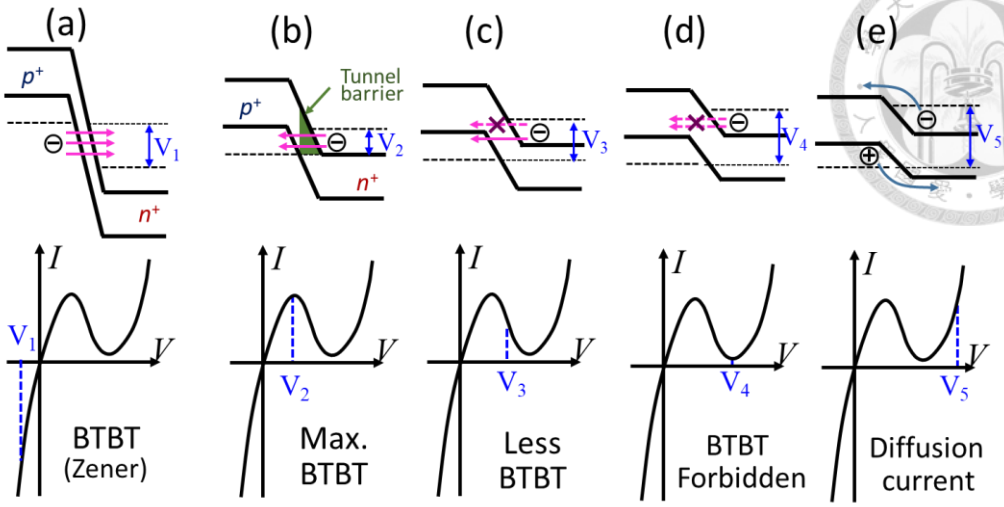

Figure 4-2 Band diagrams (top) and I-V curves (bottom) of an Esaki tunnel diode at different biases.

Operations and I-V characteristics of an Esaki tunnel diode are illustrated in Figure 4-2, respectively. First of all, under a reverse bias, the current is contributed by the BTBT process from the valence band in the p^+ region to the conduction band in the n^+ region, which is known as Zener tunneling. Increasing the reverse bias enhances both the electric field in the depletion region and the overlap of the available states for tunneling, the Zener tunneling current increases monotonically with the reverse-bias voltage. Under a small forward bias (Figure 4-2(b)), the BTBT current flows from the conduction band of the n^+ region to the valence band of the p^+ region and increases with the bias due to the larger overlap of the available states. As the available states at both n- and p-regions are aligned, the tunneling current will reach a local maximum (J_{peak}). A further larger forward-bias voltage will reduce the overlapped states, so the BTBT current decreases with a larger forward-bias voltage (Figure 4-2(c)). A negative dI/dV region in the I-V curve is observed and called the NDR region. At a larger voltage, the conduction band edge of the n^+ region is over the valence band edge of the p^+ region (i.e. $E_{c,n} > E_{v,p}$), the BTBT is forbidden due to the band misalignment (Figure 4-2(d)). The diode current will reach a local minimum, which is called the valley current (J_{valley}). The non-zero valley current is attributed to

doi:10.6342/NTU202300648

defect-assisted tunneling (DAT), where electrons tunnel via the defect states within the bandgap across the p-n junction. At last, in Figure 4-2(e), as the forward bias is large enough, the diffusion current will dominate and the device works as a normal p-n junction diode.

The existence of NDR in Esaki diodes is the evidence of the band-to-band tunneling. A peak-to-valley current ratio (PVCR), defined as the ratio of peak current over valley current (J_{peak}/J_{valley}) is used to evaluate the quality of the tunnel junction/processes. If the PVCR is rather small (or disappears without NDR), the peak current (density) might consist of a large amount of DAT current, leading to an overestimation of BTBT rates.

4.2.2 Band-to-Band Tunneling Rate and Tunneling Current

The band-to-band tunneling rate and the tunneling current (density) are crucial for a tunnel device. The BTBT current in an Esaki diode is calculated based on Kane's model [90][91]. The tunneling probability T_t is given by the WKB (Wentzel-Kramers-Brillouin) approximation:

$$T_t \approx \exp\left[-2\int_{x_p}^{x_n}|k(x)|dx\right] \qquad \text{Eq. 4-1}$$

where $|k(x)|$ is the absolute value of the electron wavevector in the tunneling barrier, and x_p and x_n are the two terminal positions of the tunneling process, which are at the valence band edge and conduction band edge in the p^+ and n^+ regions, respectively. Assume the piecewise band diagram and the triangular tunneling barrier, as shown in Figure 4-2(b). The tunneling probability is [91]

$$T_t \approx \exp\left(-\frac{4\sqrt{2m^*}E_g^{\frac{3}{2}}}{3q\hbar F_{field}}\right) \qquad \text{Eq. 4-2}$$

where E_g is the bandgap energy, F_{field} is the electric field of the triangular barrier,

doi:10.6342/NTU202300648

which can be referred to as the average electric field of a p-n junction:

$$F_{field} = \sqrt{\frac{q(\psi_{bi} - V)N_A N_D}{2\varepsilon_s(N_A + N_D)}} = \sqrt{\frac{q}{2\varepsilon_s}(\psi_{bi} - V_p)N^*} \quad \text{Eq. 4-3}$$

where ψ_{bi} is the built-in potential and V is the applied voltage to the junction. $N^* = N_A N_D/(N_A + N_D)$ is the effective doping concentration of an Esaki diode. N_A and N_D are the doping concentrations of the p-type and n-type layers, respectively. Note that the tunneling probability in Eq. 4-3 does not include the momentum perpendicular to the tunneling direction, $k_\perp$. There is an additional reduction in tunneling probability by the energy $E_\perp$ associated with perpendicular momentum:

$$T_t \approx \exp\left(-\frac{4\sqrt{2m^*}E_g^{\frac{3}{2}}}{3q\hbar F_{field}}\right)\exp\left(-\frac{E_\perp \pi\sqrt{2m^* E_g}}{q\hbar F_{field}}\right) \quad \text{Eq. 4-4}$$

Next, the expression of the BTBT current is derived by assuming direct tunneling without perpendicular momentum. At thermal equilibrium, there are two components of the tunneling current: from the occupied conduction band to the empty valance band $I_{C\to V}$ and from the occupied valance band to the empty conduction band $I_{V\to C}$:

$$I_{C\to V} = C_1 \int F_C(E)N_C(E)T_t[1 - F_V(E)]N_V(E)dE \quad \text{Eq. 4-5}$$

$$I_{V\to C} = C_1 \int F_V(E)N_V(E)T_t[1 - F_C(E)]N_C(E)dE \quad \text{Eq. 4-6}$$

where C_1 is a constant, $F_C(E)$ and $F_V(E)$ are the Fermi-Dirac distribution functions. $N_C(E)$ and $N_V(E)$ are the density of states of the conduction band and valence band, respectively. The tunneling probability T_t is assumed to be equal for both directions. At zero bias, these two tunneling current components are balanced, and the net tunneling current I_t is zero. As the diode is forward-biased, the net tunneling current I_t is given by

doi:10.6342/NTU202300648

$$I_t = I_{C\to V} - I_{V\to C} = C_1 \int_{E_{v,n}}^{E_{v,p}} [F_C(E) - F_V(E)] T_t N_C(E) N_V(E) dE \quad \text{Eq. 4-7}$$

Thus, the tunneling current in an Esaki diode can be calculated as [91]

$$J_t = \frac{q^2 E_{field}}{36\pi\hbar^2} \sqrt{\frac{2m^*}{E_g}} \cdot D \cdot \exp\left(-\frac{4\sqrt{2m^*} E_g^{\frac{3}{2}}}{3q\hbar E_{field}} \right) \quad \text{Eq. 4-8}$$

with the integral *D* defined as

$$D \equiv \int_{E_{c,n}}^{E_{v,p}} [F_C(E) - F_V(E)] \left[1 - \exp\left(-\frac{2E_s}{\bar{E}} \right) \right] dE \quad \text{Eq. 4-9}$$

$$\bar{E} = \frac{\sqrt{2} q\hbar E_{field}}{\pi\sqrt{m^* E_g}} \quad \text{Eq. 4-10}$$

where E_s is the smaller energy difference compared to $E_{v,p}$ and $E_{c,n}$. At zero bias, $F_C(E)$ and $F_V(E)$ are equal, so the integral *D* is zero. At $V_{valley} = V_p' + V_n'$, $E_{v,p}$ and $E_{c,n}$ are aligned, and the tunneling window ($E_{v,p} - E_{c,n}$) is closed. The integral *D* is zero again due to no integral interval. Typically, the peak voltage V_{peak} is roughly $(V_p' + V_n')/3$ by calculation and in the experimental results [92].

To enhance the tunneling current, a larger electric field or a smaller bandgap energy is preferred. Moreover, the higher doping concentration with larger degeneracy (V_p' and V_n') can increase the tunneling window, which is relative to the integral interval of the integral *D*, and further increase the tunneling current.

4.2.3 Defect-Assisted Tunneling (DAT)

Ideally, the BTBT drops to zero as the available states are fully misaligned, and only very little thermal diffusion current at the valley voltage. However, in practice, the valley current is considerably in excess of the diffusion current of a p-n diode and sometimes comparable to the peak current [93]. For example, in Figure 4-3(a), the J-V characteristic

doi:10.6342/NTU202300648

of an epitaxial Ge Esaki diode shows a certain region (gray) that does not belong to the BTBT or diffusion current. This excess current is mainly contributed by the electron tunneling via the defect states within the bandgap [93], commonly called defect-assisted tunneling (DAT) current. In Figure 4-3(b), a tunneling junction with defects states in the bandgap is illustrated to show the possible paths of DAT. Under a relatively large bias to misalign the available states across the pn junction, the BTBT is forbidden, while the diffusion barrier is still too high to generate sufficient diffusion current. With the presence of defects states, the electron in the n^+ region can move to the valence band of the p^+ region through the several steps of tunneling and recombination. A defect state can be a single state D_p (D_n) or a series of states within the bandgap in the depletion region. For simplicity, assuming that the limiting step is the tunneling process rather than the recombination process, the DAT current is given by [91]

$$J_x \approx C_2 D_x \ \exp\{-C_3[E_g + q(V_n' + V_p') - qV]\} \qquad \text{Eq. 4-11}$$

where C_2 and C_3 are constants, and D_x is the density of the available defect states; that is, empty states of D_p or occupied stated of D_n. The DAT current increase exponentially with the applied voltage V, and thus Eq. 4-11 can be simplified as

$$J_x = J_{valley} \ \exp[C_4(V - V_{valley})] \qquad \text{Eq. 4-12}$$

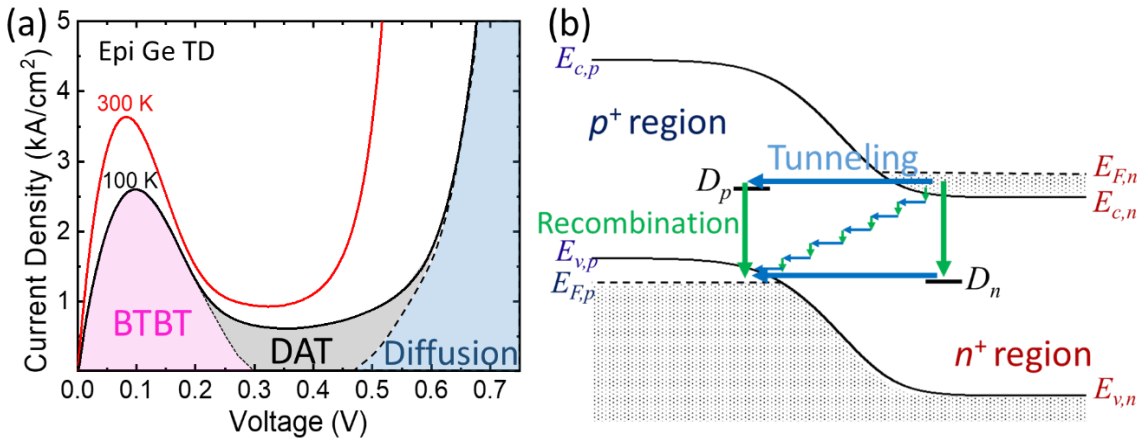

Figure 4-3 (a) A diagram showing major current components in a Ge Esaki diode. (b) A band diagram showing possible paths for DAT current.

doi:10.6342/NTU202300648

The valley current is dominated by the density of defect states, which depends on the preparation method of the tunnel diode, such as dopant diffusion, solution regrowth, CVD, or MBE. For a fixed peak current, the PVCR can be improved by suppressing the defect density. Besides, the DAT current can also be suppressed at low temperatures. In addition to the temperature dependence of the bandgap energy, the pre-factor $C_2 D_x$ is strongly temperature dependent due to the recombination process [92].

4.2.4 Direct and Indirect Tunneling in GeSn Esaki Diodes

The expression of BTBT current in Eq. 4-8 is derived based on the assumption of direct tunneling without the change of momentum; that is, the wave vectors of the initial state and the final state are identical. In semiconductors, the valley of the valence band is located at Γ ($\vec{k} = 0$), and the direct tunneling occurs between Γ valleys of the conduction band and the valence band, while the indirect tunneling occurs as the valley of the conduction band is located at a valley with a non-zero momentum, such as <100> X-direction in Si or <111> L-direction in Ge. Indirect tunneling requires the participation of phonons for the momentum reservation in k-space, which is called phonon-assisted

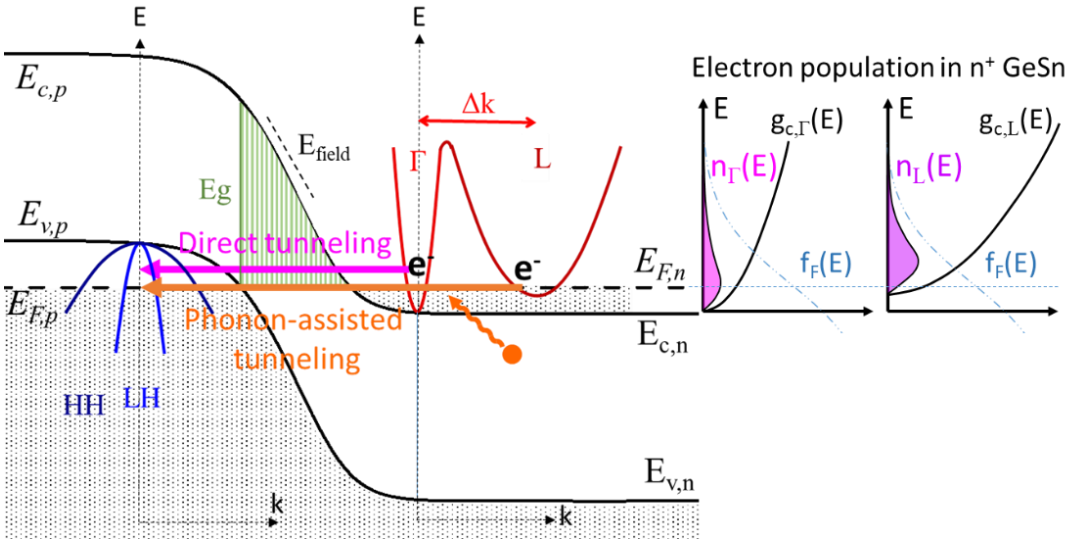

Figure 4-4 A band diagram of a direct-bandgap GeSn Esaki diode, where the energy levels of the direct Γ-valley and indirect L-valley are closed. The inset shows the electron population in two valleys.

doi:10.6342/NTU202300648

tunneling [94]. Sometimes, the momentum difference during the tunneling process can also be compensated by impurity scattering, which is called phonon-unassisted indirect tunneling [94][95]. The indirect tunneling possibility is much lower due to the momentum difference and required phonon participation. In this work, the BTBT generation rates are simulated by the TCAD package. In Ge, the direct BTBT generation rate is ~ 100 times higher than the indirect rate at an electric field of 1 MV/cm [96].

For GeSn Esaki diodes, the energy level of the direct Γ-valley is close to the level of the indirect L-valley (Figure 4-4). Direct- and indirect-tunneling processes both contribute to the BTBT current. Not only the tunneling rate, but also the electron population need to be considered for the tunneling current. In the indirect L-valley, due to the larger effective mass and 4-fold degeneracy, the density of state (DOS) is much larger than that in the direct valley. For instance, in Ge, the DOS of the L valley is 64 times larger than the DOS of the Γ valley. On the other hand, the larger effective electron mass of the indirect L-valley leads to a much smaller tunneling rate. Considering the requirement of phonon participation, the tunnel current is low in Ge diodes. For GeSn, since the energy difference between the L- and Γ-valley minima is much smaller than that in Ge, the electron population in Γ-valley can be much higher, leading to a higher contribution to the tunneling current.

4.3 Epitaxial Structures and Material Characterization of GeSn Esaki Diodes

Figure 4-5 shows the epitaxial structures for GeSn Esaki diodes. A n^+-Ge VS was deposited on a Si substrate, followed by annealing at 800 °C for the required strain relaxation and the low dislocation density. The epitaxial structures for Ge Esaki diodes were also grown as a baseline (Figure 4-5(a)) at 350 °C. B_2H_6 and PH_3 with high flow

doi:10.6342/NTU202300648

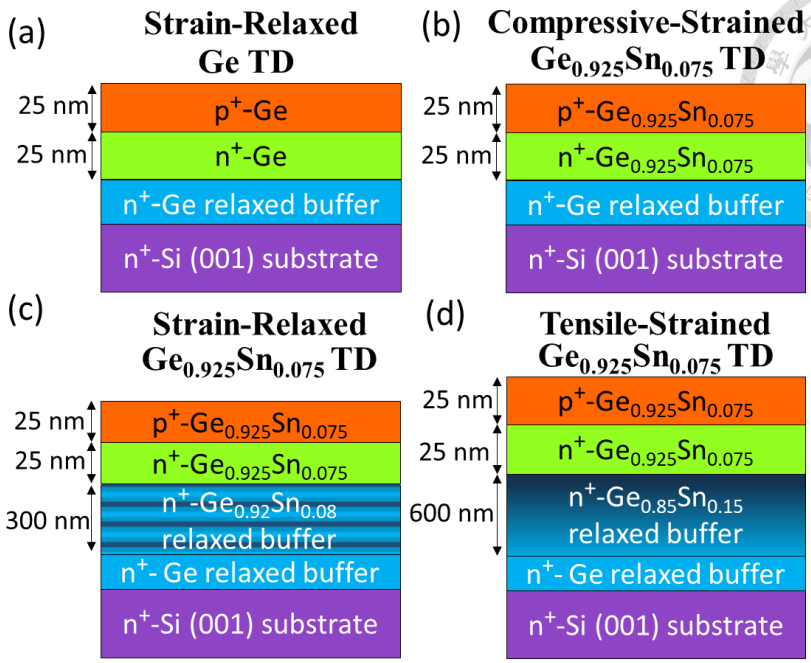

Figure 4-5 Epitaxial structures of (a) strain-relaxed Ge, (b) compressive-strained GeSn, (b) strain-relaxed GeSn, and (c) tensile-strained GeSn Esaki diodes.

rates were injected to provide the required degenerate doping concentrations for Esaki diodes. For the compressive-strained $Ge_{0.925}Sn_{0.075}$ diodes, a stack of a p^+-GeSn layer and a n^+-GeSn layer was pseudomorphically grown on the Ge VS (Figure 4-5(b)). For the strained-relaxed $Ge_{0.925}Sn_{0.075}$ diodes, a 300-nm GeSn superlattice relaxed buffer was grown, including a periodic structure of $Ge_{0.88}Sn_{0.12}$/$Ge_{0.92}Sn_{0.08}$ /$Ge_{0.96}Sn_{0.04}$ (Figure 4-5(c)). The strained-relaxed p^+/n^+ $Ge_{0.925}Sn_{0.075}$ stack was subsequently grown on the $Ge_{0.92}Sn_{0.08}$ relaxed buffer. For the tensile-strained $Ge_{0.925}Sn_{0.075}$ diodes, a $Ge_{0.85}Sn_{0.15}$ graded relaxed buffer was grown to induce tensile stresses on the top active layers (Figure 4-5(d)). The relaxed buffer is not fully relaxed and equivalent to a fully relaxed $Ge_{0.885}Sn_{0.115}$ buffer by RSM. The tensile-strained p^+/n^+ $Ge_{0.925}Sn_{0.075}$ stack was pseudomorphically grown on the buffer without strain relaxation. All GeSn films were grown at 320 °C.

Cross-section TEM and HR-TEM images of compressive-strained, strain-relaxed, and tensile-strained $Ge_{0.925}Sn_{0.075}$ epitaxial layers are shown in Figure 4-6. For the

doi:10.6342/NTU202300648

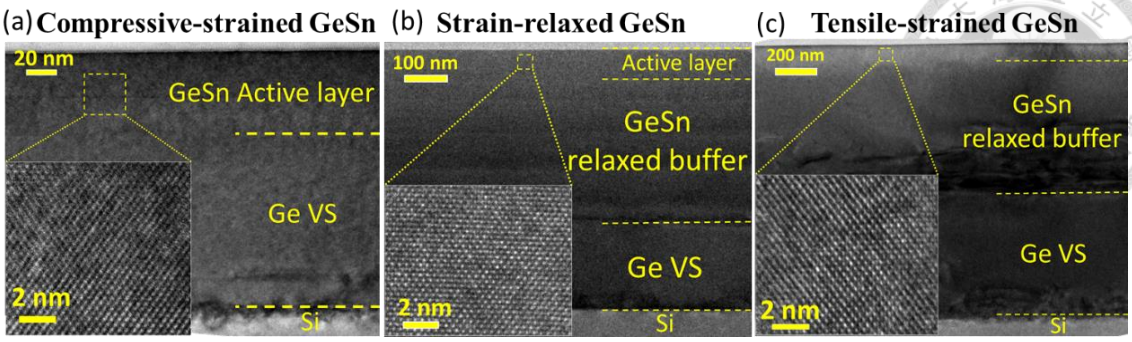

Figure 4-6 TEM pictures of (a) compressive-strained, (b) strain-relaxed, and (c) tensile-strained $Ge_{0.925}Sn_{0.075}$ epitaxial structures.

compressive-strained GeSn epitaxial structure, dislocations and defects are confined at the Si/Ge interface, and the thickness of GeSn active layers is below the critical thickness. On the other hand, for the strained-relaxed and tensile-strained structures, defects exist at both the Si/Ge interface and in the bottom of GeSn relaxed buffers owing to a large lattice mismatch between GeSn and Ge. Very few threading dislocations through the active layers are observable. Furthermore, the insets show the zoom-in images of the defect-free crystal within GeSn active layers, which is critical for the device performance of Esaki diodes.

Sn fractions and strains of the GeSn epi-layers were characterized by XRD and HR-RSM (Figure 4-7). Figure 4-7 (a) ~ (c) show the (224) RSM contours of compressive-strained, strain-relaxed and tensile-strained structures, respectively, while Figure 4-7(d) shows their rocking curves. The Ge-VS's were slightly tensile strained ($\varepsilon = +0.18\%$) due to the difference in thermal expansion coefficients between Ge and Si. Thus, the epitaxial structure of the Ge Esaki diode is slightly tensile strained, so the bandgap energy and effective mass could be slightly different from those of bulk Ge. For the compressive-strained GeSn structure, the RSM peaks of the GeSn active layers are clearly observed and vertically aligned with Ge VS with the strain of −0.89 %. For the strain-relaxed structure, the peaks of the active layers and relaxed buffer are merged at the same position.

doi:10.6342/NTU202300648

The extracted residual strain is −0.1 %, which is a small and represents a high relaxation rate of 92 % in the relaxed $Ge_{0.92}Sn_{0.08}$ buffer. This high relaxation rate is attributed to the presence of the $Ge_{0.88}Sn_{0.12}$ layer in the superlattice relaxed buffer. For the $Ge_{0.85}Sn_{0.15}$ graded relaxed buffers in Figure 4-7(c), the residual strain is −0.54 %, and the relaxation is 73 %. The peak of the tensile-strained active layer is clearly observed and fully strained on the relaxed buffer with a strain value of +0.58 %. In Figure 4-7(d), the peaks of all GeSn active layers were observed in rocking curves. The peak position of the active GeSn layer is shifted to a higher angle as the strain increases from compressive → relaxed → tensile with a decreasing out-of-plane lattice constant. The extracted strains of the GeSn active layers are -0.89 %, -0.1 %, and +0.58 %, with the corresponding Sn fractions of

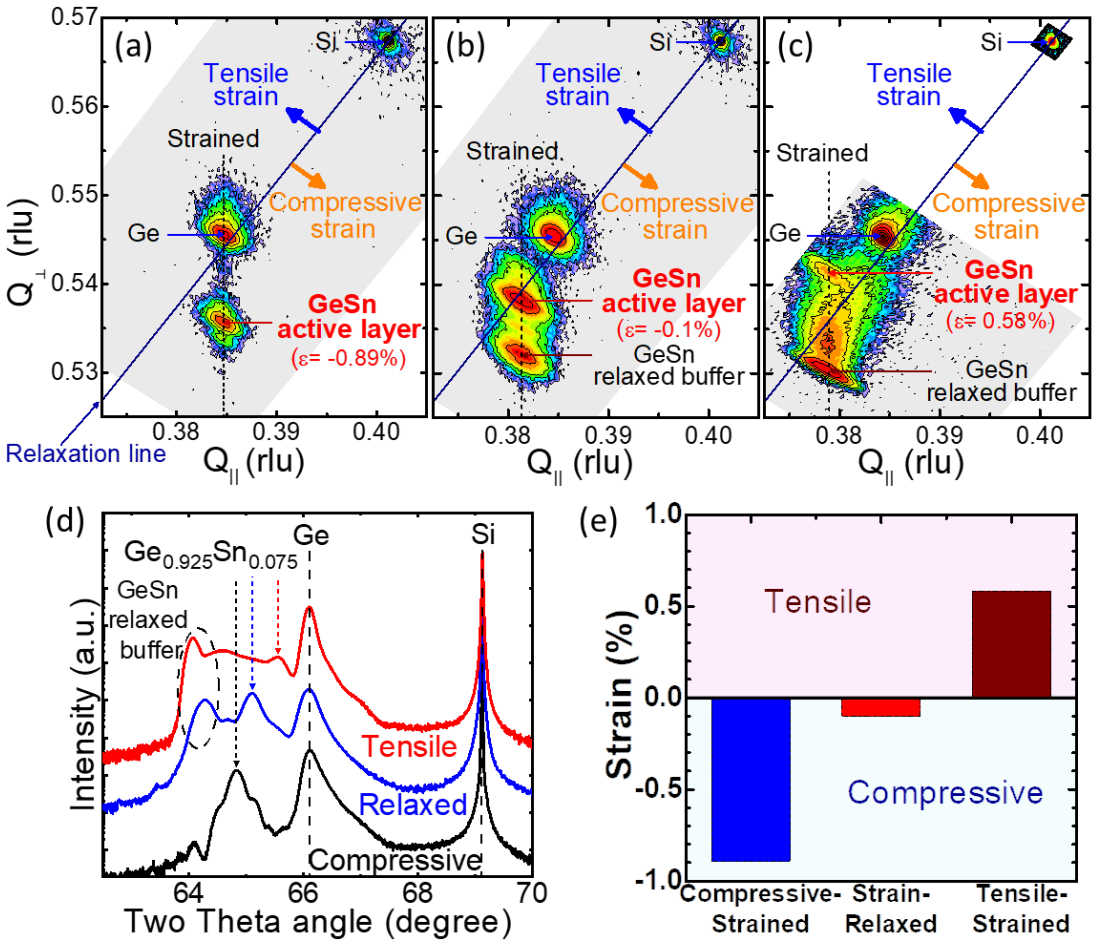

Figure 4-7 (224) RSM contour plots of (a) compressive-strained, (b)strain-relaxed, and (c) tensile-strained GeSn epitaxial structures with (d) the associated XRD (004) rocking curves and (e) strains in the GeSn active layers extracted by RSM.

doi:10.6342/NTU202300648

6.7 %, 7.5 %, and 7.1 % for the compressive-strained, strain-relaxed, and tensile-strained GeSn structures, respectively (Figure 4-7(e)).

In order to characterize the doping levels, secondary ion mass spectrometry (SIMS) was used to determine the phosphorus and boron concentrations in the GeSn active layers, as well as the background oxygen and carbon concentrations in the epi-layers. For high precision and accuracy, the SIMS measurements were performed by EAG Laboratories with separate Cs^+ or O_2^+ ion bombardment for the phosphorus and boron profiles, respectively. Figure 4-8(a) shows SIMS results of the strain-relaxed GeSn Esaki diode. The GeSn superlattice relaxed buffer is clearly observed with four periods of $Ge_{0.88}Sn_{0.12}$. The PH_3 flow rate was constant during the growth of the GeSn relaxed buffer, so the different phosphorus concentrations in the GeSn superlattice layers are due to their different incorporation rates (lower in GeSn with a higher Sn fraction). In the active layers, the Sn fraction in the p^+ GeSn is 1.5 % smaller than that of n^+ GeSn. Since the G_2H_6 and $SnCl_4$ flow rates are the same in p^+ and n^+ GeSn, the Sn fraction drop results from the high incorporation of boron atoms. This phenomenon is more serious with a higher B_2H_6 flow rate and/or in GeSn with a higher Sn fraction, which is observed in the separate experiments and in prior work [97][98], which is attributed to the more energetically favorable boron atoms to replace Sn atoms rather than Ge atoms [97]. The zoom-in of the

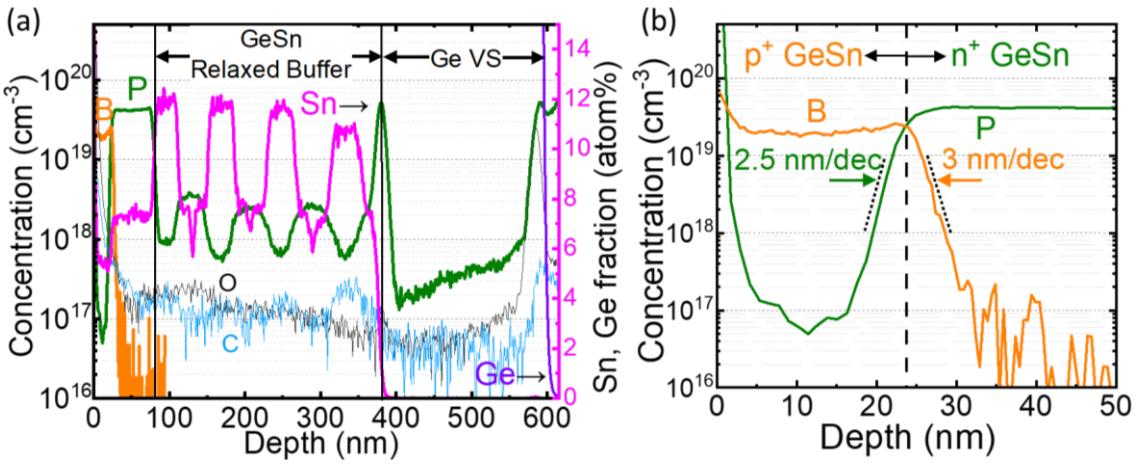

Figure 4-8 (a) SIMS profiles of a strained-relaxed $Ge_{0.925}Sn_{0.075}$ Esaki diode and (b) the zoom-in in the active layers (top 50 nm).

doi:10.6342/NTU202300648

doping profiles in the active layer is shown in Figure 4-8(b). Both doping concentrations in the n^+-region ([P]=4×10^{19} cm^{-3}) and p^+-region ([B]=2.1×10^{19} cm^{-3}) are higher than the degenerate concentrations for GeSn. Due to the low-temperature CVD growth, the turn-off profiles for both phosphorus and boron atoms are very steep (≤ 3 nm/decade). Meanwhile, the high activation rates of dopants (almost 100 %), even at high doping levels > 10^{19} cm^{-3}, were confirmed by Hall measurements [99]. These two features are important for high-performance Esaki diodes since the tunneling rate depends on the junction electric field, determined by the activated doping levels and abruptness in the depletion region.

4.4 Device Fabrication of GeSn Esaki Diodes

Since the current density of the GeSn Esaki diode is high, the series resistance effect is strong and small devices are required. The process flow of an Esaki diode is shown in Figure 4-9 (a). After the CVD growth, the wafers were diced into small pieces (1.1 cm × 1.1 cm). The samples were ultrasonically cleaned with solvents, followed by dipping in diluted HF(1:50) and HCl(1:10) to remove native oxides on the GeSn surfaces [100].

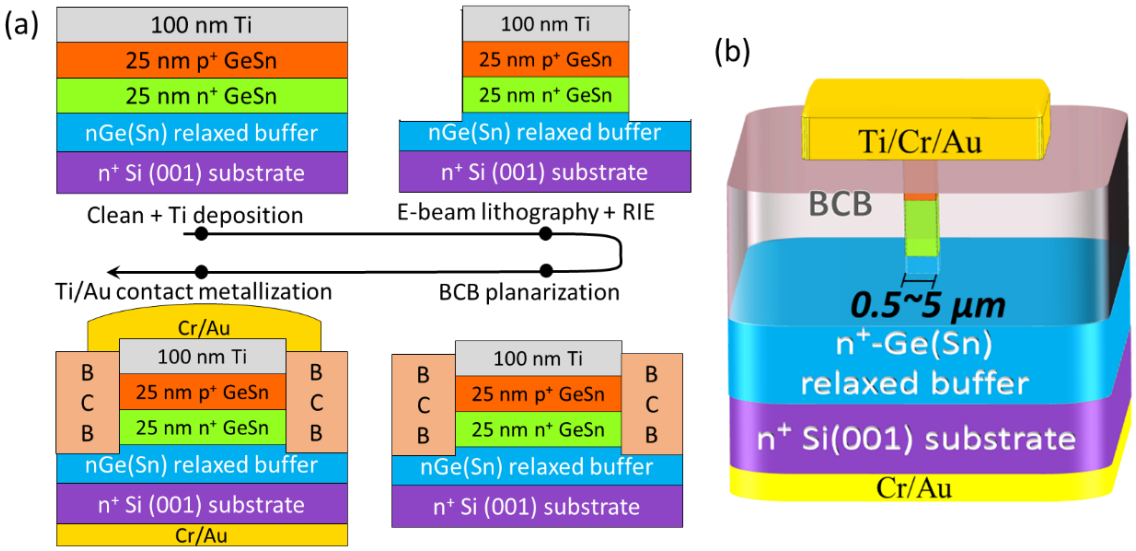

Figure 4-9 (a) The process flow of an Esaki diode by e-beam lithography and self-aligned planarization process. (b) A 3D schematic of the Esaki diode device.

doi:10.6342/NTU202300648

100-nm Ti was deposited by e-beam evaporation for the contact metal and served as a spacer for the following planarization process. The device sizes were defined by e-beam lithography with the device areas of 500 × 500 nm^2 ~ 5×5 μm^2. Ti and GeSn layers were both dry-etched by Cl_2/BCl_3 reactive ion etching (RIE) to form the mesas. Since the size of the top contact (< 5×5 μm^2) is too small to be probed directly, an insulating layer of benzocyclobutene (BCB) was used for self-aligned planarization to isolate the p-n junction. The liquid BCB was spin-coated on the sample surface and cured at 200 °C in an oven for three hours. The solidified BCB layer (~ 1.2 μm) was etched by CF_4/O_2 RIE until the top surface of the mesa was uncovered with the p-n junction covered by BCB. Since the p^+-GeSn layer is thin (~ 25 nm), the presence of the top Ti layer is important to prevent over-etching. Finally, a photolithographic step and a lift-off process of 10-nm Cr/100-nm Au were performed for the metallization of the top contact pad. The size of contact pads is 50 × 50 μm^2. At last, the device fabrication was completed by the deposition of Cr/Au as the bottom contacts. A 3D schematic of the finished device is shown in Figure 4-9 (b). The devices were characterized by Keysight B1500A on a probe station at room temperature. The devices were wire-bonded by Ag glue and loaded in a cryostat system for temperature-dependent measurement from 300 K to 1.5 K.

The cross-section TEM of a 500-nm device (tensile-strained GeSn Esaki diode) is shown in Figure 4-10(a). The actual mesa width is close to the pattern width of e-beam lithography. The BCB thickness of this device is smaller than expected, which may be due to over-etching or the collapse of the soft BCB layer when TEM sample preparation by focus-ion beam (FIB). The EDS (Energy-dispersive X-ray spectroscopy) scan result on the yellow dash line ($\overline{LL'}$) is shown in Figure 4-10(b). The top metal layers of Ti/Cr/Au were stacked on the GeSn active layer with the Sn fraction of 6 ~ 10 % by EDS, which is consistent with XRD and SIMS results.

doi:10.6342/NTU202300648

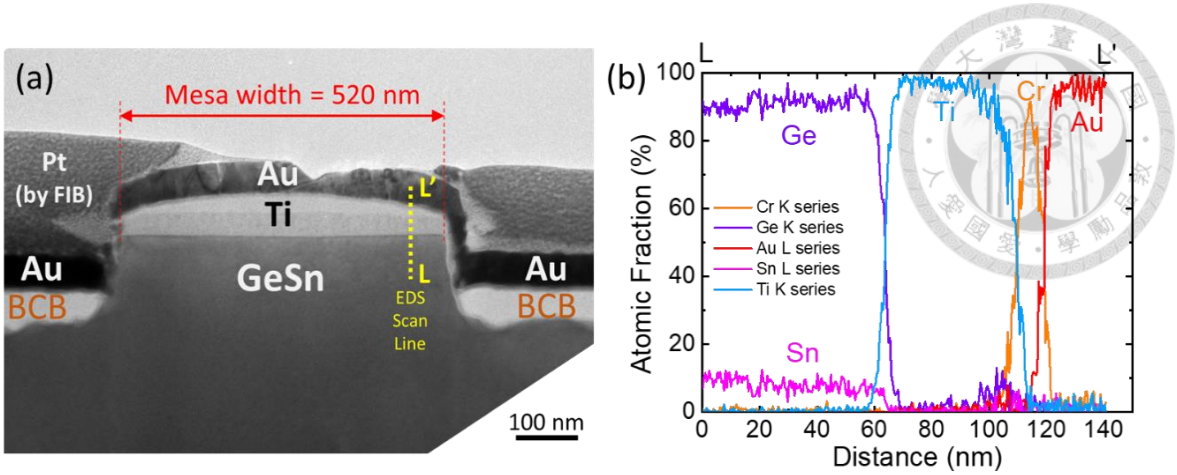

Figure 4-10 (a) Cross-section TEM of a device with a mesa area of 500 × 500 nm^2 device and (b) EDS line scan of top metal layers on the GeSn Esaki diode.

4.5 Room-Temperature I-V Characteristics of GeSn Esaki Diodes

4.5.1 Effects of Device Sizes and Series Resistance

The J-V curves of a strain-relaxed $Ge_{0.925}Sn_{0.075}$ Esaki diode are shown in Figure 4-11(a) with the device area of 0.5 × 0.5, 10 × 10, and 20 × 20 μm^2. The two large-area devices (10 × 10 and 20 × 20 μm^2) were patterned by photolithography without BCB planarization. For the small-area device (0.5 × 0.5 μm^2, red curve), the peak current density J_{peak} is 16 kA/cm^2 at a peak voltage of 55 mV. While for the large-area devices

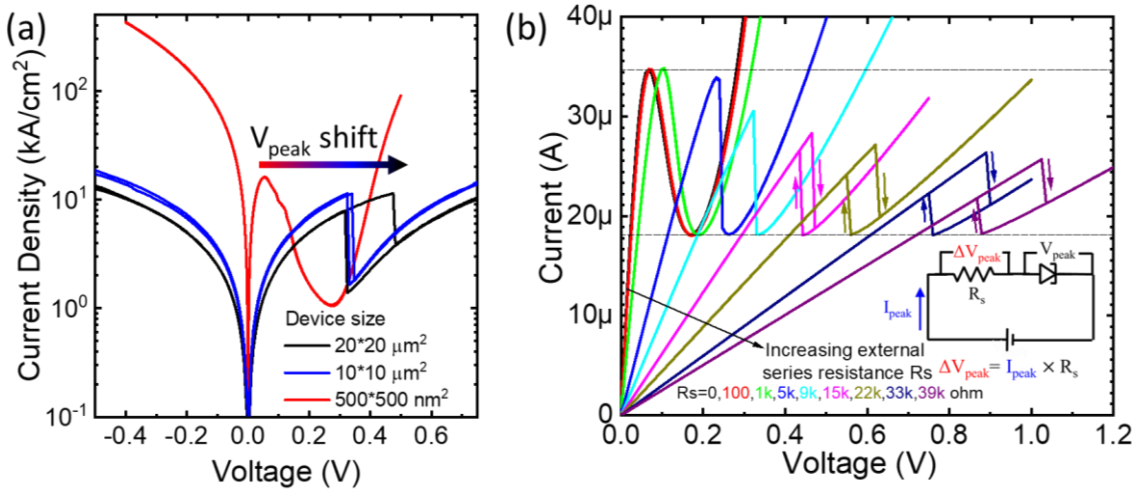

Figure 4-11 (a) J-V curves of a strain-relaxed $Ge_{0.925}Sn_{0.075}$ Esaki diode with different device sizes. (b) I-V curves with different external series resistances.

doi:10.6342/NTU202300648

(blue and black curves), the peak voltage is shifted to a higher voltage up to 0.5 V. For the largest device of 50 × 50 μm^2, the NDR cannot be observed due to the current limit of the measurement equipment. The reason for the shift of peak voltages is the series resistance effect for high-current devices [101]. The series resistance may include external resistance (wire, pad-probe contact) and internal resistance (semiconductor and metal-semiconductor interface resistance). A test of external series resistance is shown in Figure 4-11(b). The tested device had a peak current of 35 μA at 67 mV, corresponding to an effective resistance of 2 kΩ. When an external 1-kΩ resistance is in series to the measurement circuit (green curve), an observable 40-mV V_{peak} shift occurred. By increasing the external resistance to 39 kΩ, the V_{peak} was up to 1 V with a large hysteresis (forward and backward scan) in the NDR region. The presence of hysteresis is because the voltage shift is proportional to current ($\Delta V_{peak} = I_{peak} \times R_s$ and $\Delta V_{valley} = I_{valley} \times R_s$, where $I_{peak} > I_{valley}$), and the final V_{peak} ($V_{peak} = V_{peak,\ no\ Rs} + \Delta V_{peak}$) is larger than V_{valley} due to a larger voltage shift of V_{peak}. Therefore, the small area devices are required to show the a more ideal I-V characteristics of the tunneling junction, where the current of the device is reduced.

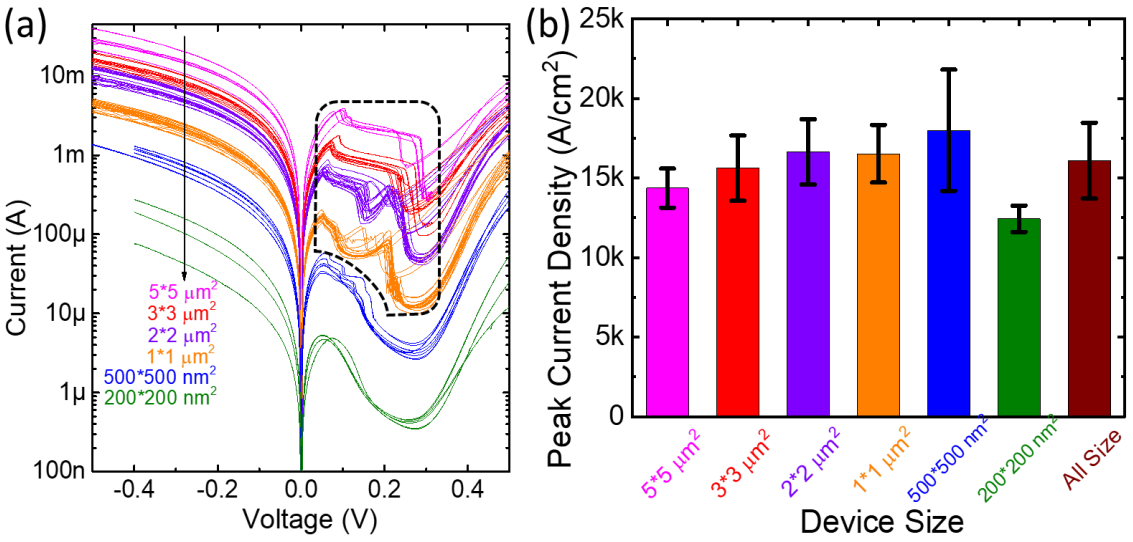

Figure 4-12 (a) I-V curves and (b) a statistical diagram of peak current density of strain-relaxed $Ge_{0.925}Sn_{0.075}$ Esaki diodes with different device sizes.

doi:10.6342/NTU202300648

Figure 4-12(a) plots the I-V curves of all device sizes with clear NDR. Note that for devices with higher current (device size > 1 × 1 μm^2), weird and unstable features appeared in the NDR region (circled) due to the resonance oscillations of the measurement circuit in series with Esaki diodes with negative differential resistance [102]. At small current levels (blue and green curves), the curves were smoother since the entire circuit is more off resonance. The statistics diagram of J_{peak} with their standard deviations are plotted in Figure 4-12(b). The peak current density of different device sizes is in the range of 14 ~ 18 kA/cm^2 with an overall average J_{peak} of 16.1 $\pm$ 2.3 kA/cm^2.

4.5.2 Doping Effects on BTBT Current

Room-temperature I–V characteristics of compressive-strained $Ge_{0.925}Sn_{0.075}$ Esaki diodes with different doping levels are illustrated in Figure 4-13(a). An effective doping level of a diode is defined as $N^* = N_A N_D/(N_A + N_D)$. The NDR characteristic is observed for all devices due to the abrupt doping profiles at the p–n junction, high doping activation rates, and the suppressed DAT. All devices show clear NDR with PVCR's of 1.8 ~ 5.5, which suggests that the peak current is dominated by the BTBT current. As the effective doping concentration increases from 1.0×10^{19} to 3.0×10^{19} cm^{-3}, J_{peak} increases

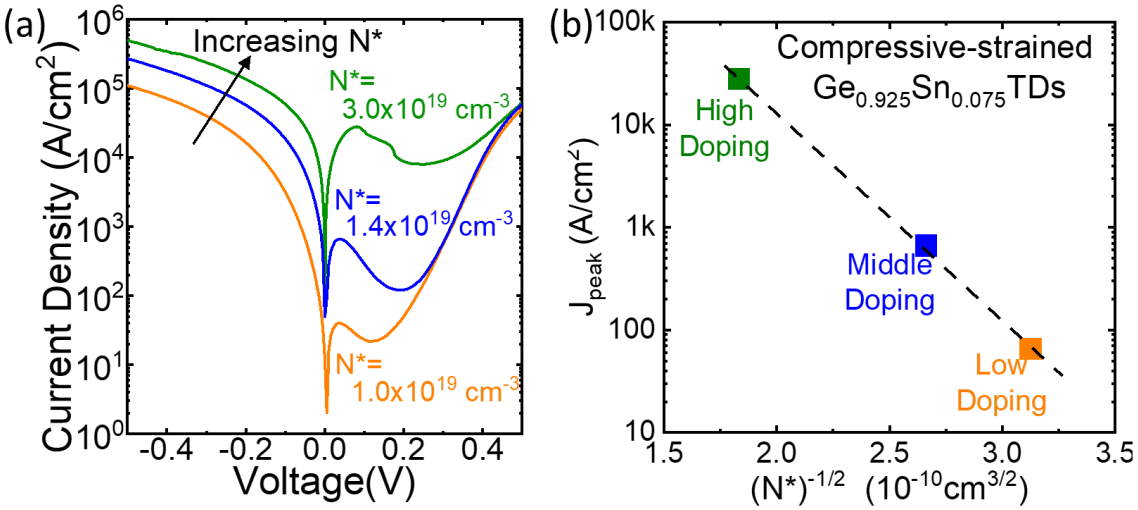

Figure 4-13 (a) I–V curves of compressive-strained $Ge_{0.925}Sn_{0.075}$ Esaki diodes with different effective doping concentrations and (b) corresponding J_{peak} versus $1/\sqrt{N^*}$.

doi:10.6342/NTU202300648

by three orders of magnitude. The logarithmic J_{peak} is plotted with $1/\sqrt{N^*}$ in Figure 4-13(b), where $\sqrt{N^*}$ is proportional to the junction electric field F_{field}. A linear fitting of the peak current densities indicates the BTBT current is well modulated by the electric field. A larger electric field leads to a shorter tunneling distance and increases tunneling possibility. Due to the exponential dependence of tunnel current on the electric field, it is effective to adjust doping concentrations for high BTBT current.

4.5.3 Bandgap Effects on BTBT Current in Ge(Sn) Esaki Diodes

Next, the BTBT current is characterized for Ge and GeSn Esaki diodes to investigate the bandgap effects with the same (or close enough) effective doping concentration. I–V characteristics of strain-relaxed Ge and compressive-strained $Ge_{0.925}Sn_{0.075}$ with the same N^* =3.0×10^{19} cm^{-3} are shown in Figure 4-14 (a). The peak current density of a compressive GeSn Esaki diode is slightly larger than that of a Ge Esaki diode by 2.4 times. On the other hand, the J_{peak} enhancement from relaxed Ge to relaxed $Ge_{0.925}Sn_{0.075}$ is much larger, as shown in Figure 4-14 (b). Even with a lower N^* in strain-relaxed GeSn, its peak current density is still 12 times larger than that of the Ge Esaki diode. Note that the

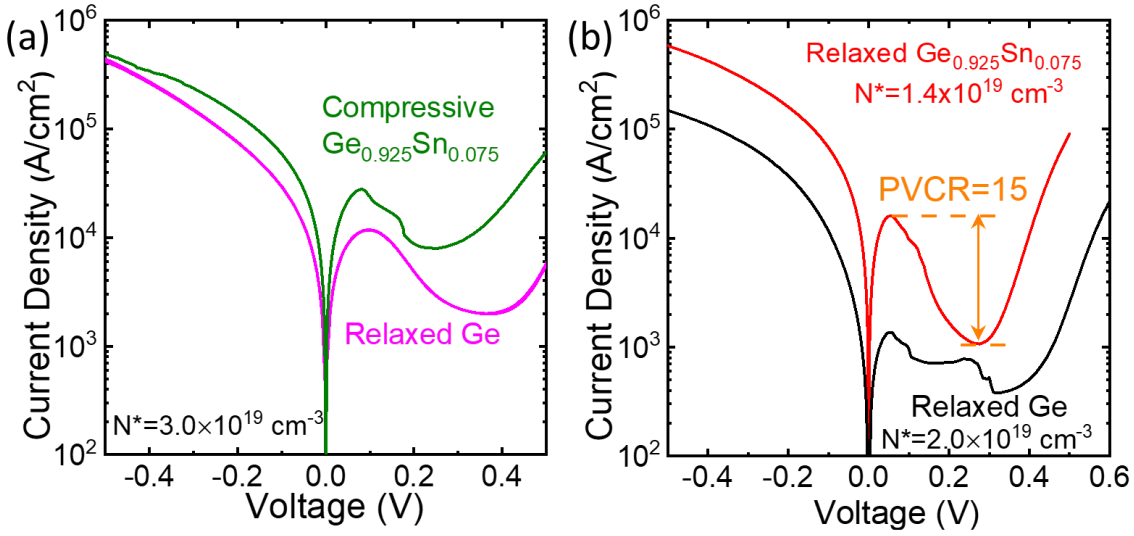

Figure 4-14 J–V curves of (a) strain-relaxed Ge and compressive-strained $Ge_{0.925}Sn_{0.075}$ Esaki diodes and (b) strain-relaxed Ge and $Ge_{0.925}Sn_{0.075}$ Esaki diodes.

doi:10.6342/NTU202300648

high room-temperature PVCR of 15 was demonstrated in the strain-relaxed GeSn diodes, which is close to the highest PVCR of 16 among group IV Esaki diodes by solution-regrowth Ge [103]. The enhancement of peak current results from two characteristics of GeSn. First, the reduced bandgap energy of $Ge_{0.925}Sn_{0.075}$ lowers the tunneling barrier and enlarge the tunneling possibility. Another possible reason is that $Ge_{0.925}Sn_{0.075}$ may become direct- bandgap, so the BTBT current is boosted.

4.5.4 Strain Effects on BTBT Current in GeSn Esaki Diodes

I–V characteristics of the GeSn Esaki diodes under different strains are shown in Figure 4-15(a). The effective doping concentrations of those devices were controlled at ~ 1.4×10^{19} cm^{-3} to eliminate the doping effects. It is clear that the strain relaxation and tensile strains leads to the enhancement of the peak current. A very high peak current density of 325 kA/cm^2 with a high PVCR of 8.2 is achieved for the tensile-strained $Ge_{0.925}Sn_{0.075}$ Esaki diode. This peak current is larger than those of the strain-relaxed and compressive-strained devices by factors of 20 and 450, respectively. Owing to the series resistance effects, the peak voltage of the tensile-strained device with a high current

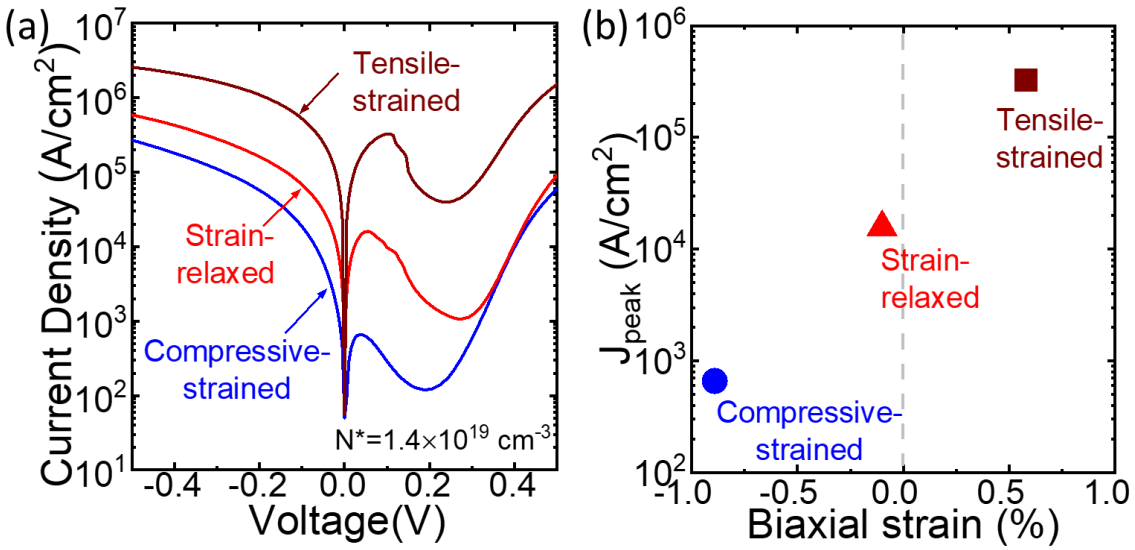

Figure 4-15 (a) I–V curves of $Ge_{0.925}Sn_{0.075}$ Esaki diodes under different strain conditions. (b) J_{peak} versus biaxial strain for the $Ge_{0.925}Sn_{0.075}$ Esaki diodes [104].

doi:10.6342/NTU202300648

density is large (at 0.1 V) even in a small (200×200 nm^2) device. As shown in Figure 4-15(b), as the strain linearly increases, the peak current increases exponentially. For the tensile-strained GeSn films, the bandgap energy is smaller, and the energy difference between the minima of Γ and L valleys ($E_{g\Gamma}$-E_{gL}) is also smaller. Moreover, several papers on the simulation of GeSn band structures reported $Ge_{0.925}Sn_{0.075}$ with a strain of +0.58 has already become a direct-bandgap material with the energy difference between indirect and direct valleys (E_{gL}-$E_{g\Gamma}$) of 30 ~ 70 meV [18][19][105]. Therefore, direct tunneling could play an important role on BTBT in GeSn Esaki diodes.

Finally, peak current densities of all Ge and GeSn Esaki diodes plotted against $1/\sqrt{N^*}$ in Figure 4-16. With the same effective doping concentration, the strain-relaxed devices or those under tensile stresses show much higher peak current. Comparing the effect of Sn fraction (Ge → compressive GeSn) and strain engineering (compressive → tensile GeSn) on BTBT, the J_{peak} enhancement is stronger through strain engineering. Furthermore, a slightly smaller slope for the tensile-strained device suggests the smaller dependence of doping concentrations on BTBT current since the direct-band tunneling becomes more dominant.

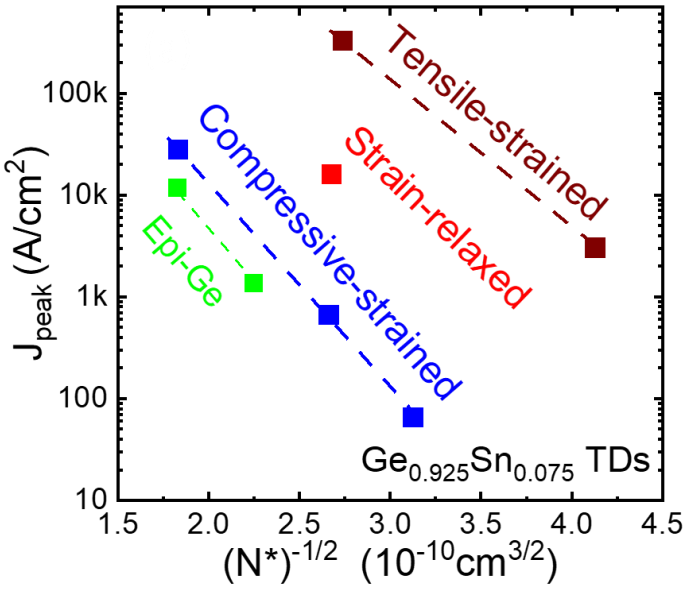

Figure 4-16 Room-temperature peak current densities of all Ge and GeSn Esaki diodes. versus $1/\sqrt{N^*}$.

doi:10.6342/NTU202300648

4.6 Direct and Indirect Tunneling in GeSn Esaki Diodes

4.6.1 Simulation of GeSn Band Structures

A nonlocal empirical pseudopotential method (NL-EPM) was used to calculate band structures of $Ge_{0.92}Sn_{0.08}$ under different strain conditions. Detailed information and clear physical explanation of band structure simulation could be referred to [106]. The local form factors, nonlocal and spin-orbit parameters of Ge and Sn used for the calculation are listed in Appendix. The modified virtual crystal approximation (VCA) was adopted to interpolate the parameters for $Ge_{0.92}Sn_{0.08}$. The local form factors of $Ge_{0.92}Sn_{0.08}$ as a function of wave vector (q) are interpolated as

$$V_{Ge_{1-x}Sn_x}(q) = (1-x)\frac{\Omega_{Ge}}{\Omega_{Ge_{1-x}Sn_x}}V_{Ge} + x\frac{\Omega_{Sn}}{\Omega_{Ge_{1-x}Sn_x}}V_{Sn} - Px(1-x)\frac{\Omega_{Sn}V_{Sn} - \Omega_{Ge}V_{Ge}}{\Omega_{Ge_{1-x}Sn_x}} \quad \text{Eq. 4-13}$$

where **Ω** is the atomic volume, V_{Ge} and V_{Sn} are the form factors for Ge and Sn, and x is the Sn fraction. *P* is the fitting parameter which is -0.3 in this work. The simulated band structures of compressive-strain (ε=−1%), strain-relaxed (ε=0), and tensile strained (ε=+1%) $Ge_{0.92}Sn_{0.08}$ are shown in Figure 4-17. The energy difference ΔE between the minima of Γ and L valleys is defined as $\Delta E = E_{g\Gamma} - E_{gL}$. The energy differences ΔE are 63

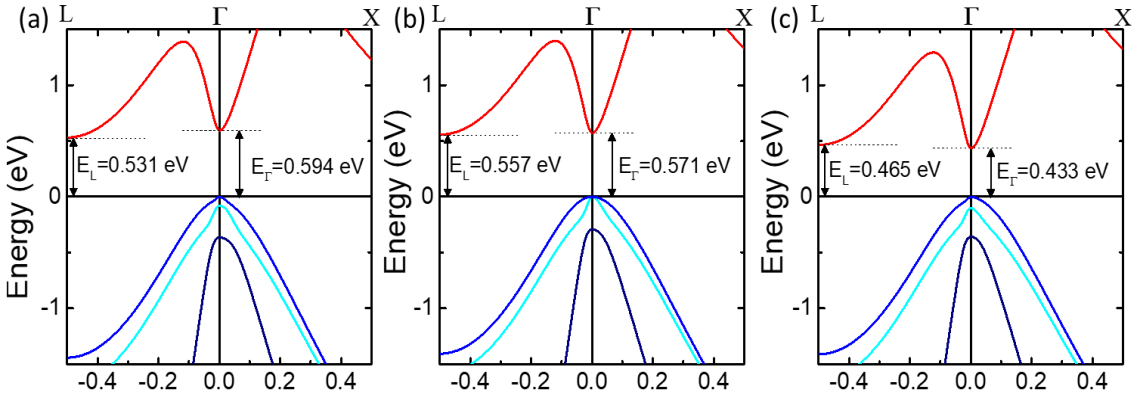

Figure 4-17 Simulated $Ge_{0.92}Sn_{0.08}$ band structures under different strain conditions of (a) compressive-strain (ε=−1%), (b) strain-relaxed (ε=0), and (c) tensile strain (ε=+1%).

doi:10.6342/NTU202300648

meV, 13.5 meV, and -31.4 meV in compressive-strained, strain-relaxed, and tensile-strained $Ge_{0.92}Sn_{0.08}$. That is, the tensile-strained $Ge_{0.92}Sn_{0.08}$ alloy becomes a direct-bandgap material.

4.6.2 Band Alignment of GeSn Esaki Diodes

The band alignment in a Ge Esaki diode is shown at different biases in Figure 4-18. Doping concentrations of 3×10^{19} cm^{-3} at both p^+- and n^+-regions ($N^* = 1.5\times10^{19}$ cm^{-3}) were used with $V_n' = 48.9$ mV and $V_p' = 49.7$ mV at T=20 K from the TCAD simulation. The peak voltage is defined as $V_{peak} = (V_p' + V_n')/3$ [92]. At zero bias (Figure 4-18(a)), the energy minimum of the Γ valley at the n-type region is higher than the valence band maximum at the p-type region. A reverse bias over 40 meV is required to align the Γ valley in the conduction band at the n-type region with the valence band at the p-type region (Figure 4-18(a)). Direct tunneling is allowed if there are electrons near the edge of the valence band. Therefore, at the peak voltage, the Γ-electrons are fully misaligned with the hole band, so indirect tunneling is dominant in Ge Esaki diodes at forward biases.

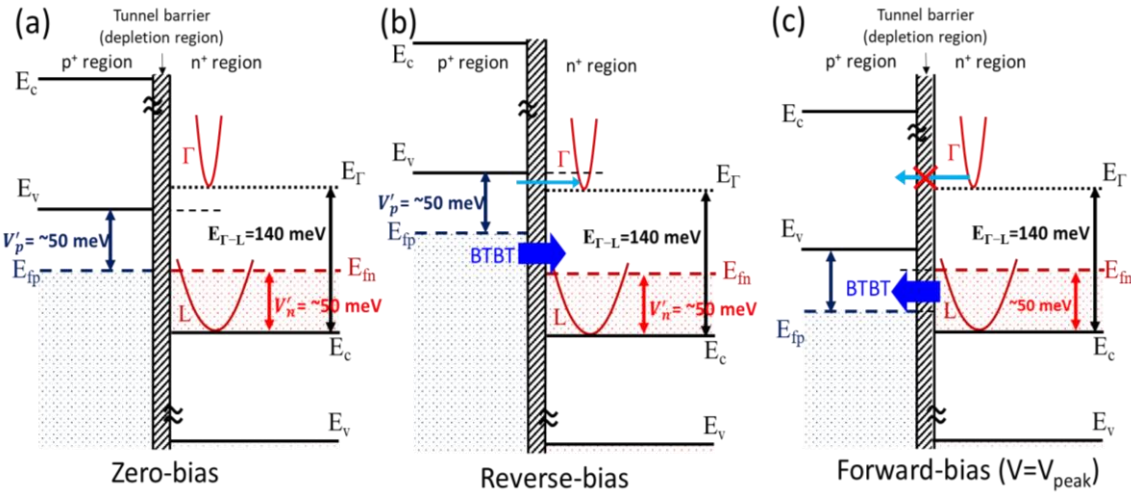

Figure 4-18 Simulated band diagrams of a Ge Esaki diode at different biases of (a) zero bias (b) reverse bias (c) forward bias at $V=V_{peak}$

doi:10.6342/NTU202300648

Then, we consider the band alignment at V = V_{peak} in GeSn Esaki diodes with the same doping concentration for simple illustration. For compressive-strained GeSn (Figure 4-19(a)), according to the simulated band structure, the energy difference ($E_\Gamma - E_L$) of compressive-strained $Ge_{0.92}Sn_{0.08}$ is much smaller (~ 63 meV) than the Ge case (140 meV), and a certain part (~ 4 meV) of Γ valley overlaps with the valence band. However, the indirect bandgap characteristic and the small DOS of the Γ valley limit the electron population at Γ valley, even at room temperature. Due to the limited energy overlap and available electrons in Γ valley, the contribution of direct tunneling to the BTBT current is weaker than indirect tunneling. Therefore, the J_{peak} enhancement from Ge to compressive-strained GeSn is simply due to the reduced tunneling barrier (with a smaller bandgap) (Figure 4-16). For strain-relaxed or tensile-strained GeSn Esaki diodes, since $E_\Gamma - E_L$ is very small (still positive) or negative, direct tunneling could become dominant because of much higher populations of Γ-electrons. Once the direct tunneling current is dominant, the BTBT current will increase rapidly with the population of the Γ-electrons. In addition, the energy overlap between electrons and holes in the Γ valley at conduction band in the n-type region and valence band in the p-type region, respectively, is enhanced in strain-relaxed and tensile-strained GeSn, leading to more electrons participating the tunneling processes.

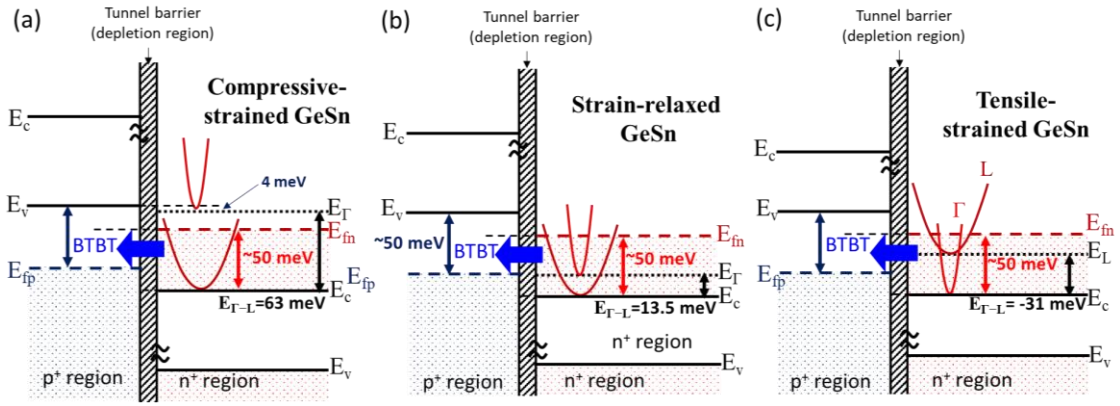

Figure 4-19 Simulated band diagrams at V_{peak} for (a) a relaxed Ge, (b) a compressive-strained, (b) a strain-relaxed, and (c) a tensile-strained $Ge_{0.92}Sn_{0.08}$ Esaki diodes.

doi:10.6342/NTU202300648

Chapter 5 Temperature-Dependence and Phonon Spectra in GeSn Esaki Diodes

5.1 Introduction

5.1.1 Reviews on Temperature-Dependent I-V Characteristics of Esaki Diodes

Although quantum tunneling is a temperature-independent process, the peak current would vary with temperature due to other temperature-dependent parameters. Difference parameters in BTBT current result in different temperature dependences, which are positive or negative. A positive temperature dependence of the peak current is shown in Figure 5-1(a) [107], where the peak current decreases with the reducing temperature from 303 K to 4.2 K. The bandgap broadening at lower temperatures leads to this positive trend by increasing the tunneling barrier. Two clear humps are observed due to the onset of phonon-assisted tunneling, which will be discussed in the next section. In contrast, a negative temperature dependence of the peak current is shown in Figure 5-1 (b) [107], where the peak current increases with the reducing temperature. The larger peak current

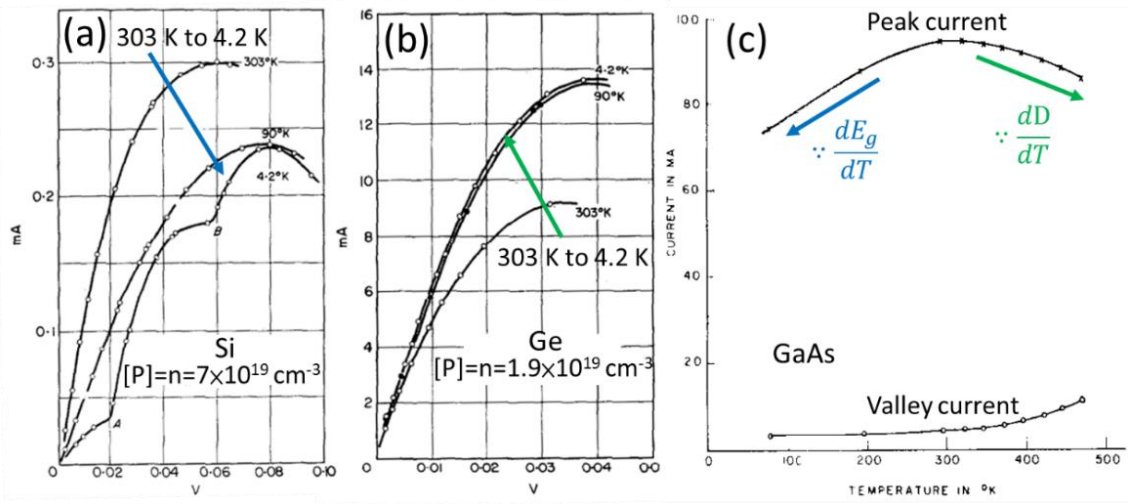

Figure 5-1 Temperature-dependence I-V curves of (a) a Si and (b) a Ge Esaki diode [107]. (c) Temperature-dependence peak and valley currents in a GaAs Esaki diode [108].

doi:10.6342/NTU202300648

at lower temperatures is mainly due to the increase of the integral *D* parameter, which is relative to the tunneling window (available states). This will be further explained in a physical picture in Section 5.2.1. These two opposite effects compete and dominate at different temperature regions (Figure 5-1 (c)). The temperature dependence of the integral *D* is stronger at a higher temperature, especially for the doping concentration close to the effective density of state $N_{c,v}(T)$. Unlike the peak current, the valley current monotonically decreases with lowering temperature since the DAT current is effectively suppressed at lower temperatures.

The temperature dependence of peak current in Ge diodes with different doping levels was illustrated in Figure 5-2(a) [92]. The peak current is dominated by bandgap energy for devices with higher doping concentrations, while it is dominated by the integral *D* for devices with lower doping concentrations. These two factors are almost balanced at N^*~2.4×10^{19} cm^{-3} in Ge Esaki diodes. Our temperature-dependent J-V curves of a strain-relaxed Ge Esaki diode shows a smaller peak current at a lower temperature (Figure 5-2(b)). It is consistent with the prior work in Figure 5-2(a), where the effective density of the Ge device (N^*=3×10^{19} cm^{-3}) in this work is larger than the

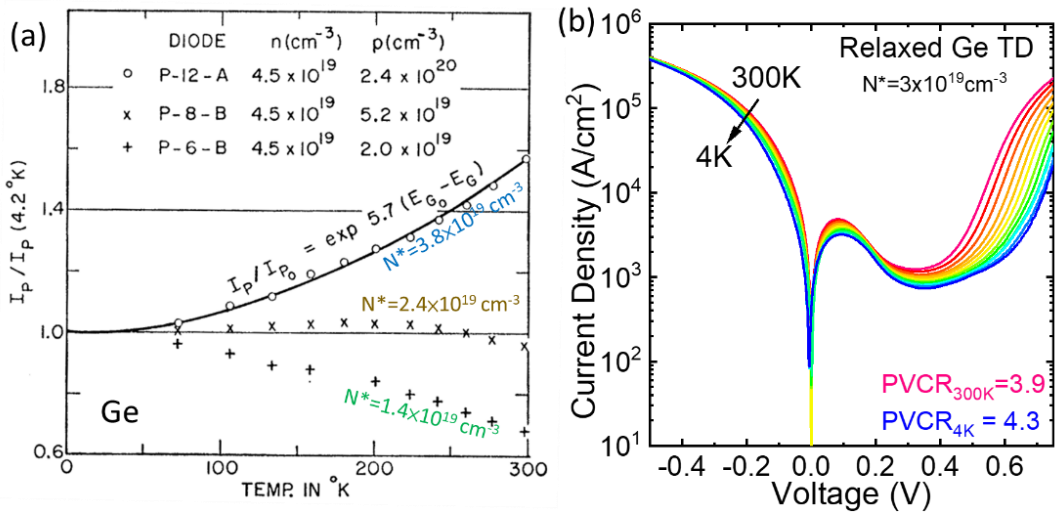

Figure 5-2 (a) Temperature-dependences of peak current in Ge Esaki diodes with different doping levels [92]. (b) Temperature-dependent J-V curves of a relaxed epi-Ge Esaki diode.

doi:10.6342/NTU202300648

balanced point at 2.4×10^{19} cm^{-3}, and the peak current show the same temperature-dependence as the higher doping sample ($N^*=3.8\times10^{19}$ cm^{-3}) in Figure 5-2(a).

5.1.2 Review on Phonon Spectra in Esaki Tunnel Diodes (Si, Ge, III-V)

The cusps in I-V curves for phonon-assisted tunneling diodes were clearly observed in Si Esaki diodes (Figure 5-1(a)) and Ge Esaki diodes (Figure 5-3(a) [109]). In order to precisely identify the onset voltage of the phonons, I-V curves are differentiated, as shown with the first-derivative I-V (dI/dV-V) in Figure 5-3(b) and the second-derivative I-V (d^2I/dV^2-V) in Figure 5-3(c). The phonon energies can be determined at the peaks in the second-derivative I-V spectrum, which is called the phonon spectra in this work. The peaks at 7.8, 27.6, 30.6, and 36.2 mV correspond to the transverse acoustic (TA), longitudinal acoustic (LA), longitudinal optical (TO), and transverse optical (LO) phonons, respectively [109]. However, the phonon-assisted tunneling may not appear in some indirect-bandgap Esaki diodes (Figure 5-3(d) [110]). In a direct-bandgap semiconductor, the electron tunneling can also be assisted with LO phonon participation near k=0. Nonetheless, phonon spectra of Esaki diodes have been used to characterize the BTBT processes.

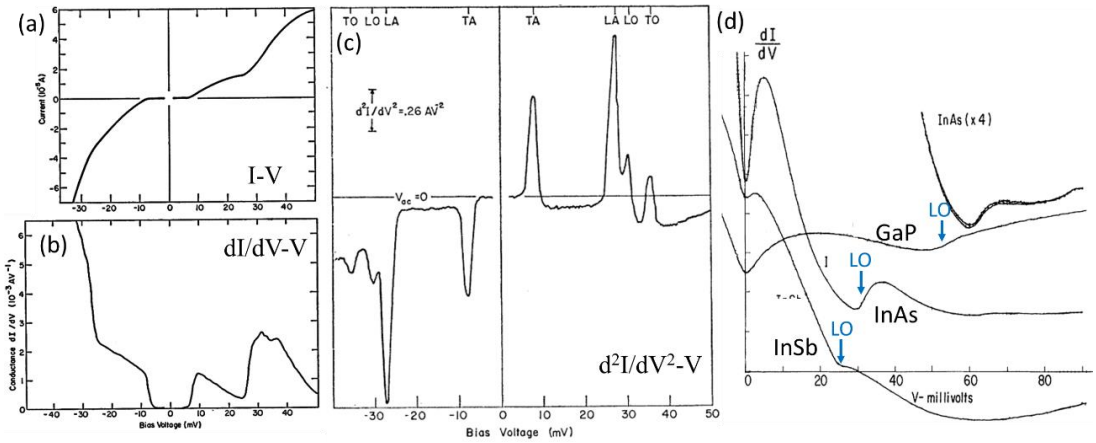

Figure 5-3 (a) I-V curve, (b) first-derivative (dI/dV-V) curve, and (c) second-derivative (d^2I/dV^2-V) curve of an Sb-doped Ge Esaki diode [109]. (d) First-derivative curves of III-V Esaki diodes [110]

doi:10.6342/NTU202300648

5.2 I-V Characteristics of GeSn Esaki Diodes at Temperatures of 4 K ~ 300 K

5.2.1 Temperature-Dependent I-V curves of Compressive-Strained GeSn Esaki Diodes

Temperature-dependent characteristics in GeSn Esaki diodes were measured at temperatures between 300 K and 4 K. The temperature-dependent J-V curves of the compressive-strained $Ge_{0.925}Sn_{0.075}$ Esaki Diodes are shown in Figure 5-4 (a) and (b) with two different effective densities. For both cases, the valley current monotonically decreases with a reducing temperature because of the suppressed DAT current, while the temperature dependence of the peak current is different. The temperature-dependent J_{peak}

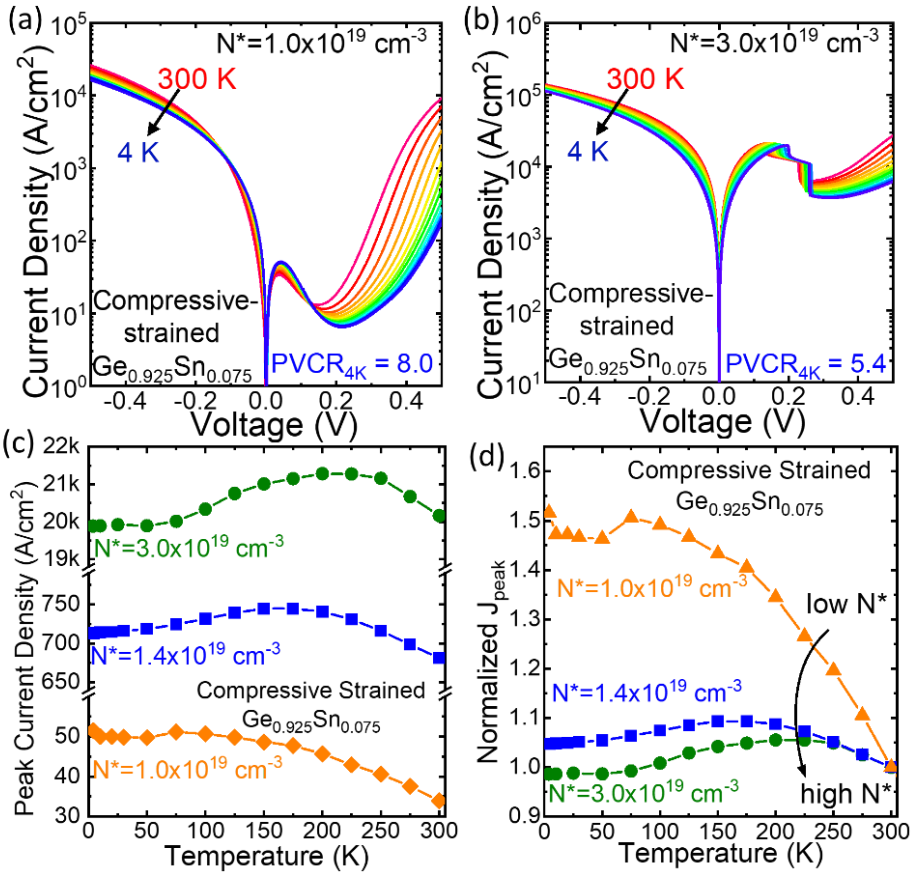

Figure 5-4 Temperature-dependent J-V curves with (a) $N^*=1\times10^{19}$ cm^{-3} and (b) $N^*=3\times10^{19}$ cm^{-3}. (c) Peak current density and (d) normalized J_{peak} versus temperature in compressive-strained $Ge_{0.925}Sn_{0.075}$ Esaki diodes.

doi:10.6342/NTU202300648

and normalized J_{peak} with different doping levels are shown in Figure 5-4 (c) and (d). The peak current is normalized to their peak current density at 300 K. For the Esaki diode with a lower effective doping concentration, in spite of its low J_{peak}, the enhancement of the peak current is the largest among the diodes of the three doping levels. Thus, the PVCR increases from 2 at 300 K to 8 at 4 K. For the Esaki diode with a higher effective doping concentration, as the temperature increases, the peak current increases initially and starts to decrease at 200 K, which suggests two competing effects on the peak current.

At a lower temperature, the peak current decreases due to the widened bandgap, leading to a larger tunnel barrier, which is confirmed by temperature-dependent GeSn PL spectra in Chapter 3. On the other hand, the peak current also depends on the integral factor *D*, which monotonically increases as the temperature decreases. A physical schematic of the temperature dependence of integral *D*(T) is shown in Figure 5-5(a). The

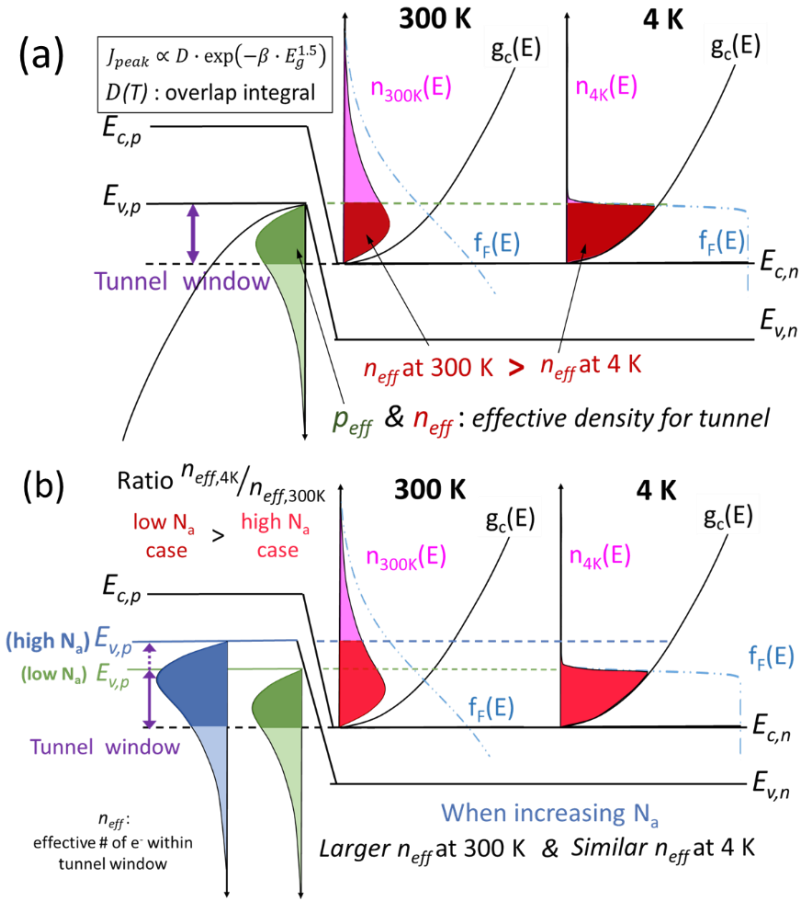

Figure 5-5 (a) A schematic on temperature-dependence of integral *D*(T) and (b) a schematic on the doping effects on *D*(T).

doi:10.6342/NTU202300648

physical meaning of *D* can be understood that the available electrons and holes at a certain energy (n(E) × p(E)) for tunneling are integrated through the tunneling window ($E_{v,p}-E_{c,n}$). At a high temperature of 300 K, electrons in the n^+-region with higher energies (magenta area) distribute beyond the tunneling window (above the maximum of the valence band), and so do the holes in the p^+-region (light green area). When the temperature is reduced to 4 K, electrons are condensed under the Fermi level owing to the step-function-like Fermi distribution. Thus, more electrons and holes are condensed within the tunneling window, leading to an increase of *D* at low temperature.

The doping effects on the temperature-dependence of peak current in Figure 5-4(d), where the low-temperature enhancement of J_{peak} is smaller with a higher N^*, could be also explained by the doping effects on the temperature-dependence of *D* in Figure 5-5(b). To briefly illustrate the doping effect, we can simply change the doping concentration of the p^+ region (say a higher N_a as the blue distribution graph) and characterize the available holes within the tunneling window. At a high temperature of 300 K, compared to lower N_a case in Figure 5-5(a), more electrons are distributed the tunneling window and available for tunneling ($n_{eff,\ high\ Na} > n_{eff,\ low\ Na}$ at 300 K). While at 4 K, all holes are condensed under the Fermi level and within the tunneling window, where the amount of

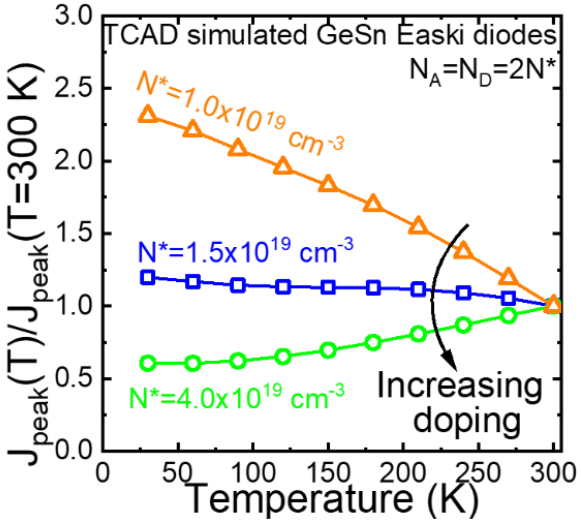

Figure 5-6 Normalized J_{peak} in GeSn Esaki tunnels by TCAD simulation with different doping levels.

doi:10.6342/NTU202300648

available holes is equal to the lower N_a case ($n_{eff,\ high\ Na} = n_{eff,\ low\ Na}$ at 4 K) since the tunneling window is limited by the n-type doping concentration. Therefore, the low-temperature enhancement on the available carriers for tunneling is suppressed by higher N_a ($R \equiv n_{eff,4K}/n_{eff,300K}$, $R_{high\ Na} < R_{low\ Na}$). As a result, the low-temperature enhancement on D(T) decreases with the doping level, leading to a reduced peak current of the Esaki diode. The temperature-dependence of J_{peak} is also confirmed with TCAD simulation. Simulated normalized J_{peak} for GeSn Esaki diodes are shown with different effective doping concentrations in Figure 5-6. For a lower (higher) doping level, the normalized J_{peak} increases (decreases) monotonically as the temperature decreases.

Due to the doping effect on the temperature-dependence of J_{peak}, the comparison of the J_{peak} temperature-dependence is also required on the similar doping level. Figure 5-7 shows the temperature-dependent J_{peak} and normalized J_{peak} in strain-relaxed Ge and compressive-strained GeSn Esaki diodes with the similar $N^* \sim 3\times10^{19}$ cm^{-3}. In the compressive-strained $Ge_{0.884}Sn_{0.116}$ device, both J_{peak} and low-temperature J_{peak} enhancement are the largest among the three devices of similar doping levels. The normalized J_{peak} at 4 K is evidently increased with the higher Sn fraction in GeSn Esaki

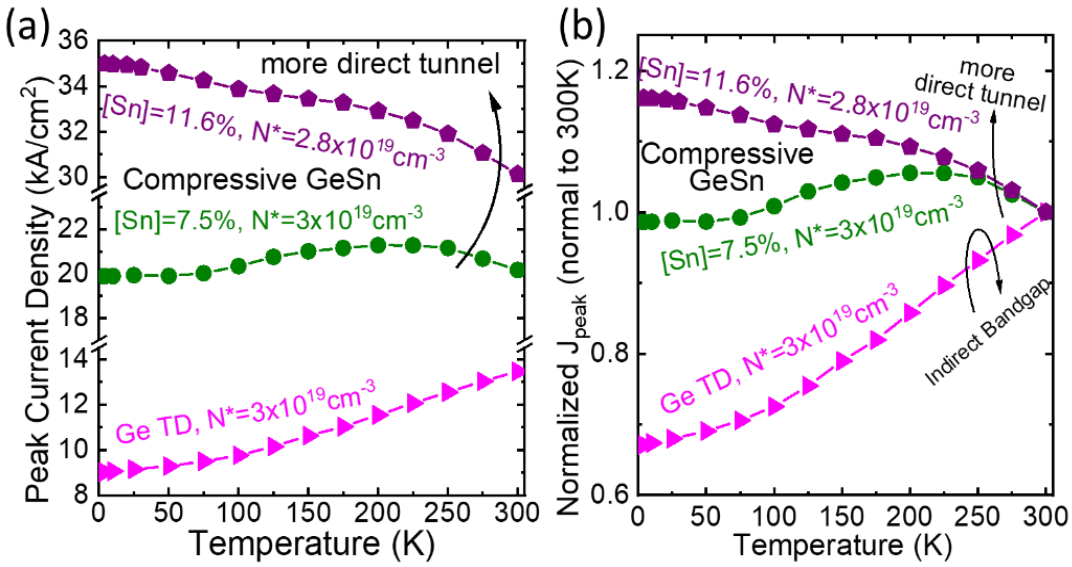

Figure 5-7 (a) Peak current density and (b) normalized J_{peak} versus temperatures in relaxed Ge and compressive-strained GeSn Esaki Diodes with $N^* \sim 3\times10^{19}$ cm^{-3}.

doi:10.6342/NTU202300648

diode increases, which may be due to the reduction of energy difference (E_{gr}-E_{gL}) and the more direct tunneling current in total BTBT current.

5.2.2 Temperature-Dependent I-V of Strain-relaxed and Tensile-strained GeSn Esaki Diodes

The temperature-dependent J-V curves of the strain-relaxed and tensile-strained $Ge_{0.925}Sn_{0.075}$ Esaki diodes are shown in Figure 5-8 (a) and (b). The effective doping concentrations were controlled at ~ 1.4×10^{19} cm^{-3}. The V_{peak} shift in the relaxed device is attributed to the increased series resistance at lower temperatures. Both device have enhanced peak current at lower temperatures. For the strain-relaxed GeSn device, the valley current was suppressed by a factor of 2.5, which may be thanks to the high-quality growth of relaxed buffers with low-TDD. Thus, a PVCR of 15 is achieved at room temperature and it is further enhanced to 53 at 4 K. For the tensile-strained GeSn device, the high peak current density was further enhanced to 545 kA/cm^2 at 4 K with the PVCR of 19. The normalized J_{peak} at 4 K was about 1.7 times than that of the strain-relaxed device. The normalized J_{peak} of GeSn diodes under different strain conditions are plotted

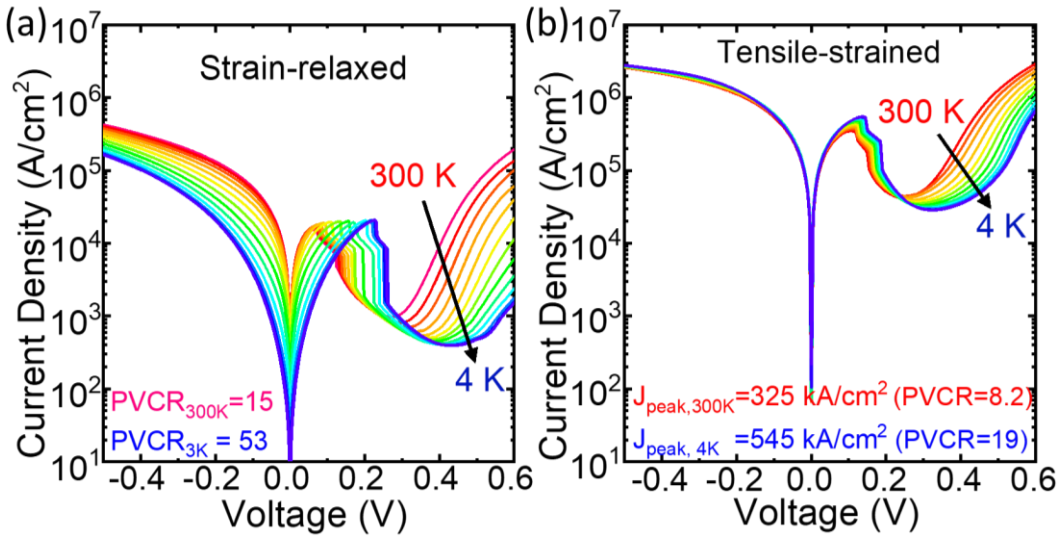

Figure 5-8 Temperature-dependent J-V curves of (a) a strain-relaxed $Ge_{0.925}Sn_{0.075}$ Esaki and (b) a tensile-strained $Ge_{0.925}Sn_{0.075}$ Esaki Diodes.[104]

doi:10.6342/NTU202300648

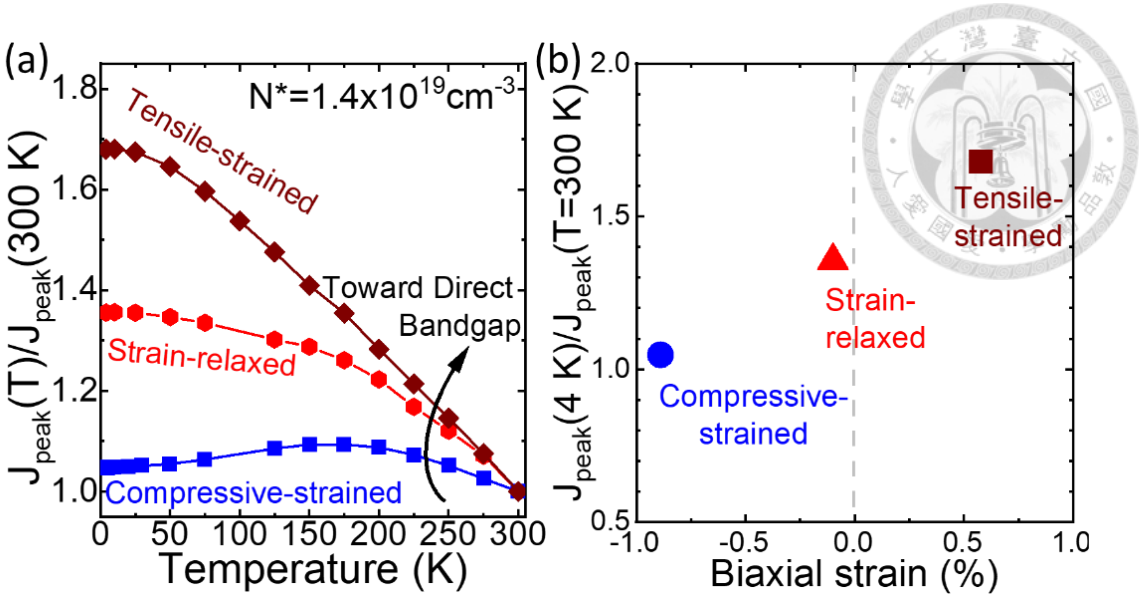

Figure 5-9 (a) Normalized J_{peak} versus temperature for Esaki diodes underh different strain conditions. (b) Normalized J_{peak} at 4 K versus biaxial strain for $Ge_{0.925}Sn_{0.075}$ devices. [104]

against temperature in Figure 5-9(a). By applying tensile stresses, the low-temperature J_{peak} enhancement (J_{peak}(4K)/ J_{peak}(300K)) becomes larger and is quite linear to the strain (Figure 5-9(b)) owing to the indirect-direct bandgap transition. Schulte-Braucks *et al.* suggested that the low-temperature J_{peak} enhancement is attributed to the increase of the electron population in the direct valley for direct-bandgap GeSn [85]. While this argument is reasonable, without considering the doping level effect on the temperature dependence of J_{peak}, the conclusion might be inaccurate. More analysis of temperature-dependent electron population on the BTBT will be introduced in the next section.

The ratio of J_{peak}(4K)/J_{peak}(300K) is improved for the strain-relaxed device with low doping levels (Figure 5-10). Due to the low doping, the peak current density is ~ 0.35 kA/cm^2 with a PVCR of 11 at 300 K. At 4 K, the peak current was increased by 4.8 times, with the valley current is reduced by a factor of 4.1 times. The highest PVCR of 219 was achieved at 4 K, a record-high PVCR among all Esaki diodes.

doi:10.6342/NTU202300648

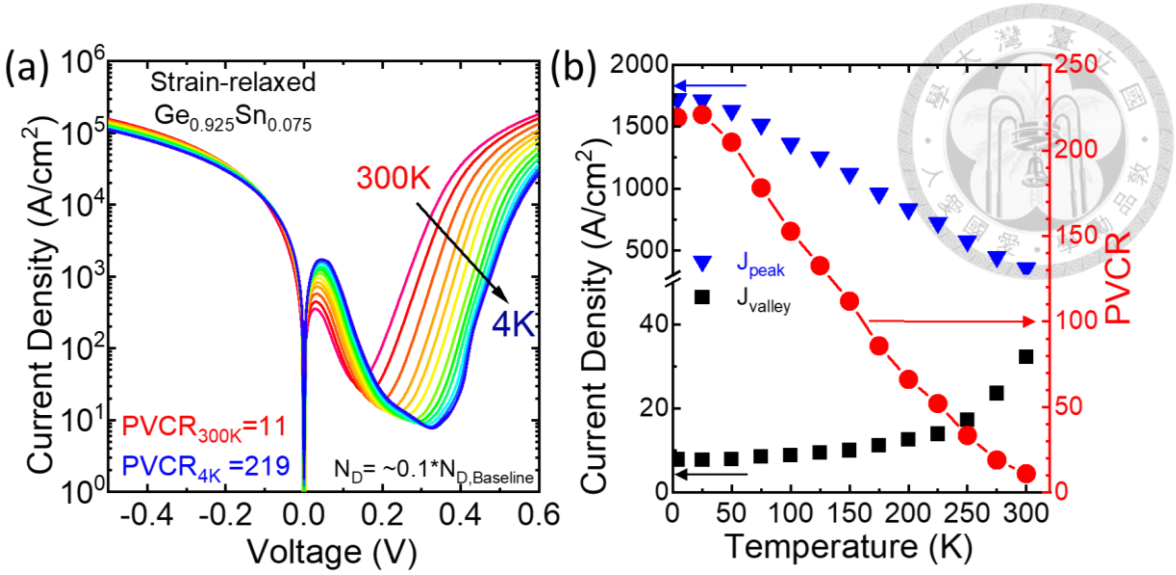

Figure 5-10 (a) Temperature-dependent J-V curves with an extremely high PVCR at 4 K. (b) Peak and valley current densities versus temperature with corresponding PVCR's.

5.3 Electron Populations in GeSn at Different Temperatures

5.3.1 Electron Populations in Direct and Indirect Valleys of GeSn

The energy difference between the minimum of the Γ and L valleys ($E_{g\Gamma}$-E_{gL}) is rather small (~ 100 meV) in GeSn. Especially for $Ge_{0.92}Sn_{0.08}$, based on our EPM simulation, the energy difference is close to the doping degeneracy, defined as the energy difference between the Fermi level and conduction band minimum (typically 30 meV or higher) and thermal energy kT/q (26 meV at 300 K). For indirect-bandgap GeSn with a larger energy difference between two valleys (Figure 5-11(a)), the Fermi level is located between $E_{c\Gamma}$ and E_{cL}, similar to the case of pure Ge. The thermal tail of Femi distribution allows the electron population in the higher Γ-valley at 300 K. While at 4 K, the step-function-like Femi distribution condenses all electrons in the lower L-valley. For indirect-bandgap GeSn with a smaller energy difference between two valleys (Figure 5-11(b)), the Fermi level is above both $E_{c\Gamma}$ and E_{cL}. Thus, there are still some electrons in Γ valley at 4 K. When GeSn becomes a direct-bandgap material (Figure 5-11 (c)), more electrons populate in the Γ valley, but the amount of Γ-electrons is still fewer than that of L-

doi:10.6342/NTU202300648

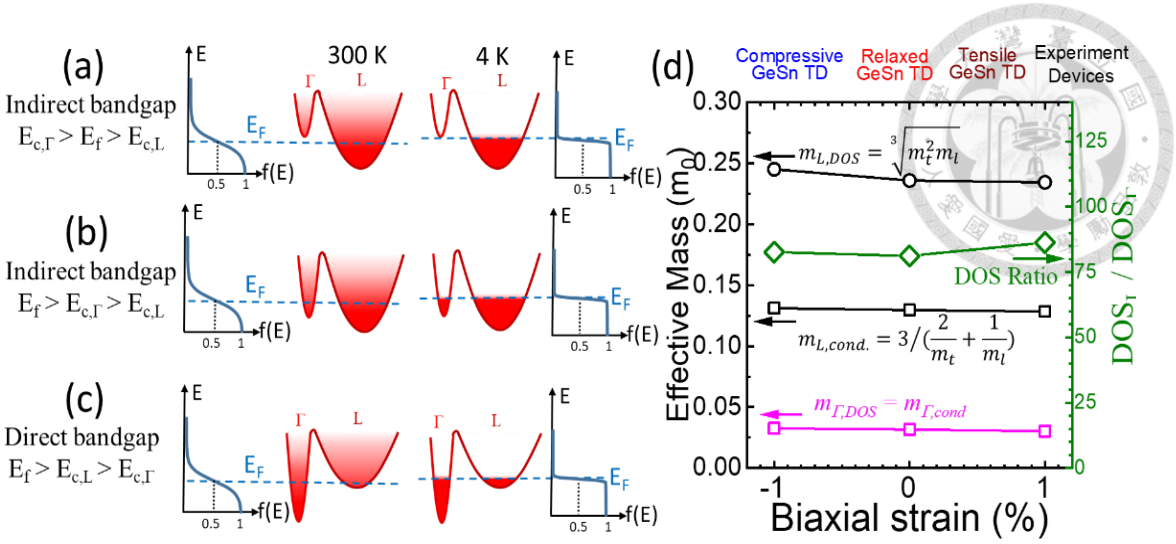

Figure 5-11 Schematics of the populations in Γ and L valleys of GeSn at 300 K and 4 K for (a) indirect bandgap, (b) indirect-direct transition, and (c) direct bandgap. (d) Effective mass and DOS ratio vs. strain

electrons at 300 K and 4 K since the DOS of the Γ-valley is too small. The DOS effective mass is extracted from band structures by EPM simulation (Figure 5-11 (d)). The DOS effective mass of the L-valley is eight times larger than that of the Γ-valley, resulting in ~ 85 times in density of states ($\propto M_c \cdot m_{DOS}^{1.5}$).

Then, the electron densities in L and Γ valleys are calculated by Fermi-Dirac distribution with the parabolic band approximation:

$$n_{L,\Gamma} = \int_{E_{cL,\Gamma}}^{\infty} g_{L,\Gamma}(E) f(E) dE = \int_{E_{cL,\Gamma}}^{\infty} \frac{M_c \sqrt{2} m_{L,\Gamma}^{*\,1.5} \sqrt{E - E_{cL,\Gamma}}}{\pi^2 \hbar^3} \times \frac{1}{1 + \exp(\frac{E - E_f}{kT})} dE \quad \text{Eq. 5-1}$$

For degenerate-doped semiconductors, the carrier concentration is fixed at all considered temperatures (0 K~300 K)[111][112]. Therefore, a fixed total electron density is given as

$$n_{total} = n_L + n_\Gamma = \int_{E_{cL}}^{\infty} g_L(E) f(E) dE + \int_{E_{c\Gamma}}^{\infty} g_\Gamma(E) f(E) dE \quad \text{Eq. 5-2}$$

doi:10.6342/NTU202300648

Figure 5-12(a) shows the Γ-electron density with a fixed total electron of 2×10^{19} cm^{-3}. For the compressive-strained GeSn (E_Γ-E_L=63 meV), electron density in the Γ valley is ~ 3×10^{16} cm^{-3} at 300 K, which is only 0.18 % of the L-electron density. However, the direct tunneling current might still contribute significantly to the overall BTBT current due to its high efficiency. At 4 K, the Γ-electron density is reduced to zero (a very small number). For the strain-relaxed GeSn (E_Γ-E_L=13.5 meV), the Fermi level is above the minima of both two valleys (Figure 5-11(b)), the Γ-electron density only slightly decreases from 300 K to 4 K. For tensile-strained GeSn (E_Γ-E_L=-31 meV), which is a direct-bandgap material, the Γ-electron density slightly increase at lower temperatures. Note that the number of Γ-electrons is still much less than that of L-electrons (n_Γ/n_L ratio ≈2.7 %), as shown in Figure 5-12(b). In Figure 5-12(c), the low-temperature Γ-electron enhancement defined as ratio of the 4 K Γ-electrons over 300 K Γ-electrons (n_Γ(4K)/n_Γ(300K)) is plotted against temperature. Whether the population of Γ-electrons at a lower temperature increases or decreases is determined by the energy difference between two valleys. It is clear that the low-temperature Γ-electron enhancement is larger with the biaxial strain, which is similar to the dependence of J_{peak} enhancement on the strain in Figure 5-9(b).

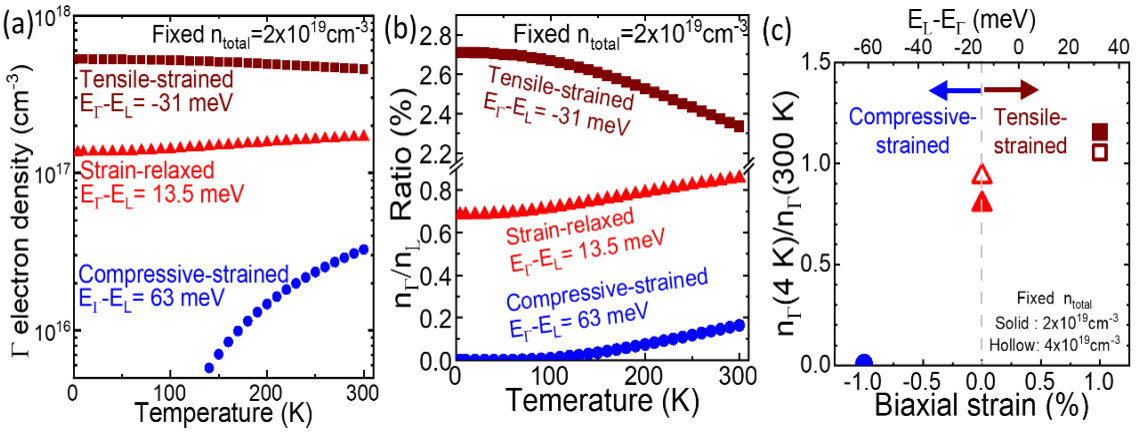

Figure 5-12 Simulated (a) Γ-electron density and (b) n_Γ/n_L ratio in GeSn vs. temperature under different strain conditions. (c) n_Γ(4K)/n_Γ(300K) versus biaxial strain.

doi:10.6342/NTU202300648

5.3.2 Electron Mobility Enhancement in GeSn by Strain Engineering

While the population analysis of the Γ and L valleys suggests the direct BTBT process dominates for the tensile-strained device, more evidence is required to further confirm the direct-bandgap characteristics of the tensile-strained $Ge_{0.925}Sn_{0.075}$ films. The prior work on tensile-strained $Ge_{0.96}Sn_{0.04}$ n-MOSFETs demonstrated a higher channel mobility than the compressive-strained and strain-relaxed transistors [113], implying a higher electron population in the Γ valley. In this work, low-temperature Hall measurements were performed to characterize the electron mobilities in n-type $Ge_{0.925}Sn_{0.075}$ films under different strain conditions. The n-type GeSn films were grown by CVD with a similar epitaxial structure as GeSn Esaki diodes (Figure 4-5). In order to eliminate the contribution of conduction from the buffer layers and the substrate, the silicon-on-insulator (SOI) substrates were used, and all Ge VS and GeSn relaxed buffers were undoped. The Hall measurements on the n-$Ge_{0.925}Sn_{0.075}$ films were done by a lab co-worker Kai-Ying Tien [114].

The Hall mobilities of the n-type tensile-strained $Ge_{0.925}Sn_{0.075}$ films with different doping concentrations are shown in Figure 5-13(a), where the inset shows the temperature dependence of the electron concentration. Note that the electrons aren't frozen out even below a concentration of 1×10^{18} cm^{-3}. For the heavily doped GeSn films (black), the Hall

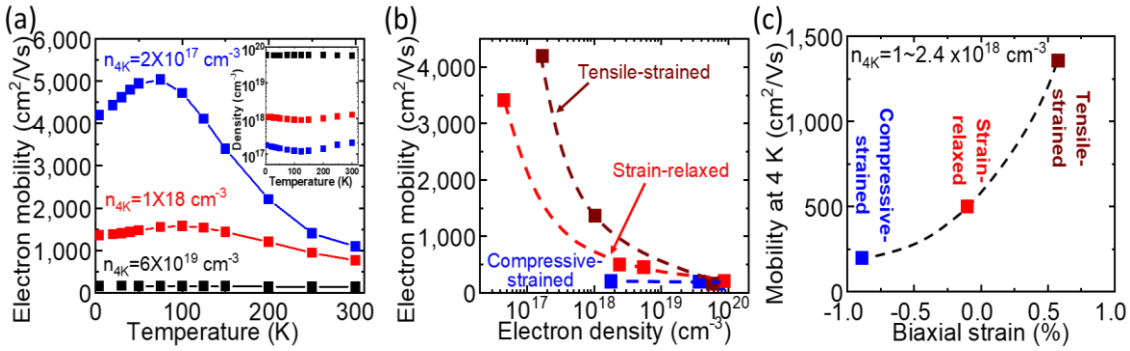

Figure 5-13 (a) Hall mobility of tensile-strain n-$Ge_{0.925}Sn_{0.075}$ films with different doping concentrations versus temperature. (b) Hall mobility versus density at 4 K under different strain conditions. (c) Hall mobility at 4 K versus biaxial strain. [104]

doi:10.6342/NTU202300648

mobility does not change with temperature since the impurity scattering is dominated at all temperatures. For a lower doping concentration (blue), the mobility is much higher, and phonon scattering dominates at temperatures higher than 75 K, while at lower temperatures, impurity scattering dominates. In Figure 5-13(b), the 4 K Hall mobility is plotted against the electron density under different strain conditions. For heavily-doped GeSn ($n_{4K} > 10^{19}$ cm^{-3}), regardless of the strain conditions, the electron mobility is very low (~100 cm^2/Vs), which is dominated by the strong impurity scattering. The mobility is enhanced by decreasing the doping concentration due to the suppressed impurity scattering. The Hall mobility is significantly enhanced to 4,200 cm^2/Vs in the tensile-strained GeSn film. With electron densities of 1 ~ 2.4×10^{18} cm^{-3}, the Hall mobility of $Ge_{0.925}Sn_{0.075}$ is enhanced by applying more tensile stresses due to a higher contribution of Γ-electrons with smaller effective masses (Figure 5-11(b)). The results strongly suggest that the Γ-electron population is significantly increased by strain relaxation or applying tensile strain in $Ge_{0.925}Sn_{0.075}$ films.

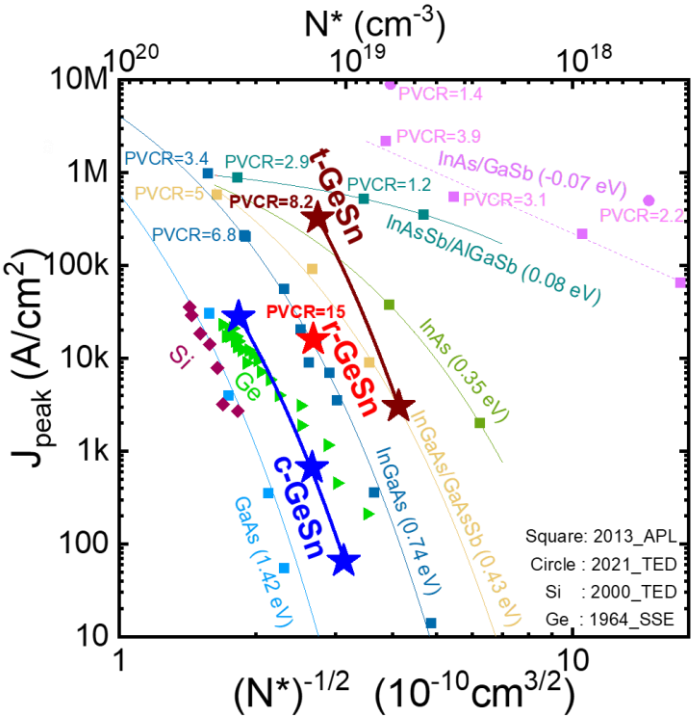

Figure 5-14 Peak current density vs. $\frac{1}{\sqrt{N^*}}$ of Esaki diodes on different material platforms [115][116][117][118].

doi:10.6342/NTU202300648

At last, in Figure 5-14, the peak current density is plotted against the effective doping concentration to evaluate the performance of Esaki diodes on different material platforms [115][116][117][118]. The room-temperature (4 K) J_{peak} of 325 (545) kA/cm^2 in the tensile-strained $Ge_{0.925}Sn_{0.075}$ is the highest among all reported group IV tunnel diode, including RITDs [119][120] and RTDs. For compressive-strained $Ge_{0.925}Sn_{0.075}$ ($E_g \cong 0.53$ eV) with a smaller E_g than InGaAs (direct bandgap), and its peak current density is lower due to its indirect-bandgap characteristics. By apply tensile stresses on $Ge_{0.925}Sn_{0.075}$ ($E_g \cong 0.5$ eV), the tunneling current density is higher than that of InAs (E_g=0.35 eV) and the staggered InGaAs/GaAsSb (effective E_g=0.43 eV) even though the latter two materials have smaller bandgap energies. To reach a high drive current in a TFET, a current density of 1MA/cm^2 is required and this can be achieved by increasing the doping concentration and/or the Sn fraction in GeSn devices or applying larger tensile stresses.

Furthermore, the PVCRs are marked for those devices with high peak current densities (J_{peak} > 100 kA/cm^2). The PVCR of 8.2 in the tensile-strained $Ge_{0.925}Sn_{0.075}$ is the highest due to the suppressed DAT (J_{valley}), which is attributed to the high-quality GeSn and less defect states within the bandgap. In addition to the defects in the crystal film, the surface states at the side walls of etched mesas by dry etching may also contribute the DAT current to the valley current (Figure 4-9(a)). The surface passivation can reduce the surface defect density. For example, GeSn photodiodes with sidewall passivation by GeON have smaller dark current and higher responsivity [121], and the PL intensity of GeSn is stronger with Al_2O_3 surface passivation [122]. Thus, an addition step of sidewall surface passivation may help to decrease the total DAT current and further increase PVCR.

doi:10.6342/NTU202300648

5.4 Phonon Spectra of GeSn Esaki Diodes

In addition to the population analysis of electrons for the indirect and direct BTBT processes, phonon spectra of GeSn Esaki diodes were also investigated to further understand the tunneling mechanisms. The phonon-assisted tunneling can only be observed in I-V curves at cryogenic temperatures due to much reduced thermal broadening [123]. While phonon cusps are clearly observed in the I-V curve in some of Si and Ge Esaki diodes, phonon spectra derived from second-derivatives of I-V curves (d^2I/dV^2-V) are a clearer indication to identify the phonon participation in the BTBT processes for most of the tunneling devices, such as III-V Esaki diodes [110][124], metal-semiconductor (MS) tunnel junction [125], metal–insulator–semiconductor (MIS) tunnel junction [126]. For all Esaki diodes in this work, the I-V curves at 4 K were smooth without any observable cusp. In addition, the noise levels were large in the phonon spectra by performing second-order differentiations on those I-V curves. Thus, the differential conductance (dI/dV-V) of the devices was characterized by ac lock-in techniques to enhance the signal fidelity [127]. Then the second-derivative curve is extracted by further performing another differentiation on the conductance data.

5.4.1 Phonon Spectrum of A Commercial Ge Esaki Diode

A commercial Ge Esaki diode (1N3717) was characterized at 4 K as a baseline to justify the measurement setup and extraction procedures. Figure 5-15(a) shows the I-V curve, dI/dV-V (differential conductance), and the d^2I/dV^2-V (phonon spectrum) at 4 K. The I-V curve is smooth under a small bias ($V < V_{peak}$) without any observable phonon cusp. The peak current was 4.7 mA at room temperature and went down to 3.1 mA at 4 K. Since detailed information, such as area and doping concentration, is not available, temperature dependence of peak current was not considered for comparison. In Figure

doi:10.6342/NTU202300648

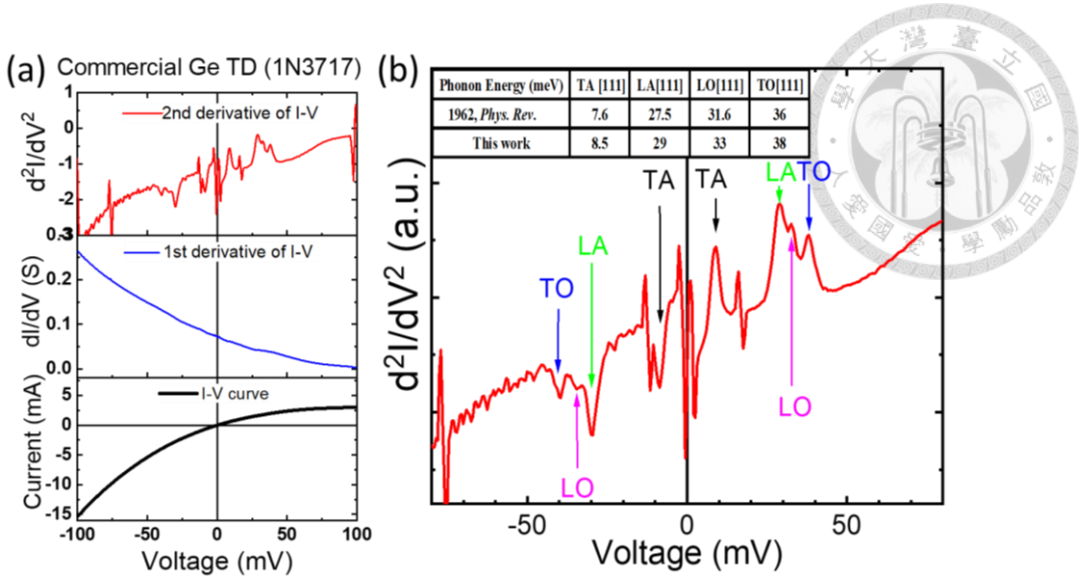

Figure 5-15 (a) I-V curves and the associated first and second derivatives of a commercial Ge tunnel diode (1N3717) at 4 K (b) Enlarged phonon spectra with labeled phonon peaks.

5-15(b), the phonon peaks are asymmetric at forward and reverse biases. The TA, LA, LO, and TO phonons were observed, and their positions of the peaks are consistent with the phonon energies of Ge reported in [83].

5.4.2 Phonon Spectra of Epi-Ge and GeSn Esaki Diodes

The phonon spectra of the epitaxial Ge(Sn) Esaki diodes are shown in Figure 5-16 with their I-V curves in the insets. For the epi-Ge Esaki diode (Figure 5-16(a)), peaks of the TA and the LA phonons are clearly observed, while the signals of the TO and LO phonon are mixed with the LA phonon peak. The signals at the reverse bias were less pronounced than those at the forward bias. The positions of those phonon peaks are consistent with the commercial Ge Esaki, while the numbers are slightly larger due to the series resistance effect. For the phonon spectrum of the tensile-strained $Ge_{0.925}Sn_{0.075}$ Esaki diode (Figure 5-16(b)), the curve is much smoother with less prominent phonon peaks even at a lower temperature of 1.5 K. Only a broad peak at 30 mV at forward bias is observed, which may be attributed to the presence of LO phonons by referring to the

doi:10.6342/NTU202300648

phonon of III–V Esaki diodes [110][124]. While phonon participation is not required for the direct BTBT process for most III–V direct-bandgap materials, the emission of LO phonons still occurs during the tunneling process since their momentum can be zero with non-zero energy at the Brillouin zone center [110]. As electrons at the Γ valley in the n^+-region tunnel to the valence band at the p^+-region, the deformation-potential coupling of electrons to optical phonons leads to the presence of LO peaks in the phonon spectrum [128]. For the spectrum of the tensile-strained GeSn device, the absence of other prominent phonon peaks with similar patterns to that of III–V Esaki diodes suggests that the phonon participation is much weaker than in the Ge case.

For the phonon spectrum of the compressive-strained $Ge_{0.945}Sn_{0.055}$ Esaki diode (Figure 5-16(c)), broad humps were observed and seemed to be antisymmetric feature.

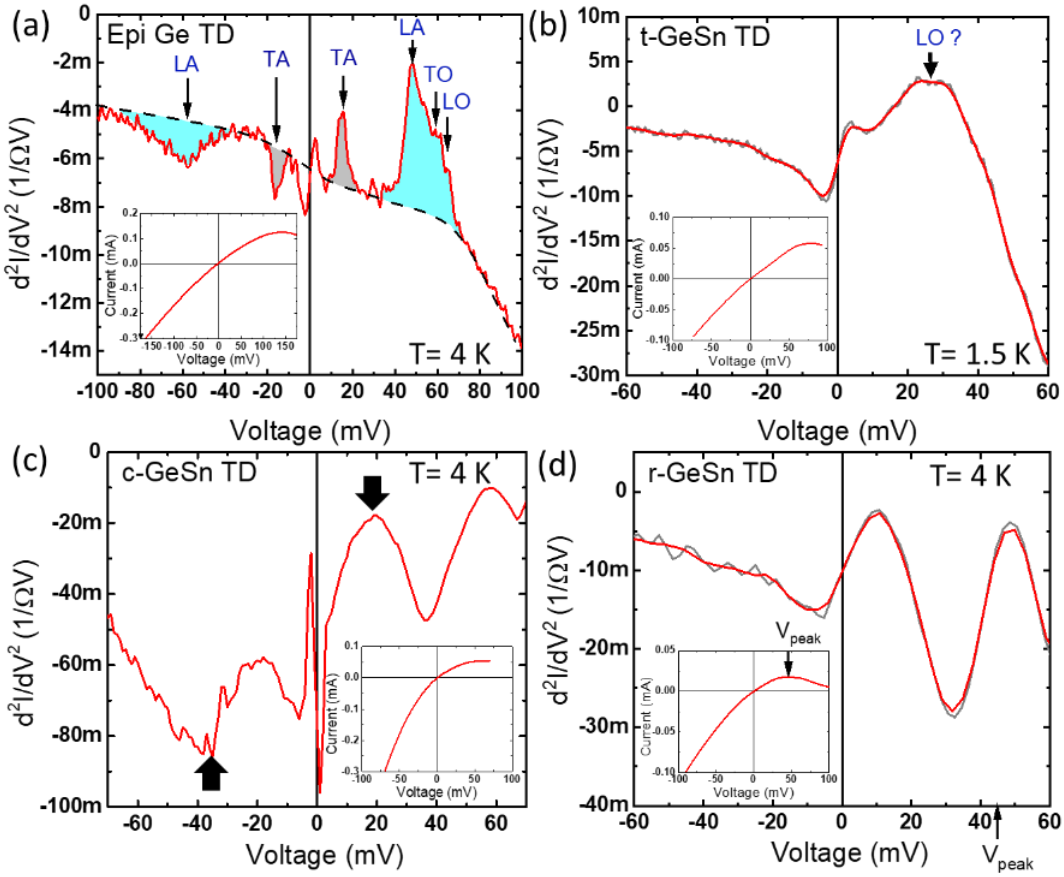

Figure 5-16 Phonon spectra of (a) relaxed Ge, (b) tensile-strained $Ge_{0.925}Sn_{0.075}$, (c) compressive-strained $Ge_{0.945}Sn_{0.055}$ and (d) strain-relaxed $Ge_{0.925}Sn_{0.075}$ Esaki diodes. [104]

doi:10.6342/NTU202300648

Unlike the Ge case, it is not straightforward to identify the types of phonon peaks since the signals are rather broad. This might be attributed to the mixing of indirect and direct tunneling and suggests the onset of direct tunneling. In fact, in the literature [84], the phonon peaks in Si-Ge alloy were slightly broader than those of pure Si and pure Ge, while their peaks were still prominent. In our devices, the elastic strain could further deform and broaden the phonon energies. For the strain-relaxed GeSn device (Figure 5-16(d)), the phonon spectrum is smoother with less pronounced peaks observed and similar to that of the tensile-strained GeSn device owing to the dominance of direct tunneling. The results suggest that direct tunneling dominates in the strained-relaxed and tensile-strained GeSn Esaki diodes.

doi:10.6342/NTU202300648

Chapter 6 Electron Transport in GeSn Epitaxial Films with High Sn Fractions

In addition to excellent performance for optical device applications, direct-bandgap GeSn is also promising for electrical devices due to its great carrier transport properties. Especially for the electron transport, direct-bandgap GeSn is expected to have much boosted electron mobility due to the small electron effective mass in the direct Γ valley. GeSn with a Sn fraction ~ 10 % is near the crossover of indirect-to-direct bandgap, and electrons in the indirect L valley still play an important role in the overall electron transport due to small energy difference between the indirect and direct valleys. However, the direct-bandgap GeSn films require high-Sn fractions ([Sn]>15%) were only experimentally studied for their optical properties [129]. The experimental results on electron transport in GeSn were reported with a Sn fraction below 10 % by means of Hall measurements [104] or n-FETs [113][130]. In this work, the Hall measurement results on n-type $Ge_{1-x}Sn_x$ films up to 21 % are demonstrated, and GeSn electron mobility is studied with wide a Sn fraction from 4 % to 21 %, which covers indirect and direct-bandgap GeSn. Furthermore, a detailed calculation on electron mobility is demonstrated to further investigate the electron transport in GeSn.

6.1 Hall Measurements of n-GeSn Epitaxial Films

6.1.1 Electron Transport in GeSn

Classical electron transport in semiconductors can be described by Drude model. In semiconductors or metals at finite temperatures, free electrons move randomly with the thermal velocity without creating a net current. Once an electric field ($\mathcal{E}_x$) is applied, electrons are accelerated by the electric field until scattering processes occur, such as

doi:10.6342/NTU202300648

impurity or phonon scattering. Those electrons will lose their momentum and/or change their travelling direction, and then are accelerated by the electric field again until the next scattering events. The average drift velocity υ_d can be derived by considering an average scattering time τ

$$\upsilon_d = \frac{q\tau}{m^*}\mathcal{E}_x = \mu_n \mathcal{E}_x \Rightarrow \quad \mu_n = \frac{q\tau}{m^*} \qquad \text{Eq. 6-1}$$

where m^* is the effective mass for conductivity, and μ_n is the electron mobility. The approach on the holes in valance band is similar. The net current density follows the Ohm's law by giving the electron density *n* and hole density *p*,

$$J_{drift} = q\left(n\mu_n + p\mu_p\right)\mathcal{E}_x = \sigma\mathcal{E}_x \qquad \text{Eq. 6-2}$$

where n and p are the concentrations of electrons and holes, respectively, μ_p is the hole mobility, and σ is the conductivity of the material. In semiconductors, the carrier mobility is limited by several scattering mechanisms, such as phonon scattering and impurity scattering. According to Matthiessen's rule, the effective scattering time can be calculated by considering the scattering rates of the individual processes, where the scattering rate is the inverse of scattering time [131].

$$\frac{1}{\tau_{overall}} = \sum_i \frac{1}{\tau_i} \quad \Rightarrow \quad \frac{1}{\mu_{overall}} = \sum_i \frac{1}{\mu_i} \qquad \text{Eq. 6-3}$$

In a GeSn alloy, the electron effective mass at the Γ valley is smaller than that at the L valley [2], which is similar to GaAs. When GeSn becomes a direct-bandgap material, the electron transport is dominated by the Γ-electrons, whose mobility is predicted over 10^5 cm^2/Vs at room temperature (with a carrier density of ~ 10^{15} cm^{-3}) [132][133]. By increasing the Sn fractions or applying tensile stresses [133], the electron effective mobility is enhanced due to the dominance of the Γ-electrons with a higher mobility than electrons in the L valley. This mobility enhancement results from the bandgap transition, which was experimentally reported in $GaAs_{1-x}P_x$ alloys, as shown in Figure 6-1(a) and (b)

doi:10.6342/NTU202300648

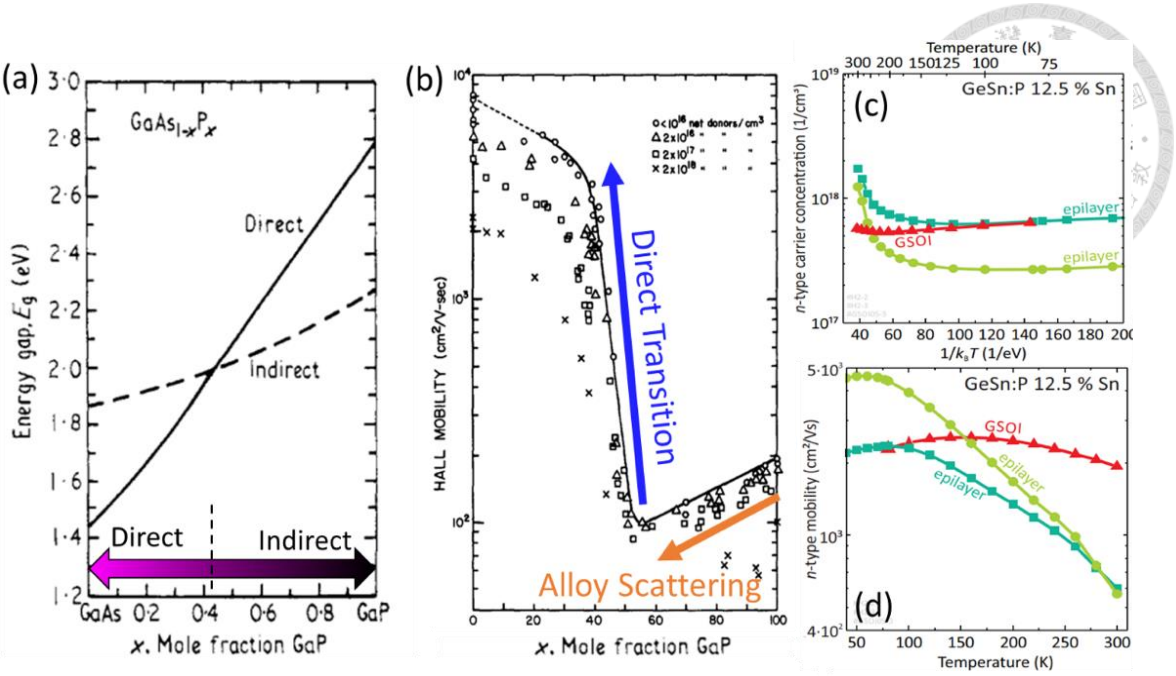

Figure 6-1 (a) Bandgap energy and (b) electron Hall mobility in $GaAs_{1-x}P_x$ alloy. [134] (c) Electron concentration and (d) Hall mobility of n-type $Ge_{0.875}Sn_{0.125}$ epilayers and GeSn on insulator (GSOI) [135].

[134]. GaP is an indirect-bandgap material, and the transition of indirect-to-direct bandgap occurs at x ~ 0.4. The electron Hall mobility is enhanced by over an order of magnitude. However, the experimental result on the electron mobility in direct-bandgap GeSn with a high Sn fraction has not yet been investigated systematically. Only Schulte-Braucks reported the electron Hall mobility of 4,500 cm^2/Vs at 50 K in n-type $Ge_{0.875}Sn_{0.125}$ films [135] (Figure 6-1(c) and (d)). In this work, the electron Hall mobility of GeSn epitaxial films is characterized to investigate the transition of indirect-to-direct bandgap in GeSn alloys.

6.1.2 Hall Effects

Hall measurement is a well-developed method to simultaneously extracting carrier concentrations and mobility in materials. The Hall effect is schematically shown in Figure 6-2(a). Assuming a current I_x flowing in x-direction and an out-of-plane magnetic field

doi:10.6342/NTU202300648

B_z applied in z-direction, the induced Lorentz force deflects the electrons and builds up an electric field $\mathcal{E}_H$ in y-direction across the width W. The corresponding voltage $V_H = \mathcal{E}_H W$ is called Hall voltage and given by [136]

$$V_H = -\frac{r}{qn}\frac{B_z I_x}{t} = R_H \frac{B_z I_x}{t} \qquad \text{Eq. 6-4}$$

where t is the thickness of the conduction layer, and r is the Hall scattering factor, which is $1 \leq r \leq 2$, depending on the scattering mechanism. R_H is called Hall coefficient, which is $-1/qn$ (negative) in n-type conduction and $+1/qp$ (positive) in p-type conduction, respectively, by assuming r=1. One can calculate the Hall mobility by $\sigma = qn\mu_n$ by measuring the conductivity

$$\sigma = \frac{1}{\rho_x} = \frac{I_x}{V_x}\frac{Wt}{L} \qquad \text{Eq. 6-5}$$

For practical measurements on bridge-type Hall-bar devices (Figure 6-2(b)), an ac current source I_{xx} with an amplitude of 100 nA and a frequency of 13 Hz is injected to the Hall-bar device in series of a 10-MΩ resistor. The voltage V_{xx} and the Hall voltage V_{xy} are measured by lock-in amplifiers. In order to exclude a non-ideal voltage drop at zero magnetic field, the 2-D electron density (cm^{-2}) is determined by the slope of Hall voltage (V_{xy}) and applied magnetic field (B_z)

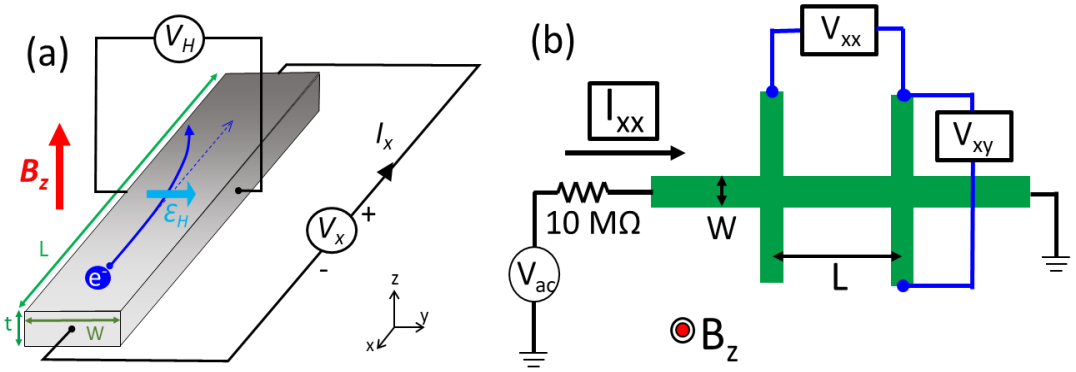

Figure 6-2 (a) Schematic of Hall effects and (b) Hall measurement setup in this work.

doi:10.6342/NTU202300648

$$n_{2D,Hall} = n_{Hall} \cdot t = -\frac{I_{xx}}{q}\frac{1}{\partial V_{xy}/\partial B_z} \quad \text{Eq. 6-6}$$

The electron Hall density n_{Hall} (cm^{-3}) is then derived by multiplying the thickness t (assuming uniform distribution). At the same time, the electron Hall mobility is measured as follows:

$$\mu_{Hall} = \frac{I_{xx}}{q n_{2D,Hall} V_{xx}}\frac{L}{W} \quad \text{Eq. 6-7}$$

If two conducting channels contribute to the electric current, the total (measured) Hall carrier density and mobility are given by a bilayer model [136]

$$n_{2D,total} = \frac{(n_1\mu_1 + n_2\mu_2)^2}{n_1{\mu_1}^2 + n_2{\mu_2}^2} \quad and \quad \mu_{total} = \frac{n_1{\mu_1}^2 + n_2{\mu_2}^2}{n_1\mu_1 + n_2\mu_2} \quad \text{Eq. 6-8}$$

in a low magnetic field limit, where n_1 and n_2 are the 2-D carrier densities of two conducting channels. The two channels can be two separated layers (a n-type film on a p-type buffer), two-subband conduction in a quantum well, or two types of carriers in a material, such as electrons and holes [137], or Γ-electrons and L-electrons in GeSn.

6.2 Hall Measurement on Electron Mobility in GeSn

6.2.1 Epitaxial Structures of GeSn Films

In order to epitaxially grow ([Sn]>18%) GeSn films with high Sn fractions, the GeSn relaxed buffer is required to reduce compressive strains, as discussed in Chapter 2. The epitaxial structures are designed to investigate the effects of strain and Sn fractions on the electron mobility (Figure 6-3). In Figure 6-3(a), the p- Si wafers ($\rho \sim 10$ Ωcm) were served as the substrates, and the Ge VS and $Ge_{0.88}Sn_{0.12}$ relaxed buffer are undoped to minimize the residual conduction. Before the deposition of the n-type strained $Ge_{0.82}Sn_{0.18}$ layer, a thin 20-nm Ge layer is served as a marking layer to separate the underlying relaxed buffer and the n-type GeSn active layer. The compressive strain of -0.99 % in the strained

doi:10.6342/NTU202300648

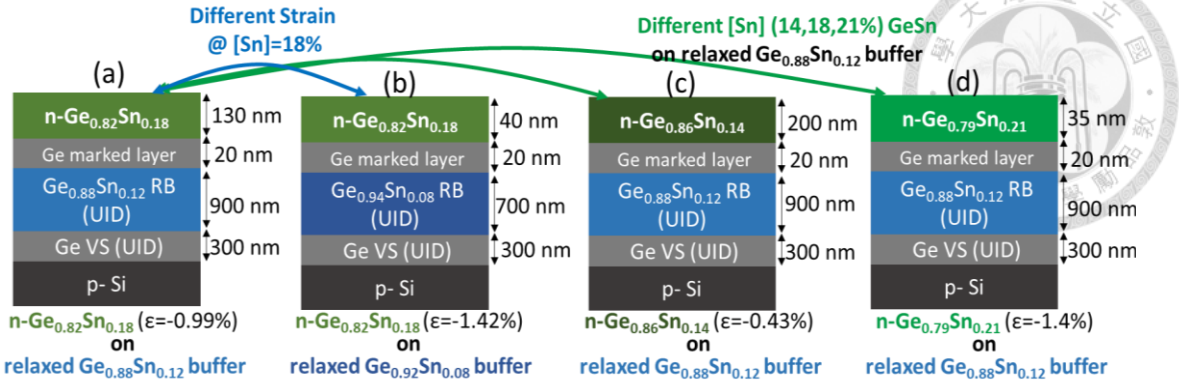

Figure 6-3 Epitaxial structures of n-type strained $Ge_{0.82}Sn_{0.18}$ layers on (a) $Ge_{0.88}Sn_{0.12}$ or (b) $Ge_{0.82}Sn_{0.08}$ relaxed buffers. (c) Strained $Ge_{0.86}Sn_{0.14}$ and (d) strained $Ge_{0.79}Sn_{0.21}$ on the same $Ge_{0.88}Sn_{0.12}$ relaxed buffer as (a).

$Ge_{0.82}Sn_{0.18}$ is determined by RSM. The $Ge_{0.92}Sn_{0.08}$ relaxed buffer is used to modify the strain condition of the strained $Ge_{0.82}Sn_{0.18}$ layer with a larger compressive strain of -1.42 % (Figure 6-3(b)). The n-type GeSn layers with a lower and a higher Sn fraction are grown on the $Ge_{0.88}Sn_{0.12}$ relaxed buffer in Figure 6-3(c) and (d), respectively. The strains of the active GeSn layers are -0.43 % and -1.4 %, respectively. For each structure in Figure 6-3, at least three doping concentrations in the active n-GeSn layers were used.

The analysis of TEM and RSM was performed to measure the thicknesses of n-type

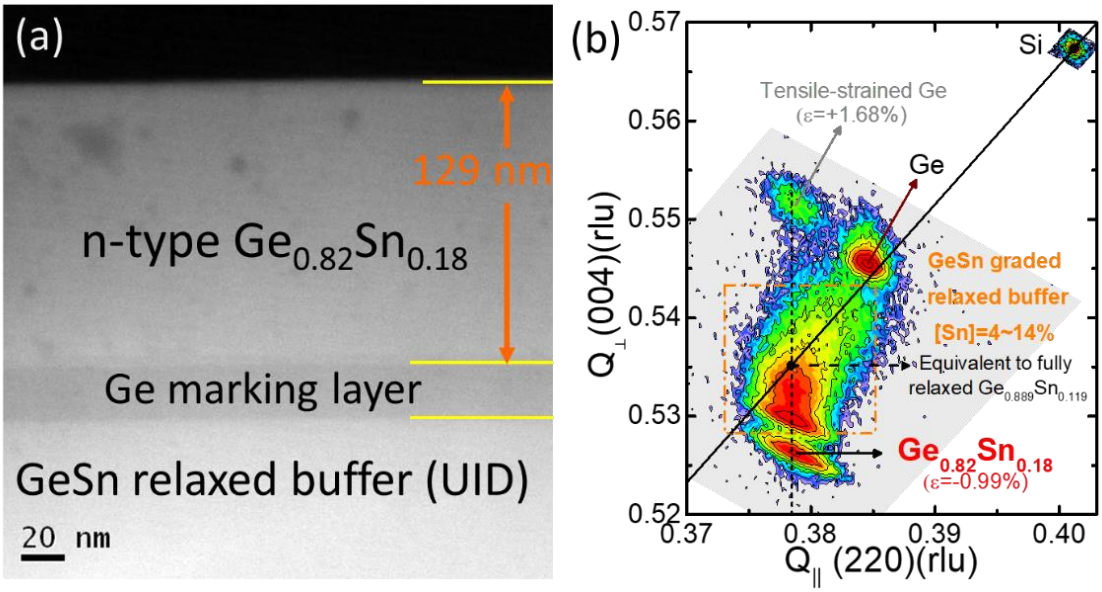

Figure 6-4 (a) Dark-field scanning TEM image and (b) RSM contour mapping of strained $Ge_{0.82}Sn_{0.18}$ on a $Ge_{0.88}Sn_{0.12}$ relaxed buffer.

doi:10.6342/NTU202300648

GeSn layers and to characterize the strain conditions, respectively. The thickness of $Ge_{0.82}Sn_{0.18}$ is 129 nm (Figure 6-4(a)). In Figure 6-4(b), the $Ge_{0.82}Sn_{0.18}$ layer is fully strained (ε=-0.99 %) to the $Ge_{0.88}Sn_{0.12}$ relaxed buffer, and the mark Ge layer is slightly tensile-strained.

6.2.2 Device Fabrication of Hall-Bar Devices

To measure electron mobility and density in the n-type GeSn layer, the Hall-bar devices were fabricated for the low-temperature Hall measurement. The process flow of the Hall-bar device is shown in Figure 6-5(a). After the CVD growth, the wafers were diced into small pieces (1 cm × 1 cm). The samples were ultrasonically cleaned with solvents, and the Hall-bar region was defined by photolithography. The Hall-bar mesa was dry-etched by Cl_2/BCl_3 RIE until the p- Si substrate is uncovered. The samples were cleaned with solvents again followed by diluted HF dips to remove surface native oxides. A photolithographic step and a lift-off process of 10-nm Cr/200-nm Au were performed for the contact pad. The size of contact pads is 100 × 100 μm^2 for wire bonding. At last,

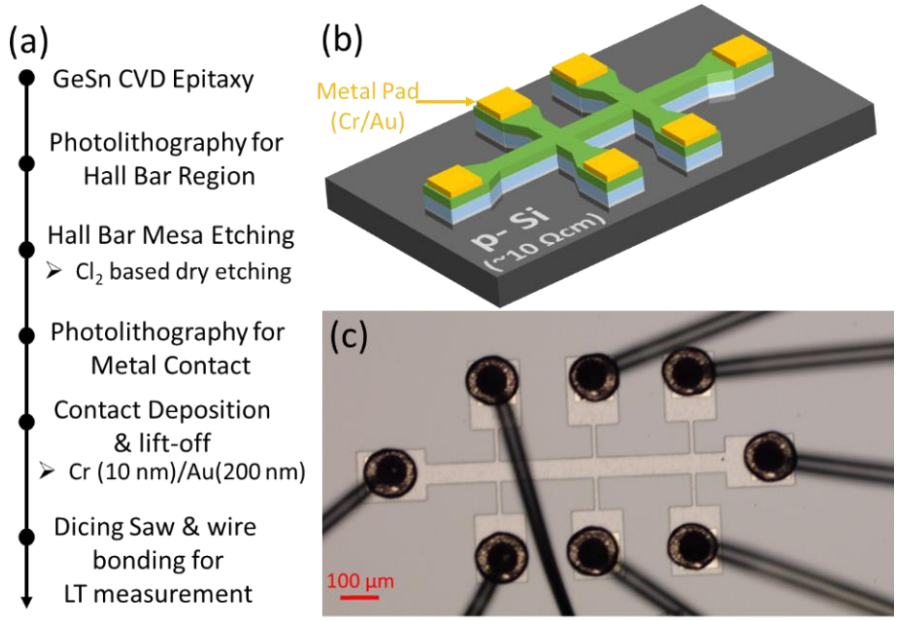

Figure 6-5 (a) A process flow and (b) an aerial schematic of a Hall-bar device. (c) An OM image of a Hall-bar device with wires bonded.

doi:10.6342/NTU202300648

samples were diced into pieces of 4 mm× 4 mm and wire-bonded on the sample holder for low-temperature measurements. The aerial schematic of the Hall-bar device is shown in Figure 6-5(b) with the OM image of the device with wire bonding in Figure 6-5(c). The Hall measurement was performed by SR830 lock-in amplifiers in a cryostat system at 4 K ~ 300 K.

6.3 Electron Mobility in GeSn with High Sn Fractions

6.3.1 Hall Measurements of n-type $Ge_{0.82}Sn_{0.18}$ under Different Strains

Hall mobility and Hall density of n-type $Ge_{0.82}Sn_{0.18}$ with different strains are shown in Figure 6-6. Figure 6-6 (a) and (b) show the results of four different doping levels in the n-$Ge_{0.82}Sn_{0.18}$ layers with a strain of ε =-0.99 %, corresponding to the structure in Figure 6-3(a). For the highest doping of $n_{4K} = 4\times10^{19}$ cm^{-3} (black curve), the Hall mobility is

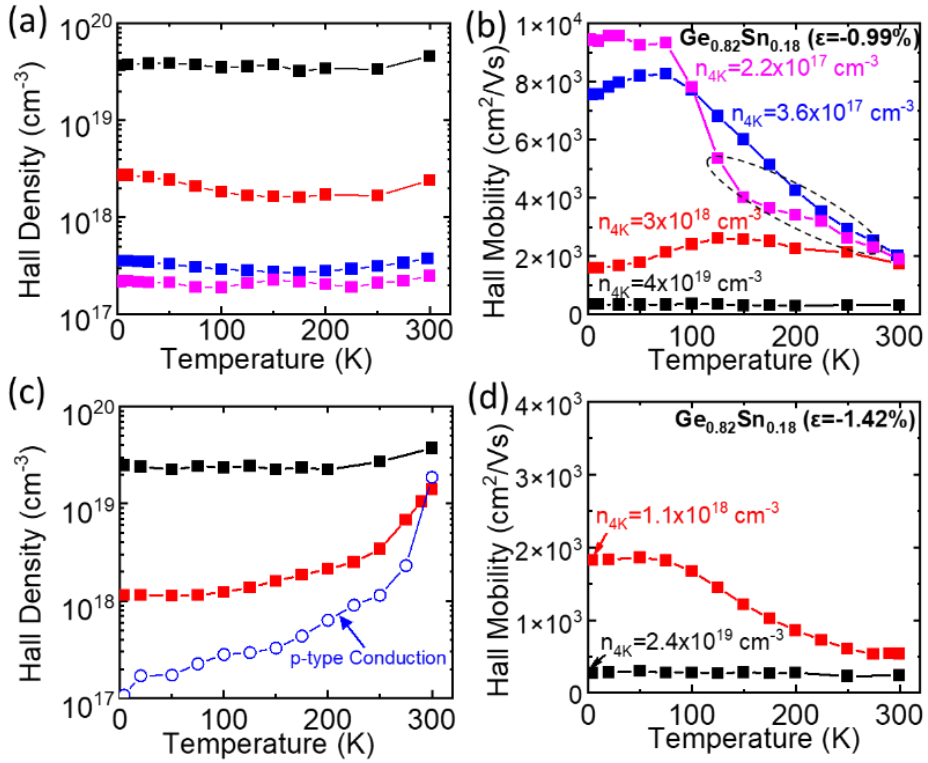

Figure 6-6 (a) Hall density and (b) Hall mobility of n-type strained $Ge_{0.82}Sn_{0.18}$ (ε =-0.99 %) on a $Ge_{0.88}Sn_{0.12}$ relaxed buffer. (c) Hall density and (d) Hall mobility of n-type strained $Ge_{0.82}Sn_{0.18}$ (ε =-1.42 %) on a $Ge_{0.82}Sn_{0.08}$ relaxed buffer.

doi:10.6342/NTU202300648

about 350 cm^2/Vs and almost constant at all temperatures. For the medium doping of n_{4K} = 3×10^{18} cm^{-3} (red curve), the Hall mobility is increased to 2,500 cm^2/Vs at 150 K due to the suppressed ionized impurity scattering. For the low doping of n_{4K}= 2.2×10^{17} cm^{-3} (magenta curve), the Hall mobility is enhanced up to 9,500 cm^2/Vs below 75 K. The Hall mobility at temperatures above 100 K is smaller than that of the sample with a slightly higher doping (blue curve), which may be due to the effect of p-type conduction from the undoped GeSn buffer, Ge buffers, or the p^- Si substrate. For a sample with a lower doping level, the effect of parallel conduction is stronger, reducing the measured Hall mobility and increasing the measured Hall density (will be explained by the bilayer model in Section 6.3.3). At a lower temperature (< 100 K), the parallel conduction becomes much suppressed since the buffer layer and the Si substrate become insulating due to the carrier frozen-out.

For the $Ge_{0.82}Sn_{0.18}$ layer with a larger compressive strain of ε =-1.42 %, corresponding to the structure in Figure 6-3(b), the Hall density and mobility are shown in Figure 6-6 (c) and (d), respectively. The Hall mobility of the sample with highest doping level shows a constant mobility of ~ 280 cm^2/Vs. For the case of a medium-doping level (n_{4K} = 1.1×10^{18} cm^{-3}, red curve), the Hall mobility is 1,850 cm^2/Vs at 4 K ~ 50 K. Because of the thinner n-type layer (~ 40 nm), the device with the lowest doping level show the p-type conduction at all temperatures (blue hollow points) due to the residual conduction.

The mobilities for the two devices with a similar doping concentration (n_{4K} = 1 ~ 3×10^{18} cm^{-3}, red curves in Figure 6-6(b) and (d)) on different GeSn buffers at low temperatures (below 100 K) are compared. The electron mobility in the less compressive-strained $Ge_{0.82}Sn_{0.18}$ layer (ε =-0.99 %) is slightly higher than that of larger compressive-strained epitaxial layer (ε =-1.42 %). In Figure 6-7, the band structures by EPM simulation

doi:10.6342/NTU202300648

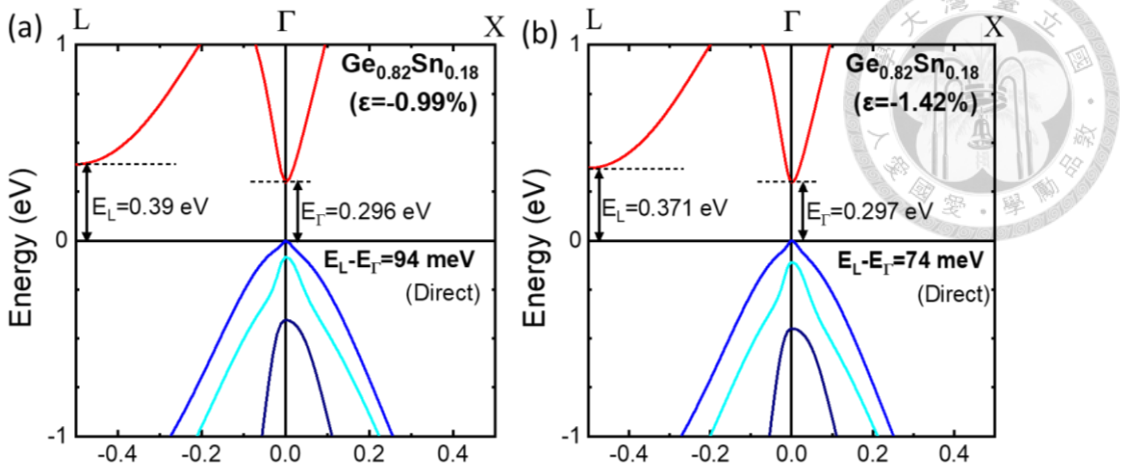

Figure 6-7 Simulated EPM band structures of $Ge_{0.82}Sn_{0.18}$ with the compressive strain of (a) ε =-0.99 % and (b) ε =-1.42 %.

suggests that both conditions are already direct-bandgap, while the larger compressive strain (|ε|=0.99 %→1.42 %) leads to a smaller energy difference between the L and Γ valleys (E_L-E_Γ=94 meV → 74 meV). Therefore, there are more L-electrons, whose electron effective mass is larger, leading to a lower mobility.

6.3.2 Hall Measurements of n-GeSn with Different Sn fractions (14 % ~ 21 %)

The Hall density and Hall mobility of n-type $Ge_{0.86}Sn_{0.14}$ and $Ge_{0.79}Sn_{0.21}$ epitaxial films (Figure 6-3(c) and (d)) on the same GeSn relaxed buffer are shown in Figure 6-8. Figure 6-8 (a) and (b) show the Hall measurement results for four different doping levels in $Ge_{0.86}Sn_{0.14}$ with a strain of ε =-0.43 %. The Hall density of the device with the lowest doping level increases significantly at temperatures higher than ~ 250 °C because of the parallel conduction in the buffer and substrate. The Hall mobility becomes higher with a lower doping concentration at all temperatures due to the less impurity scattering. For the lowest-doping sample (n_{4K}=2×10^{17} cm^{-3}), the highest Hall mobility of ~ 8,700 cm^2/Vs is reported below 75 K.

doi:10.6342/NTU202300648

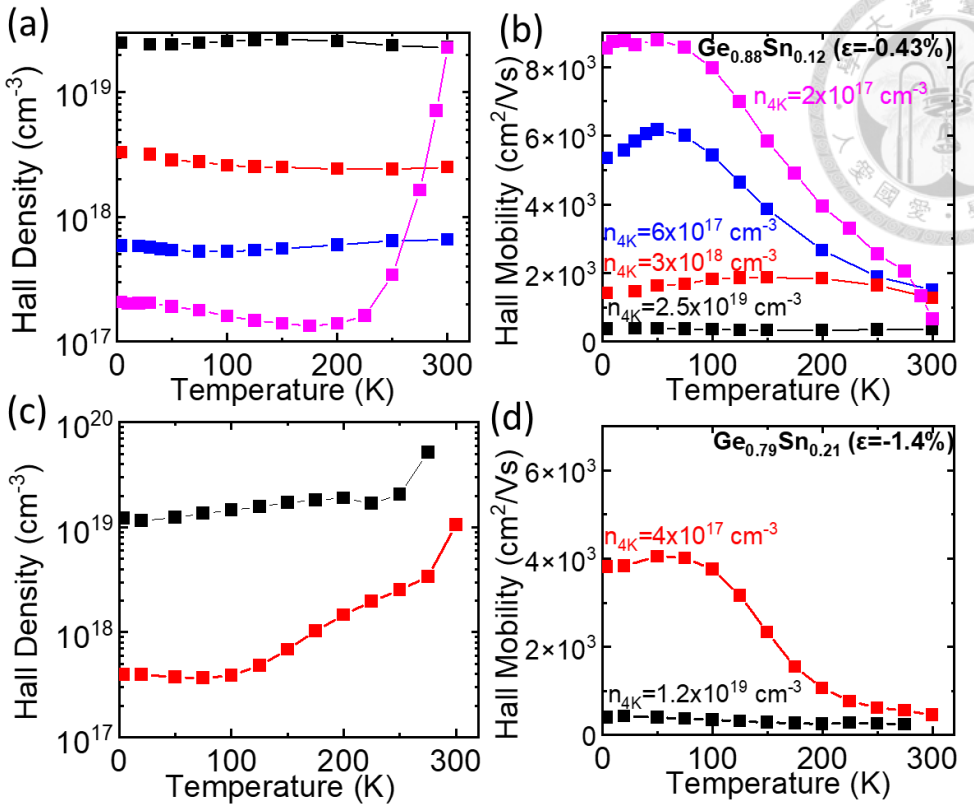

Figure 6-8 (a) Hall density and (b) Hall mobility of n-type strained $Ge_{0.86}Sn_{0.14}$ (ε =-0.43 %), and (c) Hall density and (d) Hall mobility of n-type strained $Ge_{0.79}Sn_{0.21}$ (ε =-1.42 %).

For the n-type $Ge_{0.79}Sn_{0.21}$ layer (ε =-1.4 %) on the $Ge_{0.88}Sn_{0.12}$ relaxed buffer, the Hall density and mobility are shown in Figure 6-8 (c) and (d). The Hall mobility of the device with a high doping concentration (n_{4K} = 1.2×10^{19} cm^{-3}, black curve) shows a constant mobility of ~ 400 cm^2/Vs, while for the lower doping concentration (n_{4K} = 4×10^{17} cm^{-3}, red curve), the mobility is much larger (4,000 cm^2/Vs at T < 100 K). The Hall density is also increased due to the bilayer effect at a higher temperature. Considering the Hall mobility at low temperatures (say 4 K), the mobility does not increase with the Sn fraction (from 14 % to 21 %) in GeSn, and seems to slightly decrease in n-type $Ge_{0.79}Sn_{0.21}$, which might be due to no few Γ-electrons or stronger alloy scattering. Further analysis will be introduced in Section 6.3.4.

doi:10.6342/NTU202300648

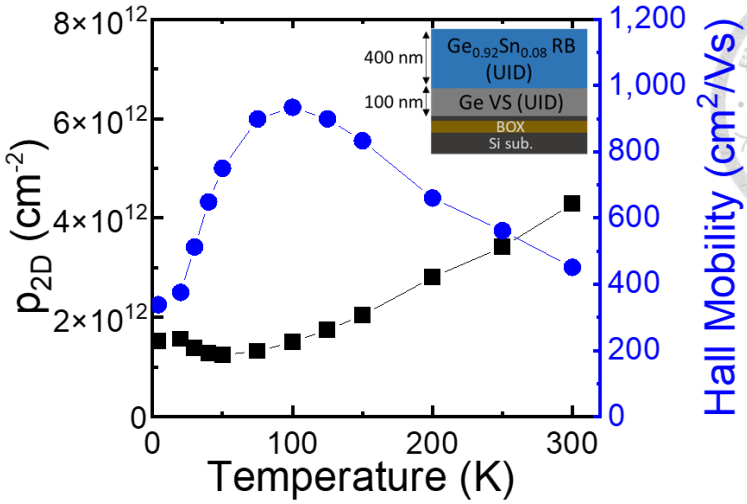

Figure 6-9 Hall measurement results of p-type UID $Ge_{0.92}Sn_{0.08}$ relaxed buffer/Ge VS.

6.3.3 Effects of GeSn Relaxed Buffers

The majority carrier type in undoped Ge or GeSn epitaxial layers is p-type (hole) [135][138]. Using a SOI wafer can effectively eliminate the conduction of the thick Si substrate. Figure 6-9 shows the Hall measurement results of an undoped GeSn epitaxial layer on a thin Ge buffer using a SOI substrate. The integrated 2D hole density is 4×10^{12} cm^{-2} at 300 K, corresponding to a 3D density of 8×10^{16} cm^{-3} for a 500-nm buffer layer. The 2D hole density deceases to 1.5×10^{12} cm^{-2} at 4 K, where the freeze-out effect is not significant in Ge and GeSn buffers. Therefore, the effects of p-type buffers on the active n-type GeSn layers need to be considered for the characterization of the electron mobility by Hall measurements.

The schematic of the bilayer conduction in the n-type GeSn epitaxial structure is shown in Figure 6-10(a). Part of injected current flows across the GeSn p-n junction between the active n-type GeSn and the unintentional-doped p-type GeSn relaxed buffer. Since the GeSn p-n junction is leaky due to the small bandgap energy [113], the Hall transport shows bilayer characteristics, especially at 300 K. The total conduction can be simplified by a bilayer model with a n-type layer (μ_n, n_{2D}) and a p-type layer (μ_p, p_{2D}). The effective Hall mobility and density can be derived from Eq. 6-8

doi:10.6342/NTU202300648

$$n_{2D,total} = \frac{(n_{2D}\mu_n + p_{2D}\mu_p)^2}{n_{2D}{\mu_n}^2 - p_{2D}{\mu_p}^2} \quad \text{and} \quad \mu_{total} = \frac{n_{2D}{\mu_n}^2 - p_{2D}{\mu_p}^2}{n_{2D}\mu_n + p_{2D}\mu_p} \qquad \text{Eq. 6-9}$$

assuming the overall conduction is still n-type ($n_{2D}{\mu_n}^2 - p_{2D}{\mu_p}^2 > 0$). The deviation between the effective Hall results ($n_{2D,total}$ and μ_{total}) and original parameters in the n-type layer (n_{2D} and μ_n) can be evaluated by the ratio of p-type and n-type conductance

$$R = \frac{p_{2D}\mu_p}{n_{2D}\mu_n} \qquad \text{Eq. 6-10}$$

Then, Eq. 6-9 can be derived to

$$n_{2D,total} = n_{2D} \cdot \frac{(1+R)^2}{1-\left(\frac{\mu_p}{\mu_n}\right)R} \quad and \quad \mu_{total} = \mu_n \cdot \frac{1-\left(\frac{\mu_p}{\mu_n}\right)R}{1+R} \qquad \text{Eq. 6-11}$$

The plot of effective Hall results versus conductance ratio is shown in Figure 6-10(b). As the bilayer effect is strong, where the conductance ratio R is close to 1, the Hall density ($n_{2D,total}$) become much larger than the original n-type doping density ($n_{2D} = n \cdot t_1$), while the effective Hall mobility (μ_{total}) becomes smaller than the original n-type mobility (μ_n). The bilayer effect explains the deviation of the Hall density in the device

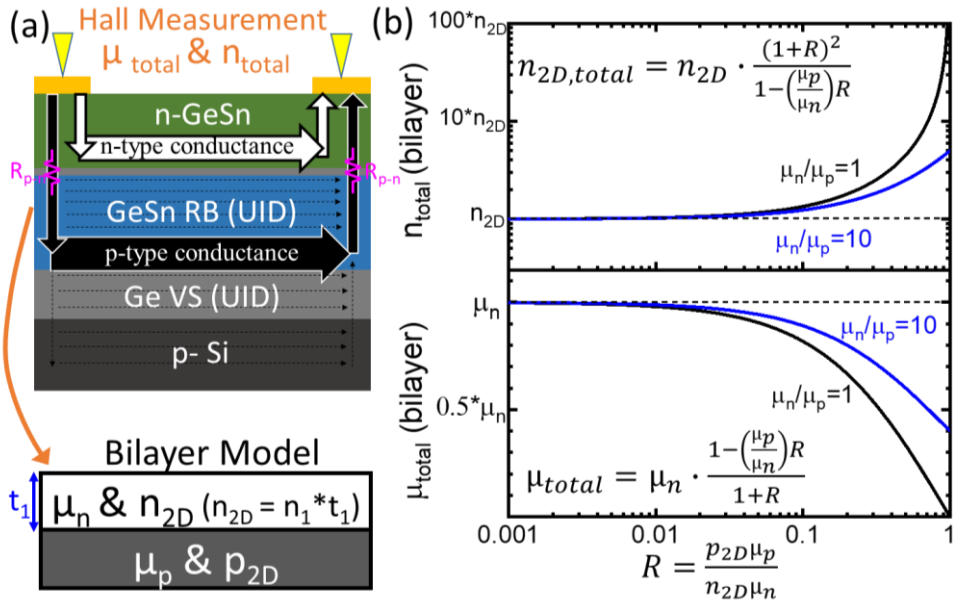

Figure 6-10 (a) Schematics of the bilayer conduction in the GeSn epitaxial structure. (b) Effective Hall density and mobility due to the bilayer effect.

doi:10.6342/NTU202300648

with the lowest doping sample at 300 K in Figure 6-8 (a). At low temperatures, the conductance of the p-type buffer layers (including p^- Si substrate) becomes much smaller due to the free-out, leading to an increase of the resistance of p-n junction [139] and preventing current leakage into GeSn buffer layers significantly. Therefore, the bilayer effect is much suppressed at low temperatures, and the Hall measurement results are much closer to the actual transport characteristics of the active n-type GeSn layer.

6.3.4 Comparison and Analysis

To rule out the bilayer effect, the Hall mobility at 4 K is chosen for the following analysis. Figure 6-11(a) shows the Hall mobility versus Hall density in the n-type $Ge_{0.92}Sn_{0.08}$ devices, (replotted version of Figure 5-13(b) in a log-log scale). For each strain condition, the mobility is decreased with the doping concentration due to the enhanced impurity scattering. According to the prior discussion in Section 5.3.2, the mobility of $Ge_{0.92}Sn_{0.08}$ is enhanced by strain engineering toward tensile strain due to more electrons populating in the Γ valley. The Hall mobility versus Hall density in the n-type $Ge_{0.82}Sn_{0.18}$ samples is plotted in Figure 6-11(b). For $Ge_{0.82}Sn_{0.18}$, with a smaller strain (ε =-0.99 %), the Hall mobility is higher. According to simulated band structures in

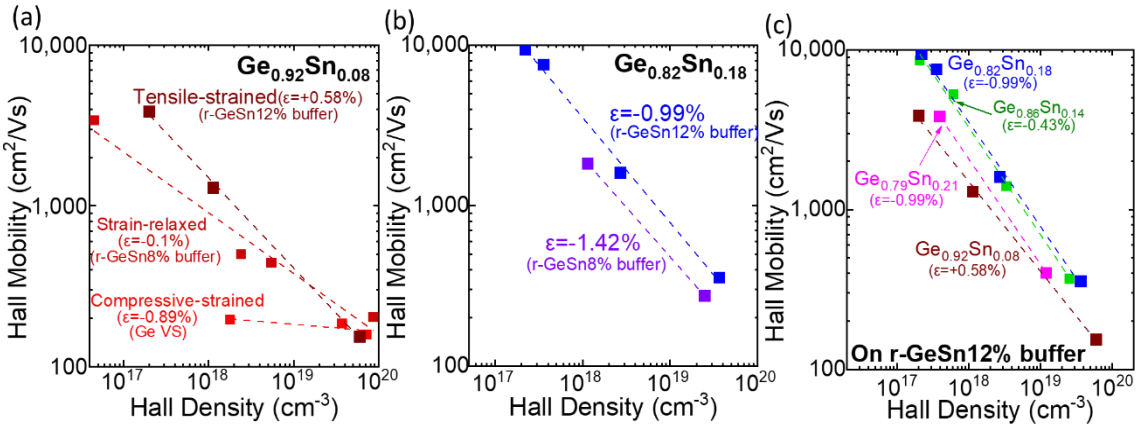

Figure 6-11 4 K Hall mobility versus Hall density for (a) $Ge_{0.92}Sn_{0.08}$, (b) $Ge_{0.82}Sn_{0.18}$ under different strain conditions, and (c) strained GeSn with [Sn] = 8 ~ 21 % on the same $Ge_{0.88}Sn_{0.12}$ relaxed buffer.

doi:10.6342/NTU202300648

Figure 6-7, the larger compressive strain reduces the energy difference between Γ and L valleys (E_L-E_Γ), which affects the electron population in two valleys.

Figure 6-11(c) plots the Hall mobility in GeSn with different Sn fractions (8 % ~ 21 %) using the same $Ge_{0.88}Sn_{0.12}$ relaxed buffer. The electron mobility increases with the Sn fraction until 14 % (green scatters). Further increasing the Sn fraction to 18 % (blue scatters) does not enhance the electron mobility, and the mobility becomes even smaller for $Ge_{0.79}Sn_{0.21}$. In addition to the effects of the electron population, other factors relevant to the Sn fraction may influence the mobility, such as the alloy scattering in GeSn alloys. Increasing the Sn fraction in the active GeSn layer leads to a stronger alloy scattering and reduces the mobility.

To further investigate the effect of the Sn fraction on electron mobility, the Γ-electron

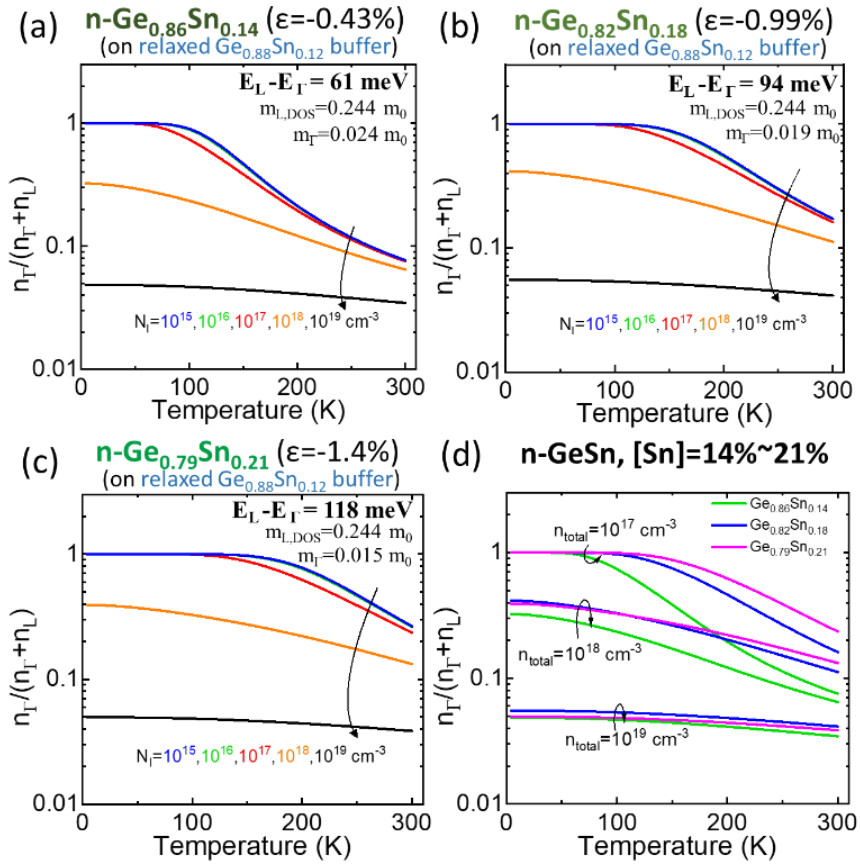

Figure 6-12 Γ-electron population ratio in n-type (a) $Ge_{0.86}Sn_{0.14}$, (b) $Ge_{0.82}Sn_{0.18}$, and (c) $Ge_{0.79}Sn_{0.21}$. (d) Γ-population ratios with total electron concentrations of 10^{17}, 10^{18}, 10^{19} in these three GeSn.

doi:10.6342/NTU202300648

density over the total electron density ($\frac{n_\Gamma}{n_L+n_\Gamma}$) in $Ge_{0.86}Sn_{0.14}$, $Ge_{0.82}Sn_{0.18}$, and $Ge_{0.79}Sn_{0.21}$ is calculated and shown in Figure 6-12. The energy difference and effective masses are extracted from the EPM simulation results. The EPM results suggest the direct bandgap in these three conditions with the direct energy difference (E_L-E_Γ) from 61 meV to 118 meV. For a high doping density of 10^{19} cm^{-3}, the ratio is only 5 % and do not change much with temperature. For a low doping density below 10^{17} cm^{-3}, the Γ-electron population is much lower (0.08 ~ 0.3) at 300 K for the Sn fractions of 14 % ~ 21 %, while most of all electrons condense to the lower Γ valley ($\frac{n_\Gamma}{n_L+n_\Gamma} = 1$) at lower temperatures. The electron population of the three conditions are shown in Figure 6-12(d). For the doping density of 10^{17} cm^{-3}, Γ-electron population rate is 100 % at 75 K, regardless of the Sn fraction. The electron effective mobility is fully dominated by the Γ-electron mobility. For the higher doping density (n_{total}=10^{19} cm^{-3}), the 4 K population of Γ-electrons increase slightly from $Ge_{0.86}Sn_{0.14}$ to $Ge_{0.82}Sn_{0.18}$. For a higher electron density, most electrons populate in L-valley. Meanwhile, increasing the Sn fraction leads to a smaller electron effective mass of Γ-electrons ($m_{\Gamma,14\%}$=0.024 m_0 and $m_{\Gamma,21\%}$=0.015 m_0), so the DOS of Γ-valley and the number of Γ-electrons become smaller. Thus, effects of a larger energy difference between L and Γ valleys to increase the Γ-population are counterbalanced at the same time. Therefore, for a high Sn fraction ([Sn] > 14 %), increasing the Sn fraction does not effectively increase the Γ-electron population at low temperatures.

Last, 4 K mobility of all n-type GeSn devices is illustrated in Figure 6-13. The data points of Ge are the 77 K mobility in the reference [140]. The data points of experimental mobility are classified into several doping ranges (n ~ 3×10^{17}, ~1×10^{18} , ~ 3×10^{18}, ~ 1×10^{19} and ~ 1×10^{20} cm^{-3}) with different marks. The fitting experimental mobility at n = 1×10^{18} cm^{-3} is shown as the column bars. The mobility trend starts from Ge, which is an indirect material with the largest energy difference between L and Γ valleys (E_Γ-E_L=140

doi:10.6342/NTU202300648

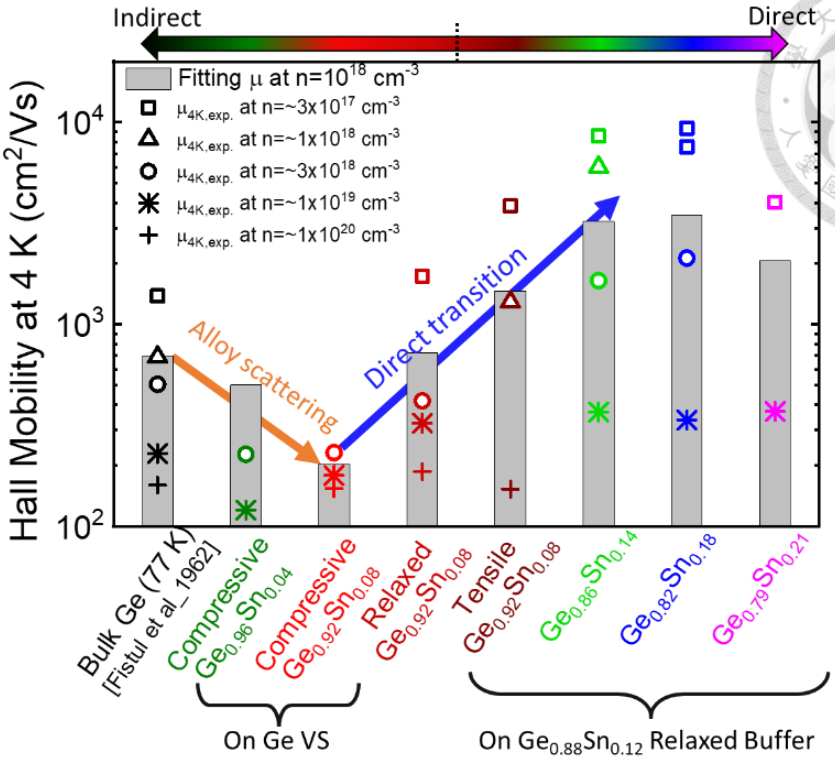

Figure 6-13 4 K electron mobility of n-Ge to n-$Ge_{0.79}Sn_{0.21}$ films.

meV). By increasing the Sn fraction in GeSn, the mobility decreases due to the enhanced alloy scattering. By relaxing the compressive strain and applying tensile stresses on $Ge_{0.92}Sn_{0.08}$, GeSn becomes direct-bandgap and more Γ-electrons contribute a higher effective mobility. By increasing the Sn fraction further (up to 18 %), the energy difference between the L and Γ valleys becomes larger, leading to more electrons populating in the Γ valley and thus, a higher mobility. By increasing the Sn fraction further to 21 %, although there are more electrons in the Γ valley due to the larger energy different between the L and Γ valleys (Figure 6.12(d)), the mobility decreases, which suggests the alloy scattering becomes dominates again since the strains for the $Ge_{0.82}Sn_{0.18}$ and $Ge_{0.79}Sn_{0.21}$ films were controlled at ~ -0.99 % to rule out their effects.

doi:10.6342/NTU202300648

6.4 Theoretical Calculation of Electron Mobility in GeSn

The theoretical calculation on GeSn electron mobility is demonstrated in order to further understand the carrier transport in GeSn, which is complex due to the mixing results of many factors, such as different scattering mechanisms and the relative populations in the Γ and L valleys. In addition, the strain condition of GeSn also affects the electron population and mobility. Prior works only calculated the GeSn electron mobility at 300 K with a low carrier concentration of 10^{15} cm^{-3} [133] (10^{14} cm^{-3} in [132]). Therefore, the theoretical calculation in this work is extended to a higher electron density and much lower temperatures.

6.4.1 Carrier Scattering Mechanisms

The scattering rates for both Γ- electrons and L-electrons due to acoustic deformation potential (ac), optical deformation potential (op), alloy (al), and ionized impurity (imp) scatterings are expressed as follows [131][141]

$$\frac{1}{\tau_{ac}} = \frac{\sqrt{2} D_{ac}^2 (m_{\Gamma \text{ or } L})^{3/2} k_B T}{\pi \hbar^4 \rho v_s^2} E^{1/2} \quad \text{Eq. 6-12}$$

$$\frac{1}{\tau_{op}} = \frac{\sqrt{2} D_{op}^2 (m_{\Gamma \text{ or } L})^{3/2}}{2\pi \hbar^3 \rho \omega_0} \left[N_0 (E + \hbar\omega_0)^{1/2} + (N_0 + 1)(E - \hbar\omega_0)^{1/2} \right] \quad \text{Eq. 6-13}$$

$$\frac{1}{\tau_{alloy}} = \frac{\sqrt{2} a_0^3 |U_{al}|^2 (m_{\Gamma \text{ or } L})^{3/2}}{8\pi\hbar} x(1-x) E^{1/2} \quad \text{Eq. 6-14}$$

$$\frac{1}{\tau_{imp}} = \frac{q^4 N_I}{16\pi\varepsilon^2 \sqrt{2 m_{\Gamma \text{ or } L}}} L(E)\ E^{-3/2}$$

$$\text{, where } L(E) = ln\left(1 + \frac{8mL_D^2 E}{\hbar^2}\right) - \frac{\frac{8mL_D^2 E}{\hbar^2}}{1 + \frac{8mL_D^2 E}{\hbar^2}} \text{ and } L_D = \sqrt{\frac{\varepsilon k_B T}{q^2 N_I}} \quad \text{Eq. 6-15}$$

For the above equations, E is the kinetic energy of the electron in the valley, D_{ac} and

doi:10.6342/NTU202300648

D_{op} are the deformation potential constants (DPCs) for acoustic phonon and optical phonons, ρ is the mass density, v_s is the sound velocity, $N_0 = \frac{1}{e^{\hbar\omega_0/kBT}-1}$ is the phonon number, $\hbar\omega_0$ is the optical phonon energy, U_{al} is the alloy scattering potential, a_0 is the lattice constant, and x is the Sn fraction. Assuming fully ionized, the ionized impurity density N_I is equal to the donor density and total electron density (n_Γ+n_L). $L(E)$ considers the influence of the screened Coulomb potential by mobile carriers, where L_D is the screening length. $m_{\Gamma\, or\, L}$ is the density-of-state effective mass of Γ-electron and L-electron.

The average relaxation time of each energy-dependent scattering rate is derived from the average velocity under the condition of the uniform electric field [131].

$$\langle v_z\rangle = \frac{\sum_p v_z f}{\sum_p f_0} = (-q)\mathcal{E}_z\left[\frac{\sum_p {v_z}^2 \tau_f(E) f_0(E)}{nk_BT}\right] \quad \because v_z = \frac{p_z}{m^*} = (-q)\tau\frac{\mathcal{E}_z}{m^*} \qquad \text{Eq. 6-16}$$

where f_0 is the Fermi-Dirac distribution function

$$f_0 = \frac{1}{e^{\triangle}+1} \quad \triangle = \frac{(E_{C0} + p^2/2m^* - E_F)}{k_BT} \qquad \text{Eq. 6-17}$$

Eq. 6-16 can be written as

$$\langle v_z\rangle = \frac{(-q)}{m^*}\left[\frac{(1/3)\sum_p (m^* v^2/2)\tau_f(E) f_0(E)}{(1/3)\langle E\rangle}\right]\mathcal{E}_z = \frac{(-q)\mathcal{E}_z}{m^*}\frac{\langle E\tau_f(E)\rangle}{\langle E\rangle} \qquad \text{Eq. 6-18}$$

in a simple notation $\langle E\tau_f(E)\rangle/\langle E\rangle$, and compare the above equation with the expression of drift velocity $v_d = \mu_n\mathcal{E}$ (Eq. 6-1)

$$\mu_n \equiv \frac{q\,\langle\langle\tau_f\rangle\rangle}{m^*} \text{ where } \langle\langle\tau_f\rangle\rangle \equiv \frac{\langle E\tau_f(E)\rangle}{\langle E\rangle} \qquad \text{Eq. 6-19}$$

The double brackets are to indicate that $\langle\langle\tau\rangle\rangle$ is not a simple average of $\tau_f(E)$ over the distribution function. $\langle\langle\tau_f\rangle\rangle$ can be further simplified with Boltzmann approximation

$$\langle\langle\tau_f\rangle\rangle = \frac{\sum_p (p^2/2m^*)\tau_f(E) e^{-p^2/2m^* k_BT}}{\sum_p (p^2/2m^*) e^{-p^2/2m^* k_BT}} \text{ where } E = p^2/2m^* \qquad \text{Eq. 6-20}$$

doi:10.6342/NTU202300648

This can be converted to an integral below:

$$\langle\langle \tau_f \rangle\rangle = \frac{\int_0^\infty \tau_f(E) e^{-p^2/2m^* k_B T} p^4 dp}{\int_0^\infty e^{-p^2/2m^* k_B T} p^4 dp} \quad \text{Eq. 6-21}$$

By substituting $\eta = p^2/2m^* k_B T = E/k_B T$ into the above equation,

$$\langle\langle \tau_f \rangle\rangle = \frac{\int_0^\infty \tau_f(\eta) \eta^{3/2} e^{-\eta} d\eta}{\int_0^\infty \eta^{3/2} e^{-\eta} d\eta} = \tau_f \frac{\Gamma(s + 5/2)}{\Gamma(5/2)} \quad \text{Eq. 6-22}$$

with the energy-dependent scattering expressed in terms of power-law ($\tau_f(E) = \tau_0 [E/k_B T]^s$). Then, the scattering relaxation time can be calculated in a complete form, for acoustic scattering time

$$\langle\langle \tau_{ac} \rangle\rangle = \frac{4}{3\sqrt{\pi}} \tau_{0,ac} = \frac{4}{3\sqrt{\pi}} \frac{\pi \hbar^4 \rho v_s^2}{\sqrt{2} D_{ac}^2 (m_{\Gamma \text{ or } L})^{\frac{3}{2}}} (k_B T)^{-\frac{3}{2}} \quad \text{Eq. 6-23}$$

with the $T^{-3/2}$ temperature dependence, and alloy scattering time

$$\langle\langle \tau_{al} \rangle\rangle = \frac{4}{3\sqrt{\pi}} \tau_{0,al} = \frac{4}{3\sqrt{\pi}} \frac{8\pi\hbar}{\sqrt{2} a_0^3 |U_{al}|^2 (m_{\Gamma \text{ or } L})^{3/2}} \frac{1}{x(1-x)} (k_B T)^{-\frac{1}{2}} \quad \text{Eq. 6-24}$$

with the $T^{-1/2}$ temperature dependence. With a low carrier density, the impurity scattering can be also expressed in a power-law and shows the $T^{3/2}$ temperature dependence. The effective mobility by different scattering mechanisms can be calculated by Eq. 6-19, and the mobility of Γ- electron (μ_Γ) and L-electron (μ_L) are derived by Matthiessen's rule (Eq. 6-3), respectively.

The effective mobility of GeSn is combination of μ_Γ and μ_L by the populations in two valleys, where the populations (n_Γ and n_L,) can be calculated given the energy difference in Section 5.3.1. First, the effective mobility is calculated by the linear combination, based on the concept of the average drift velocity

$$\overline{v_d} = \frac{n_\Gamma}{n_\Gamma + n_L} v_\Gamma + \frac{n_L}{n_\Gamma + n_L} v_L \Longrightarrow \mu_{\text{linear}} = \frac{n_\Gamma \mu_\Gamma + n_L \mu_L}{n_\Gamma + n_L} \quad \text{Eq. 6-25}$$

However, for the measured mobility by Hall effect, the effective mobility includes the

doi:10.6342/NTU202300648

bilayer conduction, which is written as

$$\mu_{bilayer} = \frac{n_\Gamma {\mu_\Gamma}^2 + n_L {\mu_L}^2}{n_\Gamma \mu_\Gamma + n_\mathrm{L} \mu_\mathrm{L}} \quad \text{Eq. 6-26}$$

Both expressions of overall mobility will be used in the following calculations.

6.4.2 Validity of the Transport Equation and Adjustment on Impurity Scattering

In above discussion and derivation, one of the issues on the validity of the Boltzmann transport equation is from the distribution function. Since the Fermi distribution function varies rapidly near the Fermi level E_F, the inequality ΔE< kT must be satisfied for Boltzmann approximation [142]. According to the uncertainty principle, $\Delta \mathrm{E} \Delta \mathrm{t} \geq \hbar$, if we take $\Delta \mathrm{t}$ to be τ, we find that

$$\tau > \frac{\hbar}{k_B T} \quad \text{Eq. 6-27}$$

It can be written in a different form in term of the mobility [heavily]

$$\mu > \frac{q\hbar}{m^* k_B T} \quad \text{Eq. 6-28}$$

Comparing these inequalities with the measured mobility, the transport equation is applicable to Ge only for impurity concentrations on the order of 10^{18} cm^{-3} at 300 K, and not applicable for lower impurity concentrations at low temperatures [140].

D. M. Szmyd et al. derived a new impurity scattering formula for degenerately-doped material, which accurately matched with the experimental mobility of n^+ GaAs (up to 10^{19} cm^{-3}) at 300 K and 77 K [143]. The formula of impurity mobility considered the increase of effective mass due to nonparabolicity of conduction band:

doi:10.6342/NTU202300648

$$\mu_{imp} = \frac{32\sqrt{2}\pi\varepsilon^2(k_BT)^{3/2}}{3q^3N_I(m^*)^{1/2}}\left[\frac{\int_0^\infty \frac{df_0(\eta)}{d\eta}\frac{1+3s\eta}{1+12s\eta}(ln(1+\beta^2)-\frac{\beta^2}{1+\beta^2})^{-1}\eta^3 d\eta}{F_{1/2}(\eta_F)+\frac{5}{2}sF_{3/2}(\eta_F)}\right] \quad \text{Eq. 6-29}$$

$$\beta^2 = \frac{16m^*\varepsilon(k_BT)^2}{q^2\hbar^2 n}\eta(1+s\eta)\left(\frac{F_{1/2}(\eta_F)+\frac{5}{2}sF_{3/2}(\eta_F)}{F_{-1/2}(\eta_F)+\frac{15}{2}sF_{3/2}(\eta_F)}\right), f_0(\eta) = \frac{1}{e^{\eta-\eta_F}-1}$$

where ε is permittivity, η_F is the normalized Fermi energy (E_F/k_BT), $F_j(\eta_F)$ is the Fermi integral of order j, $s = (\alpha/E_g)k_BT$ is a factor for nonparabolicity, and α is the dimensionless nonparabolicity coefficient. The formula can be applied in a wider density range from non-degeneracy ($\eta_F \ll 0$) and strong degeneracy ($\eta_F \gg 0$).

In GeSn, the first-order nonparabolicity of the conduction band at Γ (α_Γ) and L (α_L) valleys can be approximated by the following expressions [144]

$$\alpha_\Gamma \approx \frac{1}{E_\Gamma}(1-\frac{m_\Gamma}{m_0})^2 \text{ and } \alpha_L \approx \frac{1}{E_L} \quad \text{Eq. 6-30}$$

Thus, the adjusted impurity scattering mobility can be adopted instead of Eq. 6-15 in the GeSn mobility calculation.

6.4.3 Parameters for Mobility Calculation

The alloy composition in $Ge_{1-x}Sn_x$ considered in the calculation is in the range $0 < x$

Table 6-1 Parameters for mobility calculation in GeSn.

Parameter	Ge	Sn
a_0 (Å) [133]	5.6573	6.4892
νs (m/s)	5,400	2,730
ρ (kg/m^3)	5,470	5,769
Acoustic deformation potential for Γ (eV) [133]	5	-6
Acoustic deformation potential for L (eV) [133]	11	-2.14
Optical phonon energy (meV) [133]	37	
Optical deformation potential (eV/cm) [133]	5.5×10^8	
U_{al} [133]	0.788	
ε (ε_0)	16	24
m_Γ (m_0) [2]	$0.0104x^2-0.1308x+0.0416$	
longitudinal $m_{L,l}$ (m_0) [2]	$-0.1770x^2+0.2759x+1.6742$	
transverse $m_{L,t}$ (m_0) [2]	$0.0266\ x^2-0.0447x+0.0914$	

doi:10.6342/NTU202300648

< 0.22. Except the bandgap energy and the electron effective mass for Γ and L valleys, other parameters are calculated by a linear interpolation between Ge and α-Sn, (Table 1 [133]). For some parameters without available data for α-Sn, such as those related to phonon scatterings, the parameter values of Ge were used.

For bandgap energies, the strain effect is also considered in this work. The bandgap energy of strained $Ge_{1-x}Sn_x$ on the $Ge_{1-y}Sn_y$ relaxed buffer (s- $Ge_{1-x}Sn_x$/r-$Ge_{1-y}Sn_y$) is given by the functions of x and y [19]. For the parameters of the effective mass, they are calculated by quadratic equations of Sn fraction x [2], instead of using a linear interpolation in [133] . The quadratic equations for the effective masses (m_Γ, $m_{L,l}$, $m_{L,t}$) are also listed in Table 1. The strain effect on the effective masses is ignored here.

6.4.4 Calculation of Electron Mobility in GeSn

Figure 6-14 (a) and (b) shows mobility of relaxed $Ge_{0.88}Sn_{0.12}$ (E_L-E_Γ=52 meV) with the doping density (N_I=n) of 10^{17} cm^{-3} against temperature for L-valley and G-valley, respectively. For the transport of L-electrons (Figure 6-14 (a)), the acoustic (black) and alloy (orange) scattering dominates the mobility (blue) at a high-temperature range and become less effective with a decreasing temperature. The impurity scattering (purple) become stronger at lower temperatures and dominates the L-mobility below 75 K. While for the transport of Γ-electrons, due to their smaller effective mass, the acoustic and alloy scattering are much weaker than that of the L-electrons. The impurity scattering, which is less dependent on the effective mass (Eq. 6-15), dominates the Γ-mobility (light blue) at all temperatures. The effective GeSn mobility depends on the electron population, where the Γ-population is only 10 % at 300 K and becomes 100 % at a low temperature. Thus, the effective mobility is dominated by the L-mobility at 300 K and by Γ-mobility below 50 K. At higher temperatures, the effective mobility calculated by the bilayer model

doi:10.6342/NTU202300648

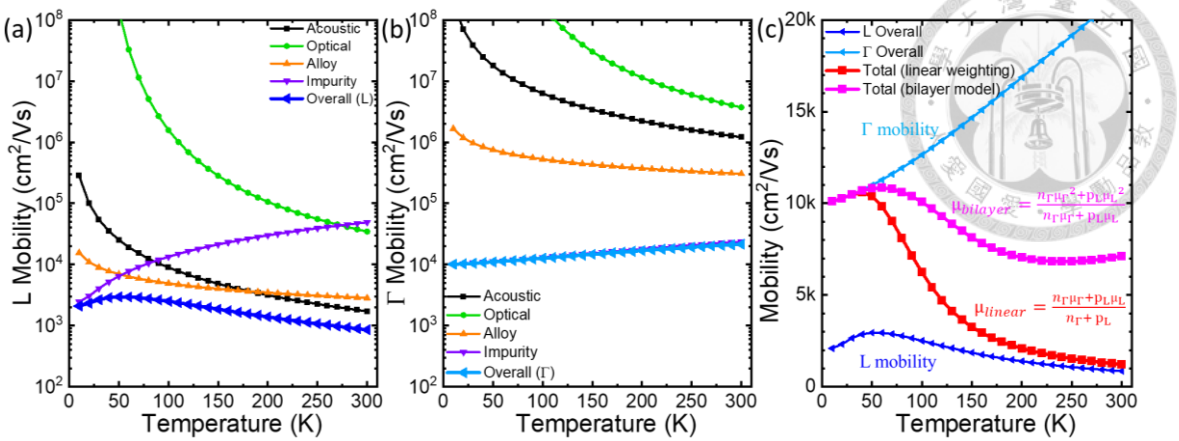

Figure 6-14 Calculated mobility in relaxed $Ge_{0.88}Sn_{0.12}$ with a doping density of 10^{17} cm^{-3} vs. temperature.

(magenta) is higher than that by the linear interpolation (red), since the weighted parameter by the bilayer model is the conductivity ($n_\Gamma \mu_\Gamma$) rather than the carrier density (n_Γ). It is noted that the temperature dependence of effective mobility is much affected by the electron population instead of individual scattering mechanisms for GeSn near a bandgap crossover.

Second, to investigate the effects of the doping density on the GeSn mobility, Figure 6-15 shows the L-, Γ-, and effective mobility versus the doping density in relaxed $Ge_{0.88}Sn_{0.12}$ at 150 K. The impurity mobility (purple) decreases with the density, while the impurity scattering becomes dominant for the L-mobility only as the doping density is

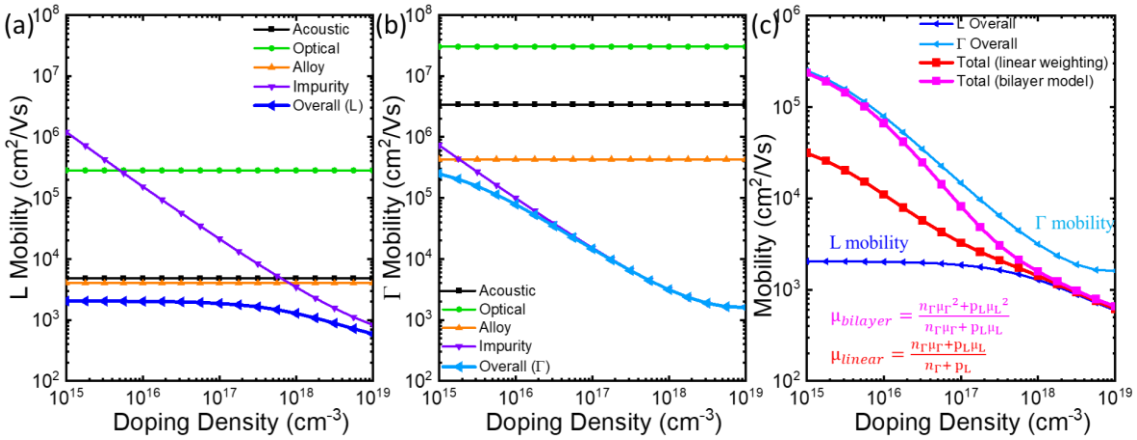

Figure 6-15 Calculated mobility of L-, Γ-, and effective mobility versus doping density in relaxed $Ge_{0.88}Sn_{0.12}$ and at 150 K.

doi:10.6342/NTU202300648

over 10^{18} cm^{-3}. On the other hand, the impurity scattering dominates for the Γ-mobility with the doping densities of $10^{15} \sim 10^{19}$ cm^{-3}. The effective GeSn mobility is dominated by the Γ-mobility for a low doping density regime and by L-mobility for a high doping density regime.

The mobility versus the Sn fraction is shown in Figure 6-16 with a density of 10^{17} cm^{-3} in relaxed $Ge_{1-x}Sn_x$ at 150 K. The crossover of indirect-to-direct bandgap occurs at a Sn fraction of 8.5 % [19]. The mobility contributed by alloy-scattering (orange) decreases with the Sn fraction for both L- and Γ-electrons. Alloy scattering only influences the L-mobility, since the Γ-mobility is dominated by the impurity scattering. A discontinuous point (purple arrow) seems to be observed in Γ-mobility since the Femi level penetrates into the Γ valley after the indirect-to-direct crossover occurs, then the effective mass will be affected by the nonparabolicity and a further adjustment in the impurity scattering formula is needed. Before the crossover occurs ([Sn] < 8%), the effective mobility is dominated by the L-mobility and slightly decreases with higher Sn fraction due to the alloy scattering. After the crossover occurs ([Sn] > 8%), the effective mobility increases rapidly with the Sn fraction due to the increasing Γ-population. For a high-Sn regime ([Sn] > 15%), the effective mobility is determined by Γ-mobility and

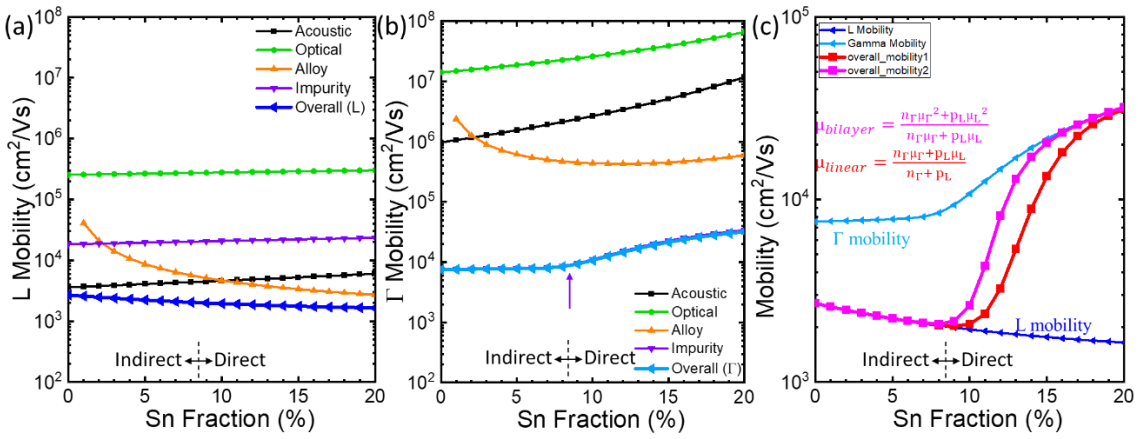

Figure 6-16 Calculated mobility versus Sn fraction in relaxed GeSn with a doping density of 10^{17} cm^{-3} at 150 K.

doi:10.6342/NTU202300648

follows the trend of Γ-mobility.

Last, the mobility in the active GeSn layers under different strain conditions is calculated (Figure 6-17). To avoid the invalidity of the transport equation at T ~ 0 K, the simulated temperature is taken as 77 K. Figure 6-17(a) shows the calculated mobility in compressive-strained $Ge_{1-x}Sn_x$ on Ge VS with different doping densities. The mobility decreases with the Sn fraction due to the alloy scattering. For a higher doping concentration, the mobility reduction by alloy scattering is less pronounced since the impurity scattering becomes dominant (Figure 6-15(a)). Figure 6-17(b) shows the calculated mobility in $Ge_{0.92}Sn_{0.08}$ on different relaxed buffers, where the Sn fraction in the GeSn relaxed buffer is from 0 % to 15 %. The strain condition of the active $Ge_{0.92}Sn_{0.08}$ layer changes from compressive strain to tensile strain (Figure 6-13). The indirect-to-direct transition boosts the overall mobility by 100 times in the doping density of 10^{15} cm^{-3}. The enhancement is limited at a higher doping density, where the enhancement factor is less than 2 in doping density of 10^{19} cm^{-3}. A similar phenomenon is also observed in the experimental data in Figure 6-13.

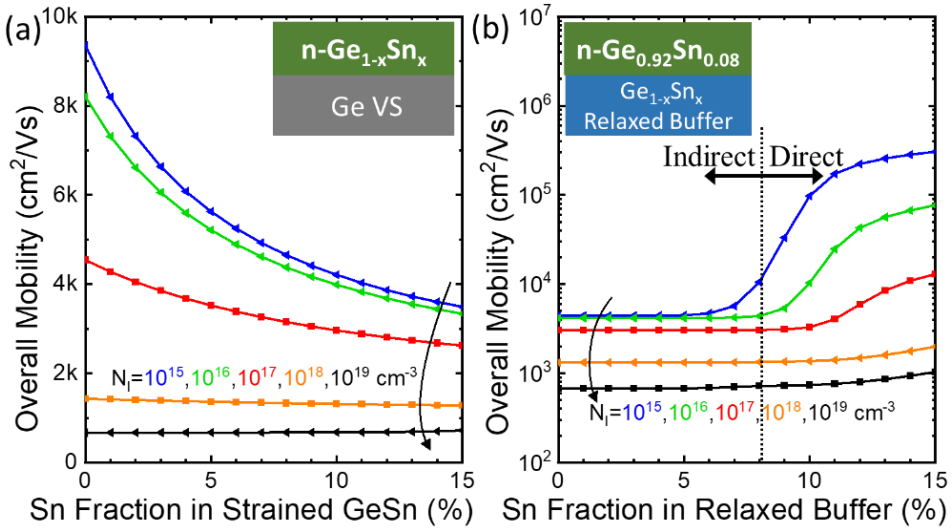

Figure 6-17 Effective electron mobility vs. Sn fraction in (a) compressive-strained $Ge_{1-x}Sn_x$ on Ge VS and (b) strained $Ge_{0.92}Sn_{0.08}$ on different $Ge_{1-x}Sn_x$ relaxed buffers.

doi:10.6342/NTU202300648

Chapter 7 Conclusion and Future Work

7.1 Conclusion

High-quality GeSn epitaxial films on Si substrates were grown by CVD and characterized for their optical, tunneling, and electrical properties. First, the epitaxy technology was developed for a wide range of Sn fraction and different strain conditions in GeSn films. GeSn with a high Sn fraction is systematically investigated for direct-bandgap applications. Low-temperature CVD (< 400 ºC) is adopted to deposit high-quality GeSn films with the help of a Ge VS on a Si wafer. Reducing the growth temperature can further increase the Sn incorporation. For the compressive-strained GeSn on Ge VS, a GeSn film with a Sn fraction up to 18 % was pseudomorphically grown with a large strain of -2.4 %. Growing GeSn films with a higher Sn fraction is limited by large compressive strains and the Sn precipitation. A GeSn relaxed buffer is used to reduce the strain in GeSn active layers and to avoid high TDD due to the strain relaxation. Using a GeSn relaxed buffer, a high Sn fraction of 24 % is achieved in a compressive-strained GeSn film.

PL spectra show the bandgap characteristics in GeSn films. At room temperature, the direct-bandgap energy of GeSn monotonically decreases with the Sn fraction. The smallest bandgap of 0.295 eV is demonstrated in compressive-strained $Ge_{0.76}Sn_{0.24}$, corresponding to a wavelength of 4.2 μm in the MWIR. At cryogenic temperatures, the PL spectra of GeSn with a low Sn fraction (≦ 8 %), the emission peak from the lower-energy L valley dominants, which suggests those GeSn films are still indirect-bandgap materials. Via the strain relaxation or increasing the Sn fraction in GeSn, the L-valley emission becomes weaker due to the small energy difference (E_Γ-E_L), which suggests the indirect-to-direct bandgap transition occurs at a Sn fraction of ~ 8 %.

doi:10.6342/NTU202300648

High-performance GeSn Esaki diodes under different strain conditions are demonstrated with clear NDR and high PVCR's. At room temperature, a very high PVCR of 15 is achieved in a strain-relaxed $Ge_{0.925}Sn_{0.075}$ Esaki diode. An extremely high PVCR of 219 is also achieved at 4 K, the highest reported among all Esaki diodes. The tunneling current is significantly increased by applying tensile stresses on the $Ge_{0.925}Sn_{0.075}$ films. Record-high peak current densities of 325 and 545 kA/cm^2 are demonstrated in the tensile-strained $Ge_{0.925}Sn_{0.075}$ diodes at RT and 4 K, respectively. The temperature-dependence of the peak current density suggests that more Γ-electrons participate in the BTBT process by applying tensile stresses. The phonon-assisted tunneling spectra in Ge and GeSn Esaki diodes also suggest the tensile-strained $Ge_{0.925}Sn_{0.075}$ film has a direct bandgap.

Last, electron mobilities in GeSn are characterized by low-temperature Hall measurements. The highest Hall mobility is 9,500 cm^2/Vs at 75 K in $Ge_{0.82}Sn_{0.18}$. With a similar doping density, the electron mobility at 4 K decreases with the Sn fraction ([Sn] < 8%) due to the dominant alloy scattering effects on the L-electron mobility. For the Sn fraction higher than 8 %, the mobility increases significantly with the Sn fraction or by strain relaxation or applying tensile stresses, which suggests more Γ-electrons with a much smaller effective mass contribute to the carrier transport. The theoretical calculation on the electron mobility in GeSn is also presented by the consideration of various scattering mechanisms and the electron population in Γ and L valleys. The calculation results support the experimental results and suggest the effective electron mobility in GeSn can be greatly enhanced by engineering the bandgap characteristics.

doi:10.6342/NTU202300648

7.2 Future Work

Some aspects of considerable interest about the topics in this dissertation are given as follows:

(i) GeSn epitaxy by CVD

In Chapter 2, the highest Sn fraction of 24 % is achieved in compressive strained $Ge_{0.76}Sn_{0.24}$ on a relaxed $Ge_{0.88}Sn_{0.12}$ buffer with the corresponding MWIR emission at 4.2 μm in Chapter 3. The strain relaxation of $Ge_{0.76}Sn_{0.24}$ or further increasing the Sn fraction over 30 % is considered to reach the LWIR band. Based on our CVD results, the GeSn growth under a further low temperature (< 280 °C) seem to have some limits due to serious Sn precipitation for a higher Sn fraction. The GeSn relaxed buffer with higher relaxation rate might help to further increase the Sn fraction in the active GeSn layer.

(ii) GeSn tunneling devices

The outstanding performance of GeSn Esaki diodes motivates the high drive current in GeSn TFETs. There is no report on any Si-based TFET with a high drive current as high as 100 μA/μm and a sharp sub-threshold slope of < 60 mV/decade at the same time. Our results on strain-relaxed and tensile-strained $Ge_{0.925}Sn_{0.075}$ Esaki diodes suggest that the boosted BTBT current and high PVCR is achieved at the same time due to the high-quality GeSn films. Future work on GeSn TFETs is expected with high potential, even without the request of higher Sn fraction.

(iii) GeSn carrier transport

The electron mobility enhancement due to direct-bandgap transition is presented in Chapter 6. However, due to the limit from our epitaxial structure, the electron mobility can only be studied at a rather high doping level ~ 5×10^{17} cm^{-3} and at low temperatures.

doi:10.6342/NTU202300648

Based on the prediction by the simulation results [133], the electron mobility is expected to be much higher (more than one order) with a lower doping level. Further work is required to investigate the limiting mechanisms on the electron mobility in the future.

doi:10.6342/NTU202300648

Appendix A

Parameters for NL-EPM Simulation				
Parameter	Symbol	Unit	Ge	Sn
Form factors[1]	V_3	R_y	-0.2378	-0.21
	V_8	R_y	0.02852	0.02359
	V_{11}	R_y	0.0469	0.01737
s-well radius[1]	R_0	A	0.0	1.0
d-well radius[1]	R_2	A	1.2788	1.453
s-well depth[1]	α_0	R_y	0.0	0.0
d-well depth[1]	α_2	R_y	0.309	0.71
s-well energy dependence[1]	β_0	1	0.0	0.365
Spin-orbit parameters[1]	μ_{LS}	R_y	0.00093	0.00225
	ζ_{LS}	1/Bohr radius	5.34	3.97
Lattice constant[2]	a_0	A	5.65	6.489
Elastic constants[2]	c_{11}	10^{11} Pa	1.287	0.690
	c_{12}	10^{11} Pa	0.477	0.293
	c_{44}	10^{11} Pa	0.667	0.362
Internal displacement parameter[2]	ζ	1	0.440	0.548

Table I

1. Santa, S. & Schenk, A. Pseudopotential calculations of strained-GeSn/SiGeSn hetero-structures. Appl. Phys. Lett. 105, 162101 (2014)

2. Liu, L., Liang, R., Wang, J. & Xu, J. Enhanced carrier mobility and direct tunneling probability of biaxially strained $Ge_{1-x}Sn_x$ alloys for field-effect transistors applications. J. Appl. Phys. 117, 184501 (2015).

doi:10.6342/NTU202300648

Reference

[1] O. Moutanabbir, S. Assali, X. Gong, E. O'Reilly, C. A. Broderick, B. Marzban, J. Witzens, W. Du, S-Q. Yu, A. Chelnokov, D. Buca, and D. Nam, "Monolithic infrared silicon photonics: The rise of (Si)GeSn semiconductors," *Applied Physics Letters*, vol. 118, no. 11, pp. 110502, 2021.

[2] L. Liu, R. Liang, J.Wang, and J. Xu, "Investigation on the effective mass of $Ge_{1-x}Sn_x$ alloys and the transferred-electron effect," *Applied Physics Express*, vol. 8, no. 3, pp. 031301, 2015

[3] H. S. Lan, S. T. Chang, and C. W. Liu, "Semiconductor, topological semimetal, indirect semimetal, and topological Dirac semimetal phases of $Ge_{1-x}Sn_x$ alloys," *Physical Review B*, vol. 95, no. 20, pp. 201201, 2017.

[4] G. E. Chang, S. Q. Yu, J. Liu, H. H. Cheng, R. A. Soref, and G, Sun, "Achievable Performance of Uncooled Homojunction GeSn Mid-Infrared Photodetectors," *IEEE Journal of Selected Topics in Quantum Electronics*, vol. 28, no. 2, pp. 1-11, 2021.

[5] R. Pillarisetty, "Academic and Industry Research Progress in Germanium Nanodevices," *Nature*, vol. 479, no. 7373, pp. 324-328, 2011.

[6] K. L. Low, Y. Yang, G. Han, W. Fan, and Y. C. Yeo, "Electronic Band Structure and Effective Mass Parameters of $Ge_{1-x}Sn_x$ Alloys," *Journal of Applied Physics*, vol. 112, no. 10, pp. 103715, 2012.

[7] S. Gupta, Y. C. Huang, Y. Kim, E. Sanchez, and K. C. Saraswat, "Hole Mobility Enhancement in Compressively Strained $Ge_{0.93}Sn_{0.07}$ pMOSFETs," *IEEE Electron Device Letters*, vol. 34, no. 7, pp. 831-833, 2013.

[8] S. Mukhopadhyay, B. Mukhopadhyay, G. Sen, and P. K. Basu, "Maximum theoretical electron mobility in n-type $Ge_{1-x}Sn_x$ due to minimum doping

doi:10.6342/NTU202300648

requirement set by intrinsic carrier density," *Journal of Computational Electronics,* vol. 20, no. 1, pp. 274-279, 2021.

[9] J. D. Sau and M. L. Cohen, "Possibility of increased mobility in Ge-Sn alloy system," *Physical Review B*, vol. 75, no. 4, pp. 045208, 2007.

[10] Y. Yang, G. Han, P. Guo, W. Wang, X. Gong, L. Wang, K. L. Low, and Y. C. Yeo, "Germanium–Tin P-Channel Tunneling Field-Effect Transistor: Device Design and Technology Demonstration," *IEEE Transactions on Electron Devices*, vol. 60, no. 12, pp. 4048-4056, 2013.

[11] A. Marchionni, C. Zucchetti, F. Ciccacci, M. Finazzi, H. S. Funk, D. Schwarz, M. Oehme, J. Schulze, and F. Bottegoni, "Inverse spin-Hall effect in GeSn," *Applied Physics Letters*, vol. 118, no. 21, pp. 212402, 2021.

[12] G. Han, Y. Wang, Y. Liu, C. Zhang, Q. Feng, M. Liu, S. Zhao, B. Cheng, J. Zhang, and Y. Hao, "GeSn Quantum Well P-Channel Tunneling FETs Fabricated on Si(001) and (111) With Improved Subthreshold Swing," *IEEE Electron Device Letters*, vol. 37, no. 6, pp. 701-704, 2016.

[13] L. Jin, H. Zhu, D. Zhang, B. Liu, H. Meng, X. Tang, M. Li, Z. Zhong, and H. Zhang, "Spin pumping and laser modulated inverse spin Hall effect in yttrium iron garnet/germanium heterojunctions," *Applied Physics Letters*, vol. 116, no. 12, pp. 122405, 2020.

[14] C. Kloeffel and D. Loss, "Prospects for Spin-Based Quantum Computing in Quantum Dots," *Annual Review of Condensed Matter Physics*, vol. 4, no. 1, pp. 51-81, 2013.

[15] C. T. Tai, P. Y. Chiu, C. Y. Liu, H. S. Kao, C. T. Harris, T. M. Lu, C. T. Hsieh, S. W. Chang, and J. Y. Li, "Strain effects on Rashba spin-orbit coupling of two-dimensional hole gases in GeSn/Ge heterostructures," *Advanced Materials*, vol. 33,

doi:10.6342/NTU202300648

no. 26, p. 2007862, 2021.

[16] Y. Gul, S. N. Holmes, P. J. Newton, D. J. P. Ellis, C. Morrison, M. Pepper, C. H. W. Barnes, and M. Myronov, “Quantum ballistic transport in strained epitaxial germanium,” *Applied Physics Letters*, vol. 111, no. 23, pp. 233512, 2017.

[17] E. J. Connors , JJ Nelson, and J. M. Nichol, “Rapid High-Fidelity Spin-State Readout in Si/Si-Ge Quantum Dots via rf Reflectometry,” *Physical Review Applied*, vol. 13, no. 2, pp. 024019, 2020.

[18] S. Gupta, B. Magyari-Köpe, Y. Nishi, and K. C. Saraswat, "Achieving Direct Band Gap in Germanium Through Integration of Sn Alloying and External Strain," *Journal of Applied Physics*, vol. 113, no. 7, pp. 073707, 2013.

[19] H. S. Lan, and C. W. Liu, “Band alignments at strained $Ge_{1-x}Sn_x$ /relaxed $Ge_{1-y}Sn_y$ heterointerfaces,” *Journal of Physics D: Applied Physics*, vol. 50, no. 13, pp. 13LT02, 2017

[20] R. W. Olesinski and G. J. Abbaschian, "The Ge−Sn (Germanium−Tin) System," *Bulletin of Alloy Phase Diagrams*, vol. 5, no. 3, pp. 265-271, 1984.

[21] H. Groiss M. Glaser, M. Schatzl, M. Brehm, D. Gerthsen, D. Roth, P. Bauer, and F. Schäffler, “Free-running Sn precipitates: an efficient phase separation mechanism for metastable $Ge_{1-x}Sn_x$ epilayers,” *Scientific Reports*, vol. 7, no. 1, pp. 16114, 2017.

[22] C. Schulte-Braucks, N. Driesch, S. Glass, A. T. Tiedemann, U. Breuer, A. Besmehn, J. M. Hartmann, Z. Ikonic, Q. T. Zhao, S. Mantl, and D. Buca, “Low Temperature Deposition of High-k/Metal Gate Stacks on HighSn Content (Si)GeSn-Alloys,” *ACS Applied Materials & Interfaces*, vol. 8, no. 20, pp. 13133-13139, 2016.

[23] W. Wang, Q. Zhou, Y. Dong, E. S. Tok, and Y. Ch. Yeo, “Critical thickness for strain relaxation of $Ge_{1-x}Sn_x$ ($x \leq 0.17$) grown by molecular beam epitaxy on Ge(001),” *Applied Physics Letters*, vol. 106, no. 23, pp. 232106, 2015.

doi:10.6342/NTU202300648

[24] R. Khazaka , E. Nolot, J. Aubin, and J. M. Hartmann, “Growth and characterization of SiGeSn pseudomorphic layers on 200mm Ge virtual substrates,” *Semiconductor Science and Technology*, vol. 33, no. 12, pp. 124011, 2018.

[25] A. Elbaz, D. Buca, N. Driesch, K. Pantzas, G. Patriarche, N. Zerounian, E. Herth, X. Checoury, S. Sauvage, I. Sagnes, A. Foti, R. Ossikovski, J. M. Hartmann, F. Boeuf, Z. Ikonic, P. Boucaud, D. Grützmacher, and M. E. Kurdi, “Ultra-low-threshold continuous-wave and pulsed lasing in tensile-strained GeSn alloys,” *Nature Photonics*, vol. 14, no. 6, pp. 375-382, 2020.

[26] J. Chretien, N. Pauc, F. A. Pilon, M. Bertrand, Q. M. Thai, L. Casiez, N. Bernier, H. Dansas, P. Gergaud, E. Delamadeleine, R. Khazaka, H. Sigg, J. Faist, A. Chelnokov, V. Reboud, J. M. Hartmann, and V. Calvo “GeSn Lasers Covering a Wide Wavelength Range Thanks to Uniaxial Tensile Strain,” *ACS Photonics*, vol. 6, no. 10, pp. 2462-2469, 2019.

[27] Y.-S. Huang, F.-L. Lu, Y.-J. Tsou, C.-E. Tsai, C.-Y. Lin, C.-H. Huang, and C. W. Liu, "First Vertically Stacked GeSn Nanowire pGAAFETs with I_{on}=1850 μA/μm (V_{ov} = V_{ds}=-1V) on Si by GeSn/Ge CVD Epitaxial Growth and Optimum Selective Etching," *2017 IEEE International Electron Devices Meeting*, pp. 37.5.1-37.5.4, 2017.

[28] I. Dascalescu, N. C. Zoita, A. Slav, E. Matei, S. Iftimie, F. Comanescu, A. M. Lepadatu, C. Palade, S. Lazanu, D. Buca, V. S. Teodorescu, M. L. Ciurea, M. Braic, and T. Stoica, “Epitaxial GeSn Obtained by High Power Impulse Magnetron Sputtering and the Heterojunction with Embedded GeSn Nanocrystals for Shortwave Infrared Detection,” *ACS Applied Materials & Interfaces*, vol. 12, no. 30, pp. 33879-33886, 2020.

[29] F. Gencarelli, B. Vincent, L. Souriau, O. Richard, W. Vandervorst, R. Loo, M.

doi:10.6342/NTU202300648

Caymax, M. Heyns, “Low-temperature Ge and GeSn Chemical Vapor Deposition using Ge_2H_6,” *Thin Solid Films*, vol. 520, no. 8, pp. 3211-3215, 2012.

[30] W. Wegscheider, J. Olajos, U. Menczigar, W. Dondl, and G. Abstreiter, “Fabrication and properties of epitaxially stabilized Ge/α-Sn heterostructures on Ge(001),” *Journal of Crystal Growth*, vol. 123, no. 1-2, pp. 75-94, 1992.

[31] H. Wang, G. Zhang, Y. Chen, J. Zhang, K. Han, Y. C. Huang, and X. Gong, “First Monolithic Integration of Group IV Waveguide Photodetectors and Modulators on 300 mm Si Substrates for 2-μm Wavelength Optoelectronic Integrated Circuit,” *2022 IEEE Symposium on VLSI Technology and Circuits*, pp. 407-408, 2022.

[32] P. C. Grant, W. Dou, B. Alharthi, J. M. Grant, H. Tran, G. Abernathy, A. Mosleh, W. Du, B. Li, M. Mortazavi, H. A. Naseem, and S. Q. Yu, “UHV-CVD Growth of High Quality GeSn Using $SnCl_4$: From Growth Optimization to Prototype Devices,” *Optical Materials Express*, vol. 9, no. 8, pp. 3277-3291, 2019.

[33] J. C. Sturm and K. H. Chung, "Chemical vapor deposition epitaxy of silicon-based materials using neopentasilane." *ECS Transactions*, vol. 16, no. 10, pp. 799-805, 2008.

[34] S. Wirths, D. Buca, G. Mussler, A. T. Tiedemann, B. Holländer, P. Bernardy, T. Stoica, D. Grützmacher, and S. Mantl, "Reduced Pressure CVD Growth of Ge and $Ge_{1-x}Sn_x$ Alloys," *ECS Journal of Solid State Science and Technology*, vol. 2, no. 5, pp. N99-N102, 2013.

[35] J. Aubin, J. M. Hartmann, M. Bauer, and S. Moffatt, "Very Low Temperature Epitaxy of Ge and Ge Rich SiGe Alloys with Ge_2H_6 in a Reduced Pressure-Chemical Vapour Deposition Tool," *Journal of Crystal Growth*, vol. 445, pp. 65-72, 2016.

[36] A. Mosleh, M. Alher, L. C. Cousar, W. Du, S. A. Ghetmiri, S. Al-Kabi, W. Dou,

doi:10.6342/NTU202300648

Perry C. Grant, G. Sun, R. A. Soref, B. Li, H. A. Naseem, and S. Q. Yu, "Buffer-Free GeSn and SiGeSn Growth on Si Substrate Using In Situ SnD_4 Gas Mixing," *Journal of Electronic Materials*, vol. 45, no. 4, p. 2051–2058, 2016.

[37] R. F. Spohn and C. B. Richenburg, "Tin Deuteride (SnD_4) Stabilization." *ECS Transactions*, vol. 50, no. 9, pp. 921-927, 2012

[38] D. R. Stull, "Vapor Pressure of Pure Substances. Organic and Inorganic Compounds," *Industrial & Engineering Chemistry*, vol. 39, no. 4, pp. 517-540, 1947.

[39] A. Mosleh, M. A. Alhe, L. C. Cousar, W. Du, S. A. Ghetmiri,T. Pham, J. M. Grant, G. Sun, R. A. Soref, B. Li, H. A. Naseem, and S.-Q. Yu, "Direct growth of $Ge_{1-x}Sn_x$ films on Si using a cold-wall ultra-high vacuum chemical-vapor-deposition system," *Frontiers in Materials*, vol. 2, no. 30, 2015.

[40] J. Nicolas, S. Assali, S. Mukherjee, A. Lotnyk, and O. Moutanabbir, "Dislocation Pipe Diffusion and Solute Segregation during the Growth of Metastable GeSn," *Crystal Growth & Design*, vol. 20, no. 5, pp. 3493–3498, 2020.

[41] D. J. Eaglesham and M. Cerullo, "Dislocation-free Stranski-Krastanow growth of Ge on Si(100)," *Physical Review Letters*, vol. 64, no. 16, pp. 1943-1946, 1990.

[42] S. Kobayashi, Y. Nishi, and K. C. Saraswat, "Effect of isochronal hydrogen annealing on surface roughness and threading dislocation density of epitaxial Ge films grown on Si, " *Thin Solid Films*, vol. 518, no. 6, pp. S136-S139, 2010.

[43] V. A. Shah, A. Dobbie, M. Myronov, and D.R. Leadley, "Effect of layer thickness on structural quality of Ge epilayers grown directly on Si(001)," *Thin Solid Films*, vol. 519, no. 22, pp. 7911-7917, 2011.

[44] M. T. Currie, S. B. Samavedam, T. A. Langdo, C. W. Leitz, and E. A. Fitzgerald, "Controlling threading dislocation densities in Ge on Si using graded SiGe layers

doi:10.6342/NTU202300648

and chemical-mechanical polishing," *Applied Physics Letters*, vol. 72, no. 14, pp. 1718-1720, 1998.

[45] D. Choi, Y. Ge, J. S. Harris, J. Cagnon, and S. Stemmer, "Low surface roughness and threading dislocation density Ge growth on Si (001)," *Journal of Crystal Growth*, vol. 310, no. 18, pp. 4273-4279, 2008.

[46] D. Chen, Z. Xue, X. Wei, G. Wang, L. Ye, M. Zhang, D. Wang, and S. Liu, "Ultralow temperature ramping rate of LT to HT for the growth of high quality Ge epilayer on Si (100) by RPCVD," *Applied Surface Science*, vol. 299, pp. 1-5, 2014.

[47] A. Mosleh, S. A. Ghetmiri, B. R. Conley, M.Hawkridge, M. Benamara, A. Nazzal, J. Tolle, S. Q. Yu, and H. A. Naseem, "Material Characterization of $Ge_{1-x}Sn_x$ Alloys Grown by a Commercial CVD System for Optoelectronic Device Applications," *Journal of Electronic Materials*, vol 43, no. 4, pp. 938–946, 2014.

[48] H. Cai, K. Qian, Y. An, G. Lin, S. Wu, H. Ding, W. Huang, S.Chen, J. Wang, and C. Li, "Thickness-dependent behavior of strain relaxation and Sn segregation of GeSn epilayer during rapid thermal annealing," *Journal of Alloys and Compounds*, vol. 904, pp. 164068, 2022.

[49] J. W. Matthews and A. E. Blakeslee, "Defects in epitaxial multilayers: I. Misfit dislocations," *Journal of Crystal Growth*, vol. 27, pp. 118–125, 1974.

[50] R. People and J. C. Bean, "Calculation of critical layer thickness versus lattice mismatch for Ge_xSi_{1-x}/Si strained-layer heterostructures," *Applied Physics Letters*, vol. 47, no. 3, pp. 322–324, 1985

[51] P. Kidd, D. J. Dunstan, H. G. Colson, M. A. Louren, A. Sacedo, F. G. Sanz, L. Gonzalez, Y. Gonzalez, R. Garcia, D. Gonzalez, F. J. Pacheco, and P. J. Goodhew, "Comparison of the crystalline quality of step-graded and continuously graded InGaAs buffer layers," *Journal of Crystal Growth*, vol. 169, no. 4, pp. 649-659,

doi:10.6342/NTU202300648

1996.

[52] M. S. Abrahams, L. R. Weisberg, C. J. Buiocchi, and J. Blanc, “Dislocation morphology in graded heterojunctions: $GaAs_{1-x}P_x$,” *Journal of Materials Science*, vol. 4, pp. 223–235, 1969.

[53] E. A. Fitzgerald, A.Y. Kim, M.T. Currie, T. A. Langdo, G. Taraschi, and M.T. Bulsara, “Dislocation dynamics in relaxed graded composition semiconductors,” *Materials Science and Engineering:B*, vol. 67, no. 1-2, pp. 53–64, 1999.

[54] M. Albrecht, S. Christiansen, J. Michler, W. Dorsch, and H. P. Strunk, “Surface ripples, crosshatch pattern, and dislocation formation: Cooperating mechanisms in lattice mismatch relaxation,” *Applied Physics Letters*, vol. 67, no.9, pp. 1232-1234, 1995.

[55] J. Aubin and J. M. Hartmann, "GeSn Growth Kinetics in Reduced Pressure Chemical Vapor Deposition from Ge_2H_6 and $SnCl_4$," *Journal of Crystal Growth*, vol. 482, pp. 30-35, 2018.

[56] K. Tamaru, "The Thermal Decomposition of Tin Hydride." *The Journal of Physical Chemistry*, vol. 60, no. 5, pp. 610-612, 1956.

[57] W. Dou, M. Benamara, A. Mosleh, J. Margetis, P. Grant, Y. Zhou, S. Al-Kabi, W. Du, J. Tolle, B. Li, M. Mortazavi, and S. Q. Yu, "Investigation of GeSn Strain Relaxation and Spontaneous Composition Gradient for Low-Defect and High-Sn Alloy Growth," *Scientific Reports*, vol. 8, no. 1, pp. 1-11, 2018.

[58] S. Assali, J. Nicolas, and O. Moutanabbir, “Enhanced Sn incorporation in GeSn epitaxial semiconductors via strain relaxation,” *Journal of Applied Physics*, vol. 125, no. 2, pp. 025304, 2019.

[59] M. Nakamura, Y. Shimura, S. Takeuchi, O. Nakatsuka, and S. Zaima, “Growth of $Ge_{1-x}Sn_x$ heteroepitaxial layers with very high Sn contents on InP(001) substrates,”

doi:10.6342/NTU202300648

Thin Solid Films, vol. 520, no. 8, pp. 3201-3205, 2012.

[60] J. A. Nelson, “The Physics of Solar Cells,” World Scientific Publishing Company, 2003.

[61] X. Sun, J. Liu, L. C. Kimerling, and J. Michel, “Direct gap photoluminescence of *n*-type tensile-strained Ge-on-Si,” *Applied Physics Letters*, vol. 95, no.1, pp. 011911, 2009.

[62] S. A. Ghetmiri, W. Du, B. R. Conley, and A. Mosleh, “Shortwave-infrared photoluminescence from $Ge_{1-x}Sn_x$ thin films on silicon,” *Journal of Vacuum Science & Technology B*, vol. 32, no. 6, pp. 060601, 2014.

[63] C. Wang, B.Wang, R. I. Made, S. F. Yoon, and J. Michel, “Direct bandgap photoluminescence from n-type indirect GaInP alloys,” *Photonics Research*, vol. 5, no. 3, pp. 239-244, 2017.

[64] S. A. Ghetmiri, W. Du, J. Margetis, A. Mosleh, L. Cousar, B. R. Conley, L. Domulevicz, A. Nazzal, G. Sun, R. A. Soref, J. Tolle, B. Li, H. A. Naseem, and S.-Q. Yu, "Direct-Bandgap GeSn Grown on Silicon with 2230 nm Photoluminescence," *Applied Physics Letters*, vol. 105, no. 15, pp. 151109, 2014.

[65] https://www.edmundoptics.com.tw/f/ig6-ir-aspheric-lenses/14800/

[66] S. Q. Yu, S. A. Ghetmiri, W. Du, J. Margetis, Y. Zhou, Aboozar Mosleh, S. Al-Kabi, A. Nazzal, G. Sun, Richard A. Soref, J. Tolle, B. Li, H. A. Naseem, “Si based GeSn light emitter: mid-infrared devices in Si photonics,” *Silicon Photonics X. SPIE*, vol. 9367, pp. 146-153, 2015.

[67] S. Assali, J. Nicolas, S. Mukherjee, A. Dijkstra, and O. Moutanabbir, “Atomically uniform Sn-rich GeSn semiconductors with 3.0–3.5 μm room-temperature optical emission,” *Applied Physics Letters*, vol. 112, no. 25, pp. 251903, 2018.

[68] M. Kittler, T. Arguirov, M. Oehme, Y. Yamamoto, B. Tillack, and N. V. Abrosimov,

doi:10.6342/NTU202300648

"Photoluminescence study of Ge containing crystal defects," *Physica Status Solidi a*, vol. 208, no.4, pp. 754-759, 2011.

[69] T. Liu, L. Wang, G. Zhu, X. Hu, Z. Dong, Z. Zhong, Q. Jia, X. Yang, and Z. Jiang, "Dislocation-related photoluminescence of GeSn films grown on Ge (001) substrates by molecular beam epitaxy," *Semiconductor Science and Technology*, vol. 33, no. 12, pp. 125022, 2018.

[70] A. Vossier, F. Gualdi, A. Dollet, R. Ares, and V. Aimez, "Approaching the Shockley-Queisser limit: General assessment of the main limiting mechanisms in photovoltaic cells," *Journal of Applied Physics*, vol. 117, no. 1, pp. 015102, 2015.

[71] G. Sun, R. A. Soref, and H. H. Cheng, "Design of an electrically pumped SiGeSn/GeSn/SiGeSn double-heterostructure midinfrared laser," *Journal of Applied Physics*, vol. 108, no. 3, pp. 033107, 2010.

[72] P. W. Yu, and Y. S. Park, "Temperature dependence of photoluminescence from Mg-implanted GaAs," *Journal of Applied Physics*, vol. 48, no. 6, pp. 2434-2441, 1977.

[73] W. S. Yoo, K. Kang, G. Murai, and M. Yoshimoto, "Temperature Dependence of Photoluminescence Spectra from Crystalline Silicon," *ECS Journal of Solid State Science and Technology*, vol. 4, no. 12, pp. P456, 2015.

[74] M. E. Kurdi, G. Fishman, S. Sauvage, and P. Boucaud, "Band structure and optical gain of tensile-strained germanium based on a 30 band k· p formalism," *Journal of Applied Physics*, vol. 107, no. 1, pp. 013710, 2010.

[75] https://cleanroom.byu.edu/opticalcalc/

[76] D. A. Neaman, "Semiconductor physics and devices 4th edition," McGraw-Hill, 2011.

[77] D. M. Wieliczka, S. Weng, and M. R. Querry, "Wedge shaped cell for highly absorbent liquids: infrared optical constants of water," *Applied Optics*, vol. 28, no.

doi:10.6342/NTU202300648

9, pp. 1714-1719, 1989.

[78] https://webbook.nist.gov/cgi/cbook.cgi?ID=C124389&Units=SI&Mask=80#IR-Spec/

[79] K. Gopalakrishnan, P. Griffin, and J. Plummer, "I-MOS: a novel semiconductor device with a subthreshold slope lower than kT/q," *Digest. International Electron Devices Meeting*, pp. 289-292, 2002.

[80] A. Saeidi, F. Jazaeri, I. Stolichnov, C. C. Enz, and A. M. Ionescu, "Negative Capacitance as Universal Digital and Analog Performance Booster for Complementary MOS Transistors," *Scientific Reports*, vol. 9, pp. 9105, 2019.

[81] A. M. Ionescu, and H. Riel, "Tunnel field-effect transistors as energy-efficient electronic switches," *Nature*, vol. 479, pp. 329-337, 2011.

[82] S. Ahmad, N. Alam, and M. Hasan, "Robust TFET SRAM cell for ultra-low power IoT application," *2017 International Conference on Electron Devices and Solid-State Circuits*, pp. 1-2, 2017.

[83] A. G. Chynoweth, R. A. Logan, and D. E. Thomas, "Phonon-Assisted Tunneling in Silicon and Germanium Esaki Junctions," *Physical Review*, vol. 125 , no. 3, pp. 877-881, 1962.

[84] R. A. Logan, J. M. Rowell, and F. A. Trumbore, "Phonon Spectra of Ge-Si Alloys," *Physical Review*, vol. 136 , no. 6A, pp. 1751, 1964.

[85] C. Schulte-Braucks, D. Stange, N. Driesch, S. Blaeser, Z. Ikonic, J. M. Hartmann, S. Mantl, and D. Buca, "Negative differential resistance in direct bandgap GeSn p-i-n structures," *Applied Physics Letters*, vol. 107 , no. 4, pp. 042101, 2015.

[86] L. Esaki, "New Phenomenon in Narrow Germanium p-n Junctions," *Physical Review*, vol. 109, no. 2, pp. 603, 1958.

[87] K. Ismail, B. S. Meyerson, and P. J. Wang, "Electron resonant tunneling in Si/SiGe

doi:10.6342/NTU202300648

double barrier diodes," *Applied Physics Letters*, vol. 59, no.8 , pp. 973-975, 1991.

[88] N. Jin, S. Y. Chung, A. T. Rice, and P. R. Berger, "151 kA/cm^2 peak current densities in Si/SiGe resonant interband tunneling diodes for high-power mixed-signal applications," *Applied Physics Letters*, vol. 83, no. 16, pp. 3308-3310, 2003.

[89] Y. Furukawa, "Magnetoresistance in Heavily Doped n-Type Germanium," *Journal of the Physical Society of Japan*, vol. 17, no. 4, pp. 630-638, 1962.

[90] E. O. Kane, "Theory of tunneling," *Journal of Applied Physics*, vol. 32, pp. 83-91, 1961.

[91] S. M. Sze and K. K. Ng, "Physics of Semiconductor Devices," Wiley, 2006.

[92] M. Dietrich, G. A. Brown, and H. S. Sommers Jr., "Degenerate germanium. I. Tunnel, excess, and thermal current in tunnel diodes." *Physical Review*, vol. 126, no. 4, pp. 1329, 1962.

[93] A. G. Chynoweth, W. L. Feldmann, and R. A. Logan, "Excess tunnel current in silicon Esaki junctions," *Physical Review*, vol. 121, no. 3, pp. 684-694, 1961.

[94] R. A. Logan, and A. G. Chynoweth. "Effect of degenerate semiconductor band structure on current-voltage characteristics of silicon tunnel diodes." *Physical Review*, vol. 131, no. 1, pp. 89, 1963.

[95] D. K. Roy, "On the Separation of the Phonon-Assisted Current Components in Germanium Tunnel Diodes," *Physica Status Solidi*, vol. 8, pp. K75-79, 1968.

[96] K. H. Kao, A. S. Verhulst, W. G. Vandenberghe, B. Soree, G. Groeseneken, and K. D. Meyer, "Direct and Indirect Band-to-Band Tunneling in Germanium-Based TFETs," *IEEE Transactions on Electron Devices*, vol. 59, no. 2, pp. 292-301, 2012.

[97] C. E. Tsai, F. L. Lu, P. S. Chen, C. W. Liu, "Boron-doping induced Sn loss in GeSn alloys grown by chemical vapor deposition," *Thin Solid Films*, vol. 660, pp. 263-266, 2018.

doi:10.6342/NTU202300648

[98] M. Frauenrath, V. Kiyek, N. Driesch, M. Veillerot, E. Nolot, D. Buca, and J. M. Hartmann, “An In-Depth Study of the Boron and Phosphorous Doping of GeSn,” *ECS Journal of Solid State Science and Technology*, vol. 10, no. 8, pp. 085006, 2021.

[99] Y. Chuang, C. Y. Liu, H. S. Kao, K. Y. Tien, G. L. Luo, and J. Y. Li, “Schottky barrier height modulation of metal/n-GeSn contacts featuring low contact resistivity by in-situ chemical vapor deposition doping and NiGeSn alloy formation,” *ACS Applied Electronic Materials*, vol. 3, no. 3, pp. 1334-1340, 2021.

[100] C. Schulte-Braucks, N. Driesch, S. Glass, A. T. Tiedemann, U. Breuer, A. Besmehn, J.-M. Hartmann, Z. Ikonic, Q. T. Zhao, S. Mantl, and D. Buca, “Low Temperature Deposition of High-k/Metal Gate Stacks on High-Sn Content (Si)GeSn-Alloys,” *ACS Applied Materials and Interfaces*, vol. 8, no. 220, pp. 13133–13139, 2016.

[101] J. Y. Li and J. C. Sturm, “The Effect of Germanium Fraction on High-Field Band-to-Band Tunneling in p^+-SiGe/n^+-SiGe Junctions in Forward and Reverse Biases,” *IEEE Transactions on Electron Devices*, vol. 60, no. 8, pp. 2479-2484, 2013.

[102] M. Bao and K. L. Wang, “Accurately measuring current-voltage characteristics of tunnel diodes,” *IEEE Transactions on Electron Devices*, vol. 53, pp. 2564 – 2568, 2006.

[103] R. Glicksman, and R. M. Minton, “The effect of p-region carrier concentration on the electrical characteristics of germanium epitaxial tunnel diodes,” *Solid-State Electronics* ,vol. 8, no. 5, pp. 517-519, 1965.

[104] C. Y. Liu, K. Y. Tian, P. Y. Chiu, Y. J. Wu, Y. Chuang, H. S. Kao, and J. Y. Li, "Room temperature negative differential resistance and high tunneling current density in GeSn Esaki diodes," *Advanced Materials*, vol. 34, no. 41, p. 2203888, 2022.

[105] L. Liu, R. Liang, J. Wang, and J. Xu, "Enhanced Carrier Mobility and Direct

doi:10.6342/NTU202300648

Tunneling Probability of Biaxially Strained $Ge_{1-x}Sn_x$ Alloys for Field-Effect Transistors Applications," *Journal of Applied Physics*, vol. 117, no. 18, pp. 184501, 2015.

[106] P. Y. Chiu, "Magneto-Transport and Effective Mass of Two-dimensional Hole Gases in Ge and GeSn Quantum Wells," Master thesis, National Taiwan University, https://hdl.handle.net/11296/54pa5e.

[107] L. Esaki and Y. Miyahara, "A new device using the tunneling process in narrow p-n junctions," *Solid-State Electronics*, vol. 1, no. 1, pp. 13-21, 1960.

[108] N. Holonyak and I. A. Lesk, "Gallium-Arsenide Tunnel Diodes," *Proceedings of the IRE*, vol. 48, no. 8, pp. 1405-1409, 1960.

[109] R. T. Payne, "Phonon Energies in Germanium from Phonon-Assisted Tunneling," *Physical Review*, vol. 139, no. 2A, pp. A570, 1965.

[110] R. N. Hall, J. H. Racette, and H. Ehrenreich, "Direct Observation of Polarons and Phonons During Tunneling in Group 3-5 Semiconductor Junctions," *Physical Review Letters*, vol. 4, no. 9, pp. 456, 1960.

[111] P. W. Chapman, O. N. Tufte, J. David Zook, and Donald Long, "Electrical Properties of Heavily Doped Silicon," *Journal of Applied Physics*, vol. 34, no. 11, pp. 3291, 1963.

[112] Y. Furukawa, "Magnetoresistance in Heavily Doped n-Type Germanium," *Journal of the Physical Society of Japan*, vol. 17, no. 4, pp. 630-638, 1962.

[113] Y. Chuang, C. Y. Liu, G. L. Luo, and J. Y. Li, "Electron mobility enhancement in GeSn n-channel MOSFETs by tensile strain," *IEEE Electron Device Letters*, vol. 42, no. 1, pp. 10-13, 2021.

[114] K. Y. Tian, "Electron Transport and Simulation of Band Structures of GeSn Alloys," Master thesis, National Taiwan University.

doi:10.6342/NTU202300648

[115] B. Romanczyk, P. Thomas, D. Pawlik, S. L. Rommel, W. Y. Loh, M. H. Wong, K. Majumdar, W. E. Wang, and P. D. Kirsch, "Benchmarking current density in staggered gap $In_{0.53}Ga_{0.47}As/GaAs_{0.5}Sb_{0.5}$ heterojunction Esaki tunnel diodes," *Applied Physics Letters*, vol. 102, no. 21, pp. 213504, 2013.

[116] W. C. Hou, P. C. Shih, H. H. Lin, B. Wu, and Jiun-Yun Li, "High band-to-band tunneling current in InAs/GaSb heterojunction Esaki diodes by the enhancement of electric fields close to the mesa sidewalls," *IEEE Transactions on Electron Devices*, vol. 68, no. 8, pp. 3748-3754, 2021.

[117] R. M. Minton and R. Glicksman, "Theoretical and experimental analysis of germanium tunnel diode characteristics," *Solid-State Electronics*, vol. 7, no. 7, pp. 491-500, 1964.

[118] M. W. Dashiell, R. T. Troeger, S. L. Rommel, T. N. Adam, P. R. Berger, C. Guedj, J. Kolodzey, A. C. Seabaugh, and R. Lake, "Current–Voltage Characteristics of High Current Density Silicon Esaki Diodes Grown by Molecular Beam Epitaxy and the Influence of Thermal Annealing," *IEEE Transactions on Electron Devices*, vol. 47, no. 9, pp. 1707-1714, 2000.

[119] N. Jin, S. Y. Chung, A. T. Rice, and P. R. Berger, "151 kA/cm^2 peak current densities in Si/SiGe resonant interband tunneling diodes for high-power mixed-signal applications," *Applied Physics Letters*, vol. 83, no. 16, pp. 3308-3310, 2013.

[120] S. Y. Chung, R. Yu, N. Jin, S, Y. Park, P. R. Berger, and P. E. Thompson, "Si/SiGe Resonant Interband Tunnel Diode With f_{r0} 20.2 GHz and Peak Current Density 218 kA/cm^2 for K-Band Mixed-Signal Applications," *IEEE Electron Device Letters*, vol. 27, no. 5, pp. 364-367, 2017.

[121] H. Tran, T. Pham, J. Margetis, Y. Zhou, W. Dou, P. C. Grant, J. M. Grant, S. Al-Kabi, G. Sun, R.A. Soref, J. Tolle, Y. H. Zhang, W. Du, B. Li, M. Mortazavi, and S.

doi:10.6342/NTU202300648

Q. Yu, “Si-Based GeSn Photodetectors toward Mid-Infrared Imaging Applications,” *ACS Photonics*, vol. 6, no. 11, pp. 2807-2815, 2019.

[122] C. Y. Lin, C. H. Huang, S. H. Huang, C. C. Chang, C. W. Liu, Y. C. Huang, H. Chung, and C. P. Chang, “Photoluminescence and electroluminescence from Ge/strained GeSn/Ge quantum wells,” *Applied Physics Letters*, vol. 109, no. 9, pp. 091103, 2016.

[123] J. Lambe and R. C. Jaklevic, “Molecular Vibration Spectra by Inelastic Electron Tunneling,” *Physical Review*, vol. 165, no. 3, pp. 821, 1968.

[124] H. W. Korb, A. M. Andrews, N. Holonyak Jr., R. D. Burnham, C. B. Duke, and G. G. Kleiman, “Defect and phonon effects in $In_{1-x}Ga_xP$ p-n tunnel junctions,” *Solid State Communications*, vol. 9, no. 17, pp. 1531-1536, 1971.

[125] F. Steinrisser, L. C. Davis, and C. B. Duke, “Electron and Phonon Tunneling Spectroscopy in Metal-Germanium Contacts,” *Physical Review*, ,vol. 176, no. 3, pp. 912, 1968.

[126] D. E. Cullen, E. L. Wolf, and W. Dale Compton, “Tunneling Spectroscopy in Degenerate p-Type Silicon,” *Physical Review B*, vol. 2, no. 8, pp. 3157, 1970.

[127] M. Bao and K. L. Wang, “Accurately Measuring Current–Voltage Characteristics of Tunnel Diodes,” *IEEE Transactions on Electron Devices*, vol. 53, no. 10, pp. 2564-2568, 2006.

[128] L. C. Davis and C. B. Duke, “Analysis of the tunneling measurement of electronic self-energies due to interactions of electrons and holes with optical phonons in semiconductors,” *Physical Review*, vol. 184, no. 3, pp. 764, 1969.

[129] H. Tran, T. Pham, J. Margetis, Y. Zhou, W. Dou, P. C. Grant, J. M. Grant, S. Al-Kabi, G. Sun, R. A. Soref, J. Tolle, Y. Zhang, W. Du, B. Li, M. Mortazavi, and S. Q. Yu, “Si-Based GeSn Photodetectors toward Mid-Infrared Imaging Applications,”

doi:10.6342/NTU202300648

ACS Photonics, vol. 6, no. 11, pp. 2807-2815, 2019.

[130] T. H. Liu, Y. Chuang, P. Y. Chiu, C. Y. Liu, C. H. Shen, G. L. Lou, and J. Y. Li, "High-mobility GeSn n-channel MOSFETs by low-temperature chemical vapor deposition and microwave annealing," *IEEE Electron Device Letters*, vol. 39, no. 4, pp. 468-471, 2018.

[131] Mark Lundstrom, "Fundamentals of Carrier Transport," Cambridge University Press, 2010.

[132] C. Schulte-Braucks, S. Glass, E. Hofmann, D. Stange, N. von den Driesch, J. M. Hartmann, Z. Ikonic, Q. T. Zhao, D.Buca, and S. Mantl, "Process Modules for GeSn Nanoelectronics with High Sn-contents," *Solid-State Electronics*, vol. 128, pp. 54-59, 2017.

[133] B. Mukhopadhyay, G. Sen, R. Basu, S. Mukhopadhyay, and P. K. Basu, "Prediction of Large Enhancement of Electron Mobility in Direct Gap $Ge_{1-x}Sn_x$ Alloy," *Physica Status Solidi (b)*, vol. 254, no.11, pp. 1700244, 2017.

[134] M. G. Craford, "Properties and electroluminescence of the $GaAs_{1-x}P_x$ ternary system," *Progress in Solid State Chemistry*, vol. 8, pp. 127-134, 1973.

[135] C. Schulte-Braucks, "Investigation of GeSn as Novel Group IV Semiconductor for Electronic Applications," Ph.D. dissertation, RWTH Aachen University, 2018.

[136] D. K. Schroder, "Semiconductor Material and Device Characterization," Wiley, 2006.

[137] A. Zemel, Ariel Sher, and D. Eger, "Anomalous Hall effect in p-type $Hg_{1-x}Cd_xTe$ liquid-phase-epitaxial layers," *Journal of Applied Physics*, vol. 62, no. 5, pp. 1861-1868, 1987.

[138] L. Wei, Y. Miao, Y. Ding, C. Li, H. Lu, and Y. F. Chen, "Ultra high hole mobility in Ge films grown directly on Si (100) through interface modulation," *Journal of*

doi:10.6342/NTU202300648

Crystal Growth, vol. 548, pp. 125838, 2020.

[139] L. Seidel, D. Schwarz, M. Oehme, A. Causevic, H. S. Funk, D. Weißhaupt, F. Berkmann, and J. Schulze, "Electrical Characterization of SiGeSn/Ge/GeSn-pin-Heterodiodes at Low Temperatures," *International Convention on Information, Communication and Electronic Technology (MIPRO)*, pp. 55-59, 2021.

[140] V. I. Fistul, M. I. Iglitsyn, and E. M. Omelyanovskii, "Mobility of electrons in germanium strongly doped with arsenic," *Soviet Phys. Solid State*, vol.9, no. 4, pp. 784-785, 1962.

[141] Y. Fu, K. B. Joelsson, K. J. Grahn, W.-X. Ni, G. V. Hansson, and M. Willander, "Hall factor in strained p-type doped $Si_{1-x}Ge_x$ alloy," *Physical Review B*, vol. 54, no. 16, pp. 11317, 1996.

[142] Victor I. Fistul, "Heavily Doped Semiconductors," Springer New York, 1969.

[143] D. M. Szmyd, M. C. Hanna, and A. Majerfeld, "Heavily doped GaAs:Se. II. Electron mobility," *Journal of Applied Physics*, vol. 68, no. 5, pp. 2376-2381, 1990.

[144] K. Kumar, Y. F. Hsieh, J. H. Liao, K. H. Kao, and Y. H. Wang, "Significance of Multivalley and Nonparabolic Band Structure for GeSn TFET Simulation," *IEEE Transactions on Electron Devices,* vol. 65, no. 10, pp. 4709-4715, 2018.

doi:10.6342/NTU202300648

Publication List

A: Journal Paper (學術期刊論文)

1. **Chia-You Liu**, Kai-Ying Tian, Po-Yuan Chiu, Yu-Jui Wu, Yen Chuang, Hsiang-Shun Kao, and Jiun-Yun Li, "Room temperature negative differential resistance and high tunneling current density in GeSn Esaki diodes," *Advanced Materials*, vol. 34, no. 41, p. 2203888, 2022.
2. A. J. Miller, M. Brickson, W. J. Hardy, **Chia-You Liu**, Jiun-Yun Li, A. Baczewski, M. P. Lilly, T. M. Lu, and D. R. Luhman, "Effective out-of-plane g-factor in strain-Ge/SiGe quantum dots," *Physical Review B*, vol. 106, no. 12, p. L121402, Sep. 2022
3. Wei-Chih Hou, Nai-Wen Hsu, Tz-Ming Wang, **Chia-You Liu**, Hsiang-Shun Kao, Miin-Jang Chen, and Jiun-Yun Li, "Cryogenic Si/SiGe heterostructure flash memory devices," *ACS Applied Electronic Materials*, vol. 4, no. 6, pp. 2879 – 2884, 2022.
4. Chia-Tse Tai, Po-Yuan Chiu, **Chia-You Liu**, Hsiang-Shun Kao, C. T. Harris, T. M. Lu, C. T. Hsieh, S. W. Chang, and Jiun-Yun Li, "Strain effects on Rashba spin-orbit coupling of two-dimensional hole gases in GeSn/Ge heterostructures," *Advanced Materials*, vol. 33, no. 26, p. 2007862, 2021.
5. Yen Chuang, **Chia-You Liu**, Hsiang-Shun Kao, Kai-Ying Tien, G. L. Luo, and Jiun-Yun Li, "Schottky barrier height modulation of metal/n-GeSn contacts featuring low contact resistivity by in-situ chemical vapor deposition doping and NiGeSn alloy formation," *ACS Applied Electronic Materials*, vol. 3, no. 3, pp. 1334 – 1340, 2021.
6. Yen Chuang, **Chia-You Liu**, G. L. Luo, and Jiun-Yun Li, "Electron mobility enhancement in GeSn n-channel MOSFETs by tensile strain," *IEEE Electron Device Letters*, vol. 42, no. 1, pp. 10 – 13, 2021.
7. X. Liu, T. M. Lu, C. T. Harris, F. L. Lu, **Chia-You Liu**, Jiun-Yun Li, C. W. Liu, and R. R. Du, "Thermoelectric transport of the half-filled lowest Landau level in a p-type

doi:10.6342/NTU202300648

Ge-SiGe heterostructure," *Physical Review B*, vol. 101, no. 7, p. 075304, 2020.

8. Chung-Tao Chou, N. T. Jacobson, J. E. Moussa, A. D. Baczewski, Yen Chuang, **Chia-You Liu**, Jiun-Yun Li, and T. M. Lu, "Weak antilocalization in undoped Ge/GeSi heterostructures beyond the diffusive regime," *Nanoscale*, vol. 10, no. 44, pp. 20559 –20564, 2018.
9. Tzu-Hung Liu, Yen Chuang, Po-Yuan Chiu, **Chia-You Liu**, C. H. Shen, G. L. Lou, and Jiun-Yun Li, "High-mobility GeSn n-channel MOSFETs by low-temperature chemical vapor deposition and microwave annealing," *IEEE Electron Device Letters*, vol. 39, no. 4, pp. 468 – 471, 2018.
10. Yi-Hsin Su, Yen Chuang, **Chia-You Liu**, T. M. Lu, and Jiun-Yun Li, "Effects of surface tunneling of two-dimensional hole gases in undoped Ge/GeSi heterostructures," *Physical Review Materials*, vol. 1, no. 4, p. 044601, Sep. 2017.

B: Conference Paper (研討會論文)

1. Yao-Chun Chang, Chia-Tse, **Chia-You Liu**, Cheng-Kai Hsiung, Ian Huang, Min-Jui Lin, Yu-Jui Wu, Hung-Yu Tsao, Shih-Yuan Chen, and Jiun-Yun Li, "Spin control in semiconductor heterostructures," *The 15th Asia Pacific Physics Conference (APPC15)*, August 21 – 26, 2022.
2. Kai-Ying Tien, **Chia-You Liu**, Po-Yuan, Chiu, Yen Chuang, Hsiang-Shun Kao, and Jiun-Yun Li, "Electron mobility enhancement in n-GeSn epitaxial layers by tensile strain," *2021 International Conference on Solid State Devices and Materials (SSDM)*, Virtual, Japan, Sep. 6 – 9, 2021.
3. **Chia-You Liu**, Yen Chuang, Chia-Tse Tai, Hsiang-Shun Kao, Kai-Ying Tien, and Jiun-Yun Li (invited talk), "High-performance GeSn n-MOSFETs and Esaki diodes and spin-orbit coupling in GeSn/Ge heterostructures" *2021 IEEE Summer Topicals Meeting Series*, Virtual, July 19 – 21, 2021.

doi:10.6342/NTU202300648

4. A. J. Miller, M. Brickson, W. J. Hardy, **Chia-You Liu**, Jiun-Yun Li, A. D. Baczewski, M. P. Lilly, T. M. Lu, and D. R. Luhman, "Measurement of the out-of-plane g-factor in strained Ge/SiGe using single-hole quantum dots," *2021 APS March Meeting Session J29*, Virtual, Mar. 15 – 19, 2021.
5. Chia-Tse Tai, Po-Yuan Chiu, Yen Chuang, **Chia-You Liu**, Tz-Ming Wang, Cheng-Yu Lin, C. T. Harris, T. M. Lu, and Jiun-Yun Li, "Weak anti-localization in undoped Ge/GeSn heterostructures," *2020 APS March Meeting Session L42*, Denver, CO, U.S.A., Mar. 2 – 6, 2020.
6. Chia-Tse Tai, Po-Yuan Chiu, Yen Chuang, **Chia-You Liu**, Tz-Ming Wang, Cheng-Yu Lin, C. Thomas Harris, T. M. Lu, and Jiun-Yun Li, "Demonstration of two-dimensional hole gases (2DHG) in strained GeSn quantum wells," *2020 APS March Meeting Session D27*, Denver, CO, U.S.A., Mar. 2 – 6, 2020.
7. Chia-Tse Tai, Po-Yuan Chiu, Yen Chuang, **Chia-You Liu**, Tz-Ming Wang, Cheng-Yu Lin, C. Thomas Harris, T. M. Lu, and Jiun-Yun Li, "Magneto-transport and effective mass of two-dimensional hole gases in modulation-doped and undoped GeSn/Ge heterostructures," *2020 Annual Meeting of the Physical Society of Taiwan*, Ping-Tung, Taiwan, Feb. 5 – 7, 2020.
8. Cheng-Yu Lin, Kai-Ying Tien, **Chia-You Liu**, Yen Chuang, Chung-Tao Chu, Po-Yuan Chiu, Jiun-Yun Li, "Weak antilocalization (WAL) effects in p-GeSn epilayers," *2019 International Electron Devices and Materials Symposium (IEDMS)*, New Taipei, Taiwan, Oct. 24 – 25, 2019.
9. Yi-Hsin Su, Yen Chuang, **Chia-You Liu**, T. M. Lu, and Jiun-Yun Li, "Short-range scattering source of two-dimensional hole gases in undoped Ge/GeSi heterostructures," *236th Meeting of the Electrochemical Society*, Atlanta, GA, U.S.A., Oct. 13 – 17, 2019.

doi:10.6342/NTU202300648

10. Yen Chuang, Po-Yuan Chiu, Ching-Tsung Huang, Pao-Chuang Shih, **Chia-You Liu**, Guang-Li Luo, and Jiun-Yun Li, "Germanium-tin junctionless p-FinFETs: Effects of channel doping concentration and fin width," *236th Meeting of the Electrochemical Society*, Atlanta, GA, U.S.A., Oct. 13 – 17, 2019.
11. **Chia-You Liu** (poster), Po-Yuan Chiu, Yen Chuang, and Jiun-Yun Li, "Indirect-to-direct bandgap transition of GeSn by phonon-assisted tunneling spectra in Esaki diodes," *2019 International Conference on Solid State Devices and Materials (SSDM)*, Nagoya University, Aichi, Japan, Sep. 2 – 5, 2019.
12. **Chia-You Liu** (oral), Yen Chuang, G. L. Luo, and Jiun-Yun Li, "Strained GeSn films with a high Sn fraction of ~ 22% by reduced pressure chemical vapor deposition," *2019 2nd joint International SiGe Technology and Device Meeting (ISTDM)/International Conference on Silicon Epitaxy and Heterostructures (ICSI)*, Madison, WI, U.S.A., June 2 – 6, 2019.
13. T. M. Lu, Jiun-Yun Li, D. R. Luhman, W. J. Hardy, L. A. Tracy, C. T. Harris, N. T. Jacobson, A. D. Baczewski, J. E. Moussa, L. N. Maurer, M. Brickson, Yi-Hsin Su, Chung-Tao Chou, Yen Chuang, and **Chia-You Liu**, "Holes in germanium quantum wells and their potential applications in quantum computing," *2019 MRS Spring Meeting QN 06*, Pheonix, AZ, U.S.A., April 22 – 29, 2019.
14. Jia-You Liu, Po-Yuan Chiu, Yen Chuang, **Chia-You Liu**, G. L. Luo, and Jiun-Yun Li, "High dopant activation of phosphorus in strained and relaxed GeSn by rapid thermal annealing and microwave annealing," *3rd Electron Devices Technology and Manufacturing (EDTM) Conference 2019*, Singapore, Mar. 13 – 15, 2019.
15. Jia-You Liu, Yen Chuang, **Chia-You Liu**, G. L. Luo, and Jiun-Yun Li, "A high I_{ON}/I_{OFF} ratio of 6 x 10^5 in germanium-tin n+/p junctions by phosphorus ion implantation," *3rd Electron Devices Technology and Manufacturing (EDTM)*

doi:10.6342/NTU202300648

Conference 2019, Singapore, Mar. 13 – 15, 2019.

16. Chung-Tao Chou, Yen Chuang, **Chia-You Liu**, and Jiun-Yun Li, "Gate-tunable spin-orbit coupling effects in an undoped Ge/GeSi heterostructure," *2019 Annual Meeting of the Physical Society of Taiwan*, Hsin-Chu, Taiwan, Jan. 23 – 25, 2019.
17. Ching-Tsung Huang, Yen Chuang, **Chia-You Liu**, and Jiun-Yun Li, "Ferroelectric-based resistive RAM with an extremely high On/Off ratio of 108," *2018 eMRS Spring Meeting, Symposium R*, Strasbourg, France, June 18 – 22, 2018.
18. Ching-Tsung Huang, Yen Chuang, **Chia-You Liu**, and Jiun-Yun Li, "Direct-bandgap photoluminescence in strained and relaxed GeSn thin films and Ge/GeSn/Ge quantum well structures," *2018 eMRS Spring Meeting, Symposium G*, Strasbourg, France, June 18 – 22, 2018.
19. Nai-Wen Hsu, Po-Yuan Chiu, Chung-Tao Chou, Yen Chuang, **Chia-You Liu**, C. T. Harris, T. M. Lu, and Jiun-Yun Li, "First experimental demonstration of a two-dimensional electron gas (2DEG) in a strained Ge quantum well," *2018 eMRS Spring Meeting, Symposium G*, Strasbourg, France, June 18 – 22, 2018.
20. Po-Yuan Chiu, **Chia-You Liu**, Yen Chuang, C. T. Harris, T. M. Lu, and Jiun-Yun Li, "Effective mass of a high-mobility two-dimensional hole gas (2DHG) in a strained GeSn quantum well," *2018 eMRS Spring Meeting, Symposium G*, Strasbourg, France, June 18 – 22, 2018.
21. Po-Yuan Chiu, **Chia-You Liu**, Yen Chuang, C. T. Harris, T. M. Lu, and Jiun-Yun Li, "Modulation of two-dimensional hole gas density in an undoped Ge/GeSi heterostructure by ion implantation," *2018 eMRS Spring Meeting, Symposium G*, Strasbourg, France, June 18 – 22, 2018.
22. **Chia-You Liu** (oral), Po-Yuan Chiu, Yen Chuang, Ching-Tsung Huang, and Jiun-Yun Li, "High peak-to-valley current ratio of 15 in a relaxed GeSn Esaki diode," *2018 1st*

doi:10.6342/NTU202300648

joint International SiGe Technology and Device Meeting (ISTDM)/International Conference on Silicon Epitaxy and Heterostructures (ICSI), Potsdam, Germany, May 27 – 31, 2018.

23. Yen Chuang, Ching-Tsung Huang, **Chia-You Liu**, and Jiun-Yun Li, "Extremely low threading dislocation density (< 10^5 cm^{-2}) in relaxed GeSn on a superlattice buffer layer by reduced-pressure chemical vapor deposition," *2018 1st joint International SiGe Technology and Device Meeting (ISTDM)/International Conference on Silicon Epitaxy and Heterostructures (ICSI)*, Potsdam, Germany, May 27 – 31, 2018.
24. Yi-Hsin Su, Chung-Tao Chou, Nai-Wen Hsu, Yen Chuang, **Chia-You Liu**, and Jiun-Yun Li, "Scattering mechanisms of two-dimensional hole gases in undoped Ge/GeSi heterostructures," *2018 Annual Meeting of the Physical Society of the Republic of China (Taiwan)*, Taipei, Taiwan, Jan. 24 – 26, 2018.
25. Yen Chuang, Po-Yuan Chiu, Ching-Tsung Huang, **Chia-You Liu**, and Jiun-Yun Li, "Thermal stability of n-type germanium-tin epitaxial films," *10th International Conference on Silicon Epitaxy and Heterostructures (ICSI-10)*, Warwick, U.K., May 14 –19, 2017.
26. **Chia-You Liu** (poster), Po-Yuan Chiu, Yen Chuang, Pao-Chuan Shih, and Jiun-Yun Li, "Negative differential resistance in GeSn Esaki diodes at room temperature," *10th International Conference on Silicon Epitaxy and Heterostructures (ICSI-10)*, Warwick, U.K., May 14 –19, 2017.
27. Yi-Hsin Su, Yen Chuang, **Chia-You Liu**, Po-Yuan Chiu, Nai-Wen Hsu, T. M. Lu, and Jiun-Yun Li, "An equilibrium-nonequilibrium crossover in charge distributions and weak antilocalization of Ge and GeSn two-dimensional hole gases," *10th International Conference on Silicon Epitaxy and Heterostructures (ICSI-10)*, Warwick, U.K., May 14 –19, 2017.

doi:10.6342/NTU202300648